Shock Wave Science and Technology Reference Library 10

Friedrich Seiler
Ozer Igra *Editors*

Hypervelocity Launchers

Springer

Shock Wave Science and Technology Reference Library 10

Collection Editors

Hans Grönig
Yasuyuki Horie
Kazuyoshi Takayama

The new Springer collection, Shock Wave Science and Technology Reference Library, conceived in the style of the famous Handbuch der Physik has as its principal motivation to assemble authoritative, state-of-the-art, archival reference articles by leading scientists and engineers in the field of shock wave research and its applications. A numbered and bounded collection, this reference library will consist of specifically commissioned volumes with internationally renowned experts as editors and contributing authors. Each volume consists of a small collection of extensive, topical and independent surveys and reviews. Typical articles start at an elementary level that is accessible to non-specialists and beginners. The main part of the articles deals with the most recent advances in the field with focus on experiment, instrumentation, theory, and modeling. Finally, prospects and opportunities for new developments are examined. Last but not least, the authors offer expert advice and cautions that are valuable for both the novice and the well-seasoned specialist.

Shock Wave Science and Technology Reference Library

Collection Editors

Hans Grönig

Hans Grönig is Professor emeritus at the Shock Wave Laboratory of RWTH Aachen University, Germany. He obtained his Dr. rer. nat. degree in Mechanical Engineering and then worked as postdoctoral fellow at GALCIT, Pasadena, for one year. For more than 50 years he has been engaged in many aspects of mainly experimental shock wave research including hypersonics, gaseous and dust detonations. For about 10 years he was Editor-in-Chief of the journal Shock Waves.

Yasuyuki Horie

Professor Yasuyuki (Yuki) Horie is internationally recognized for his contributions in high-pressure shock compression of solids and energetic materials modeling. He is a co-chief editor of the Springer series on Shock Wave and High Pressure Phenomena and the Shock Wave Science and Technology Reference Library, and a Liaison editor of the journal Shock Waves. He is a Fellow of the American Physical Society, and Secretary of the International Institute of Shock Wave Research. His current interests include fundamental understanding of (a) the impact sensitivity of energetic solids and its relation to microstructure attributes such as particle size distribution and interface morphology, and (b) heterogeneous and nonequilibrium effects in shock compression of solids at the mesoscale.

Kazuyoshi Takayama

Professor Kazuyoshi Takayama obtained his doctoral degree from Tohoku University in 1970 and was then appointed lecturer at the Institute of High Speed Mechanics, Tohoku University, promoted to associate professor in 1975 and to professor in 1986. He was appointed director of the Shock Wave Research Center at the Institute of High Speed Mechanics in 1988. The Institute of High Speed Mechanics was restructured as the Institute of Fluid Science in 1989. He retired in 2004 and became emeritus professor of Tohoku University. In 1990 he launched Shock Waves, an international journal, taking on the role of managing editor and in 2002 became Editor-in-Chief. He was elected president of the Japan Society for Aeronautical and Space Sciences for one year in 2000 and was chairman of the Japanese Society of Shock Wave Research in 2000. He was appointed president of the International Shock Wave Institute in 2005. His research interests range from fundamental shock wave studies to the interdisciplinary application of shock wave research.

More information about this series at http://www.springer.com/series/8774

Friedrich Seiler · Ozer Igra
Editors

Hypervelocity Launchers

Springer

Editors
Friedrich Seiler
Institute of Fluid Mechanics (ISTM)
Karlsruhe Institute of Technology (KIT)
Karlsruhe
Germany

Ozer Igra
Department of Mechanical Engineering
Ben-Gurion University of the Negev
Beer Sheva
Israel

Shock Wave Science and Technology Reference Library
ISBN 978-3-319-26016-7 ISBN 978-3-319-26018-1 (eBook)
DOI 10.1007/978-3-319-26018-1

Library of Congress Control Number: 2015954969

Springer Cham Heidelberg New York Dordrecht London

Printed on acid-free paper

Springer International Publishing AG Switzerland is part of Springer Science+Business Media (www.springer.com)

Preface

Various types of mass accelerators have been developed worldwide in the past, based on different principles. In the early 80s Professor Abe Hertzberg, at that time a professor at the University of Washington (UW) in Seattle, USA, proposed using the Ram accelerator concept for accelerating projectiles to hypersonic velocities. This concept starts with a tube filled with compressed combustible gas mixture equipped with membranes to close both the tube ends. The projectile was injected into the tube at a supersonic speed relative to in-the-tube-gases. The combustible gas was ignited by the high temperature gas generated behind the shock wave located in vicinity of the projectile leading edge. The significant temperature increase is associated with an increase in the gas pressure needed for thrust production. On the other hand, the best known accelerator is the powder gun; the maximum achievable speed while using the powder gun is moderate because of the heavy powder gases in comparison with the light gas used in hypersonic accelerators where hypervelocity speeds in the range of several km/s are reached.

In the present volume numerous descriptions of Ram accelerators are presented as well as descriptions of light gas guns and a ballistic range including explanation of shock waves in solids. These descriptions provide a good overview of the progress made and the present state of the Ram accelerator technology worldwide.

In a light-gas gun (using helium gas), projectile velocities ranging up to 7 km/s are theoretically attainable. Such facilities are mainly used for studying projectile impact on investigated material. Typical examples for impact investigations are comets or asteroids penetrating into the Earth's atmosphere and their final impact on the Earth.

The usage of Ram accelerators is relatively new in comparison with the development of the light-gas gun and the electromagnetic accelerator, i.e., the rail gun, and its operation is still in the development stage. Many Ram accelerator facilities have been built around the globe, some having small tube calibers and some with large caliber, up to the 120 mm pipe diameter at the Army Research Laboratory (ARL) in Maryland, USA. Smaller Ram accelerators were developed at the French–German Research Institute of Saint-Louis (ISL), France: one having a

30 mm caliber and another with a 90 mm caliber acceleration tube. Additional Ram accelerators were built in Japan, at Tohoku University in Sendai with a 25 mm rectangular cross-section. In China, at the China Aerodynamics R&D Center (CARDC) a 37 mm bore accelerator was tested. Different approaches have been used: (a) where the projectile is guided by fins in a smooth pipe and (b) where the projectile is centered by rails fixed within the tube. In both cases a gap exists between the projectile and the tube.

As of today, in spite of all efforts made, the maximum projectile velocity has not exceeded 3 km/s. Therefore, the goal to reach orbital speeds has not been realized. The reason for this failure is the fact that the projectile material quickly burns up while reaching the needed high combustion temperatures required for projectile acceleration inside the Ram tube. As a result, many research institutes and companies decided to freeze their investigations of Ram accelerators at the beginning of 2000. However, some experiments have been carried out at a low level even thereafter. This lull did not involve the theoretical investigations. For example, at the National University of Seoul in Korea, numerical investigations of the combustion dynamics in a Ram accelerator are conducted and their findings are reported in this volume. Hopefully, a rebirth of the Ram accelerator concept will take place in the near future when new materials that can withstand the high gas temperatures without ablating will be found. Should this be the case, the dream of Prof. Hertzberg could be fulfilled: Using the Ram accelerator as a device to launch a capsule into orbit or to other planets. As noted, the biggest problem in reaching the desired projectile speed is the projectile material. The early projectiles were made from magnesium in order to save weight. The high combustion temperatures associated with high heat transfer into the magnesium resulted in melting and ablation. Thus, the projectile guidance became more and more difficult and eventually failed. In the next step, projectiles were made of aluminum. Ablation was lower, but still very problematic. Also, projectiles made of titanium, iron, and composite materials were tested in various Ram devices.

Finally, we would like to thank all authors for their contributions to this volume. Their participation is key to the success of this book.

Karlsruhe, Germany — Friedrich Seiler
Beer Sheva, Israel — Ozer Igra
January 2016

Contents

About the Editors

Friedrich Seiler is well-known for his studies in shock tube technology at the French-German Research Institute of Saint-Louis in France (ISL). As a scientist at the ISL, from 1980 on, his research mainly deals with high-velocity flight aerodynamics, hypersonics, optical measuring techniques and fundamental research in the field of ram acceleration. Until his retirement in the year 2011, he became in 1997 head of ISL's Aerothermodynamics & Shock Tube Laboratory. He is a member of the editorial board of the "International Journal on Shock Waves" and is also associated to the International Advisory Committee of the "International Symposium on Shock Waves (ISSW)" and the "International Symposium on Flow Visualization (ISFV)". From the University of Karlsruhe in Germany he received his "Dipl.-Phys." degree in physics and his "Dr.-Ing." degree from the same University. Also the University of Karlsruhe, now Karlsruhe Institute of Technology (KIT), has awarded him in 1992 the rank "Professor" and since then he is Lecturing Professor for Fluid Mechanics at KIT. His current interest is focused on the dynamics of Mach waves in supersonic jets. He contributed to a theory which describes the Mach wave behavior using a new approach.

Ozer Igra has devoted most of his research activities to studying various aspects of shock and blast waves phenomena. His studies include both experimental and numerical investigations of strong (ionizing shocks in argon) and moderate to weak shock/blast wave in gases and in suspensions. Results of his investigations can be found in his many publications available in leading professional journals dealing with gas-dynamic flows and shock waves. He received his B.Sc. and M.Sc. degrees from the Department of Aeronautical Engineering of the Technion, Israel Institute of Technology and his Ph.D. from the Institute for Aerospace Engineering, University of Toronto, Canada. He Joined the Ben Gurion University of the Negev in 1971. There he established the Shock Waves Laboratory, supervised many masters, doctorate, and postdoc students and served as the chairmanof the Department of Mechanical Engineering and thereafter as the Dean of the Faculty of Engineering. He is on the International Advisory Committee of the International Symposium on Shock Waves (ISSW) and the International Symposium on Shock Interactions (ISIS), and on the editorial board of the Shock Waves Journal.

Part I
Gas Gun

Light Gas Gun

Eugene B. Zaretsky

Abstract The Light Gas Gun is an important laboratory tool for study of the high strain rate response of solids and liquids. The present chapter contains a brief description of the light gas gun theory and of the measures required for successful gun operation in the laboratory environment. The chapter is concluded by an example of the use of the light gas gun in the study of the impact response of OFC copper.

1 Introduction

The Light Gas Gun (Gun, in the following) is a laboratory tool which makes it possible to accelerate a projectile of given mass up to velocities varying between several tens of m/s to much more than 1000 m/s. Usually the goal of such acceleration is to produce a high strain rate loading of the material studied (usually called sample) and to study the response of the sample to such a loading. Usually the sample studied is located close to the gun muzzle, within a chamber having a number of entrances suitable for different types of diagnostics. As a laboratory tool the Gun has to meet several requirements:

1. The Gun must allow a continuous varying of the projectile muzzle velocity within the entire velocity range,
2. The muzzle velocity of the projectile must be known in advance with reasonable certainty (usually less than 1 % deviation),
3. The triggering of the Gun must be certain and independent of the muzzle velocity,
4. The projectile must be accelerated toward the gun muzzle with no change of its shape.

E.B. Zaretsky (✉)
Department of Mechanical Engineering, Ben Gurion University, 84105 Beer Sheva, Israel
e-mail: zheka@bgu.ac.il

F. Seiler and O. Igra (eds.), *Hypervelocity Launchers*,
Shock Wave Science and Technology Reference Library 10,
DOI 10.1007/978-3-319-26018-1_1

5. The muzzle projectile velocity must be measured with high (better than 0.5 %) accuracy,
6. The Gun sample assembly must be capable of creating the required boundary conditions (usually 1-D strain loading) at the impacted sample surface, and, finally,
7. The Gun must be safe.

In the following we will discuss how the above requirements may be met and how their implementation in real laboratories looks.

2 Requirements No. 1 and No. 2

The schematic of a gas gun is shown in Fig. 1. It consists mainly of a gun barrel in which a projectile is accelerated by high pressured light gas acting on the projectile back.

Let us denote the barrel and the projectile cross-section as A, the projectile mass as M, and the acting gas pressure as P_0. The equation of motion of the projectile is

$$P_0 A = M\frac{du_p}{dt} = Mu_p\frac{du_p}{dx_p}, \tag{1}$$

where x_p is the projectile position in the Gun barrel having total length L and $u_p = dx_p/dt$ is the projectile velocity. Integrating (1) yields for the projectile muzzle velocity V_m

$$(V_m)^2 = \left[u_p(L)\right]^2 = 2\frac{A}{M}\int_0^L P_0 dx_p. \tag{2}$$

Substituting the integral in (2) by its average

$$\bar{P}_0 = \frac{1}{L}\int_0^L P_0 dx_p,$$

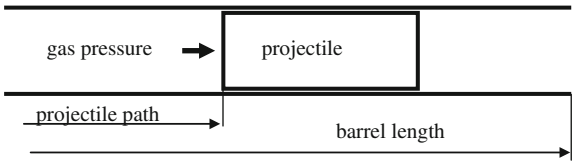

Fig. 1 Schematics of the projectile in the Gun's barrel

one has

$$V_m = \sqrt{2AL\bar{P}_0/M} = \sqrt{2L\bar{P}_0/m}, \tag{3}$$

where $m = M/A$ is the specific mass of the projectile per unit area. Equation (3) illustrates clearly on which factors the muzzle projectile velocity depends. In order to increase the muzzle velocity either the barrel length L or average pressure $\bar{P}_0$ must be increased or the projectile specific mass must be decreased. All these approaches, however, have serious limitations. The longer the barrel the more pronounced is the role of the friction forces preventing the growth of the projectile velocity; the increase of $\bar{P}_0$ finds its limitation in the barrel's strength; the decrease of m may make the experiment meaningless.

The use of Eq. (3) for estimating the projectile muzzle velocity requires the knowledge in advance of the average gas pressure during the Gun operation. Simple Eqs. (1)–(3) are not capable of providing such information. This, however, can be done by use of the following approach. Let us assume that prior to the Gun operation the gas to the left of the projectile in Fig. 1 is separated from the projectile by a partition. (Technical realizations of the partition will be discussed later.) In the theory of guns [1] such gun is called "the gun with pre-burned propellant" or PP gun. When the partition is withdrawn the projectile starts to move. The equation of motion of the projectile in the same notations is [2]

$$m\frac{du_p}{dt} = P_0\left(1 - \frac{\gamma - 1}{2}\frac{u_p}{c_0}\right)^{\frac{2\gamma}{\gamma-1}}, \tag{4}$$

where γ is the adiabatic exponent of the gas having speed of sound c_0. Integrating (4) yields the speed of the projectile u_p as a function of time

$$u_p(t) = \frac{2c_0}{\gamma - 1}\left\{1 - \left[1 + \frac{\gamma + 1}{2mc_0}P_0 t\right]^{-\frac{\gamma-1}{\gamma+1}}\right\}, \tag{5}$$

where $2c_0/(\gamma - 1)$ is the speed of outflow of the gas into a vacuum (so-called "escape velocity") equal approximately to 1700 m/s for air, to 2900 m/s for helium, and 6500 m/s for hydrogen. These values are related to the maximum muzzle velocities achievable with use of the corresponding gas when the specific projectile mass approaches zero. Equation (5) when integrated gives the location L of the projectile in the gun barrel

$$L(t) = \frac{2c_0}{\gamma - 1}\left\{t + \frac{mc_0}{P_0}\left[1 + \frac{\gamma + 1}{2mc_0}P_0 t\right]^{\frac{2}{(\gamma+1)}}\right\}. \tag{6}$$

Although Eqs. (5) and (6) cannot be solved analytically to provide the dependence of muzzle velocity $u_p(P_0, m, L)$ on barrel length such dependence may be

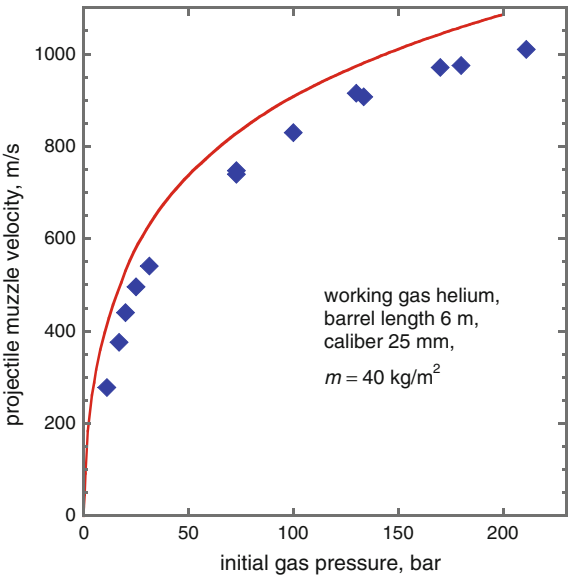

Fig. 2 The muzzle velocity calculated with the aid of Eqs. (5) and (6) for "pre-burned propellant" gun (*solid line*) and experimentally measured projectile velocities (*diamonds*)

easily computed. It is shown in Fig. 2 for the case of accelerating the projectile by helium compressed up to different initial pressures. The values of the muzzle projectile velocities measured experimentally with a 6 m smooth bore gun of the Laboratory of Dynamic Behavior of Materials at Ben Gurion University are shown for comparison.

It is apparent from Fig. 2 that Eqs. (5) and (6) are capable of predicting the muzzle projectile velocity with reasonable accuracy, to within 5–10 %. The observed overestimating of the projectile muzzle velocity has several causes.

First, Eqs. (5) and (6) do not account for finite initial volume of the compressed gas. Such a situation corresponds to the finite length of the part of the gun initially filled with compressed gas (part of the gun to the left of the projectile in Fig. 1) and, respectively, to the indefinite volume and mass M of the gas. The ratio M/m is the important characteristic of a PP gun; the shorter the gas chamber the lower the M/m ratio and the stronger is the departure of the actual muzzle velocity from the values obtained using Eqs. (5) and (6). The cause of this departure is the drop of the pressure at the projectile rear while the head release characteristic generated at the projectile/gas interface arrives at the interface after reflecting from the rear chamber wall. The shorter the chamber, i.e. the smaller the M/m ratio, the sooner this arrival takes place. Estimating the influence of the M/m ratio may be performed only with use of a computer [1]. Such calculations show that the reduction of M/m from ∞ to 1 leads to a 40 % drop in the muzzle velocity while $\mathrm{M}/m = 0.1$ leads to the almost three fold velocity decrease with respect to the $\mathrm{M}/m = \infty$ case.

Another cause of overestimating the gun performance is neglecting the build up of the pressure ahead of the moving projectile. This pressure P_f may be estimated using the following approximation [3],

$$P_f \approx P_a \left\{ 1 + \frac{\gamma_a(\gamma_a+1)}{4}\left(\frac{u_p}{c_a}\right)^2 + \gamma_a \frac{u_p}{c_a}\left[1 + \left(\frac{\gamma+1}{4}\right)^2\left(\frac{u_p}{c_a}\right)^2\right]\right\}, \quad (7)$$

where P_a is the initial gas (usually air) pressure in the gun barrel ahead of the projectile, and c_a and γ_a are the speed of sound and the adiabatic exponent of this gas, respectively. In the case of air the expression in the parenthesis varies between 1 at $u_p = 0$ and 25 at $u_p = 1000$ m/s. This means that in the case of $P_a \approx 1$ bar a muzzle velocity of about 1000 m/s, Fig. 2, will be reduced to 50 m/s. Another result of the pressure build up ahead of the projectile is the development of a shock wave in the air that propagates along the barrel toward the sample and subsequent loading of the sample by this wave prior to its loading by the projectile. This, however, is related to requirement No. 4 and will be discussed later. With respect to requirements No. 1 and No. 2 we can conclude that the PP guns allow a continuous varying of the projectile muzzle velocity within a sufficient velocity range. Using a relatively simple description of the projectile acceleration allows predicting the muzzle projectile velocity with an uncertainty of about 10–15 %. For a more accurate prediction the gun-gas-projectile system has to be calibrated over the entire velocity range.

3 Requirement No. 3

The accuracy and the repeatability of the muzzle projectile velocity strongly depend on the quality of the gun triggering. There are several methods of triggering used in different laboratories.

The usual, so-called wrap-around, design of the breach of the gas guns is shown schematically in Fig. 3 [4]. The design allows a substantial decrease in the total gun length and provides additional safety to the part of the gun under maximum gas pressure. 3–6 annular ports allow fast escape of the pressurized gas from the high pressure chamber into the gun barrel. Such a pattern of the barrel-chamber assembly dictates the design of the triggering schemes to be used.

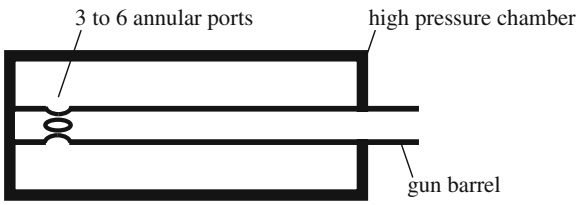

Fig. 3 Principle design of gas guns breach

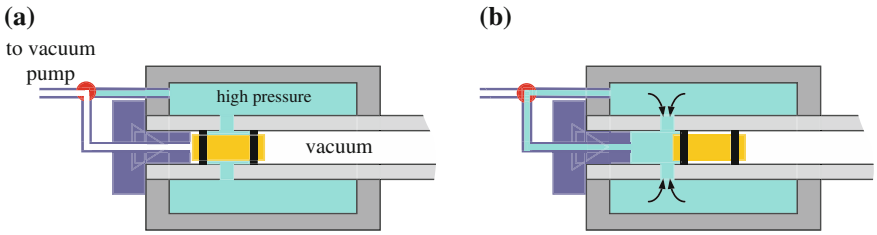

Fig. 4 The trigger mechanism without moving parts before **a** and during **b** the gun shot

The simplest trigger scheme shown in Fig. 4 does not employ any moving or ruptured part. The annular ports in the barrel are closed by the projectile itself and the closure is sealed by two O-rings, one at the head and one at the rear part of the projectile. The barrel both ahead and behind the projectile is pumped down to the same pressure (usually a few millibars) in order to prevent premature motion of the projectile due to the pressure difference.

Triggering the gun is performed by switching the vacuum pipeline to the high pressure chamber. Small amounts of the gas from the chamber start to move the projectile, thus opening the annular ports. Such a triggering scheme is very reliable (no moving parts) and is characterized by reasonable repeatability of the projectile muzzle velocity. The main disadvantage of the scheme is the impossibility to use it when the gas pressure is either very low or very high. In the former case the gas must both propel the projectile and overcome the friction force between the O-rings and the barrel surface. Although this force may be reduced by use of a lubricant, it is still difficult to keep it under control. In the case of very high gas pressures the projectile body is kept under high compressive stress which cannot be sustained by a hollow (low specific mass) projectile. This leads to the substantial increase of the specific projectile mass and, respectively, to the decrease of the muzzle velocity.

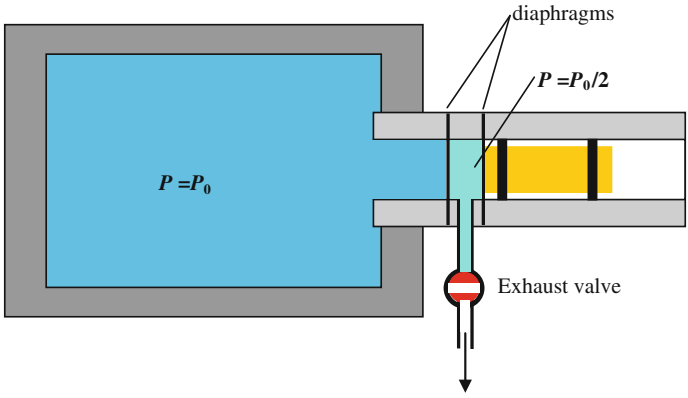

Fig. 5 Double diaphragm breach

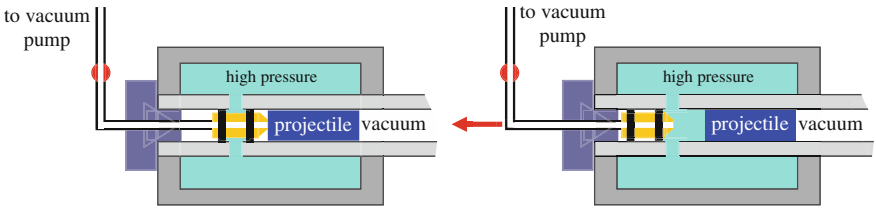

Fig. 6 Wide velocity range gun breach

The use of highly pressurized gas requires the change of the triggering scheme. Traditionally [4] this is done by substituting the breach shown in Fig. 4 by the double diaphragm breach shown in Fig. 5. The diaphragms have to be selected to withstand the pressure slightly higher than $P_0/2$. Respectively, it should be opened with certainty when reaching the pressure P_0. In this case triggering the gun is produced by opening the exhaust valve connected to the inter-diaphragm space initially pressurized up to $P_0/2$. As result, first the left and, then, the right diaphragm experiences the pressure P_0.

The two types of breaches have been successfully used since 1970 and continue to be used in the Shock Wave Institute (formerly the Shock Wave Center) at the Physics Department of the Washington State University, Pullman, WA.

The use of two breaches for different velocity ranges leads to some inconvenience in the use of gun, especially in a situation of parallel studies of several problems. The triggering scheme described below allows widening the range of the muzzle velocities without changing the breach. The schematic of this trigger is shown in Fig. 6. This trigger does contain moving parts but the projectile is free of O-rings, the pressure does not act at the projectile lateral surface and the only pressure action is the projectile acceleration.

In this scheme the annular ports are closed by the O-ring equipped dummy projectile while the real projectile is O-ring free and prior to the shot is located in the gun barrel ahead of the dummy. The dummy projectile is a solid body of tempered aluminum alloy with a tiny (3 mm diameter) axial drilling for attracting the genuine projectile to the dummy one. This "pumping" prevents escape of the O-ring free projectile while the space ahead of the projectile is pumped down to few millibars.

Triggering is performed by moving the dummy projectile to the left. Since the O-ring free projectile starts to move with the beginning of the opening of the annular barrel ports it is important that the process of the ports opening will be fast and reproducible. This may be achieved by use of a standard double acting pneumatic cylinder [5] as the trigger actuator. The experimental pressure-velocity dependence shown in Fig. 2 has been obtained using standard ISO 15552 SU50 × 75 pneumatic cylinder.

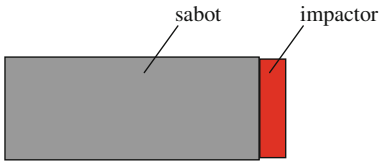

Fig. 7 Schematics of a two-part projectile

4 Requirement No. 4

Several important issues have to be taken into account in the design of the gas gun projectile. Usually the projectile consists of at least two parts as shown in Fig. 7. The sabot is the load bearing part of the projectile responsible for its regular motion through the gun barrel and for correct positioning of the second projectile part, the impactor, at the instant of its collision with the sample.

Unlike the impactor the sabot is usually partially hollow in order to avoid accelerating the "dead" mass but its wall still should have sufficient thickness for preserving the constancy of its external diameter along its entire length. The usual materials for producing the gas gun sabots are high strength aluminum alloys (large caliber guns) or either cast or extruded polymethylmethacrylate (PMMA). Although the PMMA sabots have to be made with thicker walls than those of the aluminum sabots the specific mass of the former is lower.

The specific mass of the sabot-projectile unit of the 100-mm aluminum is of about 140 kg/m^2, that of the PMMA one is about 40 kg/m^2. As apparent from the drawings shown in Fig. 8 the gliding sabot surface has to be produced with high tolerance which has to match the tolerance of the internal surface of the barrel. In the case of the 100-mm WSU gun the internal barrel diameter was 101.62 (±0.02) mm while the sabot outer diameter is 101.53 (−0.012) mm. Such level of tolerance may be easily achieved with a metal sabot. In the case of PMMA sabot a careful turning with cooling the piece is required. Moreover, to preserve the sabot tolerance the temperature in the laboratory must be 23 ± 2 °C. The required, within 0.1 mrad, orthogonality of the front and lateral sabot surfaces may be easily achieved by final turning treatment of the surfaces in a CNC turning machine. This is especially important for the Requirement No. 6.

5 Requirement No. 5

Accurate measurement of the projectile muzzle velocity is crucial for obtaining reliable experimental information on the impact response of materials. Usually this is done using electrically charged pins located in vicinity of the gun muzzle and separated from one another by some distance known in advance. Since its first use

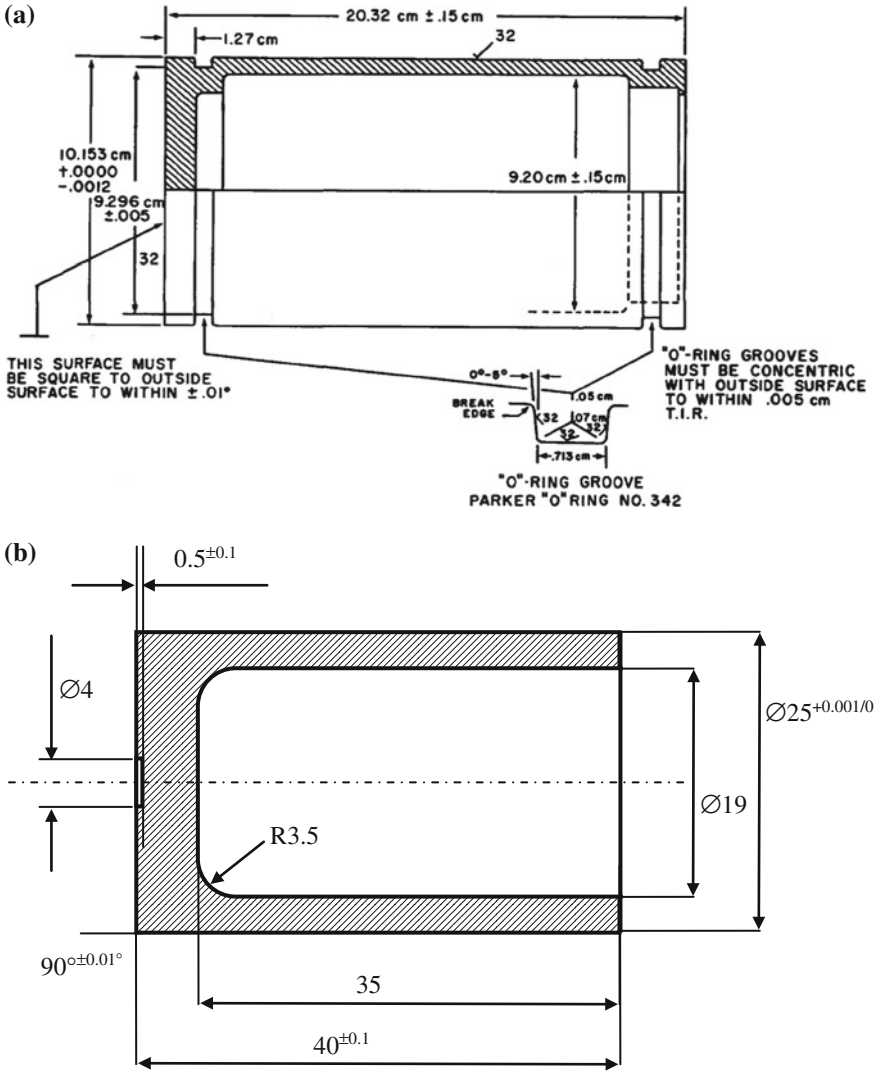

Fig. 8 Sabots drawings of the 100 mm gun **a** of the Washington State University [4]; made of aluminum alloy 6061-T6; and **b** of the 25 mm gun of the Ben-Gurion University (made of PMMA)

in the 100-mm gun of WSU [4] the technique has become widely spread in gun equipped laboratories. The schematics of such a pin assembly are shown in Fig. 9.

The four pins shown in Fig. 9 represent the real situation in which each pin in Fig. 9 stands for four pins in the real gun. Each pair of pins consists of a charged pin and a grounding pin which makes contact with the projectile shortly before that of the charged pin. The simplest electrical circuits used for producing the electrical signal while the grounding and charged pins are shorted is shown in Fig. 10.

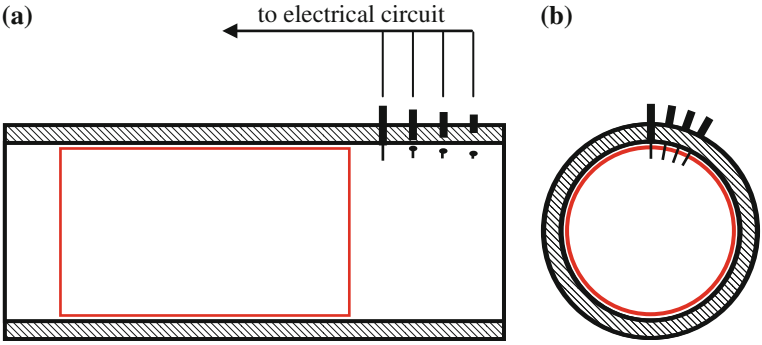

Fig. 9 Schematics of the arrangement of electrical pins in the gun barrel; the view from the side **a** and from the gun muzzle **b**

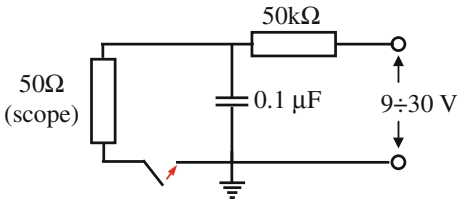

Fig. 10 Electrical circuit producing 9–30 V electrical pulse when the grounding and charged pins are shorted (shown by *arrow*)

The use of large, several tens of kilo-ohms, resistor limits the charging current of the capacitor. When the pins are shorted the capacitor discharges through the 50-Ω input of the scope. The pin circuits suitable for operation with several pins may be found in [4].

Usually the pins are assembled in a separate block which after measuring the pin spacing may be inserted in their "firing" position near the gun muzzle. The working part of the pins, a brass or steel whisker of a few tenth of a millimeter diameter, makes contact with the projectile at one third of its length. The pins must be stair stepped, as shown in Fig. 9a, in order to provide for each pin good contact with the "flush" part of the projectile. Initially the pin spacing was determined by a measuring microscope capable of providing spacing uncertainty of about 10 μm [4]. Later the spacing measurements were essentially improved by using optical translation stages with 2-μm spatial resolution [6]. By use of this technique the uncertainty of the projectile muzzle velocity has been reduced to the presently accepted level of 0.1 %.

Another method of measurement of the projectile muzzle velocity utilizes the electrical pin arrangement either directly at the sample or at the sample holder. The pins usually employed in such a measurements are pieces of a semi rigid coaxial cable shown in Fig. 11. In particular the EZ-47 (outer diameter 0.047 in.) cable [7], is widely used.

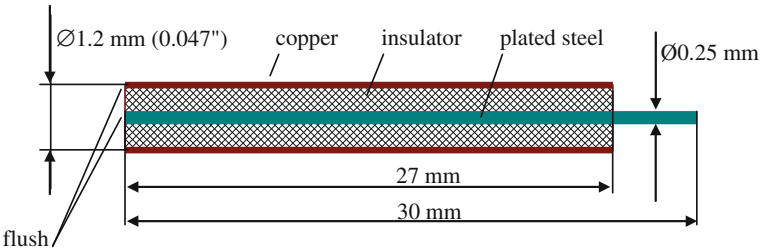

Fig. 11 Semi rigid EZ-47 coaxial cable as a coaxial charged pin

The impacted (left in the Fig. 11) edge of the pin has to be made flush in order to provide simultaneous contact of the outer and inner conductors with impactor. Shorting the outer and inner conductors of the pin corresponds to the closing of the electrical circuit shown in Fig. 10. As result the capacitor starts to discharge producing the electrical pulse of 9 ÷ 30 V amplitude at the oscilloscope entrance. Sometimes instead of coaxial charged pins piezoelectric pins are used. An example of such a pin (Dynasen Inc., CA, USA [8]) with an embedded PZT-5A crystal disk is shown in Fig. 12. The standard pin lengths are 1–3-in. The shocked PZT crystal when shocked generates an electrical pulse with amplitude from several volts at weak impact to more than 100 V at 0.2 GPa impact.

Preparation of the coaxial or PZT pins for the measurement of projectile muzzle velocity differs from that of in-barrel pins. The stages of such a preparation are shown in Fig. 13. First the studied sample is assembled with the sample ring which should fix the sample at the sample holder described in the next section. The sample must be fixed flush with the sample ring and with the pin which will be shortened by the striking impactor at the frontal sample surface. To made the assembly flush an optical flat of submicron non-planarity is used.

In such an assembly the spacers (three 1 or 2-mm gauge blocks) determine the distance between the pins and, in turn, the accuracy of the muzzle velocity measurements. The uncertainty of the projectile muzzle velocity measured by such method is about 1 %.

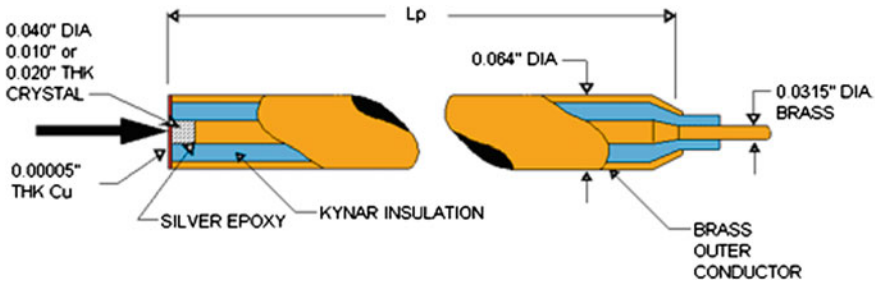

Fig. 12 Piezoelectric pin of Dynasen company

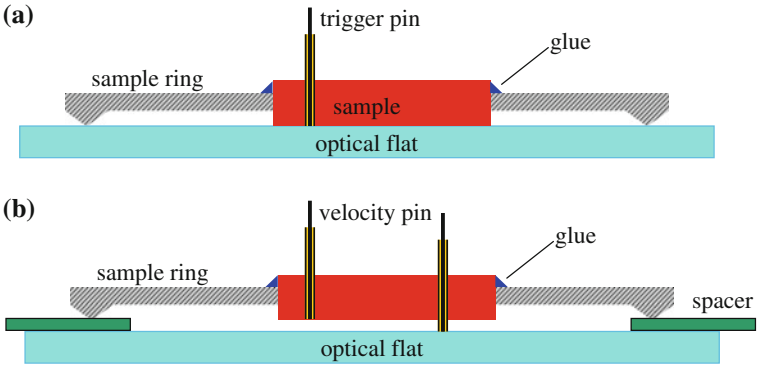

Fig. 13 Two steps of the sample assembly. The sample ring, the sample and the pin are assembled flush on the optical flat **a**. The second pin is fixed in the sample while the sample is spaced with respect to the optical flat **b**

Optical methods of measurement of the projectile muzzle velocity are much less popular than the above described electromechanical ones. Only a few such measurement techniques are reported in literature [9, 10].

6 Requirement No. 6

The main use of laboratory gas guns is characterized by strictly one-dimensional geometry loading of the studied sample. In such loading geometry all the points of the impacted sample surface simultaneously acquire the same velocity whose value is determined by the velocity of the impactor (impact velocity) and by shock impedances of both the impactor and the sample. As a result, all the points of the impacted surface start to move with the same velocity, straining the sample in the impact direction only. The strain tensor ε_{ij} of the sample material thus has only one non-zero component ε_{11}. One of the principal axes of the strain tensor coincides with that of the impact direction while two other principal axes may be chosen arbitrarily. Such loading conditions are called uni-dimensional strain (1-D strain) boundary conditions and their experimental implementation requires two types of measures. The measures of the first type involve a series of operations finalized in an installment of the sample holder prior to the gun shot. The holder has to be fixed so that that the sample ring contact points will be located at the plane parallel to the impactor front surface. The measures of the second type are aimed to the control of the impactor/sample misalignment at the instant of the impact.

The measures of the first type require a gauge plug to be inserted into the gun barrel at the gun muzzle side. It is usually a solid cylinder made of brass or high strength aluminum alloy of length 3–5 gun calibers whose lateral surface is turned to 2–3 μm tolerance with respect to the barrel internal surface of the same, 3–5 gun

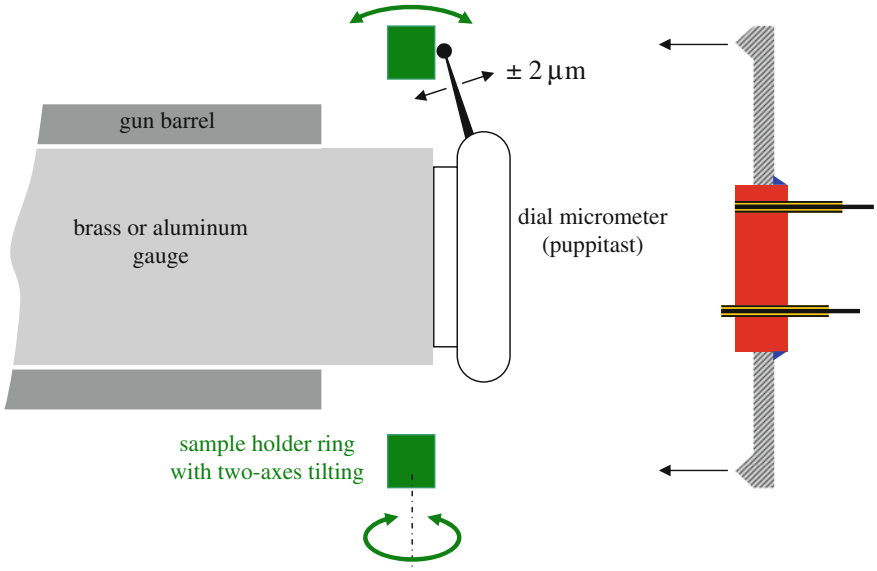

Fig. 14 Alignments of the sample holder ring with aid of the gauge and dial micrometer. The contact points of the sample ring (at the *right*) should be brought into contact with the aligned surface of the sample holder ring

calibers, length. The front surface of the gauge must be flat and perpendicular to the gun axis within 0.05 mrad. When the gauge is inserted into the barrel this surface should virtually coincide with the plane of the sample holder ring. The ring, in turn, must be ground flat and must be part of a gimbal-like mount which allows, by mean of the alignment screws, rocking and fixation of the holder ring with respect the two axes perpendicular to the axis of the barrel. The dial micrometer with flat base should be installed at the gauge frontal surface as shown in Fig. 14. Then the sample holder ring is tilted by micrometer screws so as to approximately equal the micrometer readings at four points (north-south, west-east) of the sample holder ring.

The scale interval of the dial micrometer is 2 µm, the usual diameter of the sample holder ring is 70–100 mm. The equality of the readings of the dial micrometer within 2–3 scale marks corresponds to a 0.05–0.1 mrad misalignment between the gauge front surface and the sample holder ring. With the misalignment uncertainty caused by non-planarity of the contact points of the sample ring (Fig. 13) the final impactor/sample misalignment usually does not exceed 0.5 mrad. The latter figure is usually controlled in the experiment by a set of 3–4 electrical pins installed flush with the sample front surface.

The gun recoil and the barrel vibrations during the projectile acceleration can corrupt the pre-shot impactor-sample alignment. To overcome this problem the gun is usually permitted to recoil freely while the bases of the breach-gun assembly and

the base of the target chamber are seismically uncoupled. Sometimes the problem is solved by mounting the sample holder ring with adjustment screws directly on the muzzle edge of the barrel [11].

7 Requirement No. 7

Since the laboratory gun could be operated by not highly skilled personnel (e.g., by university students) the gun design should provide a high level of safety. With this in mind the breach and the barrel are designed with a high margin of safety. The sample (test) chamber and the catcher-receiver tank should be of such volume that the inside pressure at the catcher after gun shot remains lower (or only slightly higher) than atmospheric pressure. The target chamber with the gun barrel and the catcher chamber are usually two separate volumes isolated from each other by easily perforated Mylar or PVC sheet of 0.3–0.5 mm thickness. This allows pumping the barrel—target chamber volume down to a vacuum better than 1 mbar (see Fig. 6) while the catcher chamber may be pumped down by a simple mechanical pump to a much higher pressure of 5–10 mbar.

The impact test performed in such a configuration of barrel—test chamber—catcher is terminated by the flight of the projectile sabot, impactor, sample and accompanying debris into the catcher chamber. Since all these objects possess high kinetic energy the catcher chamber must be equipped with a projectile stopper. Usually it is a basket or cage made of steel profiles and filled with rags. The rear, opposite to the gun, wall of the cage is usually a single or multiple steel plates having total mass of about 100 kg. Being struck by the projectile the cage may travel on rails towards the rear wall of the catcher chamber where it meets solid rubber blocks or other shock absorbers. The above described configuration precludes any injury to the laboratory personnel either by gas shock waves or by projectile/target debris.

8 Use of the Light Gas Gun at the Ben-Gurion University

It can be safely assumed that keeping requirements 1–7 will result in safe operation of a light gas gun inside the laboratory.

The following example illustrates the use of the light gas gun in the Laboratory of Dynamic Material Behavior at the Ben-Gurion University. This gun was designed for studying solids response to high strain rate loading. In order to quantify the velocity response of the studied sample rear surface it is continuously monitored by VISAR (Velocity Interferometer System for Any Reflector, [12]) having temporal resolution of about 1 ns. The samples of “as rolled” copper of 99.999 % purity and 2-mm thickness were shock-loaded by impactors made of OFC copper, having a thickness of 0.5 mm. The impactors were accelerated in the

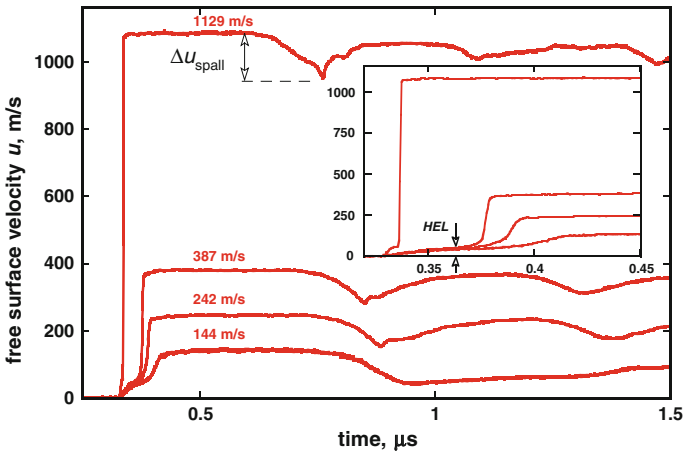

Fig. 15 Free surface velocity histories recorded with 2-mm samples of copper (99.999 % purity) shock-loaded by 0.5 mm impactors of OFC accelerated up to velocities shown next to the waveforms

25 mm diameter, 6 m length smooth gun barrel up to velocities shown in Fig. 15 [13] together with the recorded waveforms. The arrows in Fig. 15 and in the insert show the waveform parameters related to the high strain rate mechanical behavior of the studied copper. In particular, the arrow of 1129-m/s waveform shows the so-called velocity pull-back Δu_{spall} associated with the dynamic tensile strength of the material while the arrow in the inset shows the amplitude of the elastic wave followed by the plastic wave front.

The amplitude of the elastic wave marked in the inset as Hugonot elastic limit (HEL) corresponds to the dynamic material strength in compression. The compressive strength corresponding to this point of the waveform may be found using Eq. (8) [14],

$$\sigma_{HEL} = \frac{1}{2}\rho_0 c_l u_{HEL}, \tag{8}$$

where u_{HEL} is the sample free surface velocity at HEL, ρ_0 is the initial sample density, and c_l is the longitudinal speed of sound. The compressive stress (8) is related to the dynamic yield strength Y of the material (elastic limit under 1-D stress loading) as shown in the following equation [14],

$$Y = \frac{1-2\nu}{1-\nu}\sigma_{HEL} = 2\frac{G}{E'}\sigma_{HEL}, \tag{9}$$

where ν is the Poisson's ratio, and G and E' are shear and longitudinal moduli of the material, respectively. Based on the velocity pull-back signal Δu_{spall} the dynamic

tensile strength of the tested material may be estimated with accuracy of about 15 % using the following relation [15],

$$\sigma_{spall} = \frac{1}{2}\rho_0 c_b \Delta u_{spall}, \tag{10}$$

where c_b is the bulk speed of sound.

The fact that the velocity histories of the type shown in Fig. 15 are widely used for development of the high strain rate constitutive equations of metals and alloys, ceramics, plastics, and even liquids makes the light gas gun an indispensable tool for studying high strain rate response of condensed matter.

References

1. Siegel, A.E.: Theory of High Speed Guns. United States Naval Ordnance Laboratory White Oak, Silver Spring, Maryland (1965)
2. Landau, L.D., Lifshitz, E.M.: Fluid mechanics. In: A Course in Theoretical Physics, vol. 6. Pergamon Press, Oxford (1959)
3. Brown, J.R., Chappell, P.J.C., Egglestone, G.T., Gellert, E.P.: A gas-gun facility for material impact studies using low velocity, low-mass projectiles. J. Phys. E: Sci. Instrum. **22**, 771–774 (1989)
4. Fowles, G.R., Duvall, G.E., Asay, J., Bellamy, P., Feistmann, F., Grady, D., Michels, T., Mitchell, R.: Gas gun for impact studies. Rev. Sci. Instrum. **41**, 984–996 (1970)
5. Majumdar, S.R.: Pneumatic Systems: Principles and Maintenance. Tata McGraw-Hill Education, New Delhi (1996)
6. Mock Jr., W., Holt, W.H.: Device used with charged pin technique for precision gas gun projectile velocity measurements. Rev. Sci. Instrum. **45**(4), 491–493 (1974)
7. http://precision.hubersuhner.com
8. http://www.dynasen.com
9. Chhabildas, L.C., Asay, J.R.: Rise-time measurements of shock transitions in aluminum, copper and steel. J. Appl. Phys. **50**, 2749–2756 (1979)
10. Zaretsky, E.B., Kanel, G.I.: Effect of temperature, strain, and strain rate on the flow stress of aluminum under shock-wave compression. J. Appl. Phys. **112**, 073504 (2012)
11. Mock, W., Jr., Holt, W.H.: Muzzle flange alignment technique for gas gun. J. Phys. E: Sci. Instrum. **12**, 681–682 (1979)
12. Barker, L.M., Hollenbach, R.E.: Laser interferometer for measuring high velocities of any reflecting surface. J. Appl. Phys. **43**, 4669–4675 (1972)
13. Zaretsky, E.B., Kanel, G.I.: Response of copper to shock-wave loading at temperatures up to the melting point. J. Appl. Phys. **114**, 083511 (2013)
14. Kanel, G.I., Razorenov, S.V., Fortov, V.E.: Shock-Wave Phenomena and the Properties of Condensed Matter. Springer, New York (2004)
15. Antoun, T., Seaman, L., Curran, D., Kanel, G.I., Razorenov, S.V., Utkin, A.V.: Spall Fracture, pp. 90–99. Springer, New York (2002)

Author Biography

Eugene Zaretsky is known for his studies of high temperature impact response of solids at the Ben Gurion University of the Negev (Israel). His research mainly deals with shock-induced phase transitions and relaxation of shear stress behind the shock front. He received his M.Sc. Degree in Physics of Metals from Moscow Institute of Steel and Alloys and Ph.D. degree in Thermal Physics from Russian Academy of Sciences. Ben Gurion University of the Negev, where he is a lecturer for Mechanical Properties of Solids and Statistical Physics, has awarded him the rank of "Professor". His current interest is focused on the transition between different dislocation regimes in the shock-loaded relaxing solids.

Part II
Hypervelocity Test Facility

Ballistic Range

Sen Liu

Ballistic range is a kind of test facility, in which the test models or projectiles are launched at desired velocity, the aerodynamic properties of the flying models are measured during its flight, or shock and damage of the targets are measured upon the projectile impact.

Originally developed for studying the flight and/or lethality of bullets or artillery shells in 18th century, the ballistic range was adapted as a powerful facility for the study of high speed flight vehicles since World War Two, with the advent of the Aerodynamic Range at the US Army Aberdeen Proving Ground in 1943. The range is noted as "the world's first large-scale, fully-instrumented ballistic range reproducing data on the aerodynamic characteristics of missiles in free flight" [1].

With the invention of two-stage light gas gun by Crozier in 1946 and Hume in 1950s [2], ballistic range was widely used in the fields of hypervelocity aerothermodynamics and hypervelocity impact effects since the 1950s, as the results of the developments of hypervelocity reentry vehicles, protection of structures/shields against space debris, and kinetic energy weapons.

1 Introduction

Ballistic range has a long history in the development of ordnance, such as bullets, artillery shells, rifles, cannons, and warheads. In 1742, a primitive ballistic range was developed by Benjamin Robins to measure the velocity of a projectile fired from a cannon. The measurement device used by him is a ballistic pendulum.

By the end of 19th century, cannon shell design was evolved from spherical to streamlined configuration to reduce aerodynamic drag. To sustain flight stability, the streamlined shell must spin very fast. At this time, the role of ballistic range was

S. Liu (✉)
Hypervelocity Aerodynamics Institute (HAI), China Aerodynamics Research and Development Center (CARDC), Mianyang 621000, Sichuan Province, People's Republic of China
e-mail: liusen@cardc.in

F. Seiler and O. Igra (eds.), *Hypervelocity Launchers*,
Shock Wave Science and Technology Reference Library 10,
DOI 10.1007/978-3-319-26018-1_2

not only to measure projectile velocity, but also measure the flight attitude of the projectile. To meet these requirements, solenoid coils and ballistic cardboard techniques were developed.

During the 1930s, researchers of US Army Ballistic Research Laboratory (BRL) at Aberdeen Proving Ground started pioneering work on advanced measurement techniques of high speed projectiles. R.H. Kent, A.C. Charters and their colleagues developed techniques, such as spark shadowgraph and sequential imaging, which could record the flight of projectile with great precision. All these newly developed measurement instrumentations were adopted in the first aerodynamic ballistic range at BRL in 1943. "The range was recognized as the prototype for similar installations within the United States and abroad" [1].

Later, the knowledge obtained in the development of the aeroballistic range at BRL were applied to the construction of other famous hypervelocity ballistic ranges in the world, such as the range at NASA Ames Research Center, Range G at Arnold Engineering Development Center (AEDC), etc.

Roughly, there are two kinds of ballistic ranges. One is high speed range, which is mainly used for ordnance tests, and usually has a nearly one-atmosphere test chamber. The other is hypervelocity range, which is characterized by much higher muzzle velocity speed (e.g. faster than Mach number 5) and has a variable pressure test chamber for the simulation of high altitude in atmosphere.

With the advent of long range ballistic missile and civilian space program in the late 1940s and early 1950s, the ballistic range found new applications in the field of hypersonic aerothermodynamics and protection of spacecraft against meteoroids (and later space debris), thanked to the successful development of hypervelocity two-stage light gas gun by Crozier and Hume, and since then it became a unique and important part of ground test facilities for hypersonic aerothermodynamics and hypervelocity impact for MOD (Meteoroids and Orbital Debris) protection and kinetic weapon effects [3–10], therefore, this chapter will focus on the hypervelocity ballistic ranges.

2 Working Principle of Hypervelocity Ballistic Range

Most of hypervelocity ballistic ranges have three sub-systems, namely a launcher (usually two-stage light-gas gun) to accelerate the test model, a test section or test chamber to simulate the flight ambient conditions, such as altitude, and a measurement and control system to measure the model flight parameters and model impact and target damage parameters, as shown in Fig. 1. Shown in Fig. 2 is the 50 mm two-stage light gas gun and 200 m test chamber at Hypervelocity Aerodynamics Institute (HAI) of China Aerodynamics Research and Development Center (CARDC).

First, the test chamber is set to a desired condition, e.g. the chamber pressure; then the test model or projectile was launched at a pre-set muzzle velocity into the test chamber. If the test is to obtain aerodynamic or aero-thermodynamic properties

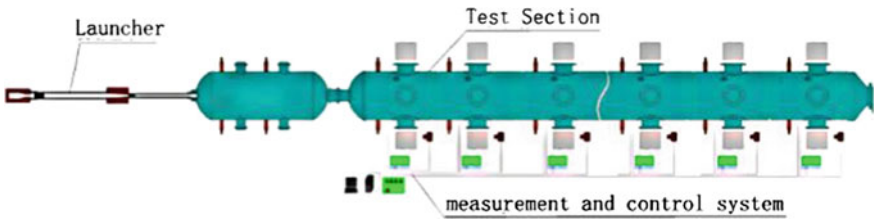

Fig. 1 Schematic of hypervelocity ballistic range

Fig. 2 Two-stage light gas gun (*upper*) and test chamber (*lower*) of 200 m free flight ballistic range at CARDC

of the model, parameters such as flight velocity, flow field structure, optical emission, and even surface pressure and heat flux would be measured during the model's flight. If the test is for hypervelocity impact effects, parameters such as projectile velocity, penetration and perforation, shock speed and temperature in target material, and debris cloud would be recorded.

The working principle of hypervelocity launcher (two-stage light gas gun), test section and measurement system will be briefly introduced.

2.1 Two-Stage Light Gas Gun

Though there are several other kinds of hypervelocity launchers, such as electro-magnetic rail gun and coil gun, the most reliable and frequently used in laboratory is the two-stage light gas gun (two-stage LGG). Compared with other launchers, the two-stage LGG has advantage in its capability of launching test models of different shapes at hypervelocity.

Since the two-stage LGG was invented by Crozier and Hume [2], many two stage LGGs have been built all over the world. Many laboratories and research institutions, such as National Aeronautics and Space Administration (NASA) Ames (USA), NASA Johnson Space Center (JSC) (USA), Arnold Engineering Development Center (AEDC) (USA), Ernst-Mach Institute EMI (Germany), French-German Research Institute of Saint-Louis (ISL) (Germany and France), HAI at CARDC, etc., have their own two-stage LGGs.

A typical two stage light gas gun consists of powder chamber/air chamber, pump tube, high pressure section, and launch tube, as shown in Fig. 3.

As its name implies, the two stage light gas gun has two stages. The first stage is the powder gun or air gun, with which a piston is accelerated in the pump tube, compressing the pre-filled light gas (e.g. hydrogen or helium). The second stage consists of the high pressure section and the launch tube. The compressed light gas (up to about 10 thousand bar) in the high pressure section accelerates the test model/projectile sabot combination.

Roughly estimated, the maximum achievable muzzle velocity is the gas escape velocity, which is attained when the gas pressure drops to zero when a complete vacuum is reached. The escape velocity is proportional to the initial gas sound speed, which is related to the molecular weight (hydrogen is lighter than helium) and temperature of the gas. The lighter the gas is, the higher is its escape velocity. Both hydrogen and helium could be used as the driving gas in the pump tube. While helium is much safer than hydrogen, the latter is considered more efficient taking into account of launch capability.

The muzzle velocity is determined by the structure of the launcher, mass of gunpowder, initial pressure of the prefilled light gas, the piston mass, the model/projectile mass, and the diaphragm pre-set rupture pressure. Interior ballistics

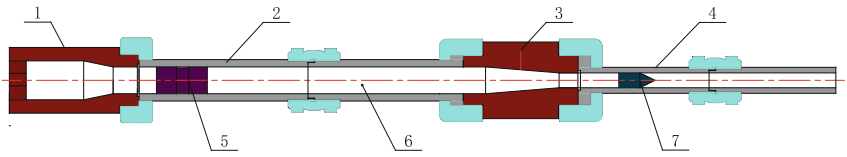

Fig. 3 Schematic of a two-stage light gas gun

analyze codes are used for finding optimal load parameters and improve the launcher design.

The piston mass is important for the optimization of a LGG. A light piston can reach high speed easily, which will form strong shock wave in the light gas, the gun turns to be a shock-heating gun, the disadvantage is obvious because of the barrel erosion. A heavy piston needs more gunpowder, and will generate a huge impact on the high pressure section.

The launch velocity is sensitive to the initial pressure of the light gas in the pump tube. Generally, the average pressure at the model base and the muzzle velocity increase with decreasing the initial light gas pressure. Though low initial pressure can yield high muzzle velocity, the erosion of gun barrel by the high temperature gas needs to be seriously considered.

Theoretically, the highest muzzle velocity that could be realized with a two-stage LGG is well above 10 km/s, and many laboratories did claim that their guns could fire a model at a velocity of 8 and even higher. However, few two-stage LGG are operated at such high velocity routinely, because of the gun barrel erosion and the model/projectile configuration. For example, the highest muzzle velocity of two-stage LGG in routine shots is about 7.5 km/s at HAI of CARDC, although the recorded highest muzzle velocity is 8.6 km/s with a 16 mm two-stage LGG.

Although most of the launch tube bore diameters of nowadays' two-stage LGGs are around ten millimeters, the biggest could be well above one hundred millimeters. The largest two stages LGG in the world is the launcher of AEDC's Range-G, with maximum bore diameter of 203 mm. Projectile velocities can reach up to 4.5 km/s for the 203 mm gun and up to 7 km/s for its inter-changeable 84 mm gun barrel [14]. The launch capability of the two-stage LGGs at AEDC and CARDC is shown in Fig. 4.

2.2 Test Chamber

As mentioned above, the role of the test chamber is to simulate flight at ambient conditions. In ballistic ranges for ordnance tests, usually there is no requirement of variable ambient pressure, so concrete-walled test chamber is a normal design, in which the projectiles fly freely and impact targets. However in those hypervelocity ballistic ranges, all the test chamber are steel or stainless steel tanks with vacuum systems, because the earth/planet atmosphere at different altitudes, or the Low Earth Orbit (LEO) condition have to be simulated in the chamber.

A test chamber usually consists of a blast tank, a test section and a diaphragm section or a fast-acting valve, and vacuum system, as shown in Fig. 5.

The blast tank, connected to the muzzle of the launcher, is used to collect the exhaust light gas which is discharged from the gun, and separate the test

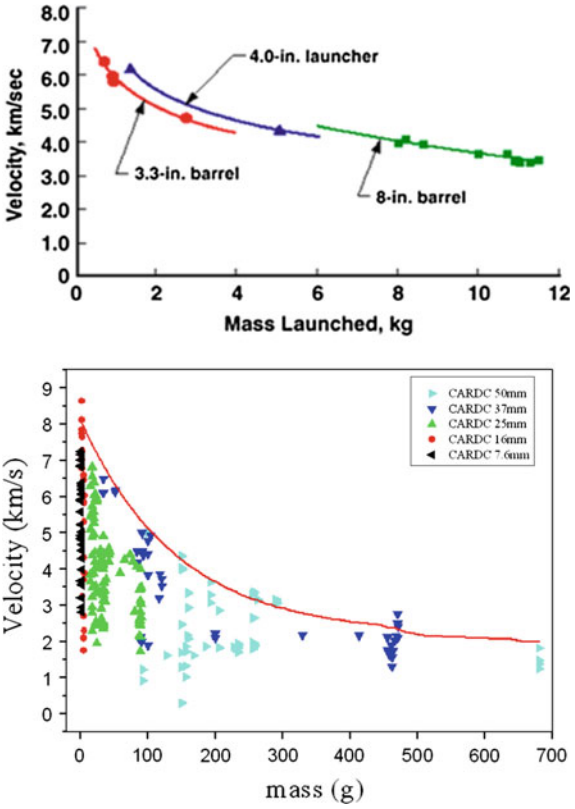

Fig. 4 Launcher capability of LGGs at AEDC [11] (*upper*) and CARDC (*lower*)

model/projectile with sabot. Between the blast tank and the test section, there is a fast-acting valve or a diaphragm, by which different pressure in blast tank and test section can be realized. The test section is one of the most important sub-systems of a hypervelocity ballistic range, because it is the place where the test model/projectile flies and impacts the target. Observation windows are set up in the test section, for recording the projectile trajectory and the resulting flow field.

Most of the test models/projectiles fly freely inside the test section; however they could fly on a track in Range G at AEDC. To reach a pre-set flight ambient condition, the blast tank and test section all have their affiliate vacuum system, to control the pressure, temperature and component of the gas in the blast tank and in the test section. In hypervelocity impact tests, usually only vacuum condition should be simulated. However, to meet the need of other tests such as hypersonic aerodynamics and erosion/ablation of thermal protection materials, some special equipment has to be installed in the test section, including rain/snow field simulator, test model recovery system, etc.

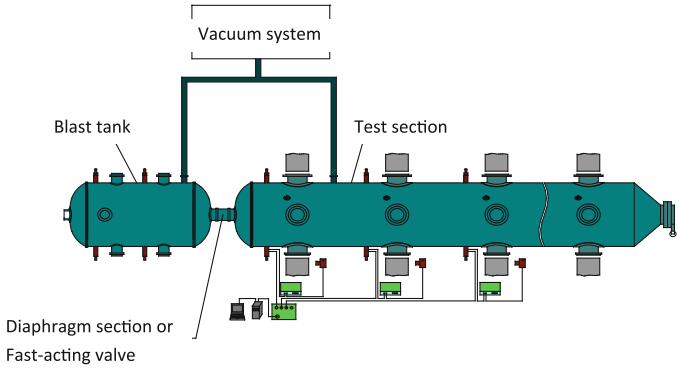

Fig. 5 Schematic of test chamber (gun shoots from *left* to *right*)

2.3 Measurement and Control System

The parameters to be measured are velocity of the tested model or projectile, its flight attitude, flow field structure, optical emission from the flow and from the tested model, surface pressure and heat flux on the tested model, shock wave parameters (such as pressure, temperature and shock wave speed in target material), velocity and geometry of the debris cloud, etc. The control system is to control different subsystems (such as gun, shadowgraphers, pulse light source, flash X-ray, etc.) of a ballistic range in order to ensure its working in a desired sequence. Because the flight speed of the tested model or projectile in a hypervelocity ballistic range is always as high as several kilometers per second, the time duration of model passing through a test station window is usually on the order of 10–100 μs. So it is not easy to accomplish all those measurement and control in a hypervelocity ballistic range test.

First of all, we have to detect the model or projectile which is flying at several kilometers per second at each measurement station. Non-contact methods could be adopted, such as radar, magnetic induction, optical emission detector. Photoelectric detection is the most common approach. A sheet of laser comes out from one side of the range chamber, perpendicular to the axis of the ballistic range. When the model or projectile flies through the laser sheet, either light decrease or light increase could be recorded by sensors on the other side of the range chamber. In this way, it is possible to know the exact time when the model or projectile arrives at the measuring station. Having at least two stations equipped with this kind of laser sheet, the velocity of the model or projectile could be easily calculated.

The second primary job of the measurement system is to visualize the flight attitude and the flow field around the model or projectile. High speed shadowgraph or flash X-ray is used, which cause no disturbance to the model's flight or to the evolved flow field. Along the test chamber of a ballistic range, there are always many test stations. The numbers of stations are different depending on the purpose

of the range. For an aero ballistic range, there might be as many as 50 test stations like in the AEDC Range G [12]. However, for an impact range, there are fewer test stations, because there is no need to record the model attitude variation along its flight path. At each station, usually a pair of orthogonal shadowgraph or schlieren or flash X-ray are installed to capture the attitude of the flight model or check the integrity of projectile before it impacts the target.

One of the important works at hypervelocity ballistic range is to measure the shock wave parameters in the target material which is generated by the projectile hypervelocity impact. The basic shock wave parameters are shock wave velocity and pressure, which can be obtained by using pressure sensors. Before a test, pressure sensors are placed at interesting points on the target surface or inside the target. During the test, a pressure history can be recorded by each of the used pressure sensors, thus the shock velocity can be obtained by comparing data obtained from at least two sensors. There are two types of pressure sensors, piezoresistive sensors and piezoelectric sensors. Polyvinylidene Fluoride (PVDF) is a piezoelectric sensor widely used in shock measurement. The other shock wave parameters, such as surface displacement and surface velocity can be obtained by using Velocity Interferometer System for Any Reflector (VISAR).

3 Representative Hypervelocity Ranges in the World

Since the 1950s, more than fifty hypervelocity ballistic ranges of different sizes have been built around the world. All of them have done good job in their research fields. However due to limited space, only a few most active ranges are introduced here. They are:

- AEDC Range G,
- Hypervelocity Free-Flight Aerodynamic Facility (HFFAF) of NASA Ames,
- hypervelocity ballistic ranges of the UAH Aerophysics Research Center (UAH-ARC),
- Hypervelocity Impact Test Facilities (HITF) of NASA JSC,
- Hypervelocity impact ranges of Ernst-Mach Institute (EMI),
- Hypervelocity Ballistic Range Complex of CARDC.

3.1 AEDC Range G

As the world's largest hypervelocity ballistic range, Range G was built in 1962 at the Arnold Engineering Development Centre of US Air Force [13]. A schematic diagram of Range G is shown in Fig. 6 [11]. Continued upgrades were carried out, for example a thorough upgrade of launchers and measurement systems in the 1990s, and upgrade of the data processing system in the year 2006.

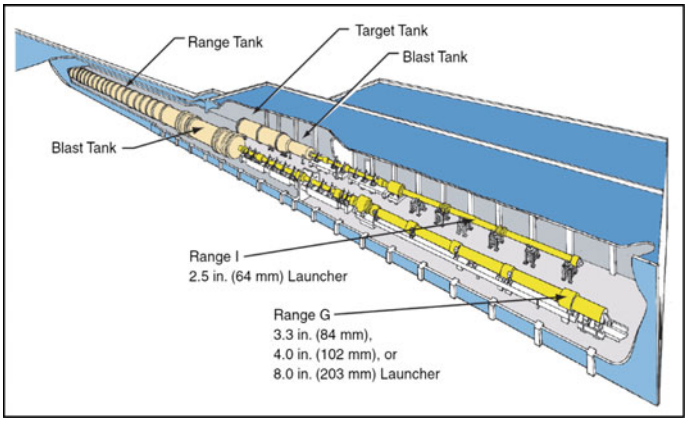

Fig. 6 Schematic of range G and range I [11]

Fig. 7 Launcher room of range G and range I [13]

Shown in Fig. 7 is the launcher room of Range G and Range I (which is a smaller range specifically for hypervelocity impact tests) [13]. The two-stage LGGs of Range G have launch tubes of 84, 102 and 203 mm bore diameters, respectively. The highest muzzle velocity is about 7 km/s, while the 203 mm gun can accelerate a 12 kg model to 4 km/s [14], and the 84 mm gun can accelerate a 908 g model to 6 km/s [15]. The launcher capability of Range G is shown in Fig. 4 [11]. The so-called "counter-fire" technique was developed by using two two-stage LLGs shooting face to face, achieving hypervelocity impact velocities greater than 12 km/s [16].

The test chamber, which is 3 m in diameter and about 300 m in length, it contains a unique track guidance system which is comprised of a four-rail system for model guidance and a 213.4 m-long model recovery system [14]. Besides of simulating the flight altitude by a vacuum system, the climatic cloud particles such as rain drops or ice crystal could be simulated in this test chamber [17].

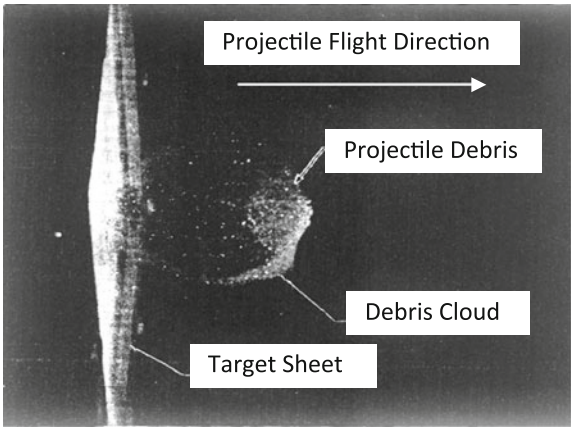

Fig. 8 Target sheet and debris cloud captured by front light imaging [15]

Powerful transient measurement instruments used in this facility, includes shadowgraph/schlieren, orthogonal flash X-ray, high-speed X-ray imaging system, ultra-high speed camera, laser front-light imager, multispectral/infrared signal measurement system, etc. [17].

Applications of Range G include tests of aerodynamics, erosion/ablation of Thermal Protection System (TPS) materials, boundary layer transition, rocket plume, re-entry aerophysics, hypervelocity impact, etc. For example, debris cloud in a hypervelocity impact test is shown in Fig. 8 [15].

3.2 HFFAF at NASA Ames Center

There are two hypervelocity ballistic ranges at NASA Ames research center. One is Ames vertical gun range (AVGR) built in 1964, which was designed to conduct experiments on lunar impact processes in support of the Apollo mission. The other is Hypervelocity Free-Flight Aerodynamic Facility (HFFAF) built in 1965, which is basically a multi-purpose range.

The HFFAF is a combined ballistic range and shock tunnel [18, 19], sketch of the facility is shown in Fig. 9. The HFFAF consists of: a model launcher (light-gas gun or powder gun), a sabot separation tank, a test section and impact/test chamber, a nozzle and a shock tube. There are four light-gas guns with launch tube bore diameters of 7.6, 12.7, 25.4, and 38.1 mm, and three powder guns with launch tube bore diameters of 20, 44, 61 mm, respectively. The highest muzzle velocity is 8.5 km/s. The test section is 22.86 m long with sixteen orthogonal shadowgraph stations as shown in Fig. 10. For very high Mach number (i.e. $M > 25$) simulation, models can be launched into a counter flowing gas stream generated by the shock tunnel [18].

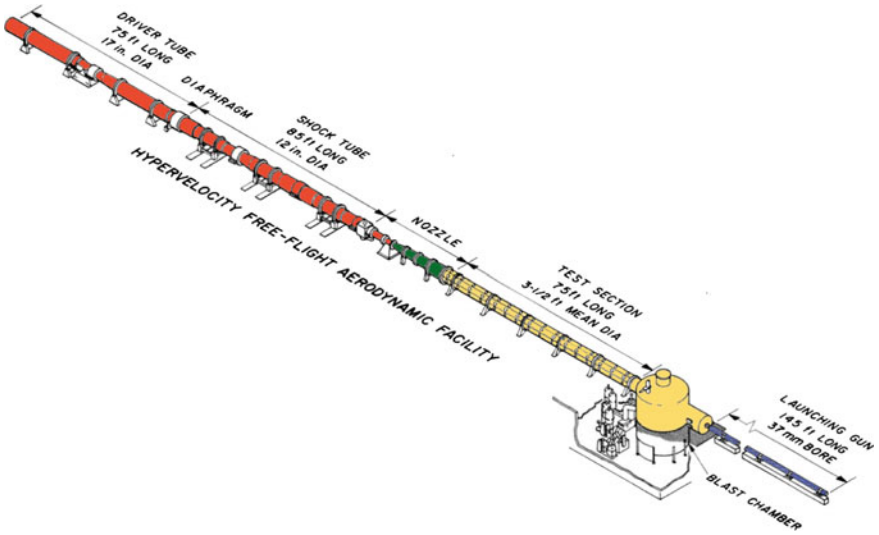

Fig. 9 Sketch of HFFAF at NASA Ames [19]

Fig. 10 HFFAF test section with sixteen shadowgraph stations [19]

The following studies have been carried out at HFFAF: earth atmospheric entry, planetary entry and vehicles aerobraking, scramjet propulsion, meteoroid/orbital debris, and various configurations for supersonic and hypersonic aircraft. The test models shot at HFFAF are shown in Fig. 11. As an example, Figs. 12 and 13 show a boundary layer transition experiment conducted at HFFAF.

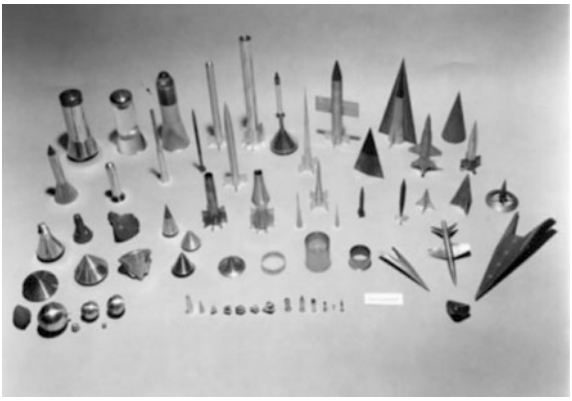

Fig. 11 Test models at HFFAF [20]

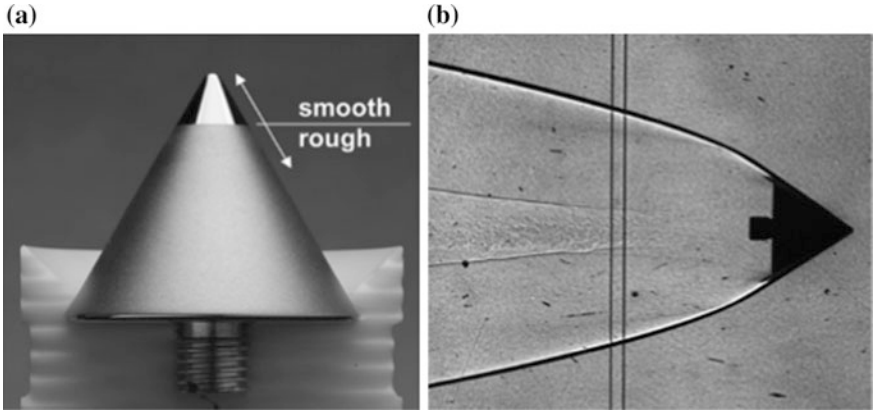

Fig. 12 Small-bluntness model, **a** mounted in launch sabot with half of sabot fingers removed, and **b** model in flight at $M_\infty = 10$ [20]

3.3 Hypervelocity Ballistic Ranges at ARC-UAH [21–23]

The three hypervelocity ballistic ranges of the University of Alabama in Huntsville, the Aerophysics Research Center (UAH-ARC) belonged to the Defense Laboratory of General Motors Corporation before the 1980s. Before and after the ranges were moved to UAH-ARC in Huntsville in the 1980s, and lots of hypervelocity impact and aerophysics experiments were conducted at the range. Though the ranges are run by UAH-ARC, their properties are owned by US Army.

There are a series of two-stage light gas guns at UAH-ARC, including a large range, an intermediate range and a small range, with launch bore diameters from 19 mm up to 152 mm. The maximum muzzle velocity is 8 km/s. The test chamber

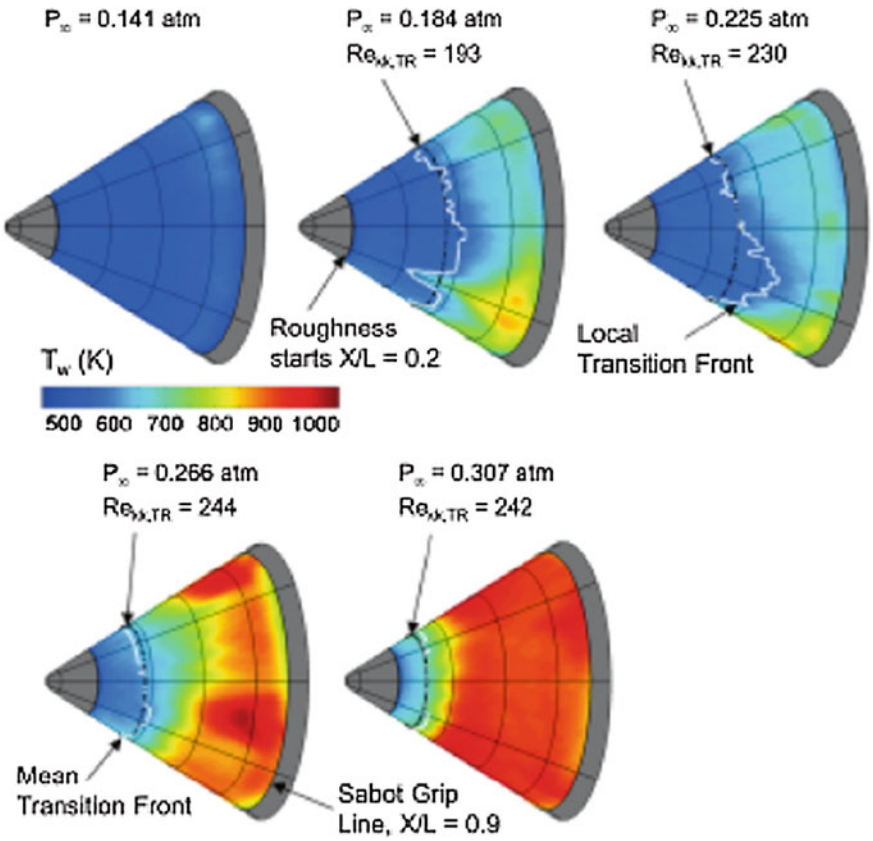

Fig. 13 Measured surface temperature distributions for the small-bluntness cones (obtained by several high speed thermal-imaging cameras) [20]

of the range for aerophysics tests is 3 m in diameter and 279 m long. Figure 14 shows the 152 mm two-stage LGG with 254 mm bore diameter pump tube and its launch capability.

The ranges are equipped with a full range of measurement instruments, such as flash X-ray imaging system, front light laser imaging system, shadowgraph/schlieren, CW Doppler radars (3, 9,17, 35, and 70 GHz), interferometers, radiometers (1.5–2 μm, 2–3 μm, 3–4 μm, 4–5.5 μm, 8–12 μm), spectrographer and others. Besides hypervelocity impact lethality tests, lots of aerophysics research could be carried out, such as wake structure, radar scattering characteristic, electron density distribution, optical radiation intensity and spectral properties. Figure 15 shows results from two of conducted tests.

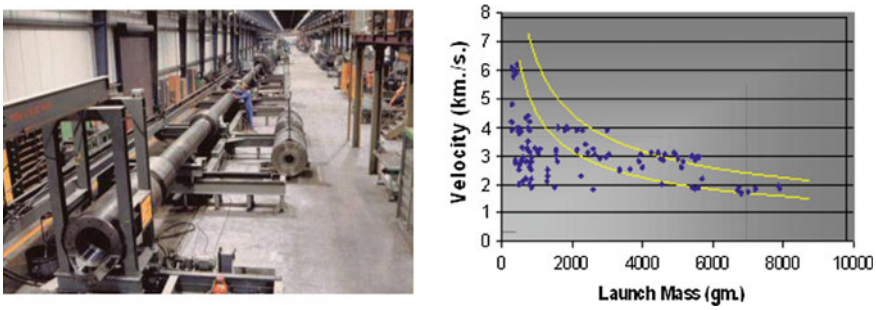

Fig. 14 The 152 mm two-stage LGG with 254 mm bore diameter pump tube and its launch capability [22]

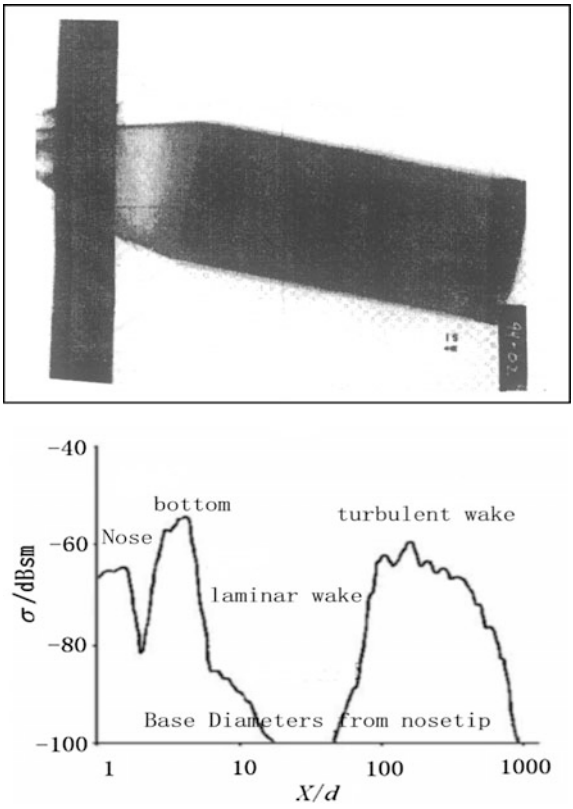

Fig. 15 Tests at UAH-ARC. *Upper* X-ray of a model impacting target. *Lower* radar cross section (RCS) of a hypervelocity vehicle and its wake [23]

3.4 Hypervelocity Impact Ranges at NASA JSC [24]

As the focus point in the development of protection shields for spacecrafts in the US, NASA Johnson Space Center (JSC) possesses a long history in hypervelocity impact tests of meteoroids and space debris. Now, there are four hypervelocity impact ranges at Hypervelocity Impact Test Facilities (HITF) of NASA JSC [24], one of which is shown in Fig. 16. The launch tube bore diameters of the two-stage LGGs are 25.4, 12.7, 4.3 and 0.18 mm, respectively. The measurement instruments consist of: laser detectors (shown in Fig. 17), high speed camera (shown in Fig. 18) and a flash X-ray (shown in Fig. 19). The high speed camera can obtain 80 images in one test at 2,500,000 frames/s.

Since the 1960s, many hypervelocity tests on spacecraft shield have been carried out at NASA JSC, trying to protect the Apollo command module, the space shuttle orbiter, the Hubble space telescope, the space suit like EMU, and the International Space Station (ISS). Based on traditional Whipple shield (A shield to protect spacecraft from meteoroid proposed by Fred Whipple in the 1940s), new shield

Fig. 16 Hypervelocity impact range at NASA-JSC

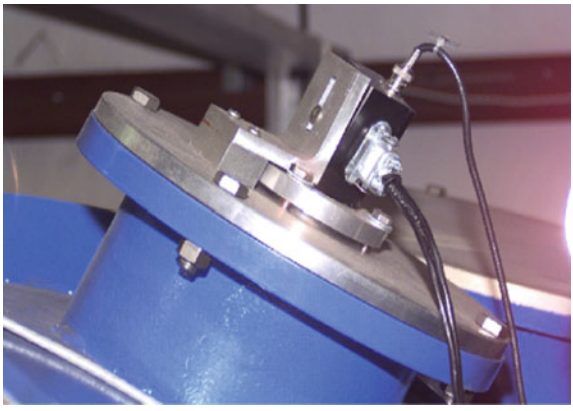

Fig. 17 Laser detectors

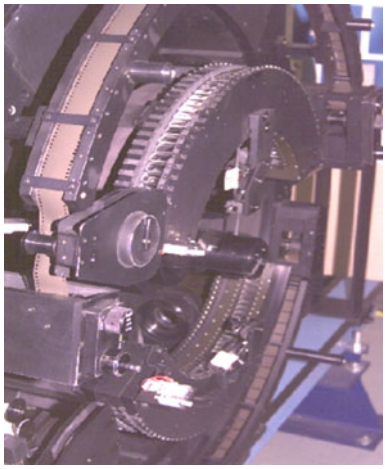

Fig. 18 High speed camera

Fig. 19 Flash X-ray heads

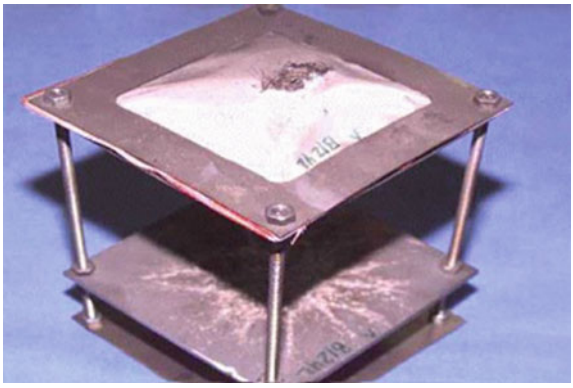

Fig. 20 β-cloth shield

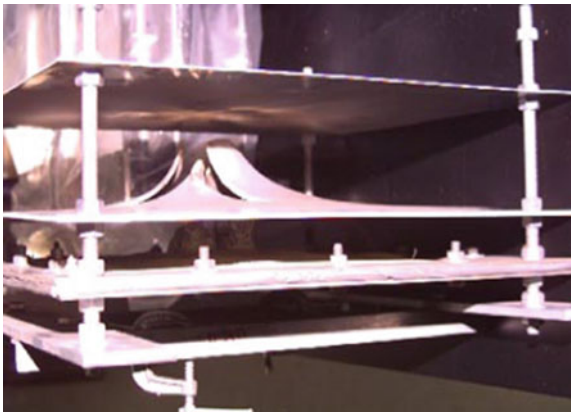

Fig. 21 Stuffed whipple shield

configurations have been developed by scientists and engineers at JSC, such as stuffed Whipple shield (Fig. 20), multi-shock shield, mesh double-bumper shield, and β-cloth shield (Fig. 21), etc.

3.5 Hypervelocity Impact Ranges at EMI, Germany

Currently, the Ernst Mach Institute (EMI) might be the most active institution in the field of hypervelocity impact in Europe. At EMI, three hypervelocity impact ranges (so-called small, medium, and large range) of different size are used for terminal ballistics, simulation of space debris and micrometeoroid impacts on spacecraft components, dynamic load on material with extra high pressure. Two of the ranges are shown in Fig. 22 [25].

The three ranges have similar configurations, including two-stage LGG, blast tank, sabot separation system, impact chamber and transient measurement instruments. The launch tube bore diameters range from 4 to 65 mm, and the highest muzzle velocity is 10 km/s with a 0.005 g projectile (Fig. 23) [25]. Projectiles as small as 100–500 μm could be launched by small light gas gun in shotgun mode

Fig. 22 Ballistic ranges at EMI (*Left* small, *right* medium) [25]

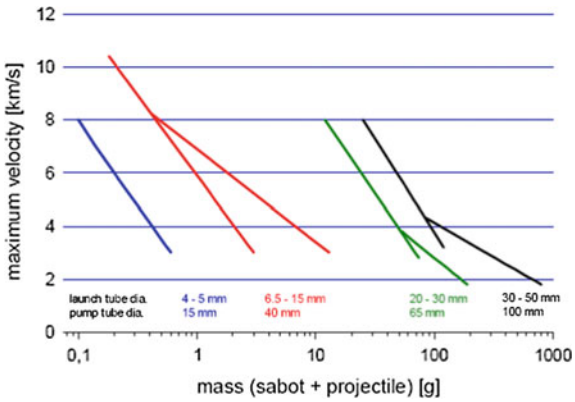

Fig. 23 Performance of EMI's light-gas guns [25]

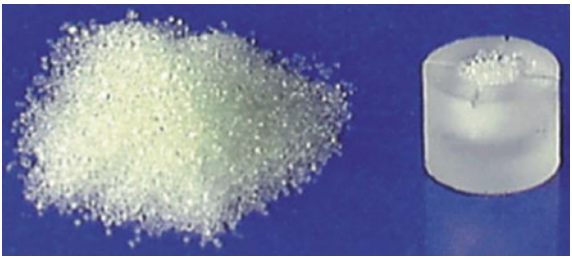

Fig. 24 Sabot (*right*) for projectiles (*left*) with diameter less than a millimeter [26]

(Fig. 24) [26]. The measurement system includes laser detectors, shadowgraph, flash X-ray, microwave radar velocimeter, high speed camera, image convertor camera, and ballistic pendulum [27].

Using the three ballistic ranges, EMI conducted large amounts of hypervelocity impact tests in the field of space debris and planetary physics. The related research works includes spacecraft shielding [28], vulnerability of satellite equipment under hypervelocity impact [29], Structural vibrations induced by hypervelocity impact [30]. planetary impact [31], Electrical signatures of hypervelocity impact plasma [32].

3.6 Hypervelocity Ballistic Range Complex of CARDC, China

At the largest hypervelocity ballistic range complex in China, there are four ranges at the Hypervelocity Aerodynamics Institute (HAI) of China Aerodynamics R. & D. Center (CARDC). The ranges were originally developed for studying hypervelocity

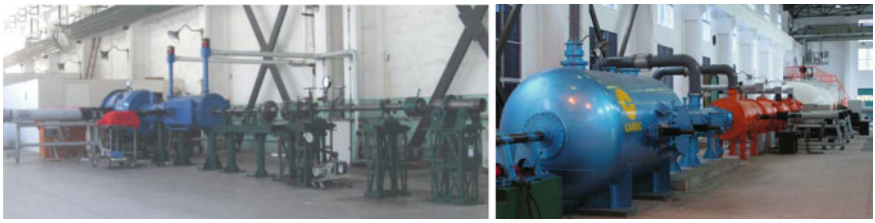

Fig. 25 Hypervelocity impact range A (*left*) and aerophysics range (*right*) of CARDC [33]

aerodynamics during the 70s of the previous century. As a result of space debris issue hypervelocity impact tests gradually became one of their primary works. For example, all the hypervelocity impact tests conducted for the first Chinese space lab "Tiangong-1" have been accomplished at this range complex.

The four ranges are Impact Range A (with 7.6 mm LGG,), Impact Range C (with 16 mm LGG), Aerophysics Range (with 25 mm LGG,), and 200 m Free Flight Range (37 and 50 mm LGG, shown in Fig. 2). Shown in Fig. 25 are Impact Range A and Aerophysics Range [33]. The highest muzzle velocity is 8.6 km/s at Impact Range C with a 180 mg projectile. The launch capability could be found in Fig. 4. While the impact chamber of Impact Range A is just 1 m in diameter and 1.8 m in length, the test chamber of the 200 m Free Flight Range is 1.5 m in diameter and 200 m in length, in which flight altitude and rain/snow could be simulated.

Transient measurement instruments at these ranges include laser detector, shadowgraph/schlieren, binoculars imaging system, high speed (5 million f/s) camera, eight-sequence laser shadowgraph, flash X-ray, visible and IR radiometer and spectograph, microwave interferometer, X and Ka band CW Doppler radar, etc.

The hypervelocity ballistic ranges at CARDC are applied for the studying hypervelocity aerodynamics/aerothermodynamics, rain/snow erosion of Thermal

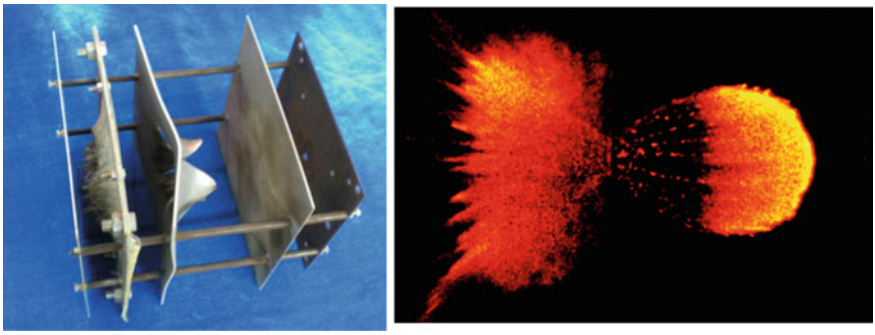

Fig. 26 Hypervelocity impact tests at CARDC. *Left* stuffed whipple shield. *Right* infrared image of debris cloud

Protection System (TPS) materials, hypervelocity impacts for spacecraft shields against space debris, aerophysics, etc. Shown in Fig. 26 are results from hypervelocity impact tests.

4 Application of a Hypervelocity Ballistic Range

A hypervelocity ballistic range is used to investigate phenomena pertinent to a hypervelocity flight body, to either reentry aerothermodynamics or Whipple shield against space debris. In general, the application of hypervelocity ballistic range falls into three categories, namely hypervelocity aerodynamics, hypervelocity aerophysics, and hypervelocity impact.

4.1 Hypervelocity Aerodynamics

Dynamic aerodynamic coefficient As for the study of hypervelocity aerodynamics, ballistic range is used to measure dynamic aerodynamic coefficients. When a model flies down the range, its time-of-flight is recorded by laser detectors. its flight speed is easily deduced from recorded passage time between two measuring stations whose separation distance is known. Optic apparatus, such as shadowgraph or schlieren and high speed camera enables recording the model time of arrival, its position, attitude, and also the flow field structure. Based on such information, the model trajectory and variations in its angle-of-attack along its trajectory could be re-constructed. Data reduction is applied to the trajectory and angle-of-attack data to determine dynamic aerodynamic coefficients, which determines the damping property of a re-entry vehicle. As for a blunted 5° half-angle cone flying at 5 km/s and at a Reynolds number of 10^6, the estimated error in measured coefficients is less than 3 %, as shown in Fig. 27.

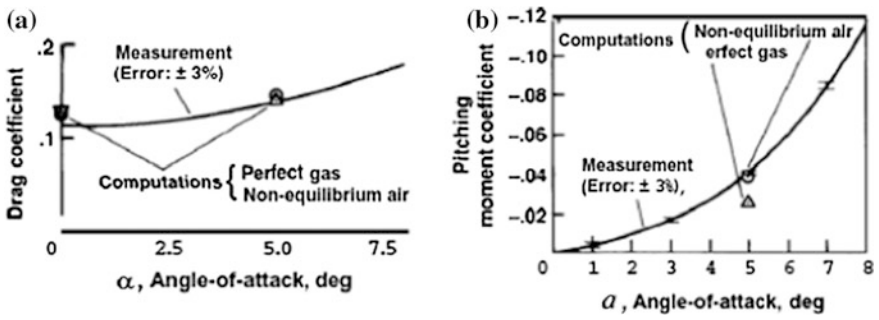

Fig. 27 Drag and pitching moment coefficient versus AOA of 1 blunt 5° half-angle cone [7]

Boundary layer transition One of the attributes of a ballistic range is the basically "quiet" flight condition compared with hypersonic wind tunnels and shock tunnels. Since the fluctuation and noise of the incoming flow at the nozzle exit may significantly affect the results of boundary layer transition at test model, the stationary, un-perturbed, un-contaminated test atmosphere inside the test section makes ballistic range a unique ground test facility in the regime of boundary layer transition research.

During the 60s and the 70s of the past century, Advisory Group for Aerospace Research and Development (AGARD) carried out tests on boundary layer transition both on the surface of a flight vehicle model and in its wake in ballistic range. Shown in Fig. 28 is a shadowgraph of turbulent boundary layer on a slender body of revolution at M = 3.5 and Re = 12×10^6 [4]. In Fig. 29, the turbulence burst is clearly shown [4]. Recently, under the hypersonic project of NASA's Fundamental Aeronautics Program, NASA Ames Centre carried out series of hypersonic boundary layer transition experiments at HFFAF, by using Intensified Charge

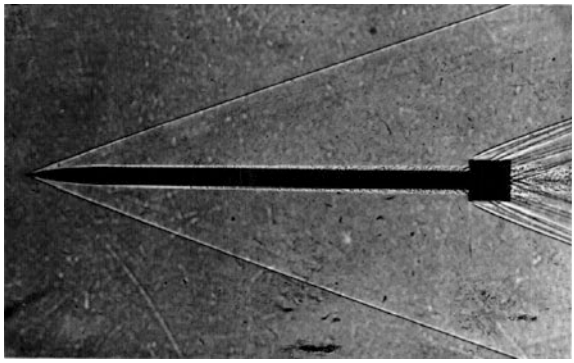

Fig. 28 Shadowgraph of turbulent boundary layer on a slender body of revolution at M = 3.5 and Re = 12×10^6 [4]

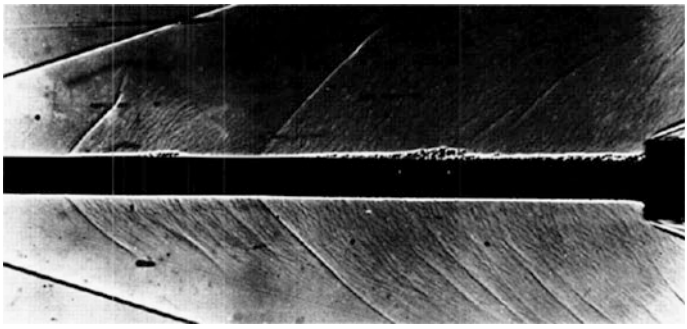

Fig. 29 Shadowgraph of isolated turbulence burst on a slender body of revolution at M = 3.5 [4]

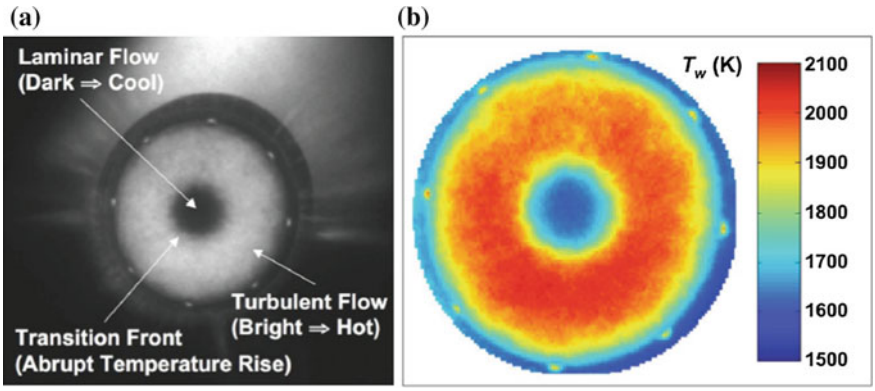

Fig. 30 Pre-ablated hemispherical POCO (graphite division of pure oil company) graphite nosetip Rn = 19.05 mm, V = 4.5 km/s, P = 0.317 atm; **a** ICCD camera image; **b** global surface temperature distribution [34]

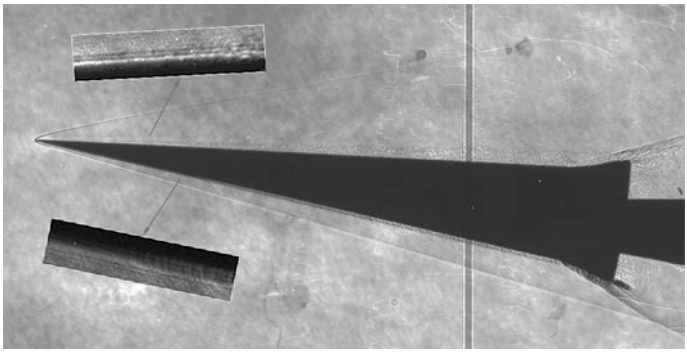

Fig. 31 Boundary layer transition test of slender cone M = 5.77, Re/L = 8.56×10^7, Re = 9.42×10^6, $\alpha = 7.9°$

Coupled Device (ICCD) to measure the transient temperature distribution on model surface. Shown in Fig. 30 is an infra-red image and reconstructed temperature distribution on a semi-spherical model [34, 35].

Shown in Fig. 31 are images of boundary layer transition experiment of a 5° sharp cone recently conducted at ballistic range of CARDC.

4.2 Hypervelocity Aerophysics

Aerophysics considers the interaction between hypervelocity moving objects and ambient gas environment into which it propagates. Due to the high temperature

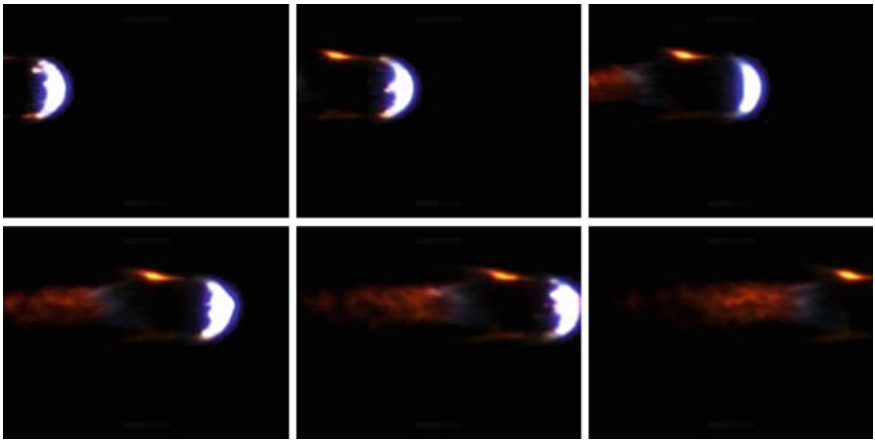

Fig. 32 Optical image of a flow field around hemispherical model at 5.0 km/s (from *upper left* to *lower right*, 186,000 fps, 1 μs exposure time)

generated around the travelling body real gas effects such as vibration, dissociation, electronic excitation, ionization, radiation and electromagnetic transmission and scattering must be considered.

Clean and un-contaminated flight environment makes hypervelocity ballistic range a unique ground test facility to reproduce phenomena associated with chemical reaction and electromagnetics. Main application of hypervelocity ballistic range in aerophysics include: measurement of optical emission, electron density in the plasma wake, electromagnetic scattering from the vehicle model and its wake. Shown in Fig. 32 is an image of a hypervelocity hemi-sphere model at the Hypervelocity Aerophisics Range of HAI at CARDC, showing the high temperature gas cap and the wake behind the hemi-sphere.

ARC-UAH and its predecessor, Delco System Operation of General Motor, have the most powerful hypervelocity ballistic range test capability in aerophysics phenomena. Typical instruments are visible to Long Wavelength Infrared (LWIR) optical emission radiometers, microwave interferometers and forward scattering radar for wake electron density measurement, and mono- and bi-static radar for Radar Cross-Section (RCS) and wake velocity measurement. Shown in Fig. 33 is RCS spectral energy of hypersonic sphere model wake obtained at ARC-UAH [21]. The curve shows the spectral function for wakes of spherical bodies. Shown in Fig. 34 is infra-red spectral radiation intensity of hypersonic wake obtained at Range G of AEDC [36]. The X axis in Fig. 34 is scaled in terms of distance behind the model nose in body diameters. A, B and C is referred to measurement locations at 130, 249 and 409 ft from range entrance, respectively.

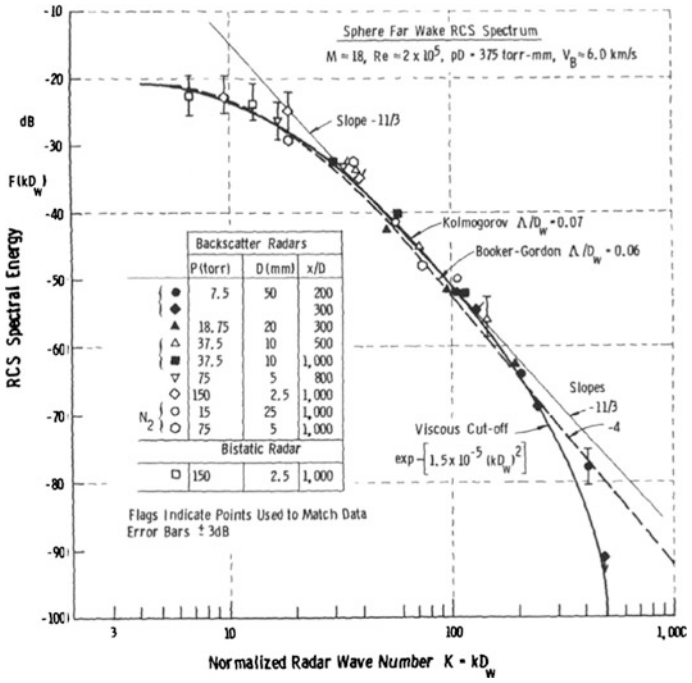

Fig. 33 RCS spectral energy of hypersonic sphere model wake obtained at ARC-UAH [21]

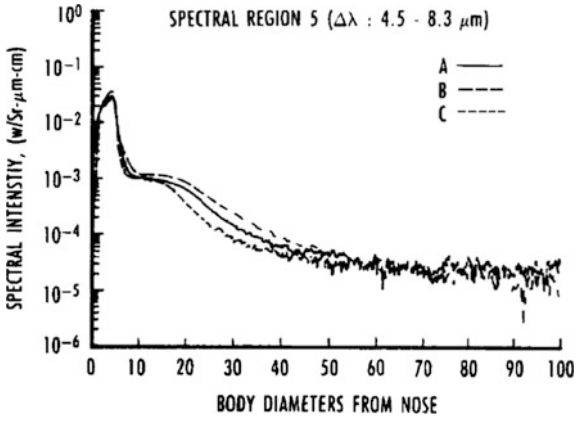

Fig. 34 Infra-red spectral radiation intensity of hypersonic model and wake [36]

4.3 Hypervelocity Impact

Studies of hypervelocity phenomena were motivated by issues such as meteor craters on the moon and other planets, interception of ballistic missiles, space debris protection of spacecraft, and solid state physics of materials at extremely high

pressures. The hypervelocity ballistic range (or may called as hypervelocity impact range in the considered case) is characterized by the formation of very strong shock waves in a hitted target, which results in very high pressure, measured in millions of atmospheres.

While the hypervelocity launcher and part of the instrumentation of the ballistic range used for impact studies are the same as those for aerodynamic tests, other subsystems might be essentially different and specialized. In hypervelocity impact tests, the instrumentation will be grouped around the target, including ultra high-speed cameras to record the externally visible impact processes, luminosity detectors, high speed flash X-ray to record the internal damage of target, and other electro-magnetic detectors. Special screens placed to catch and record the distribution of debris material ejected either forward or backward from the impact point may be installed in the impact chamber. And usually, the impacted target might be recovered and examined.

Hypervelocity impact experiments in ballistic range include the basic phenomenology of cratering, space debris impact on space structures, and the properties of materials at very high pressure [4].

Phenomenology of cratering Cratering is one of the most common phenomena in the development of planets, as seen on the moon and other planets. In planets case, the target is regarded as semi-infinite, that means its width and thickness are both many times greater than the size of the projectile, and that the reflected of shock wave from the target boundary has negligible effect on the penetration process of penetration. The most symbolic phenomenon of hypervelocity impact on a semi-infinite target is the semi-spherical crater. Target materials include metals, minerals, plastics, and organic substances. A typical eject debris, crater and SEM graph of hypervelocity impact are show in Fig. 35.

Space debris impact on space structures Numerous space debris of different sizes are now circling around the earth, and right now there is no reliable approach to clean this debris. One of the choices is to enhance the protection of our spacecraft against space debris. Many kinds of shields have been developed, based upon the concept of Whipple shield. All these newly developed shields have to be tested at hypervelocity impact ranges. Considering the damage evaluation of a spacecraft under hypervelocity impact, test articles could be more complicated, including

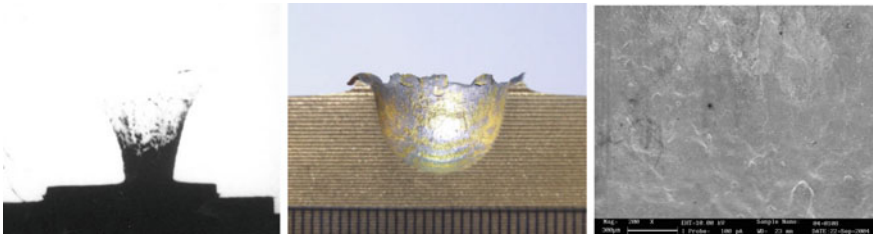

Fig. 35 Typical eject debris, crater and SEM graph under hypervelocity impact (∅3 mm copper ball impact copper semi-infinite target at 6.31 km/s, CARDC)

electronic box, fuel tank, solar cells, heat shields, propulsion units, space-suit, and even a real satellite. Reference [37] describe results of some of the many experiments in this field. A typical Whipple shield and shadowgraph of impact debris are shown in Fig. 36 [38].

Materials at very high pressure A third area of research is the study of material at high pressures attained behind the shock wave produced by impact of a high velocity projectile. The density and pressure in the shock-compressed zone can be determined by the velocity of shock propagation and of the material particle behind the shock front. The experimentally determined relation between these two quantities is generally termed the "Hugoniot" of the material, after the Rankine-Hugoniot relations describing the conditions across a shock wave (see Fig. 37). The material equation of state can be determined based on the Hugoniot findings,

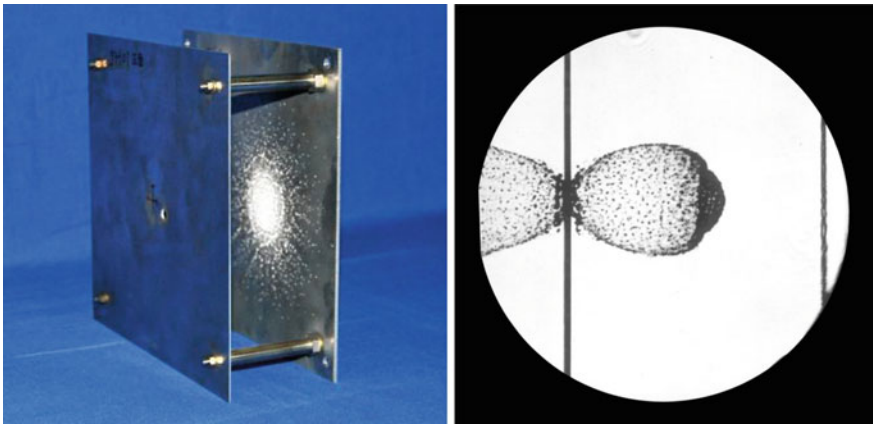

Fig. 36 Whipple shield and shadowgraph of debris cloud [38] (∅5.02 mm AL sphere impacts Whipple Shield at 5.52 km/s, CARDC)

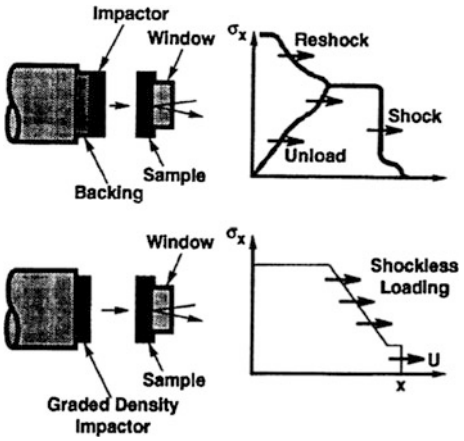

Fig. 37 Experimental techniques for off-Hugoniot measurements using gun-launched projectiles [41]

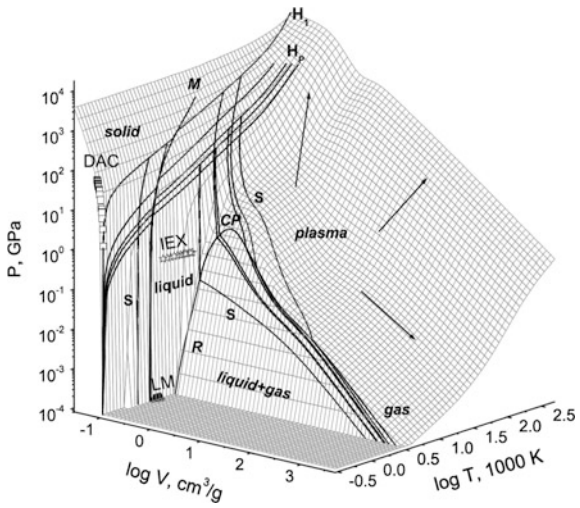

Fig. 38 3D surface of pressure-specific volume-temperature in copper [42]

(see Fig. 38). This is of great value in all scientific studies of solids at very high pressure (as e.g., studies of planetary interiors). An excellent description of this subject is given in Refs. [39, 40] including both analytical and experimental treatments.

5 Concluding Remarks

Ballistic range, especially hypervelocity ballistic range, have played a key role in researching phenomena resulted from a hypervelocity moving body in/out of the earth atmosphere or upon its impact on another object. In both fields of hypervelocity aerodynamics/aerothermodynamics and dynamic response of material/structure under hypervelocity impact, ballistic range is a main investigation tool. So far, it is the only experimental approach besides the real flight test that could provide us reliable hypervelocity data.

The advantage of hypervelocity ballistic range is that it could reproduce real hypervelocity scenery. For example, when we are interested in hypervelocity aerodynamics, the nature of free flight and non-contaminated ambient test gas makes ballistic range a better means (compared with hypersonic wind tunnels or shock tunnels) in obtaining important data such as boundary layer transition, optical emission, etc.

However, the disadvantage of hypervelocity ballistic range is also obvious: first, the relatively small model size limited by launch tube bore of a two-stage LGG; second, the difficulty in obtaining accurate measurements of that fast flying small test model/projectile.

Encouragingly, efforts have been made or are being made to further improve the test capabilities of hypervelocity ballistic ranges, such as the upgrade of the launcher and the measurement system at AEDC Range G in the 1990s. Right now at Hypervelocity Aerodynamics Institute of CARDC, the 200 m Free Flight Range is under upgrading process. Two-stage LGGs of 120 and 203 mm launch tube bore diameters are under fabrication, and the original 1.5 m diameter test section has been replaced by a 3 m diameter test section.

With bigger launcher and soft launch capability, more complicated flight vehicle models than those of today could be fired at hypervelocity, giving us greater chance to obtain desired experimental data than ever before. Together with the fast development of optical-electro instruments, miniature sensors based on Nano technology, and telemetry technology, hypervelocity ballistic range could hopefully be developed into a both reliable and affordable bridge between lab tests and real flight tests at outdoor range.

Acknowledgments The author would like to express sincere appreciation to Mr. Jinyang LUO, Mr. Yi LI, Mrs. Jie HUANG, Mr. Anhua SHI, Dr. Zhefeng YU, Mr. Hong CHEN, Mr. Dezhi JIAO, Mr. Fawei KE, Mrs. Lei ZHENG, and Mr. Yijian YAN for their invaluable help in the completion of this chapter.

References

1. National historic mechanical engineering landmark-aerodynamic range, The American Society Of Mechanical Engineers (1982)
2. Crozier, W.D., Hume, W.: High-velocity light gas gun. J. Appl. Phys. **28**(8), 892–894 (1957)
3. Pope, A., Goin, KL.: High-Speed Wind Tunnel Testing. Wiley, New York (1965)
4. Canning, T.N., Seiff, A., James, C.: Ballistic range technology, AGARDograph No. 138 (1970)
5. Lukasiewicz, J.: Experimental Methods of Hypersonics. Marcel Dekker, Inc, New York (1973)
6. Reda, D.C.: Correlation of nosetip boundary layer transition data measures in ballistic-range experiments, AIAA 1980-0286
7. Strawa, A.W., Chapman, G.T., et al.: Ballistic range and aerothermodynamic testing. J. Aircr. **28**(7) (1991)
8. Chapman, G.T.: The ballistic range—Its role and future in aerothermodynamic testing, AIAA 1992-3996
9. Jiang, W.B., et al.: Design of hypersonic test facilities, Press House of Defense Industry (of China) (2001)
10. Lu, F., Marren, D.: Advanced hypersonic test facilities. AIAA series of Progress in Astronautics and Aeronautics, vol. 138 (2002)
11. Impact and lethality Testing[EB/OL]. http://www.arnold.af.mil
12. Cable, A.J.: Upgrade of the ballistic range facilities at AEDC: now complete. AIAA-94-2493
13. http://www.arnold.af.mil
14. Carver, D., Campbell, L.L., Roebuck, B.: Large-scale, hypervelocity, high-fidelity interceptor lethality development in AEDC's range G. Int. J. Impact Eng. 35–1459 (2008)
15. Campbell, L.L., Cable, A.J.: The upgraded ballistic range facilities at aedc. Int. J. Impact Eng. **17**, 131–138 (1995)

16. Young, R.P., Rushing, J.R.: Expanded impact test capabilities of the aronold engineering development center, AIAA 96-4241
17. Cable, A.J.: Upgrade of the ballistic range facilities at AEDC: the half-way point, AIAA-92–3997
18. Salinas, I.T., Cornelison, C.: Test planning guide for ASF facilities. 029-9701-XM3 Rev. B March (1999)
19. Grinstead, J.H., Wilder, M.C., Reda, DC., Cornelison, CJ.: Shock tube and ballistic range facilities at NASA ames research center. Technical report RTO-EN-AVT-186, NATO (2010)
20. Reda, D.C., Wilder, M.C.: Transition experiments on blunt cones with distributed roughness in hypersonic flight. J. Spacecraft Rockets **50**(3), 504–507 (2013)
21. Hayami, R.A.: The application of light gas gun facilities for hypervelocity aerophysics research, AIAA 92-3998
22. http://www.uah.edu/UAH/facilities.asp.htm
23. Liquornik, D.J., Yang, F.W., Zwiener, M.C., etc.: Active attitude control of gun launched projectiles. Int. J. Impact Eng. **23,** 561–572 (1999)
24. http://hitf.jsc.nasa.gov/NASAJSCLGG/nasajscgun/HITFHVITestingHighSpeedCameras.htm
25. Stilp, A.J.: Aeroballistic and impact physics research at emi and historical overview. Int. J. Impact Eng. **17**, 785–805 (1995)
26. Alwes, D.: Columnus-viewport glass plane hypervelocity impact testing and analysis. Int. J. Impact Eng. **10**, 1–22 (1990)
27. Destefanis, R., Faraud, M.: Testing of advanced materials for high resistance debris shielding. Int. J. Impact Eng. **20**, 209–222 (1997)
28. Thoma, K., Schäfer, F., Hiermaier, S., et al.: An approach to achieve progress in spacecraft shielding. Adv. Space Res. **34**, 1063–1075 (2004)
29. Schäfer, F., Putzar, R., Lambert, M., et al.: Vulnerability of satellite equipment to hypervelocity impacts. 59th International Astronautical Congress (2008)
30. Vergniaud, J.B., Guyot, M., Lambert, M., et al.: Structural vibrations induced by HVI—Application to the Gaïa spacecraft. Int. J. Impact Eng. **35**, 1836–1843 (2008)
31. Hoerth, T., Schafer, F., Thoma, K., et al.: Hypervelocity impacts on dry and wet sandstone: observations of ejecta dynamics and crater growth. Meteorit. Planet. Sci. **48**(1), 23–32 (2013)
32. Rudolph, M., Schimmerohn, M., Osterholz, J., et al.: Electrical signatures of hypervelocity impact plasma with applications in in-situ particle detection. Acta Astronaut. **101**, 157–164 (2014)
33. Liu, S., Huang, J., Li, Y.: Hypervelocity impact tests for spacecraft against orbital debris at HAI, CARDC. 59th International Astronautical Congress (2008)
34. Reda, D.C., et al.: Aerothermodynamic testing of ablative reentry vehicle nosetip materials in hypersonic ballistic-range environments, AIAA 2004-6829
35. Wilder, M.C., et al. Free-flight measurements of convective heat transfer rates in hypersonic ballistic-range environments, AIAA 2007-4404
36. Harris, H., Hendix, R.: Upgrade in optical measurement capabilities of AEDC ballistic ranges, AIAA 1994-0672
37. IADC WG3 members. Protection manual. IADC-WD-00-03 Version 4.0, Revision 8. March 12 (2010)
38. Liu, S., Li, Y., Huang, J., Luo, JY., Xie, A.M., Shi, A.H.: Hypervelocity impact test results of whipple shield for the validation of numerical simulation. J. Astronaut. **26**(4) (2005)
39. Mayer, M.A.: Dynamic Behavior of Materials. Wiley, New York (1994)
40. Solid State Physics, vol. 6, pp. 1–63. Academic Press. Inc., New York (1958)
41. Asay, J.R.: The use of shock-structure methods for evaluating high-pressure material propertics. Int. J. Impact Eng. **20**, 27–61 (1997)
42. Sultanov, V.G., Kim, V.V., Lomonosov, I.V., et al.: Numerical modeling of deep impact experiment. Int. J. Impact Eng **35**, 1816–1820 (2008)

Author Biography

Sen Liu is well-known for his studies in hypervelocity Impact and hypersonic aerodynamics at China Aerodynamics Research and Development Center (CARDC). He has worked as the head of Hypervelocity Ballistic Range Laboratory, Chief Scientist of Hypervelocity Aerodynamics Institute of CARDC. He is the vice-chairman of both the Committee of Hypersonic Aerodynamics and the Committee of Flow Visualization under the Chinese Society of Aerodynamics. Also, he is the associate editor-in-chief of the Journal of Experiments in Fluid Mechanics. He received his Bachelor and doctor degrees from Department of Aircraft at Northwestern Polytechnical University, and Master degree from the graduate school of CARDC. His current research mainly deals with hypervelocity impact of space debris against spacecraft, hypersonic boundary layer transition, and high temperature aerothermodynamics.

Part III
Shock Waves in Solids

Experimental Methods of Shock Wave Research for Solids

Toshimori Sekine

1 Introduction

Shock waves in solids are more complex than those in gases, because a solid behaves as elastic and plastic media depending upon the stress level and strain rate. A shock wave generates high pressure and high temperature simultaneously and alters the atomic and molecular structures of solids. A shock wave also is always accompanied by a rarefaction wave that reduces the shock-compressed state compared to the original pressure. The rarefaction wave velocity at the compressed state is faster than the shock wave velocity, but generates later than the shock wave. As a result, the shock compression duration is limited by the difference in arrival time between the two waves mentioned. Herein we overview the experimental methods in shock wave generation by hypervelocity impacts on solids and condensed matters. Figure 1 illustrates versatile areas in shock wave research as natural phenomena, basic scientific sides, applications to materials science, energy and safety engineering and medical and life sciences as a function of shock strength. Shock waves in solids can generate extreme high-pressures in the media beyond the strength due to the inertial principle.

Actually the stress achieved experimentally by the propagation of a shock wave in solid ranges between a few GPa and several thousands of GPa, depending on how the shock wave is generated. Compression by shock wave plays a significant role in high-pressure physics and chemistry and provides a sound base of pressure scale to the static high-pressure community. This contribution reports on hypervelocity accelerators, stress waves in solids, the shock wave equation of state, the stability of shock waves, the thermodynamics of shock-induced phase transition, high-pressure generation, shock chemistry, and laser shock experiments.

T. Sekine (✉)
Department of Earth and Planetary Systems Science, Hiroshima University,
Kagamiyama 1-3-1, Higashi-Hiroshima 739-8526, Japan
e-mail: toshimori-sekine@hiroshima-u.ac.jp

F. Seiler and O. Igra (eds.), *Hypervelocity Launchers*,
Shock Wave Science and Technology Reference Library 10,
DOI 10.1007/978-3-319-26018-1_3

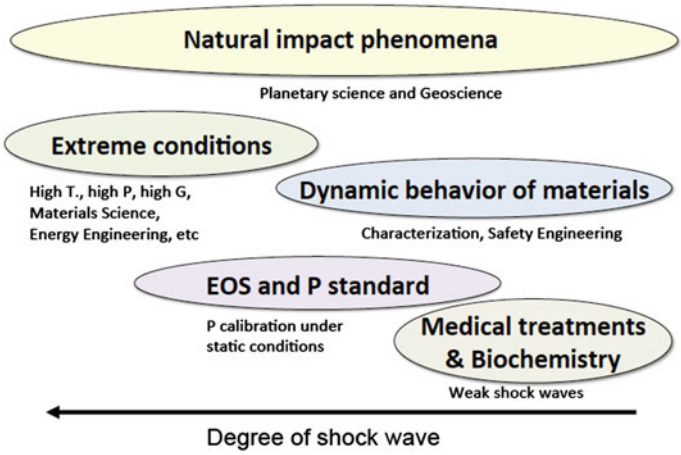

Fig. 1 Shock wave research areas for condensed matters

2 Hypervelocity Accelerators and High-Pressure Generation

Shock waves are generated using hypervelocity accelerators. There exist many accelerators such as gas gun, propellant gun, two-stage light gas gun, explosive, laser gun, Z-pinch, rail gun, magnetic accelerator, and high power laser as summarized in Fig. 2. They have been used since the 20th century.

Most of these accelerators have been described already by Cable [4] and Nellis [47] or elsewhere, and the essential parts of them are not much different. We will not describe all of them. However, there are many differences in the structure of the impact chambers in research fields between gas and condensed matters because the measuring and observing methods of shock waves differ considerably. For solids, plane impact experiments have been conducted frequently to analyze the shock-compressed states easily. Here we focus on recent developments of laser guns, and for the others references are given by Roybal et al. [55], Langenhorst et al. [36], Lemke et al. [39], and Knudson et al. [35].

Figure 3 illustrates target assemblages for laser gun and direct laser shock. In both, focused lasers are used to ablate the surface of a target; a mini-flyer foil in laser gun (Fig. 3a) or a target material in laser shock (Fig. 3b). Ablated plasma, by relatively long pulsed laser such as a nanosecond laser, expands rapidly and keeps pushing the target to accelerate it. A mini-flyer has a velocity in a gap between sample and thin foil and impacts onto a sample, and a target material subjected to direct laser ablation also has shock wave in target. These methods are recent very

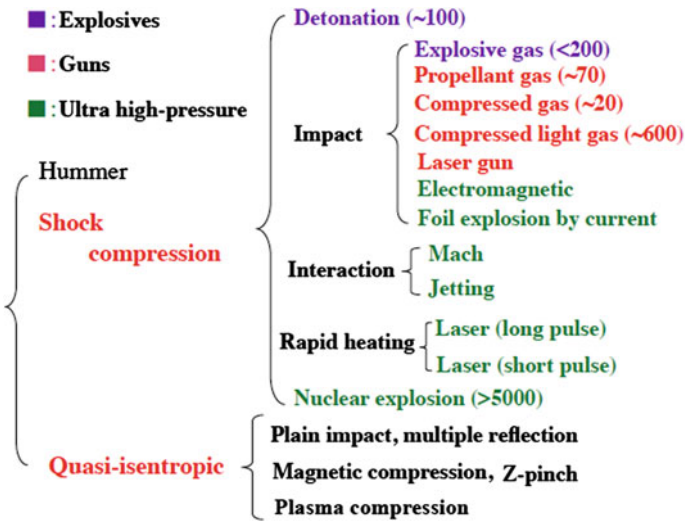

Fig. 2 Experimental methods for generating dynamic compression in solids. *Number* in parenthesis gives briefly attainable pressure (GPa)

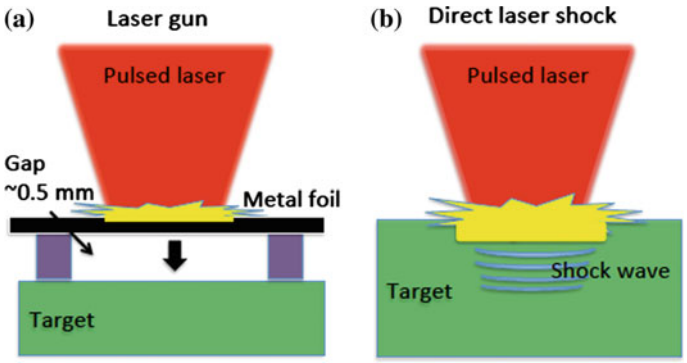

Fig. 3 Shock wave generated by pulsed lasers. **a** Laser gun to accelerate a mini flyer of thin metal, and **b** laser ablation to generate shock wave in target

popular to pump and probe experiments [10]. Figure 4 shows velocity profiles as a function of the applied energy flux for a 10-μm aluminum foil [25, 26], directly measured by VISAR, recorded with a streak camera. This method has been successful in finding experimentally the phase transformation of cubic diamond to hexagonal diamond [28], due to shear.

When the shock wave propagates in a solid, high pressure and temperature are simultaneously generated as well as entropy increase. The Shock compression

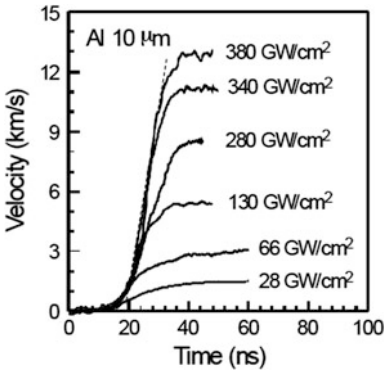

Fig. 4 Velocity-time profiles of mini-flyers accelerated by pulsed laser, determined by optically recorded signals with a streak camera [25–27]. *Broken line* indicates a fast acceleration of $\sim 10^{12}$ m/s^2, a high gravity field achieved for ~ 10 ns by the acceleration

process is irreversible. When we are interested in having high-density state and relatively low temperature, in order to keep temperature below the melting point, isentropic and quasi-isentropic compressions (Fig. 2) are required. Such methods are important for compressing a compressible material like a fluid [47]. Isentropic and quasi-isentropic compressions are realized dynamically by Z-pinch [1, 23] and making use of laser plasma compression [70] and conventional gun experiments [47].

3 Stress Wave in Solid

A stress wave in a solid is more complicated than a pressure wave in a gas due to material strength and phase transition in the solid, and it is classified into three main categories of elastic, plastic, and phase transition regions depending on the stress level and strain rate. At a relatively low-pressure region, the solid behaves as an elastic body so that the longitudinal and shear waves are present below the Hugoniot elastic limit (HEL). The longitudinal wave velocity C_L is faster than the shear wave velocity C_S. Therefore the HEL value of a single crystal is dependent on the crystallographic orientation as well as the strain rate. It has been well known that the HEL varies with time, and we can observe their changes through time-resolved methods (e.g. [61, 84]). More plastic behavior can be observed slightly above the HEL stress while the shear remains, and the solids become complete plastic at higher pressures well above the HEL.

4 Shock Equation of State

When the initial state is at pressure P_0, volume V_0, and internal energy E_0 and changes to a new state (pressure P_H, volume V_H, and internal energy E_H) after a shock wave propagates, the flow equations can be described by the Rankine-Hugoniot equations:

$$P_H - P_0 = V_0^{-1}(U_s - u_o)(u_p - u_o) \tag{1}$$

$$V_H = V_0[1 - (u_p - u_0)/(U_s - u_0)] \tag{2}$$

$$E_H - E_0 = 0.5(P_H + P_0)(V_0 - V_H) \tag{3}$$

Here U_s is the shock velocity, and u_p and u_0 are the particle velocities before and after the shock, respectively. These three equations are derived from the conservations of mass, momentum, and energy before and after the shock compression.

The three Eqs. (1)–(3) can be combined to an expression for U_s and u_p,

$$U_s - u_0 = V_0[(P_H - P_0)/(V_0 - V_H)]^{1/2} \tag{4}$$

$$u_p - u_0 = [(P_H - P_0)(V_0 - V_H)]^{1/2} \tag{5}$$

Through these equations, we plot a compression curve of $(P - V)$ and a relation of $(U_s - u_p)$, called the Hugoniot relation. If there is no phase transition, the $(U_s - u_p)$ relation can be fitted to a straight line:

$$U_s = C + su_p \tag{6}$$

C is equal to (or very close to) the bulk sound velocity at zero pressure and s is related to the pressure derivative of the bulk modulus K_0 at constant entropy as follows:

$$C^2 = C_L^2 - \frac{4C_S^2}{3} = K_0 V_0 \tag{7}$$

$$s = \left[\left(\frac{\partial K_0}{\partial P}\right)_s + 1\right]/4 \tag{8}$$

The Rankine-Hugoniot equations do not provide directly the shock temperature T_H. Temperature must be calculated thermodynamically by comparison of internal energy gains between the Hugoniot relation and the isentropic relation in the

considered volume. The initial temperature T_0 and the temperature on the isentropic temperature T_S are given by the equation:

$$\ln\left(T_S/T_0\right) = \int_V^{V_0} \gamma \, dV/V \tag{9}$$

where the Grüneisen parameter γ is given by

$$\gamma = V\left(\frac{\partial P}{\partial E}\right)_V = \frac{V}{C_v}\left(\frac{\partial P}{\partial T}\right)_V = -\frac{V}{C_v}\left(\frac{\partial P}{\partial V}\right)_T\left(\frac{\partial V}{\partial T}\right)_P = -\frac{V}{C_P}\left(\frac{\partial P}{\partial V}\right)_S\left(\frac{\partial V}{\partial T}\right)_P \tag{10}$$

The relation between the shock temperature and the isentropic temperature is given by

$$TdS = C_v dT + T\left(\frac{\partial P}{\partial T}\right)_V dV = 0 \tag{11}$$

and

$$\ln\left(T_H/T_S\right) = \int_{S_0}^{S}\left(\frac{dS}{V}\right) \tag{12}$$

When $\eta = 1 - V/V_0$, the entropy S_H can be expressed by

$$S_H - S_0 = \frac{V_0^3}{12T_0}\eta^3\left(\frac{\partial^2 P}{\partial V^2}\right)_0 + \cdots \tag{13}$$

Then,

$$\begin{aligned}\ln\left(\frac{T_1}{T_0}\right) &= \gamma_0\eta\left[1 + \frac{V_0^2}{12K_0T_0}\eta^2\left(\frac{\partial^2 P}{\partial V^2}\right)_0 + \cdots\right] \\ &= \gamma_0\eta\left[1 + \frac{1+s}{6\alpha T_0}\eta^2 + \cdots\right]\end{aligned} \tag{14}$$

where α is the thermal expansion coefficient. For the equation of state of a solid, the third-order Birch-Murnaghan equation is used to approximate the isentropic pressure P_S;

$$\mathrm{P_S} = \frac{3\mathrm{K_{0S}}}{2}\left[\left(\frac{\mathrm{V_0}}{\mathrm{V}}\right)^{7/3} - \left(\frac{\mathrm{V_0}}{\mathrm{V}}\right)^{5/3}\right]\left\{1 + 3\left(\frac{\mathrm{K'_{0S}}}{4} - 1\right)\left[\left(\frac{\mathrm{V_0}}{\mathrm{V}}\right)^{2/3} - 1\right]\right\} \tag{15}$$

where K_{0S} and K_{0S}' are the bulk modulus and its first pressure derivative at zero pressure.

5 Stability of Shock Wave

Shock velocity increases with shock pressure for most materials, as seen from Eq. (4). For a stable shock wave, the sound velocity must increase with pressure. The steadiness is kept by the balance of steepening and broadening the velocity that caused by the competing effects of non-linear stress-strain relation and dissipative material behavior [21]. When a phase transition occurs, the steadiness is broken to form discontinuity in the (Us-up) and (P-d) relations. Figure 5 illustrates a typical Hugoniot relation in plots of (P-V) and (Us-up) with a discontinuity at point 2, where two particle velocities u_{p2} and u_{p4} are present at a shock velocity U_{S2}.

This situation is observed frequently at elastic-plastic transformation and many phase transitions. While there is a single shock at pressures up to P_2 and above P_4, two-wave structure is observed in a range of pressure between P_2 and P_4 where $U_{s2} - u_{p0} > U_{s3}$, that is

$$\frac{P_3 - P_2}{V_2 - V_3} < \frac{P_2 - P_0}{V_0 - V_2} \tag{16}$$

In case of a phase transition displaying a single wave as illustrated in Fig. 6, the following relation is confirmed:

$$\frac{P_3 - P_2}{V_2 - V_3} > \frac{P_2 - P_0}{V_0 - V_2} \tag{17}$$

Under this circumstances, the path 1-2-3′-3-4 may be possible when the phase transition or reaction is very sluggish and the low-pressure phase survives metastably up to P_3. Then a sudden jump at u_{p3} can be observed in the plot of (Us-up)

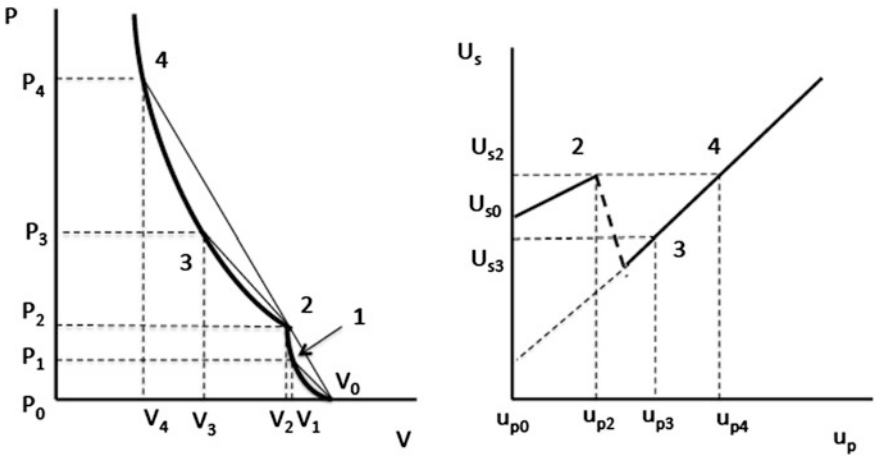

Fig. 5 Hugoniot relation for a material with high-pressure phase transition displaying two-wave structure

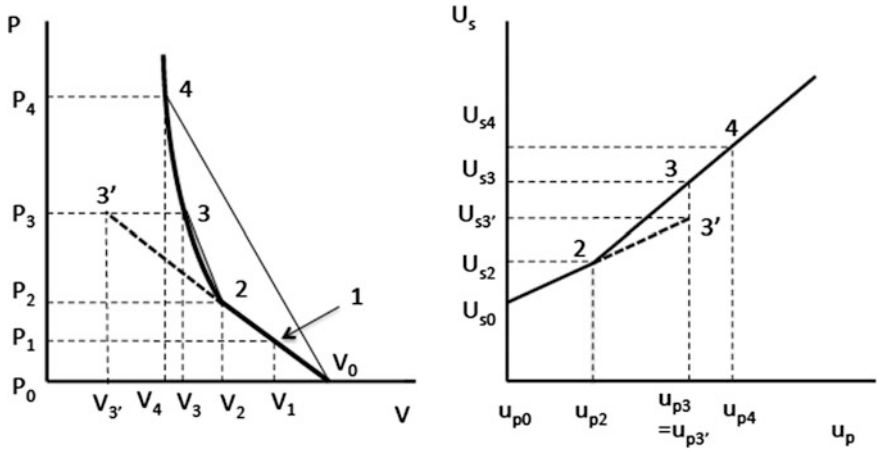

Fig. 6 Hugoniot relation for a material with high-pressure phase transition displaying single wave structure

and a volume increase at P_3 also can be seen in the (P-V) plot, as illustrated in Fig. 6. These two cases may have a relatively large volume change associated with the phase transition as indicated by extrapolation of the compression curve for high-pressure phase. If the volume change is too small, then it will be difficult to find a discontinuity in the (Us-up) plot.

When the pressure reaches the threshold for a phase transition, the phase transition can be observed above the threshold. For a phase transition, the threshold pressure is often dependent on temperature as well on the kinetics. The phase transition associated with a significant amount of volume change can be detected experimentally by Hugoniot measurements. Figure 7 illustrates four types of phase transitions: the changes in volume, entropy, and latent heat of reaction depend in similar way on the previous discussions [13, 42].

The first and the second ones are for the phase boundary with $\frac{dP}{dT} > 0$, and $\Delta V > 0$ (Fig. 7a) or $\Delta V < 0$ (Fig. 7b). The third and forth are with $\frac{dP}{dT} < 0$ and $\Delta V < 0$ (Fig. 7c) or $\Delta V < 0$ (Fig. 7d). In most materials melting is associated with a volume increase, and the measured (Us-up) relation cannot detect the melting as illustrated in Fig. 7a. First-order high–pressure phase transitions are accompanied with significant decreases in volume and they are detectable using (Us-up) relations, as shown in Fig. 7b.

According to the Clausius-Clapayron relation, it is: $\frac{dP}{dT} = \frac{\Delta S}{\Delta T} = \frac{H}{T\Delta T}$. Taking H as the latent heat of reaction, endthermic ($H < 0$) and exthothermic ($H > 0$) reactions with $\frac{dP}{dT} < 0$ are illustrated as in Fig. 7c, d, respectively. The (Us-up) relations display a drop or an increase at the discontinuity. Increase in the (Us-up) relations at the discontinuity are known as ballotechnic process in shocked porous powder [22]. (Us-up) relations for silica materials with lower initial densities show such behaviors [78], due to extreme high temperature generation.

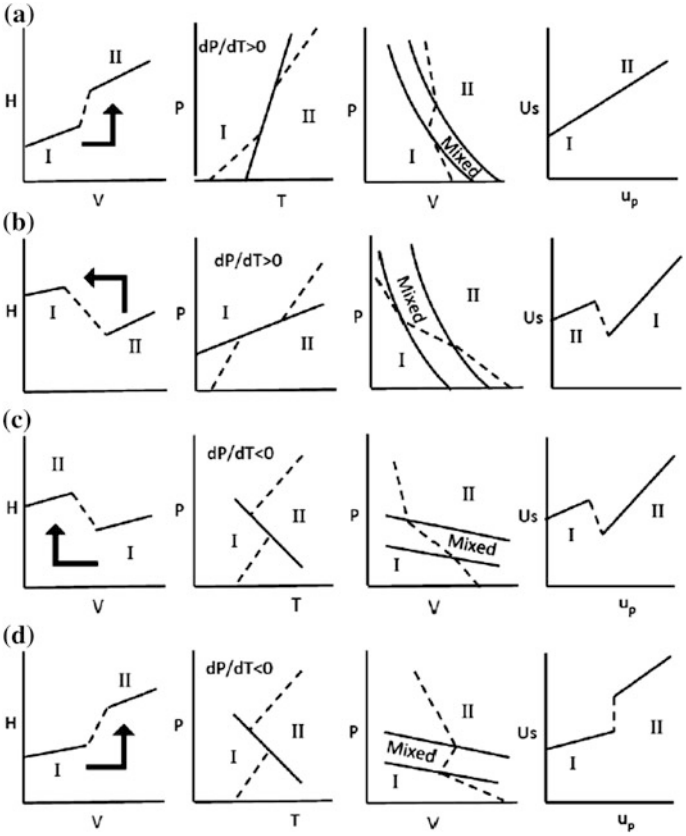

Fig. 7 Schematic illustrations of various shock-induced phase transitions. Volume (V), enthalpy (H), pressure (P), temperature (T), shock velocity (Us), and particle velocity (up) are plotted. V-H relation is illustrated at a pressure, and *arrows* give the direction of reaction. Possible paths are displayed in P-T, P-V, and Us-up relations. **a** $dP/dT > 0$ and $\Delta V > 0$, **b** $dP/dT > 0$ and $\Delta V < 0$, **c** $dP/dT < 0$ and $\Delta V < 0$, and **d** $dP/dT < 0$ and $\Delta V > 0$

6 Thermodynamics of Shock-Induced Phase Transition

The hydrostatic Gibbs function can be generalized for deducing a potential that defines equilibrium conditions for the phase transition in the absence of shear stress. The Gibbs energy is a function of pressure and temperature and the two Gibbs energies of reactant and product should be equal to each other under equilibrium. In case of heterogeneous transformation, the nuclei for the new phase begin to grow heterogeneously in the originally homogeneous mass in the stress distribution. Under such circumstances, the stress for the original phase and the new phases is not simply described. When one considers the limited interface area between the nucleus and the original grain, it is difficult to consider the hydrostatic Gibbs

function like in the case of a fluid. Detailed discussions on this matter have been done by Paterson [49], Robin [54], and Duvall and Graham [13].

According to these references, there are three basic questions in describing shock-induced phase transitions. (1) Do shock experiments give the same thermodynamic properties as the static high-pressure experiments? (2) Do the shock-induced transformations are completed in shock experiment? (3) Do shock experiments provide results under thermodynamic equilibrium? Although these issues are essential for understanding the interactions between shock wave and material, the Hugoniot relations does not provide detailed information on the shock-induced phase. We need to develop new in situ techniques to identify the phases in time-resolved and spatial-resolved ways. Recent developments of new techniques will reveal the mechanism of phase transition with help of numerical simulations [44].

In some materials, excellent agreement is achieved between the transition pressures occurring under shock loading and in static experiments. For materials with a series of phase transitions, all of the phase transitions based on the Hugoniot measurements directly are not always observed. This depends on the mechanism of phase transition and the amount of its volume change. In some cases we need additionally to know the change of properties to confirm and detect the phase transition. Recently theoretical calculations have been developed which helped us understanding thermodynamically what process is energetically most probable, because we cannot investigate through direct experiments every characteristics of the materials induced by shock compression.

7 Shock Syntheses

There are a lot of shock-induced phase transitions that have been confirmed by quenching the high-pressure phases formed under shock compression. They are represented by shock syntheses of diamond (e.g. [8, 16]), wurtzite-type BN (e.g. [56, 71]), and spinel-type nitrides [60]. Recent developments of shock reactions from inorganic materials such as iron, nitrogen gas, carbon, and water have been demonstrated syntheses of ammonia [46] and organic materials such as biomolecules of amino acid, amine, carboxylic acid, and others [17].

Inorganic nitrides reviewed here are spinel-type nitrides, their related nitrides, and oxynitrides in the system Si–N–Mg–Al–O. The basic formula is AB_2O_4 (oxide) or AB_2N_4 (nitride), and this group of compound displays a series of phases; phenacite, olivine, spinel, and post-spinel types depending on temperature and pressure, as illustrated in Fig. 8. The typical end members and solid solutions have been investigated by the shock recovery experiments and equation of state measurements (e.g. [24, 65–68]).

The Hugoniot relations of Si_3N_4 are plotted in Fig. 9, and the measured equation of state has been compared with that for the predicted phases. The high-pressure phases have been subjected to recovery shots. The recovered samples have been

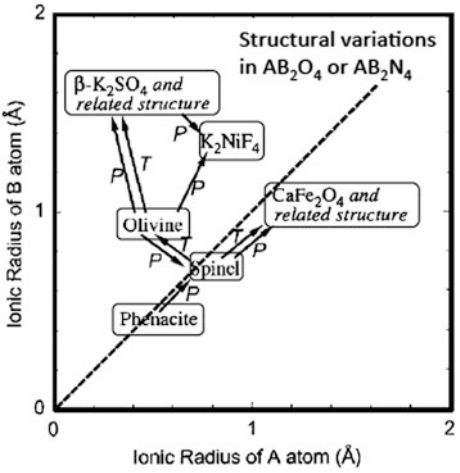

Fig. 8 Structure variations of AB_2X_4 compound as a function of pressure and temperature. *Arrows* direct increasing in pressure (P) or temperature (T) $CaFe_2O_4$ and related structure include Ca_2TiO_4 structure. Tatsumi et al. [76]

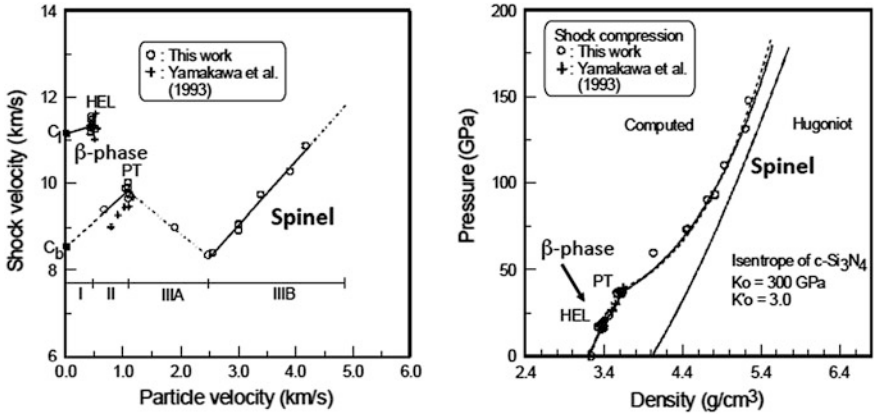

Fig. 9 Hugoniot relations of Us-up and P-d of Si_3N_4 ceramics [24]. Symbols *I*, *II*, *IIIA*, and *IIIB* correspond to one-wave elastic region, two wave lowpressure phase region, three wave mixed phase region, and three wave highpressure phase region, respectively

characterized by several structure analyses. Some of them are successful in the corresponding germanium nitride [27], but recovery for post-spinel phases was not yet successful.

Figure 10 compares the Hugoniot relations of spinel-type ceramics of $MgAl_2O_4$, Fe_3O_4, and AlON [67, 68], suggesting that post-spinel phases could be formed above $\sim$100 GPa. In recovery shots, copper powders play an important role to synthesize and recover the high-pressure phases because copper is known for

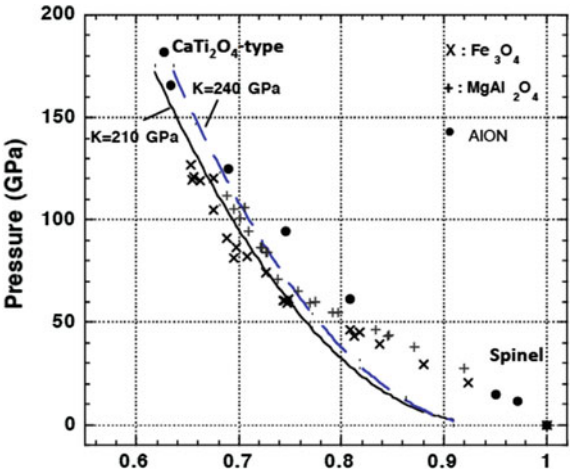

Fig. 10 Comparison of Hugoniots of spinel-type compounds (Fe_3O_4, $MgAl_2O_4$, and AlON) [67, 68], indicating a phase transition to a high-pressure phase of Ca_2TiO_4-type structure above ~100 GPa

having high shock-impedance and thermal conductivity. The presence of copper generates higher temperature than that for ceramics powder and enables ceramics powder to be quenched rapidly relative to its absence.

Due to its high shock-impedance, copper plays an important role as pressure medium to increase pressure and temperature more than nitride starting materials with low-impedance when subjected to a shock compression. It has been known in the shock synthesis of diamond [77]. We mixed about 10–20 wt% ceramics powder with a large amount of copper powder and made pellets under a load up to ~200–500 MPa to control the porosity. Figure 11 shows a calculated relationship among

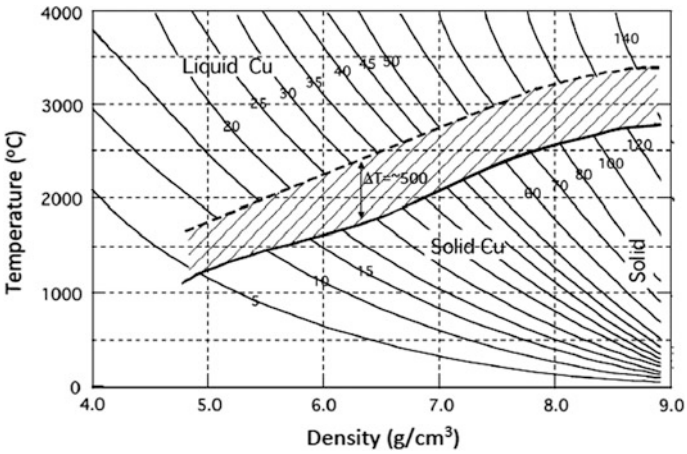

Fig. 11 Calculated temperature rise for solid and porous copper as a function of shock pressure and porosity. The temperature above the melting is reduced by the heat of fusion for copper, e.g. −500° after complete melting

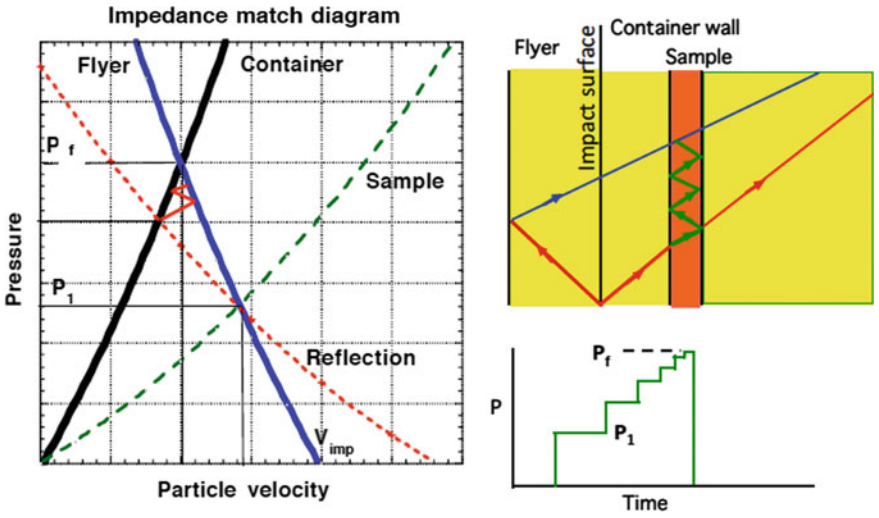

Fig. 12 Schematic illustration of pressure profile for sample encapsulated in metal recovery container, based on the impedance match method, by plate impact

initial density of pressed copper powder, shock pressure, and temperature rise. The area between solid and liquid corresponds to a state of partial copper melting.

Using this diagram the shock temperature for the copper powder with an initial density can be predicted after estimation of the shock pressure. The shock pressure is calculated using the impedance match method based on the measured impact velocity in using standard materials for flyer and container for which the relationship between shock velocity and particle velocity is known, as illustrated in Fig. 12. When a flyer with a velocity of V_{imp} impacts on a sample container made of the same metal as the flyer, the shock wave propagates into the flyer and the container from the impact surface. Then the pressures of the flyer and the container reach the pressure P_f. Once the shock wave comes into sample, the pressure drops to P_1 due to a lower shock impedance of sample, as illustrated in the pressure-particle velocity plot of Fig. 12. Then the shock wave is reflected several times by the inner wall of the container, and the pressure also increases step by step until the rarefaction wave catch up the shock wave in the sample. If the flyer is thick enough and the sample is relatively thin, then the peak pressure in the sample will reach P_f by reflections. Under such a condition, we can estimate the peak pressure of the sample without knowing the Hugoniot data of the sample as long as we use standard materials for flyer and container of which (Us-up) relations are known with measure of the impact velocity.

For the mixtures, it is also possible to estimate temperature assuming that the ceramics powders are in thermal equilibrium with the copper, as show in Fig. 11. Regarding the Cu melting, the temperature needs to be corrected due to the fusion energy. For example, it is about 500° above the complete melting. However, some

phases were recovered as amorphous phase in samples of SiAlON ceramics [62–64] and Si_2N_2O [67, 68], instead of the high pressure phases.

We also have developed the chemical methods to purify the high-pressure phases from a recovered mixture of low-pressure and high-pressure phases [62–64], and have characterized the structural, chemical, mechanical, and optical properties in detail. The properties of shock synthesized spinel-type Si_3N_4 are summarized in Table 1. These properties of spinel-type Si_3N_4 have been compared with that synthesized at static high temperature and high pressure [88]. Since the discovery of spinel nitrides in 1999, much effort in basic science has been done to further develop advanced nitrides and oxynitrides and these studies made a great progress in synthesizing nitride and related materials.

Table 1 Properties of shock-synthesized spinel-type Si_3N_4, characterized by different methods

Structure		
XRD	Spinal structure with a = 0.7739 nm and x = 0.2569	Sekine et al. [60]
NMR	29Si chemical shift −50 ppm for SiN_4 unit, −225 ppm for SiN_6 unit	Sekine et al. [62]
ELNES	Si-L_{23} and N-K	Tenaka et al. [75]
Thermal properties		
Stability	Up to 1670 K in Ar atmosphere	Sekine et al. [63]
Entalpy	29 kJ/mol relative to ΔH of Ni melting	Sekine et al. [63]
	80 kJ/mol by high-temperature drop solution method	Zhang et al. [89]
Expansion coefficient	$\alpha = (2.7 + 0.004\,T) \times 10^{-6}$	Hintzen et al. [29]
Mechanical properties		
Bulk modulus	300 GPa	He et al. [24]
	339 Gpa	Kiefer et al. [33]
Density	4.02 g/cm^3	Sekine et al. [60]
Hardness	43 GPa for oxygen-free sample	Tanaka et al. [75]
Chemical stability		
HF solution	c = Si_3N_4 survives for a limited duration	Sekine [58]
Optical properties		
Band gap	3.6 eV	Egdell et al. [14]
	4.30 eV	Leitch et al. [38]

XRD X-ray diffraction method, *NMR* nuclear magnetic resonance spectroscopy, *ELNES* electron-energy loss near edge spectroscopy

Nitrogen on the Earth exists only as gas and limited compounds of gas and organic matters, although it is one of the abundant elements in the universe. Here we extend shock synthesis trials to the system Si–N–Mg–Al–O–C [64–69] including the system Si_3N_4–C_3N_4 [59]. Since 1989 carbon nitride has been proposed as a hard material based on theoretical considerations [40].

It has been proposed that frequent meteorite falls may have occurred at 3.8–4.0 Gya just before the first appearance of biomolecule related to the origin of life. Ocean and atmosphere of CO_2 and N_2 was present well before the time. Therefore it is considered that there was a chance for simple biomolecules to be formed through reactions between oceanic water, atmosphere, and meteoritic carbon and iron. We need to simulate such reactions. For organic compounds, we tried using simple inorganic mixtures such as water, iron, carbon, and nitrogen gas in order to have implications for the origin of life materials on the Earth. Nitrogen gas was delivered from decomposition of Cu_3N. We have developed methods to recover aqueous solutions subjected to shock compression, although the achievable pressure is limited due to the container strength. We used ^{13}C-label carbon instead of ^{12}C carbon in order to confirm the existence of even a trace amount of synthesized organic compounds. Thus obtained aqueous samples were analyzed using chromatographic methods coupled with mass analysis. Furukawa et al. [17] have successfully confirmed the formation of numerous biomolecules such as fatty acids, amine, and glycine (amino acid). Meteorite impacts at the late of heavy bombardment may initialize the creation of biomolecules related to the origin of life on the Earth.

Generally the chemical effects of shock wave in solids are achieved by high temperature and high pressure, by high-rate migration of dislocations, by activation by pulverization (Fig. 13a), by accelerated mixing by jetting between particles

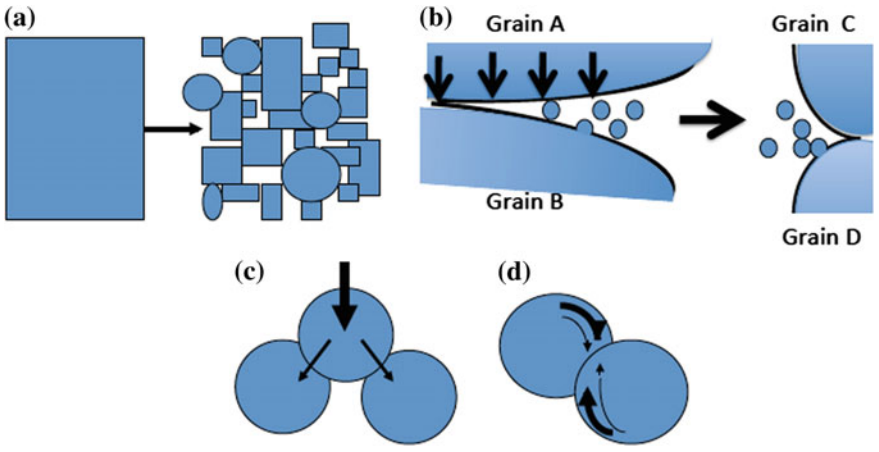

Fig. 13 Chemical effects of shock wave to promote reactions in powders. **a** Pulverization makes fresh surface with high reactivity, **b** jetting promotes reactions among grains, **c** deformation and shear, and **d** surface friction heats the grain surface hotter than the center

(Fig. 13b), by Rayleigh-Taylor instability mixing, by rapid adiabatic quenching, shear effects (Fig. 13c), by friction between particles (Fig. 13d), by limited reaction time, and so on. These effects may act to promote reactions under shock compression and provide a unique process that is not available by the other methods. It is known that some solids become amorphous under shock compression due to mechanical instability and limited time, and it is difficult to define the structure of their Hugoniot state.

8 Laser Shock Experiments

Laser shock experiments as well as ultra fast plane impacts over $\sim$10 km/s aim to achieve high pressures of several hundred GPa and above, not to be generated by the other methods, where the temperature reaches the formation field of fluid and plasma. The matters shocked to such conditions are called as warm dense matter [12], where density increases a few times relative to the initial solid and temperature surpasses 10000 K. Recent laser and Z-pinch experiments (e.g. [50]) on diamond melting (e.g. [15, 35]), phase transition in $MgSiO_3$ melt [72], and phase boundaries for MgO [7, 43] have been reported and the results of the phase boundary and melting have been compared with theoretical simulations. Pre-compressed samples in diamond anvil cells (DAC) [37] also have been investigated for water and hydrogen. Pre-compressed and Ramp experiments are achieved at relatively lower temperatures than the corresponding single shock, and these experiments prefer to investigate solid-solid phase transitions at extreme high pressures such as B1-B2 transition of MgO [7].

Laser shocked materials are normally less than 1 mm in diameter and several ten micrometers in thickness. Under shock impact they are observed by time-resolved methods listed in Table 2.

Although VISAR is popular in shock experiments for condensed matter to record velocity at a reflector, line-imaging VISAR (e.g. [5]) is used in laser shock experiments to monitor the fringe change corresponding to the velocity change observed through a slit on a streak camera. At extreme high pressures, the shock front in transparent material becomes a good reflector for visible light so that the shock velocity, instead of the particle velocity, can be determined directly by VISAR measurements. If we observe a sample and a reference material in a shot simultaneously through VISAR, the impedance match method is applied to determine the Hugoniot for a sample. Ultrafast dynamic ellipsometry [3], recently developed using high-angle and low-angle probes of transparent sample, enables to measure the Hugoniot relations in a shot. To measure temperature, a calibrated streak camera is used to determine the intensity change at a given wavelength which is popular in laser shock experiments [45], and is called a streaked optical pyrometer (SOP) in Table 2. Emissivity is estimated using the change of the VISAR signal.

Table 2 Various methods for measuring the condensed matters in recent laser shock experiments

VISAR	Velocity	Baker and Hollerbach [2], Celliers et al. [5]
DISAR (or photo Doppler Velocimetry PVD)	Velocity	Stand et al. [73], Weng et al. [83], Valenzuela et al. [80], Jensen et al. [31]
Ultrafast XRD	Structure	Johnson et al. [32], Wark et al. [82], Turneaure et al. [79], Suggit et al. [74], Rygg et al. [53], Milathianaki et al. [44]
Spectroscopy		
Raman	Temperature, vibrational	Schmidt et al. [57], Pangilran and Gupta [48], Diott [9]
Infrared	Reactivity	Renlund et al. [51], McGrane et al. [41], Wittenberg et al. [85]
X-ray absorption (XANES, XAS)	Temperature, structure	Yaakobi et al. [86], Dorchies et al. [11]
Neutron resonance	Temperature	Funk et al. [18], Yuan et al. [87]
Radiography		
X-ray	Density	Collins et al. [6]
Proton	Density, spall	Koenig et al. [34], Holtkamp et al. [30], Rigg et al. [52]
Scattering		
X-ray Thomson scattering	Free electron	Glenzer and Redmer [19], Visco et al. [81]
Small-angle X-ray scattering	Nucleation and growth of new phases	Graber et al. [20]
Ultrafast dynamic ellipsometry	Optical changes	Bolme et al. [3]
SOP (Streaked optical pyrometer)	Temperature	Miller et al. [45]

These studies on Earth and planetary materials, at extreme high pressures over the pressure of the Earth center, will reveal and help to understand the interiors of giant planets and super-Earths, of which inner pressures reach more than $\sim$500 GPa.

9 Concluding Remarks

Many Hugoniot data are available for various solids, including rocks, and we know many materials that experienced hypervelocity impacts, like meteorites and craters on the Earth and on the Moon. However, it is not easy to answer correctly what processes they passed through during impacts up to the present even if there are no weathering effects. Shock waves in solids are not fully understood as yet, although

shock wave science aims at versatile objects. Fast movement of atoms or dislocations in solid plays a critical role when a shock wave propagates in a solid.

Recent technical developments of experimental diagnostics and numerical simulation methods for shocked materials have helped in producing detailed understanding; further future developments will help to unraveling the physics of their movements. Another issue to add is the time-scale problem. High-strain rate phenomena are time-dependent and process-dependent. There are a lot of challenges to solve it. This issue and heterogeneous temperature increase by irreversible dynamic processes must be taken into account, when we compare the results between experimentally-shocked materials and the meteorite and crater materials that experienced impact shocks.

References

1. Asay, J.R.: Isentropic compression experiments on the Z accelerator. In: Furnish, M.D., Chahabildas, L.C., Hixon, R.S. (eds.) Shock Compression of Condensed Matter-1999, pp. 261–266. American Institute of Physics, New York (2000)
2. Baker, L., Hollenbach, R.: Laser interferometer for measuring high velocities of any reflecting surface. J. Appl. Phys. **43**, 4669–4674 (1972)
3. Bolme, C.A., et al.: Simple shot measurements of laser driven shock waves using ultrafast dynamic ellipsometry. J. Appl. Phys. **102**, 033513 (2007)
4. Cable, A.J.: Hypervelocity accelerators. In: Kinslow, R. (ed.) High-Velocity Impact Phenomena, pp. 1–21. Academic, New York (1970)
5. Celliers, P.M., et al.: Line-imageing velocimeter for shock diagnostic at the OMEGA laser facility. Rev. Sci. Instr. **75**, 4916–4929 (2004)
6. Collins, G.W., et al.: Measurements of the equation of state of deuterium at the fluid insulator-metal transition. Sci. **281**, 1178–1181 (1998)
7. Copparli, F. et al.: Experimental evidence for a phase transition in magnesium oxide at exoplanet pressures. Nat. Geosci. **6**, 926–929 (2013)
8. DeCarli, P.S.: Shock wave synthesis of high pressure phases; comments on the origin of meteoritic diamond. In: Burls, J. (ed.) Science and Technology of Industrial Diamonds, vol. 1. Industrial Diamond Information Bureau, London (1967)
9. Dlott, D.D.: Ultrafast spectroscopy of shock waves in molecular materials. Annu. Rev. Phys. Chem. **50**, 251–278 (1999)
10. Dlott, D.D.: New developmemts in the physical chemistry of shock compression. Ann. Rev. Phys. Chem. **62**, 575–597 (2011)
11. Dorchies, F., et al.: High-power 1 kHz laser-plasma x-ray source for ultrafast x-ray absorption near-edge spectroscopy in the keV range. Appl. Phys. Lett. **93**, 121113 (2008)
12. Drake, R.P.: High-energy-density physics. Phys. Today 28–33 (2010)
13. Duvall, G.E., Graham, R.A.: Phase transitions under shock-wave loading. Rev. Mod. Phys. **49**, 523–579 (1977)
14. Egdell, R.G., et al.: On the difference in valence electron plasmon energy and density of states between beta- and cubic-Si_3N_4. J. Appl. Phys. **94**, 6611–6615 (2003)
15. Eggert, J.H. et al.: Melting temperature of diamond at ultrahigh pressure. Nat. Phys. **6**, 40–43 (2010)
16. Erskine, D.J., Nellis, W.J.: Nature 317–349 (1991)
17. Furukawa, Y., et al.: Abiotic syntheses of amino acid, fatty acids and amines under oceanic impact conditions of the early Earth. Nature Geosci. **2**, 62–66 (2009)

18. Funk, D.J. et al.: Dynamic measurement of temperature using neutron response spectroscopy (MRS). In: Schmidt, S.C., Dandekar, D.P., Forbes, J.W. (eds.) Shock Waves in Condensed Matter-1997, pp. 887–890. American Institute of Physics, Woodbury (1998)
19. Glenzer, S.H., Redmer, R.: X-ray Thomson scattering in high energy density plasmas. Rev. Modern Phys. **81**, 1625–1663 (2009)
20. Graber, T., et al.: BioCARS: a synchrotron resource for time-resolved X-ray science. J. Synchrotron Rad. **18**, 658–670 (2011)
21. Grady, D.E.: Structured shock waves and the fourth-power law. J. Appl. Phys. **107**, 013506 (2010)
22. Graham, R.A., et al.: Pressure measurements in chemically reacting powder mixtures with the Bauer piezoelectric polymer gauge. Shock Waves **3**, 78–82 (1993)
23. Hayes, D.B. et al.: Continuous index of refraction measurements to 20 GPa in Z-cut sapphire. J. Appl. Phys. **94**, 2331 (2003)
24. He, H., et al.: Shock-induced phase transition of Si_3N_4 to c-Si_3N_4. Phys. Rev. B **62**, 114111417 (2000)
25. He, H., et al.: Accurate measurement of the velocity history of a laser-driven foil plate with a push-pull type VISAR. Appl. Opt. **40**, 6327–6333 (2001)
26. He, H., et al.: Time-resolved measurement on ablative acceleration of foil plates driven by pulsed laser beam. Rev. Sci. Instr. **72**, 2032–2035 (2001)
27. He, H., et al.: Phase transformation of germanium nitride (Ge_3N_4) under shock wave compression. J. Appl. Phys. **90**, 4403–4406 (2001)
28. He, H., et al.: Direct transformation of cubic diamond to hexagonal diamond. Appl. Phys. Lett. **81**, 610–612 (2002)
29. Hintzen, H.T., et al.: Thermal expansion of cubic Si_3N_4 with the spinel structure. J. Alloy Comp. **351**, 40–42 (2003)
30. Holtkamp, D.B. et al.: A survey of high explosive-induced damage and spall in selected metals using proton radiography. In: Furnish, M.D., Gupta, Y.M., Forbes, J.W. (eds.) Shock Compression in Condensed Matter-2003, pp. 477–482 (2004)
31. Jensen, B.J., et al.: Accuracy limits and window corrections for photon Doppler velocimetry. J. Appl. Phys. **101**, 013523 (2007)
32. Johnson, Q., Mitchell, A.C.: First x-ray diffraction evidence for a phase transition during shock-wave compression. Phys. Rev. Lett. **29**, 1369–1371 (1972)
33. Kiefer, R., et al.: Strength, elasticity, and equation of state of the nanocrystalline cubic silicon nitride-Si_3N_4 to 68 GPa. Phys. Rev. B **72**, 014102 (2005)
34. Koenig, K., et al.: High pressures generated by laser driven shocks: applications to planetary physics. Necl. Fusion **44**, S208–S214 (2004)
35. Knudson, M.D., et al.: Shock-wave exploration of the high-pressure phases of carbon.Science **322**, 1822–1825 (2008)
36. Langenhorst, F. et al.: Chapter 1. Experimental techmiques for the simulation of shock metamorphism: a case study on calcite. In: Davison, L., Horir, Y., Sekine, T. (eds.) High-Pressure Shock Compression of Solids V Shock Chemistry with Applications to Meteorite Impacts. Springer, New York (2003)
37. Lee, K.K., et al.: Laser-driven shock experiments on precompressed water: Implications for "icy" giant planets. J. Chem. Phys. **125**, 014701 (2006)
38. Leitch, S., et al.: Properties of non-equivalent sites and bandgap of spinel-phase silicon nitride. J. Phys.: Cond. Mat. **16**, 6469–6476 (2004)
39. Lemke, R.W., et al.: Magnetically accelerated, ultrahigh velocity flyer plates for shock wave experiments. J. Appl. Phys. **98**, 073530 (2005)
40. Liu, A.Y., Cohen, M.L.: Prediction of new low compressibility solids. Science 245, 841-842 (1989)
41. McGrane, S.D., et al.: Shock induced reaction observed via ultrafast infrared absorption in poly(vinyl nitrate) films. J. Phys. Chem. A **108**, 9342–9347 (2004)

42. McQueen, R.G., Marsh, S.P., Taylor, J.W., Fritz, J.N., Carter, W.J.: The equation of state of solids from shock wave studies. In: Kinslow, R. (ed.) High-Velocity Impact Phenomena, pp. 293–417. Academic, New York (1970)
43. McWilliliams, R.S., et al.: Phase transformations and metallization of magnesium oxide at high pressure and temperature. Science **338**, 1330–1333 (2012)
44. Milathianaki, D., et al.: Femtosecond visualization of lattice dynamics in shock-compressed matter. Science **342**, 220–223 (2013)
45. Miller, J.E., et al.: Streaked optical pyrometer system for laser-driven shock-wave experiments on OMEGA. Rev. Sci. Instr. **78**, 034903 (2007)
46. Nakazawa, H., et al.: High yield shock synthesis of ammonia from iron, water and nitrogen available on the early Earth. Earth Planet. Sci. Lett. **235**, 356–360 (2005)
47. Nellis, J.W.: Dynamic compression of materials: metallization of fluid hydrogen at high pressures. Rep. Prog. Phys. **69**, 1479–1480 (2006)
48. Pangilinan, G.I., Gupta, Y.M.: Use of time-resolved Raman scattering to determine temperatures in shocked carbon tetrachloride. J. Appl. Phys. **81**, 6662–6669 (1997)
49. Paterson, M.S.: Nonhydrostatic thermodynamics and its geologic applications. Rev. Geophys. Space Phys. **11**, 355 (1973)
50. Remington, B.A., et al.: Experimental astrophysics with high power lasers and Z pinches. Rev. Modern Phys. **78**, 755–807 (2006)
51. Renlund, A.M. et al.: Time-resolved infrared spectral photography. In: Gupta, Y.M. (ed.) Shock Waves in Condensed Matter-1985, pp. 237–242. Plenum, New York (1986)
52. Rigg, P.A., et al.: Proton radiography and accurate density measurements: A window into shock wave processes. Phys. Rev. B **77**, 220101(R) (2008)
53. Rygg, J.R., et al.: Powder diffraction from solids in the terapascal regime. Rev. Sci. Instr. **83**, 113904 (2012)
54. Robin, P.F.: Thermodynamic equilibrium across a coherent interface in a stressed crystal. Am. Mineral. **59**, 1286–1298 (1974)
55. Roybal, R., et al.: Laboratory simulation of hypervelocity debris. Int. J. Impact Eng. **17**, 707–718 (1995)
56. Sato, T., et al.: Formation of cubic boron nitride from rhombohedral boron nitride by explosive shock compression. J. Am. Ceram. Soc. **65**, C162 (1982)
57. Schmidt, A.C. et al.: Raman spectroscopies in shocked-compressed materials. In: Asay, J.R., Graham, R.A., Straub, R.A. (eds.) Shock Compression in Condensed Matter-1983, pp. 293–302 (1984)
58. Sekine, T.: Shock synthesis of cubic silicon nitride. J. Am. Ceram. Soc. **85**, 113–116 (2002)
59. Sekine, T.: Shock wave chemical synthesis; synthesis of carbon nitrides. Mat. Sci. Forum **566**, 125–128 (2008)
60. Sekine, T., et al.: Shock-induced transformation of b-Si3N4 to a high-pressure cubic spinel structure. Appl. Phys. Lett. **76**, 3706–3708 (2000)
61. Sekine, T., Kobayashi, T.: Time-resolved measurements of high-pressure phase transition of fluorite under shock loading. Phys. Chem. Mineral. **38**, 305–310 (2011)
62. Sekine, T., et al.: High temperature metastability of cubic spinel Si_3N_4. Appl. Phys. Lett. **79**, 2719–2721 (2001)
63. Sekine, T., et al.: 29Si magic angle spinning nuclear magnetic resonance study of spinel-type Si_3N_4. Appl. Phys. Lett. **78**, 3050–3051 (2001)
64. Sekine, T., et al.: Cubic Si6-zAlzOzN8-z (z=1.8 and 2.8) spinels formed by shock compression. Chem. Phys. Lett. **344**, 395–399 (2001)
65. Sekine, T., et al.: New high-pressure phase of SiAlON. Key Eng. Mat. **237**, 153–160 (2003)
66. Sekine, T., et al.: Aluminum oxynitride at pressures up to 180 GPa. J. Appl. Phys. **94**, 4803–4806 (2003)
67. Sekine, T., et al.: Sinoite (Si_2N_2O) shocked at pressures of 28 to 64 GPa.Am. Mineral. **91**, 463–466 (2006)
68. Sekine, T., et al.: Hugoniot of beta-SiAlON and high-pressure phase transitions. J. Appl. Phys. **99**, 053501 (2006)

69. Sekine, T. et al.: Shock compression of magnesium silicon nitride. In: Elert, M., Furnish, M. D., Chau, R., Holmes, N., Nguyen, J., (eds.) Shock Compression of Condensed Matter-2007, pp. 189–192. American Institute of Physics (2007)
70. Smith, R.F., et al.: Stiff response of aluminum under ultrafast shockless compression to 110 GPa. Phys. Rev. Lett. **98**, 065701 (2007)
71. Soma, T., et al.: Characterization of wurtzite type boron nitride synthesized by shock compression. Mat. Res. Bull. **9**, 755–762 (1974)
72. Spaulding, D.K., et al.: Evidence for a phase transition in silicate melt at extreme pressure and temperature conditions. Phys. Rev. Lett. **108**, 065701 (2002)
73. Stand, O.T., et al.: Compact system for high-speed velocimetry using heterodyne techniques. Rev. Sci. Instr. **77**, 083108 (2006)
74. Suggit, M.J., et al.: Nanosecond white-light Laue diffraction measurements of dislocation microstructure in shock-compressed single-crystal copper. Nature Comm. **3**, 1224 (2012)
75. Tanaka, I., et al.: Hardness of cubic silicon nitride. J. Mat. Res. **17**, 731–733 (2002)
76. Tatsumi, Y., et al.: heoretical prediction of post-spinel phases of silicon nitride. J. Am. Ceram. Soc. **85**, 7–10 (2002)
77. Trueb, L.F.: Microstructural study of diamonds synthesized under conditions of high temperature and moderate explosive shock pressure. J. Appl. Phys. **42**, 503–510 (1971)
78. Trunin, R.F.: Shock Compression of Condensed Materials. Cambridge University Press, Cambridge (1998)
79. Turneaure, S.J., et al.: Real-time x-ray diffraction at the impact surface of shocked crystals. J. Appl. Phys. **111**, 026101 (2009)
80. Valenzuela, A.R., et al.: Photonic Doppler velocimetry of laser-ablated ultrathin metals. Rev. Sci. Instr. **78**, 013101 (2007)
81. Visco, A.J., et al.: Measurement of radiative shock properties by x-ray Thomson scattering. Phys. Rev. Lett. **108**, 145001 (2012)
82. Wark, J.S., et al.: Subnanosecond x-ray diffraction from laser-shocked crystals. Phys. Rev. B **40**, 5705–5714 (1989)
83. Weng, J., et al.: Optical-fiber interferometer for velocity measurements with picosecond resolution. Appl. Phys. Lett. **89**, 111101 (2006)
84. Whitley, V.H., et al.: The elastic-plastic response of aluminum films to ultrafast laser-generated shocks. J. Appl. Phys. **109**, 013505 (2011)
85. Wittenberg, J.S., et al.: Wurtzite to rock salt phase transformation of cadmium selenide nanocrystals via laser-induced shock waves: Transition from single to multiple nucleation. Phys. Rev. Lett. **103**, 125701 (2009)
86. Yaakobi, B., et al.: EXAFS Measurement of Iron bcc-to-hcp phase transformation in nanosecond-laser shocks. Phys. Rev. Lett. **95**, 075501 (2005)
87. Yuan, V.W., et al.: Shock temperature measurement using neutron resonance spectroscopy. Phys. Rev. Lett. **94**, 125504 (2005)
88. Zerr, A. et al.: Recent advances in new hard high-pressure nitrides. Adv. Mat. **18**, 2933–2948 (2006)
89. Zhang, Y., et al.: Energetics of cubic Si_3N_4. J. Mat. Res. **21**, 41–44 (2006)

Author Biography

Toshimori Sekine is internationally known for his studies on shock wave interactions in condensed matters, and currently at Department of Earth and Planetary Systems Science, Hiroshima University and formerly at National Institute for Materials Science. He received his Doctor of Science degree in Geochemistry from Tokyo Institute of Technology. His research covers a wide range of subjects on shock synthesis, including Earth and Planetary materials and life-related molecules, and Hugoniot and shock temperature measurements using conventional shock guns and laser shocks to pressures of 1 TPa. He has more than 200 publications. He contributed as co-author to High-Pressure Shock Compression of Solids V Shock Chemistry with Applications to Meteorite Impacts from Springer. He is a fellow of the American Physical Society.

Part IV
Ram Accelerator

The Ram Accelerator: Review of Experimental Research Activities in the U.S.

Adam P. Bruckner and Carl Knowlen

Abstract The ram accelerator, conceived at the University of Washington in 1983, is a scalable hypervelocity launcher, capable, in principle, of accelerating projectiles to velocities greater than 8 km/s. The device operates as an in-bore ramjet in which a subcaliber projectile, shaped like the centerbody of a cylindrical supersonic ramjet, is propelled through a stationary tube filled with a pressurized gaseous propellant mixture of fuel, oxidizer, and diluent. This propellant burns near the base of the moving projectile, generating thrust. The chemical energy density and speed of sound of the propellant can be adjusted, via gas pressure and composition, to control the in-tube Mach number and acceleration history of the projectile. Successful ram accelerator operation has been obtained at gas fill pressures up to 200 bar and projectile velocities up to 2.7 km/s. Scaling has been demonstrated in bore sizes ranging from 25 to 120 mm in research facilities around the world. Potential applications of the ram accelerator include hypervelocity impact studies, hypersonic propulsion research, kinetic energy weapons, and direct launch of acceleration-insensitive payloads to low Earth orbit. This paper presents an overview of the technology of the ram accelerator and its history and state-of-the-art in the United States.

1 Introduction

The ram accelerator is a hypervelocity projectile launcher that uses chemical energy to accelerate projectiles to hypersonic speeds [39].[1] Although the ram accelerator launch tube resembles a conventional long-barreled gun, its principle of operation is

[1]The ram accelerator was conceived at the University of Washington (UW) in 1983 by these authors, based on ideas originally proposed by Hertzberg. Unknown to the UW group at the time, a concept similar to the ram accelerator had been proposed earlier [100] but was never reduced to practice by its proponents.

A.P. Bruckner (✉) · C. Knowlen
William E. Boeing Department of Aeronautics and Astronautics, University of Washington, Box 352250, Seattle, WA 98195-2250, USA
e-mail: bruckner@aa.washington.edu

F. Seiler and O. Igra (eds.), *Hypervelocity Launchers*,
Shock Wave Science and Technology Reference Library 10,
DOI 10.1007/978-3-319-26018-1_4

very different, being closely related to that of supersonic airbreathing ramjet engines. A stationary tube, analogous to the cylindrical outer cowling of a ramjet engine (Fig. 1), is filled with a combustible gaseous mixture, e.g., methane, oxygen, and a diluent such as nitrogen, at pressures of 5–200 bar. Thin diaphragms close off each end of the tube to contain the propellant. No propellant is carried aboard the projectile, which is similar in shape to the centerbody of a ramjet. The projectile has a diameter smaller than the launch tube bore, and is normally fitted with guide fins that provide for centering in the tube. The projectile travels at supersonic speed relative to the propellant gas, which it compresses in the flow area contraction between the nosecone and tube wall. The propellant flow remains supersonic with respect to the projectile as the gas passes through the throat, i.e., point of minimum flow area between the projectile and the surrounding tube wall. Below approximately Mach 4, combustion typically occurs at full tube area behind the projectile and thermally chokes the flow, thereby establishing a normal shock system on the aftbody of the projectile that renders the flow subsonic downstream. This shock system recedes as the projectile Mach number increases. The process of thermal choking replaces the nozzle of a conventional ramjet engine, resulting in a stable combustion process that travels with the projectile in a propulsion cycle referred to as the thermally choked ram accelerator mode.

The operational sequence of the ram accelerator (Fig. 2) is initiated by injecting the projectile into the ram accelerator tube at speeds greater than $\sim$700 m/s by means of a conventional powder gun or light gas gun. A lightweight obturator, or piston, in contact with the base of the projectile seals the gun bore during this initial

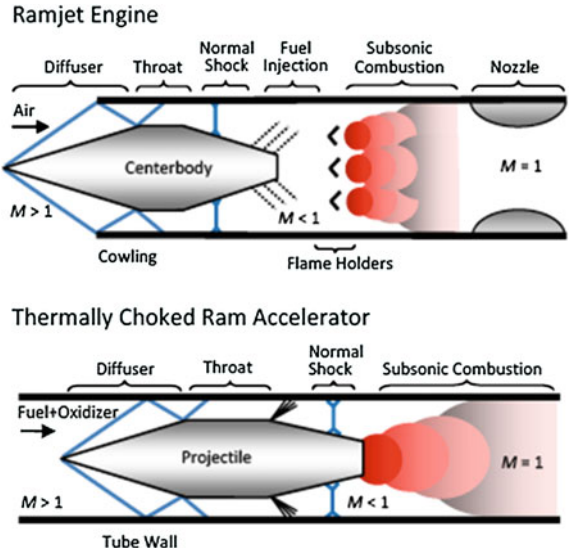

Fig. 1 Comparison of conventional ramjet engine to ram accelerator

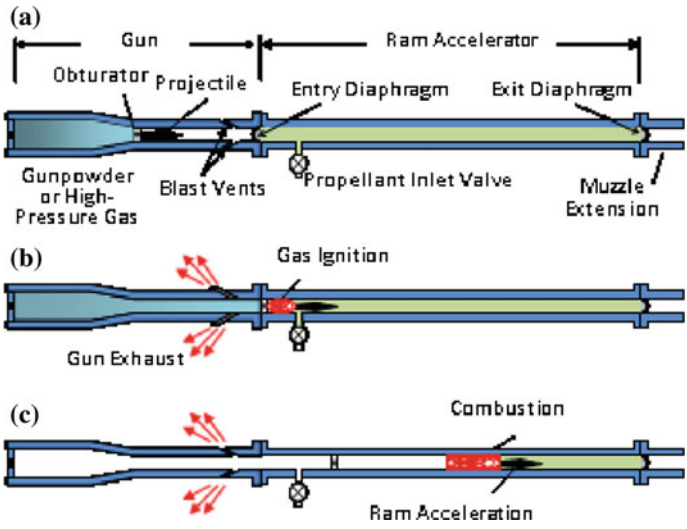

Fig. 2 Operational sequence of ram accelerator. **a** Gun is loaded with projectile and obturator, and a charge of gunpowder or high pressure gas. Ram accelerator is pressurized with propellant to 5–200 bar. **b** Gun fires obturator/projectile combination into ram accelerator. **c** Combustion is initiated and moves with projectile, sustaining high base pressure that accelerates projectile to high velocity

impulse. The acceleration from rest of the projectile/obturator combination compresses residual air in the gun's launch tube via a series of reflected shock waves [26, 105, 104]. When the projectile punctures the entrance diaphragm, the slug of shock-heated air ignites the propellant near the base of the projectile. A stable combustion zone is thus formed which travels with the projectile, maintaining a wave of high base pressure that propels the projectile forward, in a manner analogous to an ocean wave pushing a surfboard (Fig. 3). The obturator rapidly decelerates following ignition and does not participate in the subsequent acceleration process. To keep the projectile centered in the tube, the projectile is fabricated with fins that span the bore of the tube or the tube is equipped with several internal guide rails that bear on an axisymmetric projectile.

What distinguishes the ram accelerator from a gun is that its source of energy (the combustible gas mixture) is uniformly distributed throughout the entire length of the accelerator tube, whereas in a gun the energy source is concentrated at the breech as either a charge of gunpowder or high pressure gas. During the ram acceleration process the highest pressure in the tube is always at the projectile's base (see Fig. 3), rather than at the breech as in a gun, and the bulk of the combustion products moves in a rearward direction. Only a small volume of high pressure gas exits the tube with the projectile. These characteristics of the ram accelerator result in much more uniform acceleration of the projectile, very high velocity capability, and very little muzzle blast and recoil. Furthermore, the

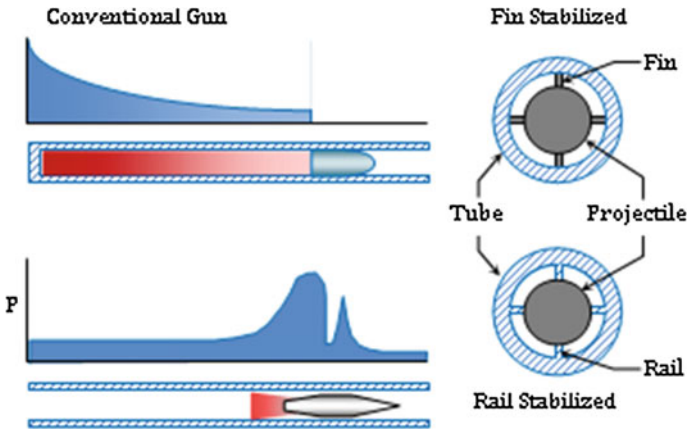

Fig. 3 Pressure distribution in conventional gun and ram accelerator. Projectiles are stabilized with either fins or rails

acceleration and muzzle velocity of the ram accelerator can be easily tailored to specific needs by adjusting the propellant composition and fill pressure.

Potential applications of the ram accelerator include hypersonic aerodynamic testing [17, 84, 108], scramjet simulation [15], and direct launch to orbit [7, 12, 48, 80, 109, 52, 56], and hypervelocity kinetic energy weapons [66].

The propulsive cycle illustrated in Fig. 1 is the thermally choked ram accelerator mode, which operates with in-tube projectile Mach numbers typically ranging from 2.5 to 4 and at velocities below the Chapman-Jouguet (CJ) detonation speed of the propellant, i.e., at subdetonative velocities [16, 39, 40]. In this mode the thrust is provided by the high projectile base pressure resulting from the normal shock system that is stabilized on the body by thermal choking of the flow at full tube area behind the projectile. The ram accelerator can be modeled analytically using a simple one-dimensional control volume approach [16, 39, 50]. The gasdynamic conservation equations and the ideal gas law are applied to a control volume that contains the projectile (Fig. 4).

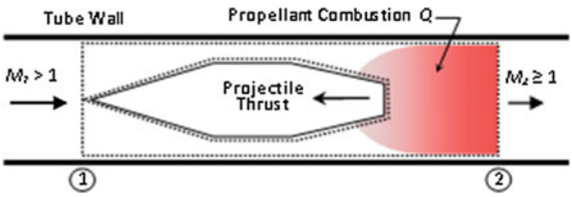

Fig. 4 Control volume for one-dimensional, quasi-steady analysis of ram accelerator

Assuming quasi-steady flow, the following expression for the non-dimensional thrust on the projectile can be derived:

$$\frac{F}{AP_1} = \frac{\gamma_1 M_1}{\gamma_2 M_2}\left(1+\gamma_2 M_2^2\right)\left[\left(\frac{\gamma_2-1}{\gamma_1-1}\right)\cdot\frac{1+\frac{\gamma_1-1}{2}M_1^2+Q}{1+\frac{\gamma_2-1}{2}M_2^2}\right]^{1/2} - \left(1+\gamma_1 M_1^2\right) \quad (1)$$

where F is the thrust, P_1 is the propellant fill pressure, A is the cross-sectional area of the tube bore, M_1 is the Mach number of the flow entering the control volume (i.e., the projectile Mach number with respect to the undisturbed propellant), M_2 is the Mach number of the flow exiting the control volume, $Q = \Delta q/c_{p1}T_1$, is the non-dimensional heat release parameter, Δq is the heat of combustion, c_{p1} and T_1 are the specific heat at constant pressure and the temperature of the undisturbed propellant, respectively, and γ_1 and γ_2 are the pre- and post-combustion specific heat ratios. This thrust coefficient equation applies to all ram accelerator propulsive modes operating in a quasi-steady manner, even though no details of the internal flow are considered in its derivation. The quasi-steady assumption is applicable for projectile accelerations up to about 15,000 g [16], and the ideal gas equation of state can be used up to about 25 bar fill pressure. Operation at higher pressures and/or accelerations requires the use of a real gas equation of state and an unsteady analysis, as summarized in a later section of this paper.

If one knows how M_2 varies with M_1 in a given propellant, then the projectile thrust can be readily computed for any flight velocity. Thermal choking of the flow behind the projectile ($M_2 = 1$) corresponds to an entropy extremum [50]; thus, the details of the process which brings the flow to choking do not affect the end state conditions of the thermally choked ram accelerator mode and do not have to be known to predict the thrust. For propulsive cycles that do not involve thermal choking, such as the transdetonative and superdetonative modes discussed later in this paper, the details of the flow field around the projectile must be considered to accurately predict the exit Mach number, M_2 [50, 53].

Figure 5 shows a plot of the non-dimensional thrust in the thermally choked mode, as a function of projectile Mach number for several typical values of the heat release parameter, Q. It can be seen that thrust increases with increasing heat release. The model also predicts that the thrust goes through a maximum and decreases with increasing Mach number, reaching zero when the projectile velocity is equal to the CJ detonation speed, V_{cj}, of the propellant [16, 39]. In order to achieve velocities higher than the V_{cj} of a particular propellant, the ram accelerator tube can be subdivided into several sections, called stages, each separated from its neighbor by a thin diaphragm and filled with a different propellant, as shown in Fig. 6 [16]. By selecting the sequence of propellants in such a manner that the speed of sound and detonation speed increase toward the exit of the ram accelerator, the projectile Mach number can be kept within limits that maximize thrust and efficiency, resulting in high average acceleration and a higher final velocity than is achievable with a single propellant stage.

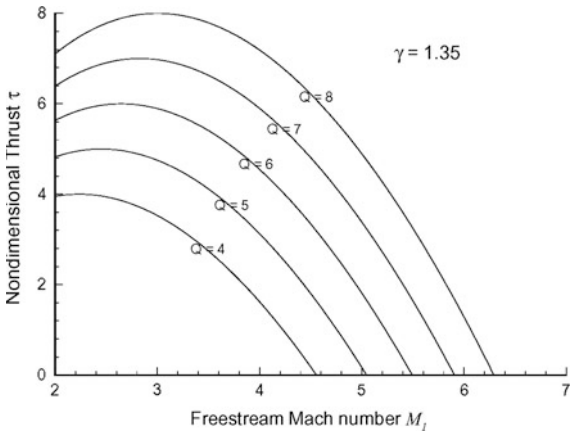

Fig. 5 Non-dimensional thrust as a function of projectile Mach number and non-dimensional heat release parameter, $Q = \Delta q/c_p/T_1$

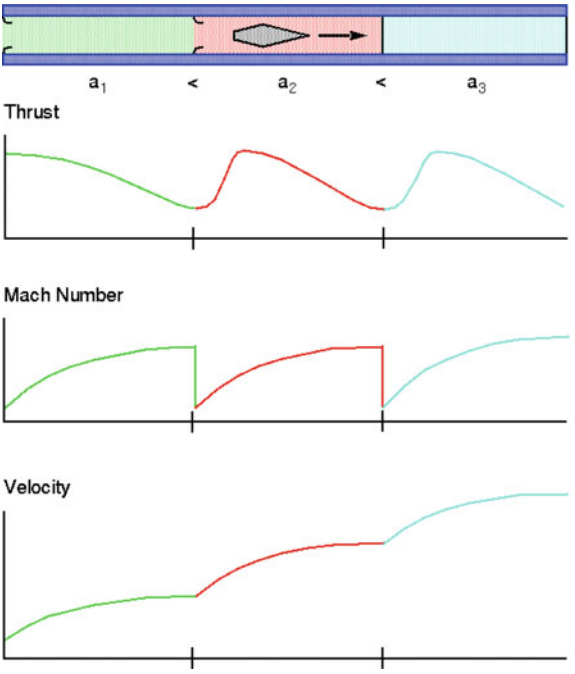

Fig. 6 Staging of ram accelerator. Pressure can be different in each stage. $a_3 > a_2 > a_1$, where a_n is the speed of sound in stage n

It has been observed that acceleration is also possible when the projectile is traveling above the CJ detonation speed of the propellant—this is called the superdetonative velocity regime [70]. The transition from subdetonative to superdetonative operation occurs smoothly, through the transdetonative velocity regime (Fig. 7) [27]. As the projectile approaches V_{cj} of the propellant in the thermally choked propulsive mode, the combustion begins to move forward relative to the projectile, so that some of it takes place in the space between the projectile

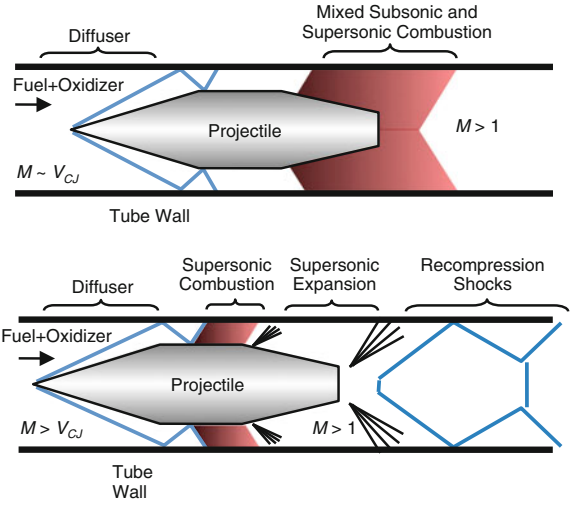

Fig. 7 Transdetonative (*upper*) and superdetonative (*lower*) propulsion modes

and the tube wall [40, 53]. As the projectile continues to accelerate to velocities above about $1.1V_{cj}$, i.e., into the superdetonative regime, the combustion appears to move almost entirely forward of the projectile's base. It is postulated that during this transition from subdetonative to superdetonative operation the combustion changes from purely subsonic to purely supersonic, and may even stabilize into an oblique detonation wave [40]. During operation in the transdetonative velocity regime, between approximately $0.9V_{cj}$ and $1.1V_{cj}$, it is believed that regions of both subsonic and supersonic combustion coexist [27].

2 Experimental Facilities and Results

The first experimental ram accelerator facility, having a 38-mm tube bore, was completed at the University of Washington (UW) in September 1985, and proof of concept was achieved in June 1986 [38]. Interest in this technology spawned facilities at several other laboratories in the U.S.A. and abroad [11]. They included a 120-mm-bore ram accelerator (the world's largest) at the U.S. Army Research Laboratory (ARL) at Aberdeen Proving Ground, MD; 90 and 30-mm bore smooth-bore systems, and a 30-mm-caliber railed-tube system, all at the French-German Research Institute (ISL, France); a 25-mm-bore installation at Tohoku University, Japan [94]; and a 15 × 20 mm rectangular-bore facility at Hiroshima University, Japan. In addition, a 37-mm-bore ram accelerator was built and successfully tested at the China Aerodynamics Research and Development Center (CARDC) in Mianyang, China [79]. Projectile masses from 5 g to 5 kg have been launched to velocities up to 2.4 km/s in these facilities. Ram accelerator research at all facilities focused on improving the understanding of the physical

principles of ram acceleration, achieving higher velocities, developing robust projectile designs, and studying various near- and long-term applications. Pertinent compendia of results from these research facilities can be found in Takayama and Sasoh [106], and Bauer [2]. Here we focus on the facilities in the U.S.

2.1 University of Washington (UW)

The University of Washington ram accelerator facility has a 16-m-long test section and a 38-mm-bore light gas gun for a pre-launcher (Figs. 8 and 9). The first 4 m of the test section are comprised of thick-walled tubes (203 mm O.D.) for high pressure experimentation, i.e., fill pressures up to 200 bar. The launch tubes of the last 12-m of the test section are limited to a fill pressure of 75 bar. The test section has electromagnetic sensors to track the time-distance history of the projectile to determine its velocity and thrust, and to locate its position relative to the tube-wall Pressure-field measurements made by piezoelectric pressure transducers. Projectiles having three, four, and five fins have been found to have very similar operating characteristics in this facility. The projectile shown in Fig. 10 is a five-fin configuration with a 10° nose cone, 29-mm-diameter throat (point of maximum projectile cross-section), and overall length of 153 mm. Projectiles fabricated from alloys of magnesium, aluminum, and titanium having a mass range of 50–140 g have been used extensively in this experimental program. Ram accelerator operation has been demonstrated at velocities ranging from 0.7 to 2.7 km s^{-1} and in-tube Mach numbers of 2.5–8.5. Sustained accelerations averaging 54,000 *g* with 110-g projectiles have been demonstrated with the thermally choked propulsive mode using propellant fill pressures up to 200 bar. While the velocities attained to date can be matched by research-grade powder guns and exceeded by light gas guns, those devices, unlike the ram accelerator, are extremely difficult to scale up to bore diameters greater than 100 mm without degrading their performance.

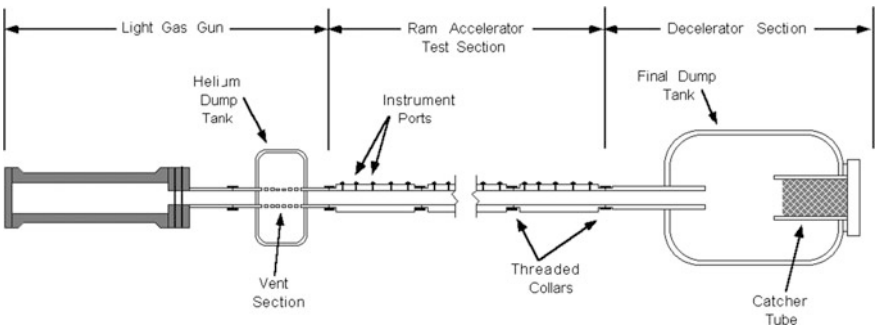

Fig. 8 Schematic of University of Washington 38-mm-bore ram accelerator. Test section is 16 m long. High-pressure section installed in 1997 (see Fig. 17 for details)

Fig. 9 View of UW 38-mm ram accelerator facility, ca. 1990. In foreground, from *left* to *right*, A.P. Bruckner, C. Knowlen, and the late A. Hertzberg

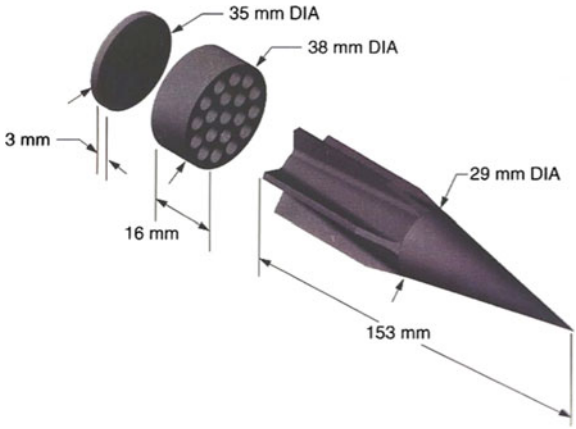

Fig. 10 Five-finned ram accelerator projectile with obturator. Fin span = 38 mm; nose half-angle = 10°

During the nearly three decades since the first experimental proof-of-concept was demonstrated at the UW [38], much has been learned about the phenomena that govern the ram accelerator, and many strides have been made. Here only some of the salient results are summarized; the interested reader is directed to the references for further details.

Figure 11 shows the pressure distribution on the projectile travelling at 1240 m/s (M = 3.4, subdetonative) past the location of the pressure transducer in a propellant mixture comprised of $2.8CH_4 + 2O_2 + 5.7N_2$, at a fill pressure of 25 bar. The time-scaled profile of the projectile is drawn in the figure to illustrate the location of

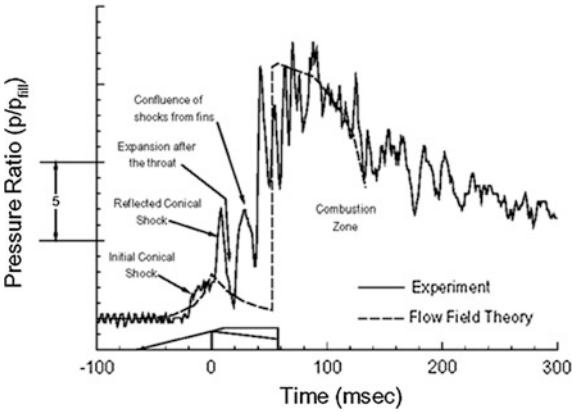

Fig. 11 Pressure profile on projectile in thermally choked, subdetonative mode

the pressure features with respect to the projectile geometry. The pressure profile of a quasi-one-dimensional flowfield model that accounts for shock losses, viscous pressure drop and finite rate heat addition is shown by the dashed line [49]. It is apparent that the predicted pressure amplitudes in the throat region and the normal shock location do not agree very well with the experiment, however, the predicted net thrust agrees quite well with the experiment, which strongly supports the assumption that the flow is thermally choked behind the projectile. In the subdetonative velocity regime, the observed pressure distribution is characteristic of the thermally choked propulsive mode and moves with the projectile as it accelerates through the tube. The evolution of this pressure distribution as the projectile approaches the propellant CJ speed is described in detail in [1, 59], and more recently in [6].

Staging a ram accelerator to attain high velocity when operating in the thermally choked propulsive mode has been demonstrated with many different propellant combinations. Shown in Fig. 12 are the velocity-distance data from a four-stage experiment carried out with an 80-g aluminum-alloy projectile that was accelerated from 1.1 to 2.6 km/s. In all four stages, the projectile velocity was less than $0.8V_{cj}$ to maintain high effective thrust. The theoretical predictions agree very well with experiment, again supporting the presumption that the combustion process is thermally choked. The velocity-distance data from a single-stage experiment with a 77-g projectile are also shown in Fig. 12. As the projectile approached the propellant CJ speed, its acceleration increased beyond that predicted for the thermally choked propulsive mode, indicating that the flow had ceased to be thermally choked at full tube area. The projectile accelerated up to $\sim$2.0 km/s, which is approximately $1.2V_{cj}$, and then coasted at nearly constant velocity for the last meter of the test section.

The experimentally observed variation in the thrust as a function of the velocity ratio V/V_{cj}, as the propulsive mode makes the transition from subdetonative to superdetonative is shown in Fig. 13 for three different propellants (including data

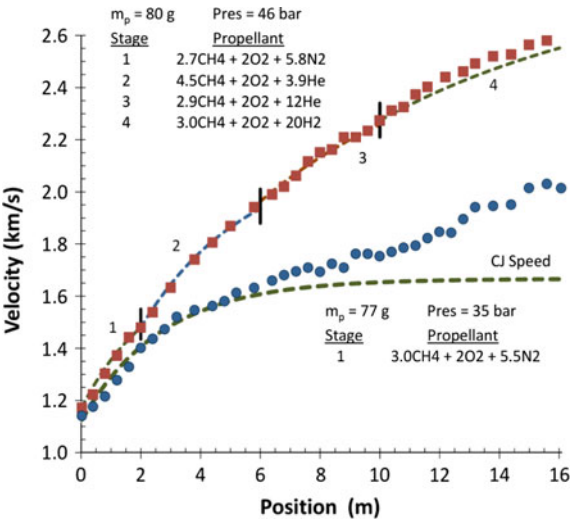

Fig. 12 Velocity-distance profile in four-stage ram accelerator [54]

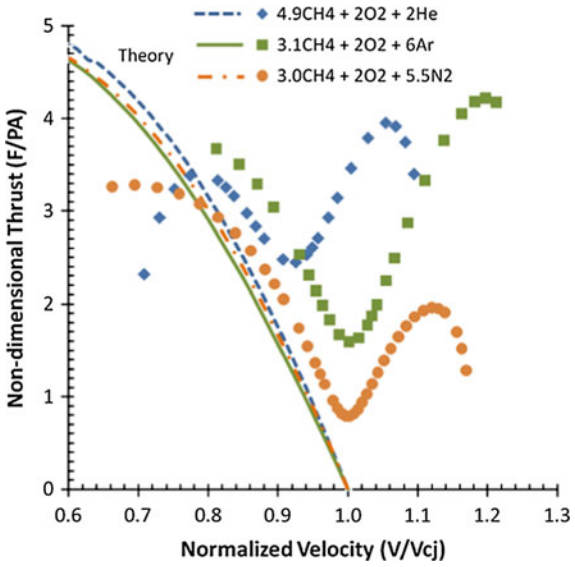

Fig. 13 Dependence of thrust on velocity ratio for various propellants [40]

from the single-stage experiment in Fig. 12). The thrust reaches a minimum in the transdetonative velocity regime and then increases in the superdetonative regime, reaching a relative maximum before decreasing in the manner predicted for supersonic combustion ram accelerator operation.

To date, maximum superdetonative velocities of $\sim 1.5V_{cj}$ have been observed at the UW [40, 70] and 1.57 V_{cj} elsewhere [99]. It has been suggested that a maximum limit of approximately $2V_{cj}$ may exist due to energy balance considerations,

i.e., the thrust equals drag limit [93], but this putative limit has yet to be confirmed experimentally, and its underlying analysis may be flawed [41]. In other work the maximum velocity of the ram accelerator has also been predicted to be about $2V_{cj}$. For example, in the superdetonative regime maximum velocities in the range of 7–9 km/s for operation in hydrogen-based propellants with CJ speeds of 3–4 km/s have been predicted [111, 112]. Although aerodynamic heating of the projectile at the associated high Mach numbers is expected to be severe, its effects can be minimized through the judicious choice of refractory projectile materials and by other means [7–9]. Another velocity limiting mechanism that has been explored is that of the so-called "doomed propellant fraction," which refers to the possibility that at sufficiently high Mach numbers the bow shock standing off the finite radius of the projectile's nose tip may pre-ignite a sufficient fraction of the propellant to cause thermal choking of the flow at or ahead of the projectile throat [34]. This limit has not yet been observed experimentally and, in any case, was predicted to occur at velocities above the thrust equals drag limit.

Experiments performed with a variety of propellants have demonstrated the existence of operational limits that are governed by the heat release of combustion, the projectile in-tube Mach number, and the projectile material. Figure 14 shows the operational envelope in terms of the propellant heat release and the projectile Mach number [43, 44]. If the heat release is too small, the driving pressure wave is unable to remain coupled to the projectile and falls behind, resulting in a cessation of thrust, while if the heat release is too high, the driving pressure wave surges ahead of the projectile, causing a sudden deceleration—this is called an "unstart". Hence, selection of the appropriate propellant composition is crucial to successful operation. The ultimate velocity limits, on the other hand, are believed to be related to projectile structural integrity and to the thrust equals drag limit. As the velocity

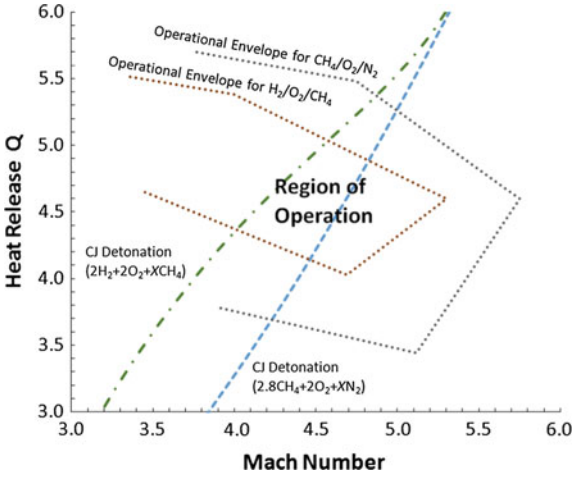

Fig. 14 Operational envelope of ram accelerator

increases, the pressure and aerodynamic heating increase markedly and are capable of causing structural failure of the projectile. Computations of heat transfer to the nose cone, and to the leading edges and lateral surfaces of the centering fins, performed at the UW [29, 30] and also at ISL [82, 83, 98], have shown that magnesium and aluminum alloys reach their melting points rapidly at these locations, resulting in potentially severe erosion by ablation, and loss of structural strength. Projectiles made of titanium alloy do not suffer these deleterious effects and have been found to attain higher velocities [55].

High spatial resolution pressure measurements of the flow around the projectile have revealed a complex three-dimensional flow structure associated with the centering fins [46]. These observations have been corroborated by high-speed in-bore photography of projectiles through transparent polycarbonate tube sections, as shown in Fig. 15 [58]. Canting of the projectile in the tube has also been frequently detected [47], and is likely due to lateral forces and pitching moments generated by non-uniform pressure distributions around the nose and body of the projectile, coupled with erosion or bending of the projectile's centering fins. This problem is mitigated through the use of titanium alloy as the projectile material, which is significantly stronger and more heat-resistant than the magnesium and aluminum alloys commonly used in the past [55].

Studies of the starting dynamics of the ram accelerator were first carried out at the UW [14, 26], and further work on this topic ensued later at other facilities [3, 5, 28, 35, 69, 93, 95–97, 104, 105]. These studies and research on low velocity starting dynamics in propellants with low acoustic speeds carried out at the UW [57, 69, 96], has shown that the starting process is very complicated and highly dependent on initial conditions, such as propellant composition, fill pressure, projectile and obturator mass, entrance diaphragm thickness, projectile velocity, and residual pressure in the launch tube of the pre-accelerator gun.

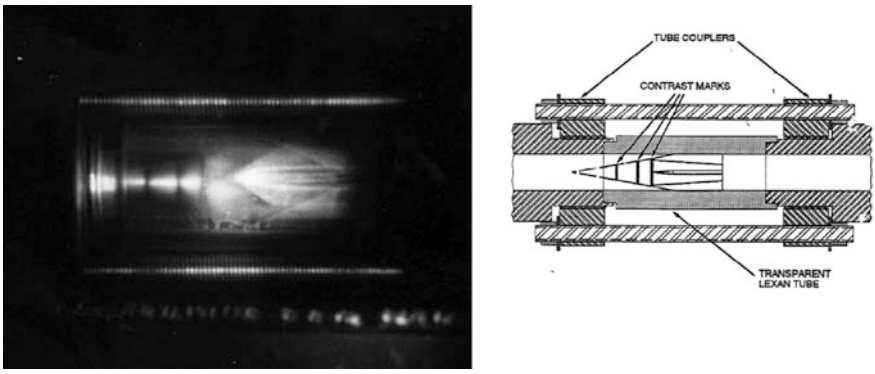

Fig. 15 In-tube photograph of ram accelerator projectile. Propellant: $2.5CH_4 + 2O_2 + 5.6N_2$, fill pressure = 6 bar, V = 1600 m/s (M = 4.4)

2.1.1 Operation at High Fill Pressures

Beginning in 1996, the attentions of the UW group turned toward operations at high propellant fill pressures, up to 200 bar [18–25, 51]. The motivation for this work was the desire to achieve higher velocities with shorter tube lengths, and to study real gas behavior and the effects of high accelerations, under which the quasi-steady ideal gas model is no longer applicable. Due to the extremely high pressures of the ram accelerator combustion process that arise when the fill pressure is greater than 25 bar, real gas effects play a significant role by shifting the chemical equilibria and increasing the exhaust pressure. Even though all the thermodynamic parameters are affected by real gas behavior, the dominant effect is the corresponding increase in heat release, Q. Thus, the influence of real gas behavior on the thrust of ram accelerator propulsive modes can be evaluated to the first order by including a corrected value for heat release into the thrust equation already presented (Eq. 1). Figure 16 shows computed results for the variation of thrust coefficient with Mach number in a particular propellant mix at fill pressures of 5 and 20 MPa, assuming quasi-steady flow and the Boltzmann equation of state.

Furthermore, operation at very high propellant-to-projectile density ratios (i.e., at high fill pressure or with a low-mass projectiles) leads to very high accelerations, which also affect the thrust performance. To investigate the effects of projectile acceleration, a_p, on net thrust, a one-dimensional unsteady flow model was developed which accounts for the accumulation of mass and momentum within the finite length of the control volume [25]. The unsteady thrust equation for the thermally choked ram accelerator propulsive mode can be expressed as:

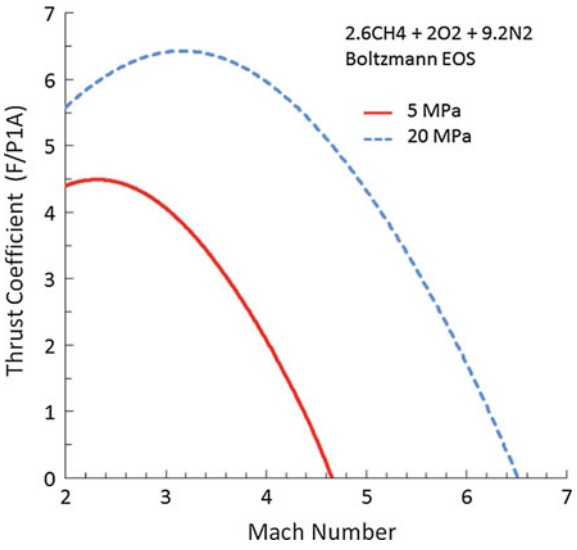

Fig. 16 Predicted thrust coefficient variation with Mach number at various fill pressures for quasi-steady flow using a real gas equation of state

$$
\begin{aligned}
&AP_1M_1\frac{\sqrt{\gamma RT_1}}{\gamma-1}\left(1+\frac{\gamma-1}{2}M_1^2+Q\right)\\
&\quad=\frac{\frac{7}{2}AP_1M_1a_pL_{CV}}{\sqrt{\gamma RT_1}}\\
&\qquad+\frac{\gamma\left(m_pa_p+AP_1\left(1+\gamma M_1^2\right)-AP_1M_1a_pL_{CV}/RT_1\right)^2}{2(\gamma^2-1)\left(AP_1M_1\sqrt{\gamma/RT_1}-AP_1a_pL_{CV}\Big/M_1\sqrt{\gamma R^3T_1^3}\right)}
\end{aligned}
\tag{2}
$$

where m_p is the mass of the projectile, L_{CV} is the control volume length, and T_1 and R are the propellant static temperature and gas constant entering the control volume, respectively. The other variables are as defined for Eq. 1. For brevity, the steps required to derive this equation are not included here; see the above-cited reference for details and Bauer et al. [4] for refinements that include real gas effects on all thermodynamic parameters and variations in the control volume length with Mach number. Equation [3] is an implicit expression for determining the dependent variable a_p as a function of projectile Mach number M_1 and real gas heat release value for Q. Based on experiments, it has been found that an appropriate approximate control volume length for illustrating unsteady effects is about twice that of the projectile length, even though it tends to decrease in length as the Mach number increases due to increases in kinetic rates [4].

For the high-pressure experimental studies a 4-m-long section of the ram accelerator was replaced with three thick-walled tubes capable of withstanding a static pressure load of 10,000 bar. Figure 17 shows a schematic of this test section. At the same time a semi-automatic gas fill system was installed that enabled delivery of mixed propellant to fill pressures up to 200 bar. Titanium alloy projectiles at entrance velocities as low as 1200 m/s were successfully started in CH_4/O_2/N_2 propellants at fill pressures of 150 and 200 bar, the latter being the highest operating pressure achieved to date in any ram accelerator. At 200 bar a velocity of 2400 m/s was achieved within the 4-m length of the high pressure section. Due to real gas effects on the acoustic speed of the propellant, the throat-to-bore diameter ratio of the projectiles had to be reduced from the nominal value of 0.76–0.60 in order to enable operation at pressures greater than 150 bar [19, 24].

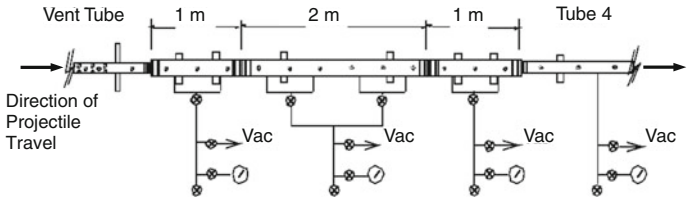

Fig. 17 Schematic of high pressure section of UW 38-mm-bore ram accelerator

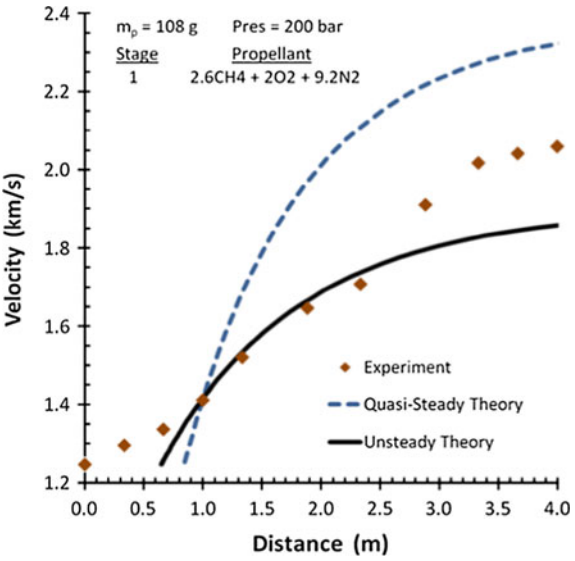

Fig. 18 Comparison of quasi-steady and unsteady control volume models with experimental data at 200 bar fill pressure, using Boltzmann equation of state [13]

The average acceleration achieved in these high-pressure experiments was much lower than that predicted by the real-gas calculations of the one-dimensional quasi-steady control volume model; an example at 200 bar is shown in Fig. 18. This discrepancy is due to the high accelerations that projectiles undergo at high pressures, which makes the quasi-steady assumption inappropriate for these conditions. The velocity-distance prediction from the unsteady one-dimensional performance model that accounts for the influence of projectile acceleration on the thrust behavior of the ram accelerator [19, 24] is also shown in Fig. 18. The agreement between this latter theory and experiment is very good over a significant velocity range. The experimentally observed velocity begins to diverge upward beyond 1.7 km/s due to the onset of the transdetonative propulsive mode [19, 24].

Figure 19 shows how non-dimensional thrust F/p_1A is predicted to behave at different pressures for a constant mass projectile, i.e., at different acceleration levels. The curve corresponding to the quasi-steady solution applies strictly for the case of zero acceleration, but is reasonably accurate up to about 15,000 g [16]. As the acceleration increases beyond this value the non-dimensional thrust begins to decrease. It should be noted that the acceleration parameters indicated in Fig. 19 apply only at the Mach number corresponding to peak thrust; at higher or lower Mach numbers the thrust is lower and hence the unsteady effects of projectile acceleration are also decreased. Thus, regardless of the level of peak acceleration, the unsteady model predicts that the thrust of the thermally choked propulsive mode goes to zero at the propellant's CJ speed. In addition, it is evident that as the fill pressure of the ram accelerator is increased, the thrust increases when the fill pressure is increased but it does not follow the latter proportionally as predicted by the ideal-gas quasi-steady model.

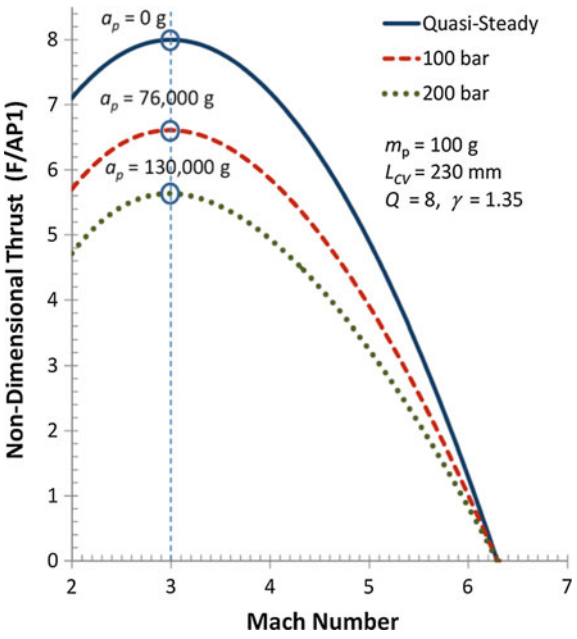

Fig. 19 Projectile acceleration effects on thermally choked ram accelerator operation at high pressures, compared to ideal quasi-steady case

2.1.2 Baffled-Tube Ram Accelerator

An alternative approach to increasing acceleration by the use of high fill pressure is to develop a means to achieve ram accelerator operation in very energetic propellants. It has been empirically determined that the heat release of $CH_4/O_2/N_2$ propellant mixtures must be reduced to $\sim$1/3 of the maximum available without diluent to effect stable ram accelerator operation, which limits the peak thrust to a value lower than the theoretical maximum. Using a propellant with a greater heat release results in the undesirable situation in which the driving combustion wave surges past the projectile, causing a diffuser "unstart" [43, 44]. In addition, the unstart phenomenon also limits the lowest Mach number at which the ram accelerator process can be initiated (e.g., Mach 2.5 for the nominal ratio of projectile throat diameter to tube bore diameter of 0.76), which puts a much bigger onus on the muzzle velocity capability of the pre-launcher for applications that require massive projectiles. Thus, the challenge for generating high ram accelerator thrust at low fill pressure is to devise a means to allow reactive propellant to be ingested by the projectile throat while keeping the combustion-driven compression waves from propagating forward through the throat, i.e., some form of "one-way valve" is needed.

A novel concept of using baffles on the wall of the tube, shown in Fig. 20, was proposed by Higgins [42] to enable ram accelerator operation in the most energetic of propellants. Baffles, or annular rings, attached to and/or machined into the tube wall act to isolate the combustion process behind the projectile from the intake of

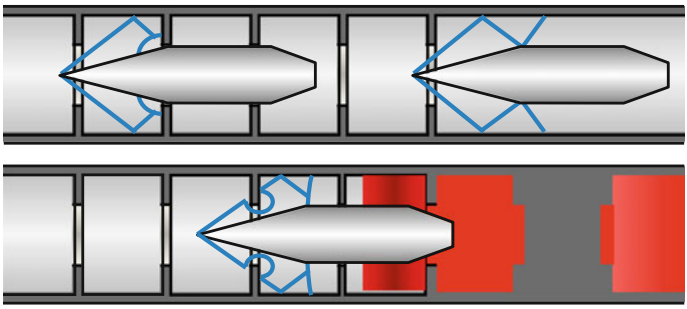

Fig. 20 Baffled tube ram accelerator flow field schematic. Baffles prevent combustion pulsations from being driven ahead of projectile

unburned propellant past the conical nose of the projectile. This isolating effect allows more energetic mixtures to be used without the risk of the combustion driving a shock wave upstream of the projectile throat and causing an unstart. Since the baffles act to contain the combustion behind the projectile, the tube-to-projectile-throat area ratio can be increased, allowing successful starting of the ram accelerator at as low as Mach 2 without unstart. The use of more energetic propellant, a greater tube area, and operation at lower Mach number all act to increase the thrust on the projectile without having to increase the propellant fill pressure. In addition, the projectile now rides on the baffles, eliminating the need for fins to center it in the tube.

The baffles have a hole bored through their centers that is just large enough to allow the passage of the projectile. The spacing of the baffles is such that the cylindrical mid-body of the projectile completely spans at least two baffles at any time. This forms a sequential series of propellant chambers down the bore of the tube, as shown in Fig. 20. The propellant is initially ignited behind the projectile and the combustion process raises the pressure at its base and in the annular chamber around the mid-body. The baffles act as one-way valves whereby propellant can be ingested by the supersonic diffuser of the projectile, yet the combustion-driven pressure wave system cannot be pushed upstream. Consequently, the propellants can be formulated to be as energetic as possible to maximize acceleration. The ultimate velocity limitation of this concept occurs when the strength of the precursor shock wave, generated by the leading edge of the projectile shoulder as it just enters a chamber, is sufficient to directly initiate a detonation wave that can travel upstream through the next chamber before the projectile shoulder seals against the next baffle. Thus, the thickness of the baffles, their spacing, and the volumes of the expansion chambers all play a significant role in the application of this concept.

Preliminary experiments in a 1-m-long, 38-mm-bore baffled tube, with a propellant fill pressure of 20 bar, have proven that axisymmetric projectiles can be accelerated in propellants having twice the maximum heat release able to be used for ram accelerators operating in smooth bore tubes [45]. The test section, projectile

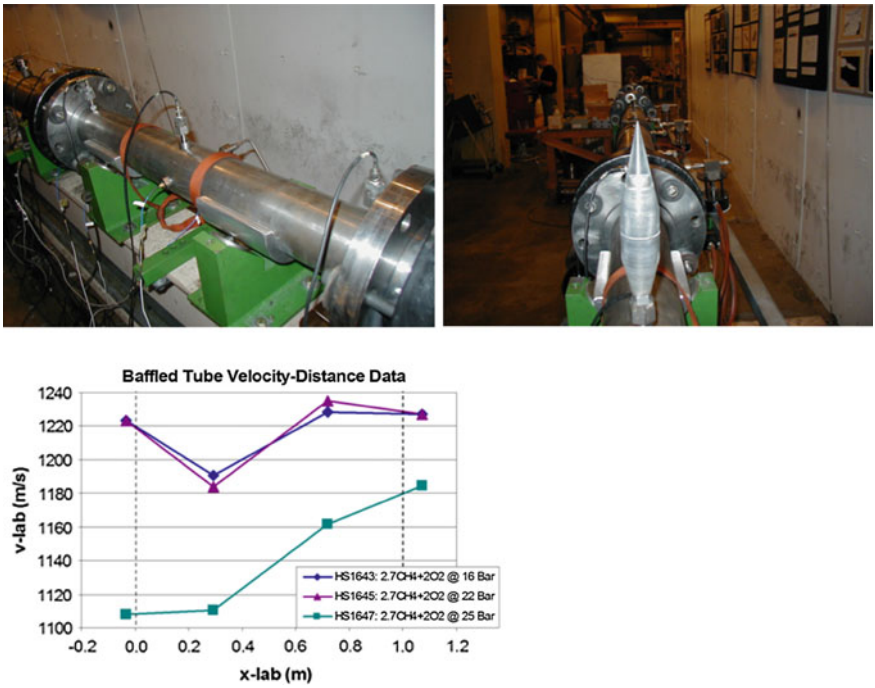

Fig. 21 One-meter-long baffled tube test section (*upper left*), axisymmetric projectile (*upper right*), and experimental velocity-distance data (*left*). Projectiles accelerated through more than 0.50 m of tube length

and representative velocity-distance data from these experiments are shown in Fig. 21. The corresponding non-dimensional thrust was twice that ever generated with propellants at this pressure. The peak operating Mach number of the baffled-tube ram accelerator has not yet been experimentally determined due to the short length of the test section. Experiments are planned for a 4-m-long baffled tube in which more of its thrust characteristics and maximum operational Mach number can be explored.

2.2 U.S. Army Research Laboratory (ARL)

At the U.S. Army Research Laboratory a ram accelerator program was pursued from 1991 to 1997. The main thrust of the work was to demonstrate operation at a larger scale (120-mm-bore) (see Fig. 22), increase its velocity capability [60–62, 64, 67, 68], and develop computational fluid dynamics (CFD) codes for improved predictive capabilities [67, 85–91]. Projectiles of 5-kg-mass were accelerated to velocities up to 2 km/s in a two-stage configuration. The experimental research also

Fig. 22 120-mm-bore ram accelerator at ARL (low pressure version). The initial launcher was a M256 120-mm tank gun, and the ram accelerator section consisted of three such gun barrels, each 4.7 m long. Another gun barrel (perforated) was used as a vent section between the launcher and the ram accelerator

included flow visualization of the thermally choked propulsive mode in sacrificial 1.83-m-long transparent acrylic tubes [63]. The results were recorded using high-speed cinematography. Figure 23 shows frames from two different runs. In Fig. 23a the projectile had already accelerated through a 9.4-m-long steel accelerator section with the same propellant mixture and pressure. It is evident that the combustion zone enveloped the aftbody of the projectile well behind the throat. Figure 23b shows a projectile as it entered the accelerator (injected at $\sim$1200 m/s) and started (in this case the accelerator consisted only of an acrylic tube). The frame

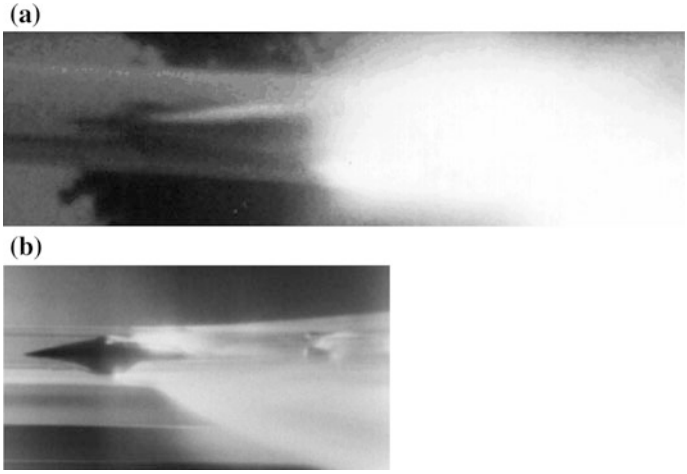

Fig. 23 Frames from high speed films of 120-mm projectile accelerating through transparent acrylic tubes [63]. **a** Projectile cruising near end of transparent tube. Propellant is $3CH_4 + 2O_2 + 10N_2$ at 51 bar, and projectile velocity is 1,480 m/s (Mach 4.1). **b** Projectile just after entering ram accelerator (note obturator at right). Propellant same as above but at 20 bar; projectile velocity is 1,300 m/s (Mach 3.6)

was taken near the end of the transparent tube, where the combustion stabilized; note the "discarded" obturator at the right.

In 1997 the 120-mm-bore ARL facility was upgraded with a new test section, consisting of a single, constant diameter (324-mm-O.D.), thick-walled tube having a length of 4.57 m, which was designed to operate at fill pressures up to 100 bar [62–64]. This facility was initially not equipped with a vent tube between the gun and the ram accelerator test section. Starting the ram accelerator without venting at high pressure was found to be more sensitive to initial conditions than with venting, and was not successful even though a previous test without venting (in the lower pressure rated tubes) was successful. Reinstalling the vent tube allowed a partially successful test at 102 bar fill pressure to be conducted in the new facility [65]. The ram accelerator program at ARL was discontinued shortly after its principal investigator (Kruczynski) left for private industry (see below).

2.3 UTRON, Inc

Low velocity ram accelerator starting was investigated by Kruczynski at UTRON, Inc., Manassas, VA, in collaboration with the UW group [69]. Starting at entrance velocities as low as 760 m/s using various combinations of CO_2 diluent levels and obturator configurations in stoichiometric CH_4/O_2 mixtures was successfully demonstrated. However, the combustion could not be stabilized beyond 2.5 m of travel or 1000 m/s under these conditions. To determine the potential upper operating limit of CO_2-diluted propellants a second $CH_4/O_2/CO_2$ fueled stage was added and the projectile, entering with established ram combustion, was able to accelerate an additional 3.5 m down bore and up to 1150 m/s. At this velocity the projectile

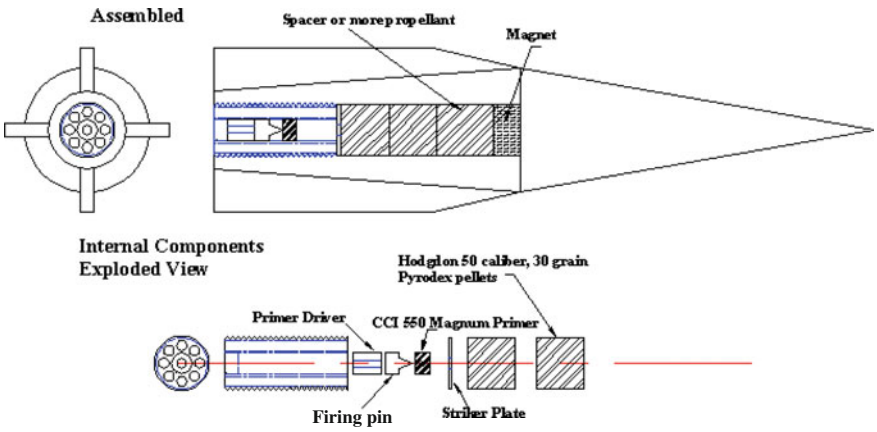

Fig. 24 Diaphragm-impact-initiated onboard igniter developed at UTRON, Inc. note arrangement of primer, firing pin, and primer driver to move forward on impact with the diaphragm [69]

can easily make a transition into propellants having higher sound speeds for continued acceleration. A mechanical pyrotechnic ignitor (Fig. 24), based on one originally developed at the University of Washington [37], was successfully tested and showed the capability to ignite previously un-ignitable propellant mixtures at low entrance velocities [69]. In this case, starting of the ram accelerator was achieved without the presence of a normal shock on the aftbody of the projectile. Such techniques offer the ability to extend the starting regime of ram accelerators further.

3 Computational Modeling

Beginning shortly after the ram accelerator was first conceived, various researchers began to engage in computational modeling of the ram accelerator, both in the U.S. and elsewhere, in support of the experimental efforts. In the U.S. such work was carried out by Brackett and Bogdanoff [10], Yungster [110], Yungster et al. [112], Kruczynski and Nusca [67], Yungster and Bruckner [111], Soetrisno and Imlay [101], Burnham [26], Hinkey et al. [46], Hinkey et al. [47], Li and Kailasanath [72–74], Li et al. [75–77], Nusca [85–89, 92] and Soetrisno et al. [102, 103]. In other countries computational work has been done by Choi et al. [31–33], Henner et al. [36], Leblanc and Fujiwara [71], Moon et al. [81], Taki et al. [107], Zhang and Taki [113], Liu et al. [78] and Bengherbia et al. [6]. It is beyond the purpose or scope of this paper to review in detail the numerous contributions in this area of ram accelerator research; the topic is worthy of a separate review paper of its own. The interested reader is directed to the listed references for additional information. Here only a very brief overview is provided of some of the more recent work performed in the U.S.

The bulk of the more recent CFD modeling of the ram accelerator in the U.S. has been conducted primarily by Li et al. and Nusca (see above-cited references). In particular, Li et al. have performed CFD analyses related to the UW 38-mm ram accelerator [72–75]. Cases they have studied include high-pressure operation, the starting process, unstarts, wave fall-offs, and aerodynamic stability of projectiles, among others. Figure 25 shows computational results for a 2-D projectile canted at 1.5° counterclockwise from the tube axis, travelling at 1250 m/s in a stoichiometric hydrogen-air mixture at 25 bar; the projectile Mach number under these conditions is 3.01 [75]. The pressure, Mach number, temperature, and water vapor concentration fields are plotted in the figure, as are the pressure distributions on the upper and lower surfaces of the projectile. It was found that the aerodynamic torque stabilizes the projectile if the normal shock is maintained on the rear part of the projectile by the thermally choked combustion, and destabilizes the projectile if this normal shock is absent. It remains to be seen if this is also the case in a 3-D computational model.

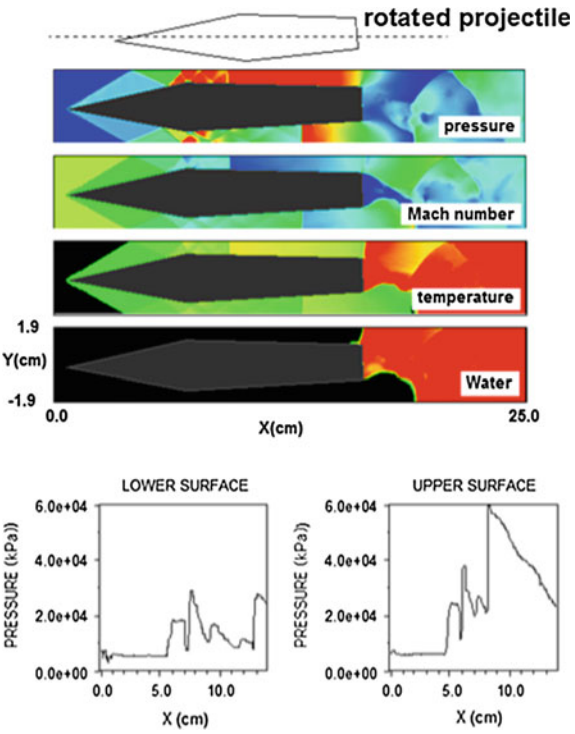

Fig. 25 Computational results for canted projectile in 38-mm UW ram accelerator. Propellant mixture is stoichiometric H_2/air, velocity is 1250 m/s, canting angle is 1.5° [75]

CFD modeling with a virial equation of state by Nusca [87] was focused on experiments in the 120-mm-bore ram accelerator at ARL. Viscous, 3-D flow was considered with frozen chemistry to examine the impact of fins on the flow field and the corresponding pressure profiles of axisymmetric projectiles. The influence on tube wall pressure measurements of fin orientation relative to pressure transducer location correlated well with experiment (Fig. 26a) and matched previous experimental results of Hinkey et al. [46]. Axisymmetric pressure profiles indicated reflected shock wave systems similar to those determined along the center-line between fins, but at a much lower strength. Quasi-steady flow modeling with axisymmetric projectiles and three-step finite rate chemistry was carried out to provide a more detailed look at how the combustion process affects the flowfield over a range of fill pressure (5–10 MPa) and Mach number (3.3–4.1) conditions. Even though the fins were not present in these calculations, the correlation between CFD predicted projectile base pressure and experiment was remarkably good (Fig. 26b). Unsteady calculations with axisymmetric projectiles and three-step chemistry with an obturator initially at the base of the projectile predicted velocity-distance profiles that agreed to within 3 % of experiment (Fig. 26c). The actual thrust prediction at any given Mach was actually even better, as evident by the similar slopes of the theoretical and experimental *V-x* profiles.

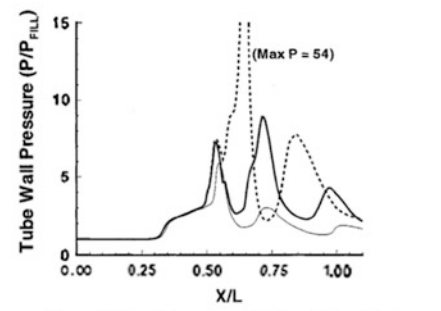

Computed tube wall pressures, M = 3.5 and fill p = 51 atm. Axisymmetric (narrow line), three dimensional between fins (thick line), and three dimensional over fin tip (broken line).

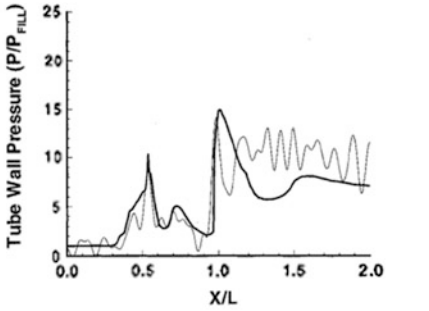

Tube wall pressures, shot 15, station 4, M = 3.45 and fill p = 51 atm. Measured (narrow) and computed (thick line).

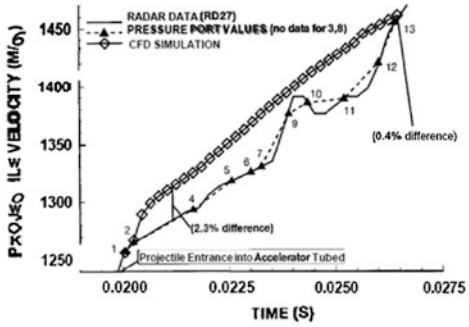

Computed and measured projectile velocity vs time of flight for shot 27. Mixture: $3CH_4 + 2O_2 + 10N_2$ at 51 atm and 300-K fill conditions.

Fig. 26 *Upper left* 3-D wall pressure calculations with inert propellant. *Upper right* wall pressure calculation for axisymmetric projectile with $3CH_4 + 2O_2 + 10N_2$ propellant. *Left* time-accurate velocity-distance profiles for axisymmetric projectile with obturator initially at its base in same propellant as above [87]

4 Future Work

Current areas of interest that continue to be investigated include operation of the ram accelerator at elevated pressures, investigation of projectile material and geometry effects, modeling of ram accelerator operation in three different velocity regimes with real gas and unsteady effects, studies of the starting dynamics, especially at high pressures and/or low initial projectile velocities, investigations of the superdetonative propulsive modes (to attain the highest possible velocities), and improved CFD modeling of all the effective propulsive modes of the ram accelerator. The baffled tube ram accelerator is being studied experimentally and computationally as well, as it holds much promise for very high acceleration performance. The ultimate aim of all ram accelerator research is to attain the

theoretical velocity capability of this launcher technology, namely 6–8 km/s, at which the most interesting applications, such as hypersonic aeroballistic testing and direct space launch become practicable.

5 Conclusions

The ram accelerator is a ramjet-in-tube hypervelocity launcher, originated at the University of Washington, that uses chemical energy to propel projectiles to very high velocities. A projectile similar to the centerbody of a supersonic ramjet travels through a tube filled with high pressure combustible gas, which burns on or behind the projectile to provide thrust. The ram accelerator has demonstrated successful operation at a variety of operating conditions and scale sizes, in a wide range of gas mixtures. Propellant fill pressures of 5–200 bar, and velocities up to 2.7 km s^{-1} have been attained with a bore size of 38 mm, while velocities of up to 2.2 km/s have been achieved with 120-mm caliber, 5-kg projectiles operating in 100-bar propellant mixtures. Three velocity regimes, centered about the Chapman-Jouguet detonation speed of the propellant gas mixture, have been identified that exhibit different acceleration characteristics, indicating the existence of several different propulsive cycles: subdetonative (characterized by thermal choking behind the projectile), transdetonative (characterized by the forward motion of the combustion process onto the projectile body and the existence of regions of mixed supersonic and subsonic combustion), and superdetonative (in which a reflected oblique shock wave induces the combustion process to occur entirely on the projectile body). Numerous computational fluid dynamic studies of the ram accelerator have also been carried out, and have shown that at fill pressures above 25 bar both real gas and non-steady flow effects significantly influence the flowfield analysis. To make better use of the full heating value of propellants and allow higher performance at lower fill pressures, a baffled-tube ram accelerator concept has been proposed and successfully tested at the University of Washington. Ram accelerator facilities have been built and successfully operated by several research groups around the world; of these, only one, at the University of Washington, is currently active (the other ram accelerator facilities are not currently operational due to a variety of factors, mostly involving fiscal constraints). The ease with which the ram accelerator can be scaled up in size offers unique opportunities for its use as a hypersonic research tool, a potentially low-cost space launcher, and other interesting applications. Progress in these areas is predicated by the further development of the velocity and scaling capabilities of this innovative launcher technology.

References

1. Auzias de Turenne, J., Chew, G., Bruckner, A.P.: Recent results from the University of Washington's ram accelerator. AIAA Paper 92-3782 (1992)
2. Bauer, P. (ed.): Fourth International Workshop on Ram Accelerators. J de Physique IV, vol. 10, Pr11. EDP Sciences, Les Ulis Cedex (2000)
3. Bauer, P., Knowlen, C., Bruckner, A.P.: Real gas effects on the prediction of ram accelerator performance. Shock Waves 8, 113–118 (1998)
4. Bauer, P., Knowlen, C., Bruckner, A.P.: One-dimensional modeling of ram accelerator at high acceleration rates in subdetonative regime. Journal de Physique, 29:253–258 (2005)
5. Bauer, P., Legendre, J.F., Knowlen, C., Higgins, A.: A review of detonation initiation techniques for insensitive dense methane-oxygen-nitrogen mixtures. Eur. Phys. J. Appl. Phys. **AP2**, 183–188 (1998)
6. Bengherbia, T., Yao, Y.F., Bauer, P., Knowlen, C.: Numerical study of gaseous reactive flow over a ram accelerator projectile in subdetonative velocity regime. Eur. Phys. J. Appl. Phys. **55**, 11102 (2011)
7. Bogdanoff, D.W.: Ram accelerator direct space launch system: new concepts. J. Propul. Power **8**, 481–490 (1992)
8. Bogdanoff, D.W.: Ram accelerator optimization and use of hydrogen core to increase projectile velocity. In: Takayama, K., Sasoh, A. (eds.) Ram Accelerator, pp. 159–166. Springer, Heidelberg (1998)
9. Bogdanoff, D.W.: Strategies to protect ram accelerator projectiles from in-tube gasdynamic heating. J de Physique IV (France) **10**, Pr11-185–Pr11-195 (2000)
10. Brackett, D.C., Bogdanoff, D.W.: Computational investigation of oblique detonation ramjet-in-tube concepts. J. Propul. Power **5**, 276–281 (1989)
11. Bruckner, A.P.: The ram accelerator: A technology overview. AIAA Paper 2002-1014 (2002)
12. Bruckner, A.P., Hertzberg, A.: Ram accelerator direct launch system for space cargo. IAF Paper 87-211 (1987)
13. Bruckner, A.P., Knowlen, C.: Ram accelerator. In: Blockley, R., Shyy, W. (eds.) Encyclopedia of Aerospace Engineering. Wiley, New York (2010)
14. Bruckner, A.P., Knowlen, C., Hertzberg, A.: Applications of the ram accelerator to hypersonic aerothermodynamic testing. AIAA Paper 92-3949 (1992)
15. Bruckner, A.P., Chew, G., Auzias de Turenne, J., Dunmire, B.: Investigation of hypersonic ramjet propulsion cycles using a ram accelerator test facility. IAF Paper No. 91-275 (1991)
16. Bruckner, A.P., Knowlen, C., Hertzberg, A., Bogdanoff, D.W.: Operational characteristics of the thermally choked ram accelerator. J. Propul. Power **7**, 828–836 (1991)
17. Bruckner, A.P., Burnham, E.A., Knowlen, C., Hertzberg, A., Bogdanoff, D.W.: Initiation of combustion in the thermally choked ram accelerator. In: Takayama, K. (ed.) Shock Waves, pp. 623–630. Springer, Berlin (1992)
18. Buckwalter, D., Knowlen, C., Bruckner, A.P.: Real gas effects on thermally choked ram accelerator performance. In: Takayama, K., Sasoh, A. (eds.) ram Accelerator, pp. 125–134. Springer, Heidelberg (1998)
19. Bundy, C.: Effects of unsteady flow and real gas equations of state on high pressure ram accelerator operation. Ph.D. Dissertation, Department of Aeronautics and Astronautics, University of Washington, Seattle (2001)
20. Bundy, C., Knowlen, C., Bruckner, A.P.: Elevated pressure experiments in a 38-mm-bore ram accelerator. AIAA Paper 98-3144 (1998)
21. Bundy, C., Knowlen, C., Bruckner, A.P.: Ram accelerator operating characteristics at fill pressures greater than 10 MPa. AIAA Paper 99-2261 (1999)
22. Bundy, C., Knowlen, C., Bruckner, A.P.: Ram accelerator operating characteristics at elevated fill pressures. J. Physique IV (France) **10**, Pr11-11–Pr11-21 (2000)

23. Bundy, C., Knowlen, C., Bruckner, A.P.: Investigation of Ram Accelerator Operation at Fill Pressures up to 20 MPa. AIAA Paper 2000-3231 (2000)
24. Bundy, C., Knowlen, C., Bruckner, A.P.: Ram accelerator operation at 15 to 20 MPa fill pressure. In: 18th International Colloquium on the Dynamics of Explosions and Reactive Systems (ICDERS), University of Washington, Seattle, July 29–August 3 (2001)
25. Bundy, C., Knowlen, C., Bruckner, A.: Unsteady effects on ram accelerator operation at elevated fill pressures. J. Propul. Power **20**, 801–810 (2004)
26. Burnham, E.A.: Investigation of starting and ignition transients in the thermally choked ram accelerator. Ph.D. Dissertation, Department of Aeronautics and Astronautics, University of Washington, Seattle (1993)
27. Burnham, E.A., Kull, A.E., Knowlen, C., Bruckner, A.P., Hertzberg, A.: Operation of the ram accelerator in the transdetonative velocity regime. AIAA Paper 90-1985 (1990)
28. Chang, X., Matsuoka, S., Watanabe, T., Taki, S.: Ignition study for low pressure combustible mixture in a ram accelerator. In: Takayama, K., Sasoh, A. (eds.) ram Accelerator, pp. 105–109. Springer, Heidelberg (1998)
29. Chew, G., Bruckner, A.P.: A computational study of nose heating in the ram accelerator. AIAA Paper 94-2964 (1994)
30. Chew, G., Bruckner, A.P.: Computational study of projectile nose heating in a ram accelerator. In: Proceedings of RAMAC II, Second International Workshop on Ram Accelerators. University of Washington, Seattle, July 17–20 (1995)
31. Choi, J.Y., Jeung, I.S., Yoon, Y.: Numerical Study of Scram Accelerator Starting Characteristics. AIAA Paper 97-0915, 35th AIAA Aerospace Sciences Meeting, Reno (1997)
32. Choi, J.Y., Jeung, I.S., Yoon, Y.: Numerical investigation of ram accelerator flow field in expansion tube. In: Takayama, K., Sasoh, A. (eds.) Ram Accelerator, pp. 313–323. Springer, Heidelberg (1998)
33. Choi, J.Y., Lee, B.J., Jeung, I.S.: Computational modeling of high pressure combustion mechanism in scram accelerator. J de Physique IV (France) **10**, Pr11-131–Pr11-141 (2000)
34. Ghorbanian, K., Pratt, D.T.: Doomed propellant fraction for a superdetonative ram accelerator. AIAA Paper 93-0359 (1993)
35. Giraud, M., Legendre, J.F., Simon, G., Henner, M., Voisin, D.: RAMAC in 90 mm Caliber or RAMAC90. Starting process, control of the ignition location and performance in the thermally choked propulsion mode. In: Proceedings of RAMAC II, Second International Workshop on Ram Accelerators, University of Washington, Seattle, July 17–20 (1995)
36. Henner, M., Giraud, M., Legendre, J.F., Berner, C.: CFD computations of steady and non-reactive flow around fin-guided ram projectiles. In: Takayama, K., Sasoh, A. (eds.) Ram Accelerator, pp. 325–332. Springer, Heidelberg (1998)
37. Hertzberg, A., Bruckner, A.P.: Study of a ram cannon for a space cargo launcher. Final Report, NASA Grant No. NAG 1-746, University of Washington, Seattle (1988)
38. Hertzberg, A., Bruckner, A.P., Bogdanoff, D.W.: The ram accelerator: a new chemical method of achieving ultrahigh velocities. In: Proceedings of 37th Meeting of the Aeroballistic Range Association, Quebec, Canada, September 9–12 (1986)
39. Hertzberg, A., Bruckner, A.P., Bogdanoff, D.W.: Ram accelerator: A new chemical method for accelerating projectiles to ultrahigh velocities. AIAA J. **26**, 195–203 (1988)
40. Hertzberg, A., Bruckner, A.P., Knowlen, C.: Experimental investigation of ram accelerator propulsion modes. Shock Waves Int. J. **1**, 17–25 (1991)
41. Higgins, A.J.: Comment on "Performance limits for projectile flight in the ram and external propulsion ram accelerators". J. Propul. Power **15**, 159–160 (1999)
42. Higgins, A.J.: Ram accelerators: outstanding issues and new directions. J. Propul. Power **22**, 1170–1186 (2006)
43. Higgins, A.J., Knowlen, C., Bruckner, A.P.: Ram accelerator operating limits, Part 1: identification of limits. J. Propul. Power **14**, 951–958 (1998)
44. Higgins, A.J., Knowlen, C., Bruckner, A.P.: Ram accelerator operating limits, Part 2: nature of observed limits. J. Propul. Power **14**, 959–966 (1998)

45. Higgins, A.J., Knowlen, C., Kiyanda, C.B.: Gasdynamic operation of baffled tube ram accelerator in highly energetic mixtures. In: 20th International Colloquium on the Dynamics of Explosions and Reactive Systems, McGill University, Montreal Canada, July 31–August 5 (2005)
46. Hinkey, J.B., Burnham, E.A., Bruckner, A.P.: High spatial resolution measurements of ram accelerator gas dynamic phenomena. AIAA Paper 92-3244 (1992)
47. Hinkey, J.B., Burnham, E.A., Bruckner, A.P.: Investigation of ram accelerator flow fields induced by canted projectiles. AIAA Paper 93-2186 (1993)
48. Kaloupis, P., Bruckner, A.P.: The ram accelerator: a chemically driven mass launcher. AIAA Paper 88-2968 (1988)
49. Knowlen, C.: Theoretical and experimental investigation of the thermodynamics of the thermally choked ram accelerator. Ph.D. Dissertation, Department of Aeronautics and Astronautics, University of Washington, Seattle (1991)
50. Knowlen, C., Bruckner, A.P.: A Hugoniot analysis of the ram accelerator. In: Takayama, K. (ed.) Shock Waves, pp. 617–622. Springer, Berlin (1992)
51. Knowlen, C., Bruckner, A.P.: Facility upgrade for high pressure ram accelerator experiments. Paper No. 9. In: Proceedings of RAMAC III, 3rd International Workshop on Ram Accelerators, Sendai, Japan, July 16–18 (1997)
52. Knowlen, C., Bruckner, A.P.: Direct space launch using ram accelerator technology, Space Technology and Applications Forum—STAIF 2001, El-Genk, M.S., ed., American Institute of Physics Conference Proceedings, pp. 583–588, February (2001)
53. Knowlen, C., Sasoh, A.: Ram accelerator performance modeling. In: Takayama, K., Sasoh, A. (eds.) Ram Accelerator, pp. 25–37. Springer, Heidelberg (1998)
54. Knowlen, C., Bruckner, A.P., Hertzberg, A.: Internal ballistics of the ram accelerator. In: 13th International Symposium on Ballistics, Stockholm, Sweden (1992)
55. Knowlen, C., Higgins, A.J., Bruckner, A.P.: Aerothermodynamics of the ram accelerator. AIAA Paper 95-0289 (1995)
56. Knowlen, C., Joseph, B., Bruckner, A.P.: Ram accelerator as an impulsive space launcher: Assessment of technical risks. International Space Development Conference (ISDC), Dallas TX, May 25–28 (2007)
57. Knowlen, C., Schultz, E., Bruckner, A.: Investigation of low velocity starting techniques for the ram accelerator. AIAA Paper 97-3174 (1997)
58. Knowlen, C., Higgins, A.J., Bruckner, A.P., Hertzberg, A.: In-tube photography of ram accelerator projectiles. In: Brun, R., Dumitrescu, L.Z. (eds.) Shock Waves @ Marseilles, vol. 1, pp. 189–194. Springer, Berlin (1995b)
59. Knowlen, C., Higgins, A.J., Hinkey, J.B., Burnham, E.A., Mattick, A.T.: Diagnostic techniques for ram accelerator phenomena. In: Proceedings of 43rd Meeting of the Aeroballistic Range Association, Columbus, OH, September 28–October 2 (1992)
60. Kruczynski, D.: Experimental demonstration of a 120 mm ram accelerator. In: 29th JANNAF Combustion Subcommittee Meeting, NASA Langley Research Center, Hampton October 19–23 (1992)
61. Kruczynski, D.: New experiments in a 120-mm ram accelerator at high pressures. AIAA Paper 93-2589 (1993)
62. Kruczynski, D.: Flow visualization of steady and transient combustion in a 120-mm ram accelerator. Report ARL-TR-1059, US Army Research Laboratory, Aberdeen (1996)
63. Kruczynski, D.: Experimental investigation of high pressure/performance ram accelerator operation. AIAA Paper 96-2676 (1996)
64. Kruczynski, D.L.: High performance ram accelerator research. In: Takayama, K., Sasoh, A. (eds.) Ram Accelerator, pp. 97–104. Springer, Heidelberg (1998)
65. Kruczynski, D.L.: Private Communication. UTRON Inc., Manassas (1998)
66. Kruczynski, D.L.: NAVRAM II: a system analysis of ram acceleration for specific naval applications. UTRON Inc., Manassas (2000)
67. Kruczynski, D.L., Nusca, M.J.: Experimental and computational investigation of scaling phenomena in a large caliber ram accelerator. AIAA Paper 92-3245 (1992)

68. Kruczynski, D., Liberatore, F.: Ram accelerator experiments with unique projectile geometries. AIAA Paper 95-2490 (1995)
69. Kruczynski, D., Knowlen, C., Bundy, C., Bruckner, A.P.: Low velocity start of ram accelerator: obturator and ignitor effects. AIAA Paper 99-2265 (1999)
70. Kull, A.E., Burnham, E.A., Knowlen, C., Bruckner, A.P., Hertzberg, A.: Experimental studies of superdetonative ram accelerator mode. AIAA Paper 89-2632 (1989)
71. Leblanc, J.E., Fujiwara. T.: Numerical simulation of the RAMAC benchmark test configuration. In: Proceedings of 3rd International Workshop on Ram Accelerators, Sendai, Japan, July 16–18 (1997)
72. Li, C., Kailasanath, K.: Highly transient flow features in ram accelerators. AIAA Paper 98-3148 (1998)
73. Li, C., Kailasanath, K.: Initiation mechanism of thermally choked combustion in ram accelerators. J. Propul. Power **15**, 151–153 (1999)
74. Li, C., Kailasanath, K.: Starting performance of thermally choked ram accelerators at high mixture pressures. AIAA Paper 99-2950 (1999)
75. Li, C., Kailasanath, K., Oran, E.S.: Stability of projectiles in thermally choked ram accelerators. J. Propul. Power **12**, 807–809 (1996)
76. Li, C., Kailasanath, K., Oran, E.S., Boris, J.P.: Numerical simulations of unsteady reactive flows in ram accelerators. In: Proceedings of First International Workshop on Ram Accelerator, Paper No. 29, French-German Research Institute (ISL), Saint-Louis, France, September 7–10 (1993)
77. Li, C., Kailasanath, K., Oran, E.S., Boris, J.P.: Pressure distributions on ram accelerator projectiles. In: Proceedings of RAMAC II, Second International Workshop on Ram Accelerators, University of Washington, Seattle, July 17–20 (1995)
78. Liu S., Bai, Z.Y., Jian, H.X.: Numerical calculation of 3-D flow field around ram accelerator projectile. AIAA Paper 2000-3238 (2000)
79. Liu S., Bai, Z.Y., Jian, H.X., Ping, X.H., Bu, S.Q.: 37-mm bore ram accelerator of CARDAC. In: Takayama, K., Sasoh, A. (ed.) Ram Accelerator. Springer-Verlag, Heidelberg, pp. 119–122 (1998)
80. Messersmith, N.L., Burke, M.J.: Ram accelerator ballistic launch requirements. AIAA Paper 95-2495 (1995)
81. Moon, G.W., Jeung, I.S., Choi, J.Y., Yoon, Y., Seiler, F., Patz, G., Smeets, G., Srulijes, J.: Numerical modeling and simulation of RAMAC 30 experiment carried out at the French-German Research Institute of Saint-Louis. J de Physique IV (France) **10**, Pr11-143–Pr11-153 (2000)
82. Naumann, K.W.: Heating and ablation of projectiles during acceleration in a ram accelerator tube. AIAA Paper 93-2184 (1993)
83. Naumann, K.W.: Thermomechanical constraints on ram accelerator projectile design, AIAA Paper 96-2678 (1996)
84. Naumann, K.W., Bruckner, A.P.: Ram accelerator ballistic range concept for softly accelerating hypersonic free-flying models. J. Aircraft **31**, 1310–1316 (1994)
85. Nusca, M.J.: Numerical simulation of fluid dynamics with finite rate and equilibrium combustion kinetics for the 120-mm ram accelerator. AIAA paper 93-2182 (1993)
86. Nusca, M.J.: Reacting flow simulation for a large scale ram accelerator. AIAA Paper 94-2963 (1994)
87. Nusca, M.J.: Reacting flow simulation for a large scale ram accelerator. J. Propul. Power **12**, 61–69 (1996)
88. Nusca, M.J.: Investigation of ram accelerator flows for high pressure mixtures of various chemical compositions. AIAA Paper 96-2946 (1996)
89. Nusca, M.J.: Computational simulation of the ram accelerator using a coupled CFD/interior ballistic approach. AIAA Paper 97-2653 (1997)
90. Nusca, M.J.: Computational simulation of starting dynamics in a ram accelerator. AIAA Paper 98-3146 (1998)

91. Nusca, M.J.: Numerical simulations of unsteady ram accelerator flow phenomena. In: Takayama, K., Sasoh, A. (eds.) Ram Accelerator, pp. 305–312. Springer, Heidelberg (1998)
92. Nusca, M.J.: Numerical simulation of the ram accelerator using a new chemical kinetics mechanism. J. Propul. Power **18**, 44–52 (2002)
93. Rom, J.: Performance limits for projectile flight in the ram and external propulsion accelerators. J. Propul. Power **13**, 583–591 (1997)
94. Sasoh, A., Hirakata, S., Ujigawa, Y., Takayama, K.: Operation Tests of a 25 mm Bore Ram Accelerator. AIAA Paper 96-2677 (1996)
95. Schultz, E., Knowlen, C., Bruckner, A.P.: Detonation Limits Applied to the Subdetonative Ram Accelerator Starting Process. AIAA Paper 97-0807 (1997)
96. Schultz, E., Knowlen, C., Bruckner, A.P.: Overview of the subdetonative ram accelerator starting process. In: Takayama, K., Sasoh, A. (eds.) Ram Accelerator, pp. 189–203. Springer, Heidelberg (1998)
97. Schultz, E., Knowlen, C., Bruckner, A.P.: Starting envelope of the subdetonative ram accelerator. J. Propul. Power **16**, 1040–1052 (2000)
98. Seiler, F., Naumann, K.W.: Bow shock wave heating and ablation of a sharp-nosed projectile flying inside a ram accelerator. In: Brun, R., Dumitrescu, L.Z. (eds.) Shock Waves @ Marseille, vol. 1, pp. 183–188. Springer, Berlin (1995)
99. Seiler, F., Patz, G., Smeets, G., Srulijes, J.: Gasdynamic limits of ignition and combustion of a gas mixture in ISL's RAMAC30 scram accelerator. In: Sturtevant, B., Shepherd, J.E., Hornung, H.G. (eds.) Proceedings of 20th International Symposium on Shock Waves, vol. II, pp. 1057–1062. World Scientific Singapore (1996)
100. Slutsky, S., Tamagno, J.: A feasibility study of the scramjet in-tube concept. Report AFAPL-TR-67-131 (classified), General and Applied Science Laboratories (GASL) Inc., Westbury, NY. (1967) (Note: Declassified in 1994)
101. Soetrisno, M., Imlay, S.T.: The flow field of a ram accelerator. AIAA Paper 91-1915 (1991)
102. Soetrisno, M., Imlay, S.T., Roberts, D.: Numerical simulations of the transdetonative ram accelerator combusting flow field on a parallel computer. AIAA Paper 92-3249 (1992)
103. Soetrisno, M., Imlay, S.T., Roberts, D.: Numerical simulations of the superdetonative ram accelerator combusting flow field. AIAA Paper 93-2185 (1993)
104. Stewart, J.F., Bruckner, A.P., Knowlen, C.: Effects of launch tube shock dynamics on initiation of ram accelerator operation. In: Takayama, K., Sasoh, A. (eds.) Ram Accelerator, pp. 181–188. Springer, Heidelberg (1998)
105. Stewart, J.F., Knowlen, C., Bruckner, A.P.: Effects of launch tube gases on starting of the ram accelerator. AIAA Paper 97-3175 (1997)
106. Takayama, K., Sasoh, A. (eds.): Ram Accelerator. Springer, Heidelberg (1998)
107. Taki, S., Zhang, C., Chang, X.: Numerical simulation of the unsteady process in starting of ram accelerator. In: Takayama, K., Sasoh, A. (eds.) Ram Accelerator, pp. 215–221. Springer, Heidelberg (1998)
108. Witcofski, R.D., Scallion, W.I., Carter, D.J., Courter, R.W.: An advanced hypervelocity aerophysics facility: A ground-based flight test range. AIAA Paper 91-0296 (1991)
109. Witherspoon, F.D., Kruczynski, D.L.: Gun launch to space: a discussion of technology options. Space Energy Transp. **5**(4) (2000)
110. Yungster, S.: Navier-Stokes simulation of the supersonic combustion flowfield in a ram accelerator. AIAA Paper 91-1916 (1991)
111. Yungster, S., Bruckner, A.P.: Computational studies of a superdetonative ram accelerator mode. J. Propul. Power **8**, 457–463 (1992)
112. Yungster, S., Eberhardt, S., Bruckner, A.P.: Numerical simulation of hypervelocity projectiles in detonable gases. AIAA J. **29**, 187–199 (1991)
113. Zhang, C., Taki, S.: Numerical study of shock induced ignition and combustion of CH_4-O_2-CO_2 mixtures in a two dimensional ram accelerator. J de Physique IV (France) **10**(Pr11), 155–164 (2000)

Author Biographies

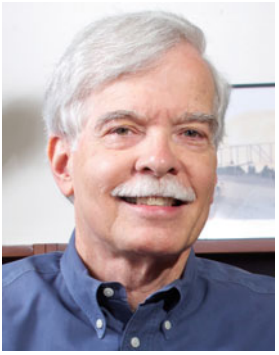

Adam Bruckner is a Professor in the William E. Boeing Department of Aeronautics and Astronautics at the University of Washington, and is one of the co-inventors of the ram accelerator hypervelocity launcher. He received his Ph.D. in Mechanical and Aerospace Engineering in 1972 from Princeton University and joined the University of Washington the same year. From 1998 to 2010 he was Chair of the department. His research has encompassed hypervelocity accelerators, planetary in situ resource utilization, space propulsion, space power systems, and energy conversion. He has published nearly 190 technical papers and reports in these areas, and is co-author on five U.S. patents, including three on the ram accelerator. He is a Fellow of the AIAA and has received several awards from NASA and other organizations.

Carl Knowlen is a Research Associate Professor in the William E. Boeing Department of Aeronautics and Astronautics at the University of Washington. He received his Ph.D. in Aeronautical and Astronautical Engineering in 1991 from the University of Washington. His research interests include energy conversion for terrestrial and space power generation, petrochemical processing using shockwaves in supersonic flows, cryogenic vortex tube applications, microrocket engines and green propellants, continuous detonation wave propulsion systems, and hypervelocity mass drivers. He has been involved with ram accelerator development since its inception in 1983. He has published more than 80 technical papers on this topic alone and is co-author on two U.S. patents. He is an Associate Fellow of the AIAA.

Experiments on Supersonic and Superdetonative Combustion at ISL's Ram Accelerator RAMAC 30

Friedrich Seiler, Günter Smeets, Gunther Patz, Julio Srulijes, Gilbert Mathieu, Berthold Sauerwein and Jean-Luc Striby

Abstract The acceleration of a projectile flying by the self-synchronized ignition of an explosive gas in a 38-mm-tube, the "Ram accelerator", was first successfully developed and tested by Hertzberg et al. [10]. From this time on, this accelerator concept has generated considerable interest in various countries, particularly in the USA, Israel, Japan, Korea and France. The ISL in France performed experiments at superdetonative flight speeds in a 30 mm-caliber ram accelerator, called RAMAC 30 which are concisely described in this chapter. At the same time, [5] operated also at ISL the RAMAC 90 in the subdetonative velocity regime. In RAMAC 30 a conventional gun, as pre-accelerator, injected a ram-projectile into a single stage ram tube filled with hydrogen, methane or ethylene based gas mixtures. A ram-tube equipped with rails for guiding smooth cylindrical projectiles was tested as accelerator: the rail tube version I with four inner rails (Sect. 2.2) and the rail tube version II with five inner rails (Sect. 2.3). The smooth bore technique was tested too (Sect. 3). The projectile was fired into the ram-tube with superdetonative speed, relative to the gas mixture, so that the combustion stabilized on the projectile body from the beginning on. The gas

B. Sauerwein · J.-L. Striby
French-German Research Institute of Saint-Louis (ISL), Saint Louis 68301, France
e-mail: berthold.sauerwein@isl.eu

J.-L. Striby
e-mail: jean-luc.striby@isl.eu

F. Seiler (✉) · G. Smeets · G. Patz · J. Srulijes · G. Mathieu
Retired from ISL, Saint-Louis 68301, France
e-mail: friedrich.seiler@kit.edu

G. Smeets
e-mail: g.smeets@t-online.de

G. Patz
e-mail: gunther.patz@t-online.de

J. Srulijes
e-mail: juliosrulijes@yahoo.com

G. Mathieu
e-mail: gilbert.mathieu8@wanadoo.fr

F. Seiler and O. Igra (eds.), *Hypervelocity Launchers*,
Shock Wave Science and Technology Reference Library 10,
DOI 10.1007/978-3-319-26018-1_5

combustion causes a temperature rise followed by a gas pressure increase at practically constant gas density propelling the ram-projectile. The heat transfer from gas to projectile causes the latter's surface temperature to increase. This can lead to melting processes followed by ablation of surface material which is obviously undesirable. Therefore, a prediction of the heat flux from gas to projectile surface becomes necessary and for this purpose a boundary layer and ablation model was developed by which the heating of the projectile and its melting ablation at nose, fins and body can be estimated (Sect. 4). Damage of projectile was observed on X-ray pictures, especially of the fins, probably by melting and burning when magnesium, aluminum or titanium alloys were used. Steel projectiles can endure the ram acceleration cycle, but the projectile mass is too large to achieve sufficient acceleration.

1 Introduction

The first scientists who developed and successfully tested the ram accelerator concept in a 38-mm-device were Hertzberg et al. [10] starting in the 80s at the University of Washington, Seattle, Washington, USA. In their ram accelerator facility described by Hertzberg [9], Knowlen et al. [12], Hertzberg et al. [11] and Bruckner et al. [2], the process always starts with subsonic combustion behind the projectile flying initially at speeds lower than the Chapman-Jouguet (CJ) detonation velocity of the combustible gas mixture. For achieving higher velocities, the projectile passes from the transdetonative combustion mode to the superdetonative mode where combustion occurs in the supersonic flow inside the slit between the sub-caliber projectile and the tube wall, see Fig. 1.

Based on the need of ISL for a hypersonic launching facility, the decision was taken to build two ram accelerators: a 30-mm-tube, called RAMAC 30, and a 90 mm-one, RAMAC 90 [5–7]. To bypass the gasdynamic problems of subdetonative ignition, the direct firing into the superdetonative combustion mode, called scram accelerator, was investigated in the RAMAC 30. The RAMAC 30 facility was built for basic research with the objective of understanding both the ignition

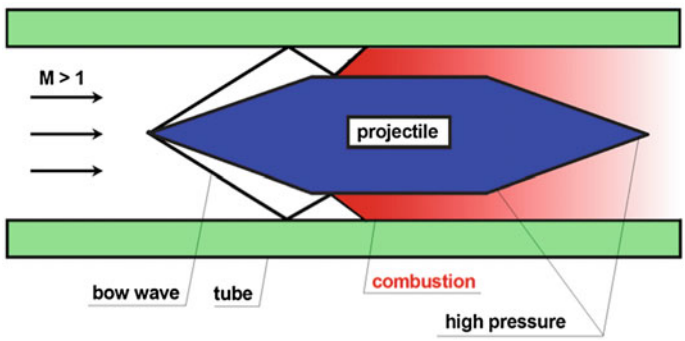

Fig. 1 Principle of the scram accelerator process with superdetonative combustion

and combustion phenomena of the various gas mixtures and different projectile shapes to be used. In particular, new tube concepts were targeted, for which purpose the RAMAC 30 was tested with rail equipped tubes: version I, with four rails [19, 20] and version II, with five rails [23, 24] and also with the smooth bore technique [14, 15] with fin guided projectiles.

The rail tube version was based on a concept published by Smeets [25] for a ram accelerator with guiding tube rails for firing rail stabilized projectiles. This was done to replace the fin stabilized projectiles, originally used at the University of Washington, which were accelerated in a cylindrical bore, [9]. The rail tube concept has some advantages, e.g., no sabot is necessary as required for fin guided projectiles; it allows simpler projectile geometries and the possibility of varying the inner tube shape. Therefore, it was decided to primarily test the rail tube principle in the RAMAC 30 with rail guided projectiles.

The compilation herein contains the most important results and describes in detail the still unsolved difficulties of the RAMAC-concept which have not yet provided a worldwide usable ram accelerator facility. Nevertheless, this research has brought new insights for future research in this area. The experimental and theoretical RAMAC-research, which was carried out at ISL for over a decade, is thoroughly described in this chapter. Its content has been compiled from the contributions to the four biannual RAMAC-workshops (1993–1999) gathering a large forum of international scientists. The workshops are chronologically listed below:

1. RAMAC I Workshop, ISL, Saint-Louis, France
2. RAMAC II Workshop, University of Washington, Seattle, Washington, USA
3. RAMAC III Workshop, Tohoku University, Sendai, Japan
4. RAMAC IV Workshop, University of Poitiers-E.N.S.M.A., Poitiers, France.

2 Rail-Guided Ram-Projectiles

2.1 Principle of Scram Acceleration

Figure 1 explains the principle of the scram accelerator process with supersonic combustion. A vehicle consisting of a cylindrical centerbody with a conical shape at its front and rear ends propels through a combustible gas mixture in a cylindrical tube having a diameter greater than that of the centerbody. By means of fins, Patz et al. [15], or rails, Seiler et al. [19, 20], which are not shown in Fig. 1, the projectile is guided centered inside the tube. This tube containing the combustible gas mixture is closed at both ends by diaphragms which are destroyed by the projectile fired by a gun accelerator.

The flow field around the projectile moving at supersonic and superdetonative speed largely corresponds to that in a scramjet engine. In the high Mach number on-flow, an attached bow shock is formed on the conical front of the projectile as seen from the reference system fixed at the projectile. The front shock undergoes one or more reflections between the wall of the tube and the cylindrical part of the projectile, thus creating a series of oblique shocks. Hereby the flow is compressed

and heated in the same way as it is inside an inlet of a scramjet engine. If ignition temperature is achieved, the combustible gas is expected to ignite and combust in the circular section between the cylindrical midbody and the tube: "the combustor". There is still an unsolved question on whether ignition occurs in an oblique detonation wave or is initiated by hot spots in the stagnation regions formed at the edges between the rails and the surface of the projectile, or otherwise, between the fins and the tube wall. At practically constant gas density the combustion generated high gas pressure produces thrust on the conical back of the projectile, which corresponds to the thrust acting on the nozzle of a scramjet engine.

The surface of the projectile propelled at high velocity becomes extremely hot during the in-tube flight as a result of the high gas pressures present in the flow around it. The surface temperature during in-bore movement has to be kept below the melting temperature of the projectile's surface material to avoid, e.g., pre-ignition of the combustible gas mixture at the nose followed by a deceleration of the ram projectile, called "unstart". To estimate the heating and melting effects we developed a computer model, see Sect. 4 [16, 17]. In case the projectile surface is heated and eventually melts as a result of high heat flux into it, chemical reactions may occur between projectile material and the combustible gas mixture, especially oxygen and/or diluents. These chemical reactions, however, are not treated herein and are not included in the computer model.

2.2 Rail Tube Version I of RAMAC 30

2.2.1 Description of the Facility

The RAMAC 30 design followed in principle the prototype ram accelerator of [10] in which fin stabilized bodies were accelerated by combustion in a circular ram tube. However, version I of RAMAC 30 was designed for testing an alternative concept of ram tube with inner rails in combination with cylindrical and finless projectiles, see [25]. Figure 2 shows such a projectile with no fins. This projectile was guided in a tube with four inner rails, see [19]. Both the front and the rear cone angles of the projectiles used are 14–16°. The combustor zone of constant diameter has a length of 45–60 mm and the projectile mass is 125–135 g. The tube cross-section is given in Fig. 3. The total cross-section area of the rail tube is

Fig. 2 Cylindrical ram-projectile used in rail tube version I

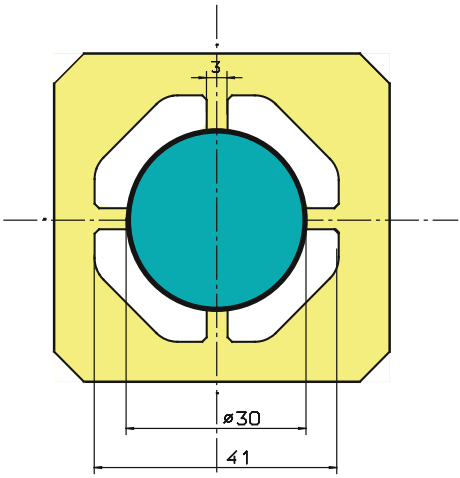

Fig. 3 Cross-section in rail tube version I

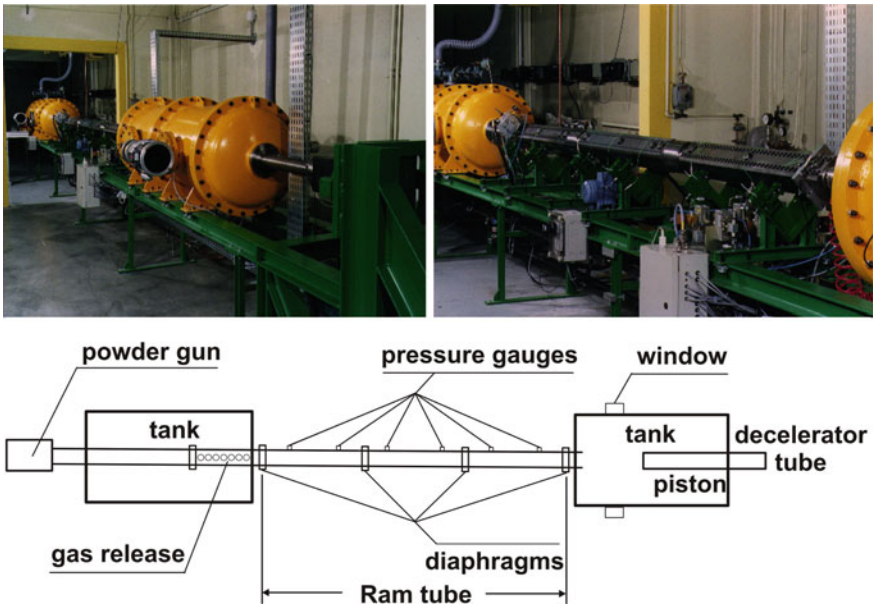

Fig. 4 RAMAC 30 facility with rail tube I between two dump tanks

1241 mm^2. Figure 4 left hand side shows a photo of the facility, with a powder gun as pre-accelerator at its right, two dump tanks, and the rail ram-tube in between. A direct view of the ram-tube is seen in Fig. 4 right hand. At the end of the ram accelerator, the projectiles hit a set of replaceable steel plates located inside of a

piston which, after impact, is propelled backwards inside of the catcher tube. A schematic drawing of the ram facility can be seen under the photos in Fig. 4.

In the first experiments we used just one ram-section of 3.6 m length. In the conventional powder gun with a tube length of 1.8 m, aluminum (Dural alloy AlMgCu1) projectiles partially fitted with an inner magnesium core with total masses of about 130 E.g. were accelerated to a muzzle velocity of about 1800 m/s which was the initial velocity at the entrance to the ram-section. As the Chapman-Jouguet speed of the gas mixture was lower than the muzzle velocity, this allowed firing directly in the superdetonative ram accelerator mode, with combustion at the cylindrical part of the projectile as sketched in Fig. 1.

2.2.2 Experimental Results

The experiments were carried out with the above mentioned projectile geometry. The projectile was made of an inner magnesium body covered all around by an aluminum cowling (forebody, combustor and afterbody). We investigated three different gas mixtures based on hydrogen (H_2), methane (CH_4) and ethylene (C_2H_4), having mainly a stoichiometric ratio of fuel with oxidizer and having carbon dioxide (CO_2) as diluents: (1) ethylene-oxygen-carbon dioxide, (2) methane-oxygen-carbon dioxide, (3) hydrogen-oxygen-carbon dioxide. With all three gas mixtures best ignition behavior as well as avoidance of unstart effects were obtained in limiting the heat release according to the limits of ignition and combustion described in Sect. 2.2.3. The maximum projectile velocity increase was about 200 m/s, fired in a 27 bar gas mixture (see Fig. 5, shot no. 97). Larger CO_2-contents (shot nos. 89, 91, 93) give less heat release and consequently lower projectile acceleration. A reduced CO_2-content increases the heat production by combustion followed by an unstart as shown for shot no. 99.

The results shown in Fig. 5 for hydrogen based mixtures and in Fig. 6 for hydrogen, methane and ethylene fuels were determined at several measuring

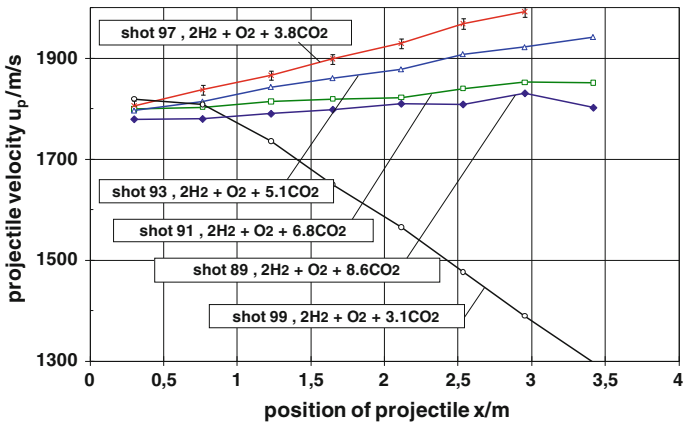

Fig. 5 Flight velocities obtained with hydrogen based mixtures in the rail tube version I

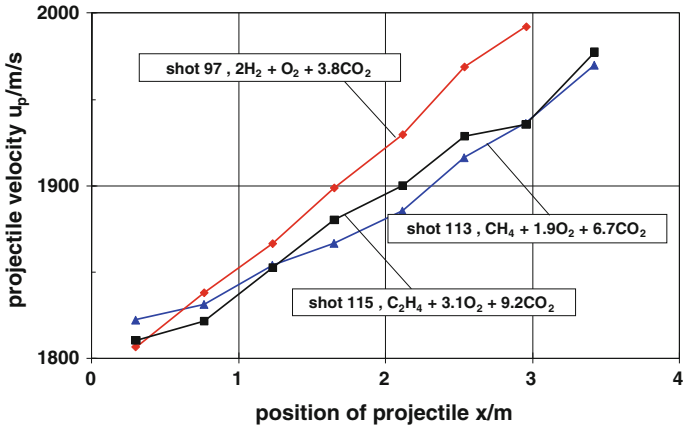

Fig. 6 Flight velocities with mixtures based on hydrogen, methane and ethylene in the rail tube version I

stations using the signals from the electromagnetic sensors identifying in better than one microsecond the passage of the magnet located inside the projectile, see Fig. 7 for shot no. 97 and Fig. 8 for no. 89 (stations M16, M18 and M19). Measured pressure signals are also plotted in Figs. 7 and 8. They show the pressure profile during the passage of the projectile at the pressure gauges.

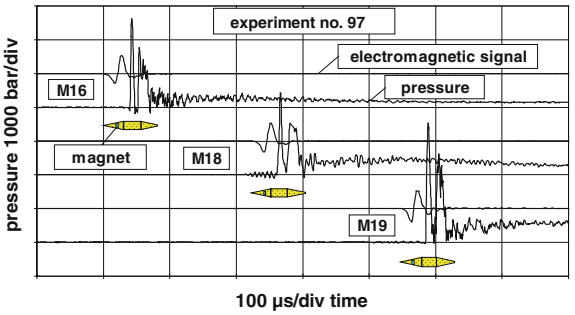

Fig. 7 Electromagnetic and pressure signals received for shot no. 97

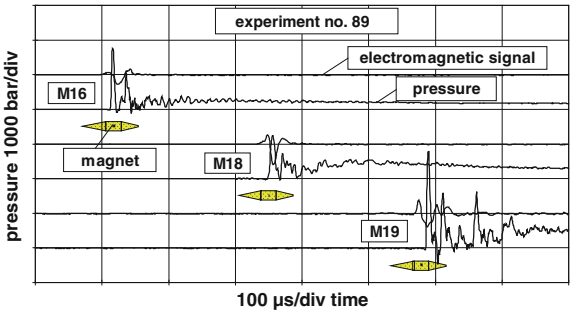

Fig. 8 Electromagnetic and pressure signals received for shot no. 89

2.2.3 Limits of Ignition and Combustion

The experiments show that stability limits exist in the superdetonative mode. One limit is set by thermal choking followed by an unstart which means that the combustion wave moves ahead of the projectile. Another limit for failure is the decoupling of the ignition and combustion from the projectile.

Figure 7 shows a set of typical signals for experiment no. 97 recorded with the electromagnetic sensors and the wall pressure gauges at three measuring locations along the tube, i.e., M16, M18 and M19. The pressure signals are directly time correlated to the position of the projectile. They show a very strong pressure increase by a front shock at the beginning of the combustor zone with a peak pressure of more than 1000 bar. This first wave is probably produced by the reflection of the incident shock wave at the tube wall forming the first reflected shock. The pressure strongly decreases in the expansion generated at the corner of the projectile shoulder. A second wave follows initiating a high pressure region. This second jump is probably located where the third (or fourth) reflected shock is formed from the second (or third) shock inducing combustion similar to the well-known detonation phenomena, described by Chapman and Jouguet, see [27].

The increase of carbon dioxide makes the combustible gas mixture more and more phlegmatic requiring a third wave to become ignited, as seen in Fig. 8 for shot no. 89 at measuring station M19. The gas reaction occurs then behind the projectile and the pressure gain is lost. Combustion decoupling or no combustion depend on the inert component mole parts of the gas mixture, i.e., the CO_2-content in the $H_2/O_2/CO_2$ mixture used herein. This outcome defines an upper dilution limit of the combustible gas mixture for getting the mixture ignited in the combustor before the expansion in the divergent rear region takes place.

To avoid thermal choking followed by an unstart, the heat release must be adapted to the flow Mach number M ahead of the combustion. For a one-dimensional flow, as present in the channel between projectile and wall, [27] gives a relation describing the maximal heat input q as follows:

$$\left(\frac{q}{c_p\,T}\right)_{max} = \frac{\left(M^2 - 1\right)^2}{2\,(\chi + 1)\,M^2} \tag{1}$$

In this relation, coupling the normalized heat release with the flow Mach number M, the parameter χ is given as $\chi = c_p/c_v$, with c_p the specific heat at constant pressure and c_v that at constant volume. T is the gas temperature ahead of combustion. The heat release as a function of the flow Mach number M shows the curve (1) in Fig. 9. We see two regions: a zone in which no stable combustion occurs and the flow is thermally choked, and a zone with stable combustion by limiting the heat input. Five points inserted in the diagram represent the normalized heat release for firings no. 89, 91, 93, 97 and 99, calculated with the code developed by Smeets et al. [26].

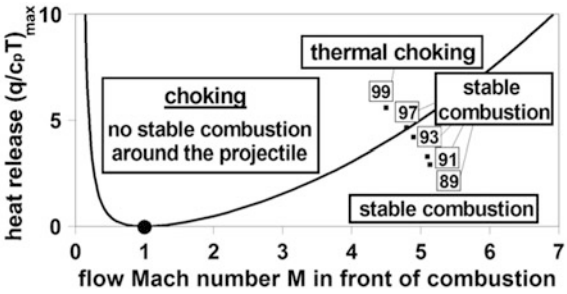

Fig. 9 Heat release inside of the combustor channel for superdetonative combustion

Figure 5 shows the projectile unstart for shot no. 99, which was well predicted by the above given relation. The other four shots are (no. 97) at the border and (no. 89, 91, 93) inside the allowed region, giving as shown in Fig. 5 a positive projectile acceleration for the latter ones.

2.3 Rail Tube Version II of RAMAC 30

2.3.1 RAMAC 30 Facility

In rail tube version II the tube is equipped with five inner rails, see geometry in Fig. 10. The total tube cross-section is about 1381 mm^2. Contrary to version I here the ram-tube consists of two tubes with a total tube length of 4.7 m. The rail tube II placed between the two damp tanks is seen in Fig. 11 left with all the equipment necessary for RAMAC 30 operation: (1) valves for gas filling, (2) pressure gauges for pressure measurement, and (3) electromagnetic sensors for determining the

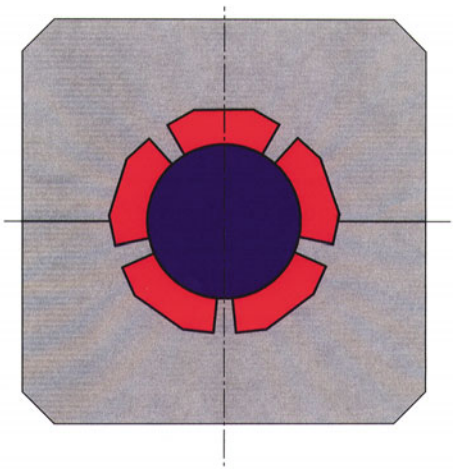

Fig. 10 Cross-section of rail tube version II with five rails

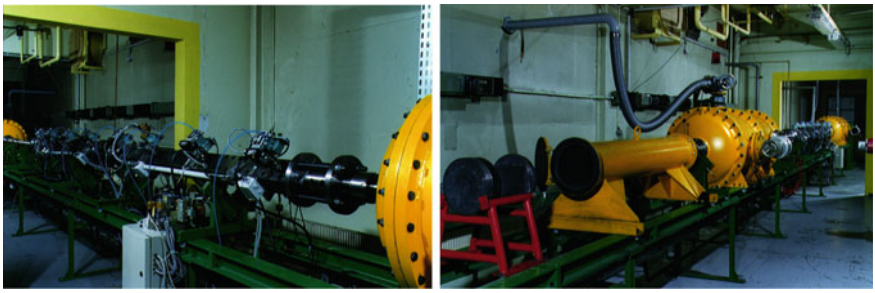

Fig. 11 Rail tube version II

Fig. 12 Catching piston with projectile impact into steel plates

projectile position. In the decelerator tube at the end of the facility, there is a piston equipped with inner replaceable steel plates for catching the projectile (Fig. 11 right hand side). An impact into these steel plates can be seen in the photograph of Fig. 12.

2.3.2 Experimental Results

Projectile with Aluminum

Successful experiments were carried out in RAMAC 30 rail tube version I with aluminum projectiles with a magnesium core to reduce weight and a total mass of about 130 g. E.g., firing no. 97 with hydrogen as fuel, no. 113 with methane or no. 115 with ethylene resulted in maximum velocity increase of nearly 200 m/s with filling pressures of 26.8 bar for no. 97, resp. 20 bar for no. 113 and 115. The heat release had to be limited to avoid thermal choking inside of the combustor channel between projectile midbody and ram-tube wall, see Fig. 9. Otherwise, as found in experiment no. 99, higher heat release induced a detonation wave moving upstream ahead of the projectile.

Heat transfer calculations done by Seiler et al. [22], and described in Sect. 4, taking into account the boundary layer formation at the fore- and midbody of the ram projectile predicted that, e.g., for firing no. 97 shown in Fig. 5 the midbody surface begins to melt because the surface temperature exceeds the melting temperature of the aluminum used. Surface melting is followed by ablation causing the midbody diameter to diminish, with the consequence that the 30 mm-caliber for projectile guidance is not guaranteed anymore. Thus, canting of the projectile begins and an asymmetric flow around the projectile develops, often causing the combustion or detonation wave to move ahead of the projectile.

Although we gathered positive results with aluminum projectiles in rail tube version I, it seems that melting and ablation can be present followed by a lack of projectile guidance, which may result in an acceleration failure. To avoid melting processes which are always coupled with surface erosion, other materials than aluminum need to be used in Tail tube version II to overcome the material problem that have been identified in version I.

Projectile with Steel Midbody Cowling

Probably the best way to prevent melting of projectile material is to use steel, as predicted by Seiler et al. [22]. For this reason we designed a new cylindrical projectile consisting of an inner plastic body (Delrin) of 24 mm diameter with aluminum forebody, and afterbody screwed to it. A steel cowling of 3 mm thickness protects the plastic core against the heat forming the constant diameter combustor, see Fig. 13.

The first firings performed with this steel projectile had the aim to reach at the muzzle of the powder gun an entrance velocity into the ram tube of 1800 m/s to initiate superdetonative combustion. The steel protected projectiles with a 3 mm thick steel cowling had a mass of about 200 g. Unfortunately, this high mass did not

Fig. 13 Rail tube version II projectiles

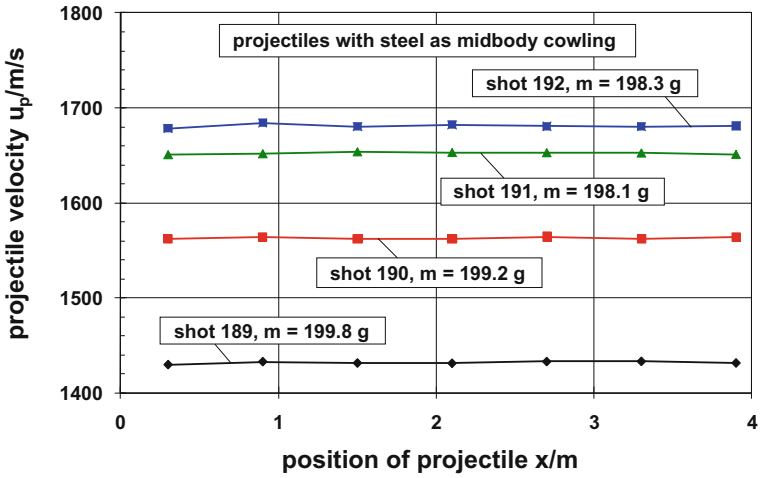

Fig. 14 Inert firings with rail tube version II using projectiles with a steel cowling at the midbody

permit to increase the projectile's velocity to the required initial velocity of 1800 m/s at the entrance to the ram accelerator tube, even if the chamber pressure was increased to the maximum allowed of 6000 bar (no. 192), as shown in the velocity paths given in Fig. 14.

Projectile with Titanium Midbody Cowling

To lessen the projectile mass, the steel cowling was replaced by a titanium one reducing its mass by about 50 g to m ≈ 150 g instead of m ≈ 200 g with a steel cowling. By using a titanium cowling with the same thickness as the steel one (3 mm), the initial projectile velocity reached 1772 m/s for firing no. 197. Ram acceleration was thus achieved with this titanium protected projectiles, as shown in Fig. 15 for shots no. 196 and 197. The inert gas firing of shot no. 198 can also be seen in Fig. 15. The reactive firing no. 196 succeeded to accelerate the projectile with immediate gas ignition and stable combustion inside of the combustor zone. The velocity increase is nearly 4 % of the initial velocity of 1739 m/s with an $\Delta u = 64$ m/s. This result is comparable to that obtained in RAMAC 30 rail tube version I for firings no. 89 or 91.

The higher heat release in shot no. 197 compared with no. 196 gives higher projectile acceleration, but ends with a slight forward motion of the combustion wave in the midbody combustor region. This is the beginning of an unstart which can be recognized in Fig. 15 by the velocity drop at the last measuring point x ≈ 4 m. The reason for the unstart behavior is surface melting. Melting occurs at the forebody aluminum surface as well as at the titanium combustor cowling, see X-ray image in Fig. 16 top for firing no. 197 with a high energetic mixture. Additionally, melting and ablation are present in the expansion region at the aluminum afterbody. The well-shaped projectile of inert firing no. 198 is also shown in

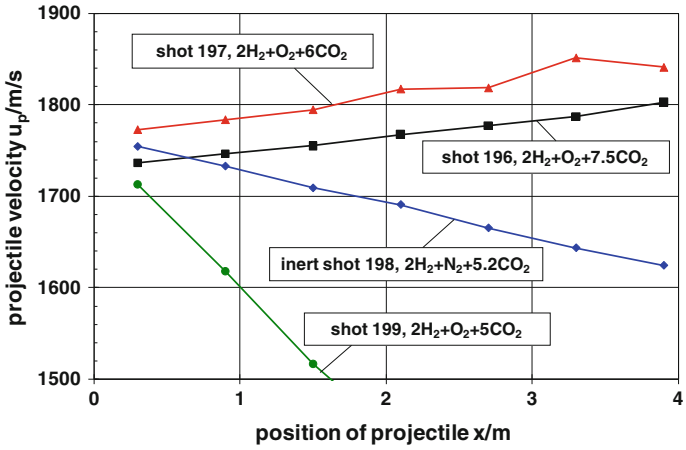

Fig. 15 Velocity distribution in rail tube version II

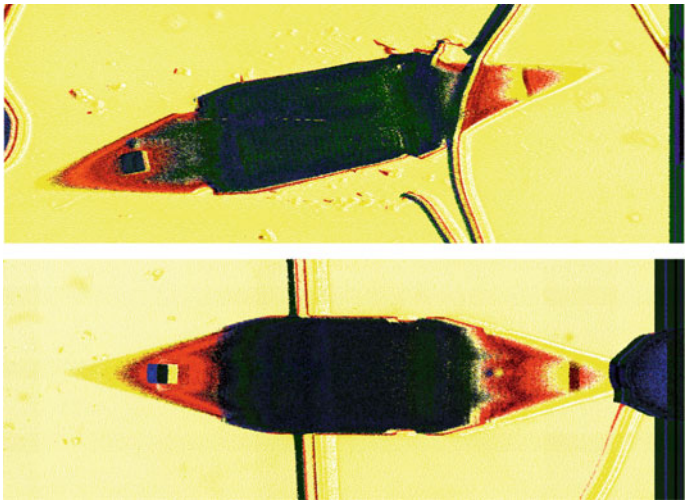

Fig. 16 X-ray photographs of firings no. 197 (*top*) and no. 198 (*bottom*)

Fig. 16 as an X-ray photograph. For firing no. 199 an unstart was produced by thermal choking, because the initial velocity at the entrance to the ram accelerator was too low for initiating the superdetonative combustion process. Here the projectile speed was u_p = 1713 m/s with a gun chamber pressure of 4000 bar.

The normalized heat release as a function of the flow Mach number ahead of the combustion is shown in Fig. 17 for shots no. 196, no. 197 and no. 199. We see that the heat release in shot no. 199 is too high to enable a stable combustion. Thermal choking is produced in the flow between projectile midbody and rail tube surface

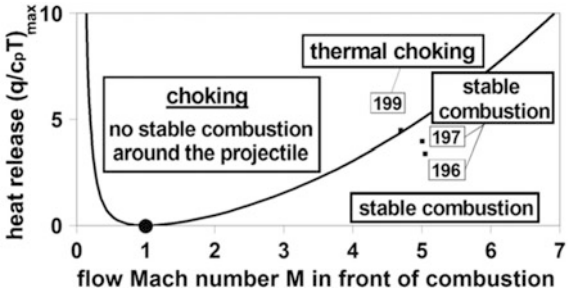

Fig. 17 Maximum heat release inside the combustor channel for superdetonative combustion (firings no. 196, 197 and 199)

followed by a detonation front moving upstream. This result shows that with increasing heat release the projectile entrance velocity must also be increased in the superdetonative combustion mode. For the $2H_2 + O_2 + 5CO_2$ gas mixture of shot no. 199, the calculated entrance velocity must be at least 1800 m/s to obtain a positive acceleration.

2.4 Summary of the Behavior of Rail Tube I and II

The experiments performed at ISL in the rail tube version I of RAMAC 30 constitute a significant breakthrough in superdetonative ram combustion. The following points can be highlighted: (1) Cylindrical bodies with conical front and rear parts are accelerated in a rail tube. In this case, pre-acceleration in a gun without sabot was possible. (2) There is no problem of an unstart with hydrogen, methane and ethylene based combustible gas mixtures when the heat release is limited. The positive experimental outcomes shown in Fig. 5 support this discussion. Surface melting occurring at the body surface has been calculated with the heating model given by Seiler et al. [22].

The first projectiles used in rail tube version II of RAMAC 30 consist of an inner plastic core (Delrin) with a forebody and an afterbody made of aluminum (Dural alloy AlMgCu1). The midbody is protected with an outer steel or titanium cowling. The photograph of Fig. 13 shows the design of the actual projectile with steel cowling. With this type of projectile it was impossible to achieve the required initial projectile velocity of 1800 m/s for entering directly into superdetonative combustion. The projectile mass of about 200 g is too high to be accelerated to the desired gun muzzle velocity with the existing powder gun. By using titanium instead of steel a reduced mass of about 150 g was reached and herewith we achieved a projectile injection into the ram accelerator tube with nearly 1800 m/s. Nevertheless, the melting and surface erosion present with titanium call for other materials for carrying out future successful acceleration cycles.

3 Smooth Bore Version

3.1 RAMAC 30 Facility Set-Up

Having shown the good applicability of the rail equipped accelerator tube concept for ram acceleration, we then investigated the conventional smooth bore technique of [9], for the superdetonative case, with a projectile guided by fins fixed at the body of the projectile.

For the 30 mm-caliber smooth ram-tube, we used two 3 m long tubes attached to each other with a total length of 6 m and a powder gun as pre-accelerator. Figure 18 shows the red painted ram-tube and between ram-tube and pre-accelerator the needed sabot stripper tube (painted blue). The latter consists of two concentrically arranged tubes: a bigger diameter outer tube and an inner so called "clarinet tube" with the bore diameter of the ram-tube. This stripper tube with 1.5 m length is filled with a gas of high compressibility, e.g., CO_2.

To become superdetonative relative to the Chapman-Jouguet (CJ) detonation velocity of the combustible gas mixture used, the projectile was injected into the smooth ram tube with about 1800 m/s. The geometry used for the aluminum and titanium projectiles is depicted in the photograph of Fig. 19, showing the fins fixed at a body with constant diameter and the conical front and rear parts. The required sabot for pre-acceleration of a fin guided projectile is attached behind. The projectiles are made of aluminum (some coated) and titanium with four or five fins having a thickness of 2–2.5 mm. The front cone and rear cones have angles of 14–16°. The combustor zone with constant diameter of 20 mm has a length of about 50 mm. The projectile mass is 80–85 g with aluminum and about 110 g with titanium. The sabot has a mass of about 32 g.

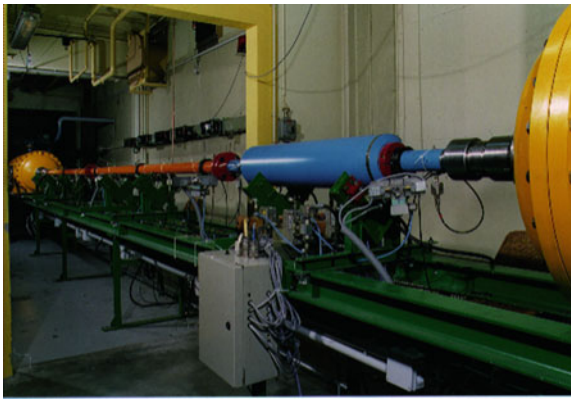

Fig. 18 Smooth ram tube (*left*) and sabot stripper tube (*right*)

Fig. 19 Ram projectile made of aluminum with guiding fins

3.2 Experimental Results

The results of shot no. 139 (aluminum), 170 (titanium), 178 (aluminum with plastic steel coating) and 172 (inert firing) are presented in Fig. 20. There the projectile velocity is shown as a function of the position of the projectile inside of the tube. For firings no. 139, 170 and 178 the velocity initially decreases in the sabot stripper tube and then increases compared with the inert firing no. 172, where the oxygen has been replaced by nitrogen. The combustion starts inside the combustor producing thrust on the back of the projectile. However, the heat flux into the ram projectile is huge due to the high combustion temperature, initiating in some cases melting processes and chemical reactions between the projectile material and the oxygen as well as the diluent CO_2 present in the combustible gas mixture. This chemical reaction produces an additional heat release which surpasses the maximum allowable heat input, see [21], and generates an unstart which begins after a projectile travelled for about 4–5 m.

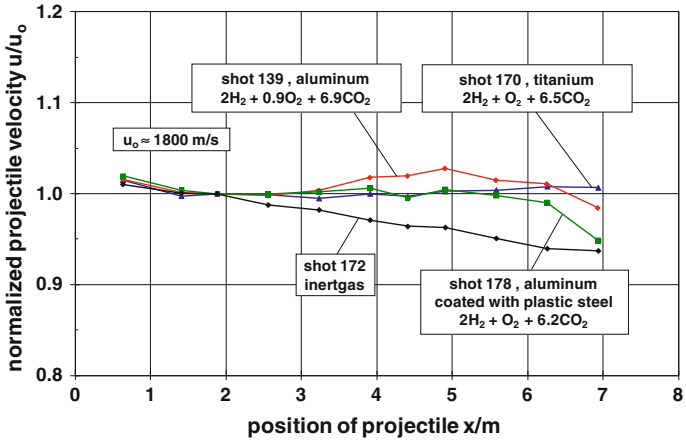

Fig. 20 Velocity distribution in RAMAC 30 with different ram projectiles

From X-ray photos it can be seen that the projectiles lose their fins and the cylindrical bodies diminishes from 20 to about 16–18 mm in diameter, as shown in Fig. 21 for shot no. 139. A similar X-ray picture of the titanium projectile of shot no. 170 shows less ablation. The fins are well visible in the inert firing no. 172 and in shot no. 178, see Fig. 22. If the projectile loses its fins canting occurs. In some cases the projectile body burns almost completely during the firing cycle. This behavior was usually present when aluminum projectiles (shot no. 139) were used. Projectiles made of titanium (shot no. 170) behave similarly to shot no. 139 but endure longer.

A comparison with a calculation of [26] is shown in Fig. 23. The calculated velocity rise is smaller compared with that given in the experiment no. 139. The higher experimentally obtained acceleration present with pure aluminum is caused by the burning of the projectile body and/or fins generating an additional heat source besides the heat release by combustion. The consequence is an undesired velocity gain by burning of projectile material which in most cases is followed by a projectile unstart.

The velocity distribution obtained with aluminum projectiles fired in fuel rich (no. 145), stoichiometric (no. 136) and fuel lean (no. 146) hydrogen based gas mixtures are drawn in the diagram of Fig. 24. There exists no significant difference in the velocity behavior of these projectiles. In all three cases the supersonic combustion starts with a projectile acceleration. But after about 3–4 m the acceleration stops and is changed into a strong projectile deceleration. The reason for this behavior is that both fins and body are damaged by melting and burning. In each of these three firings practically the whole projectile is burned, a fact proved by the negligible impact on the steel plates of the catcher tube.

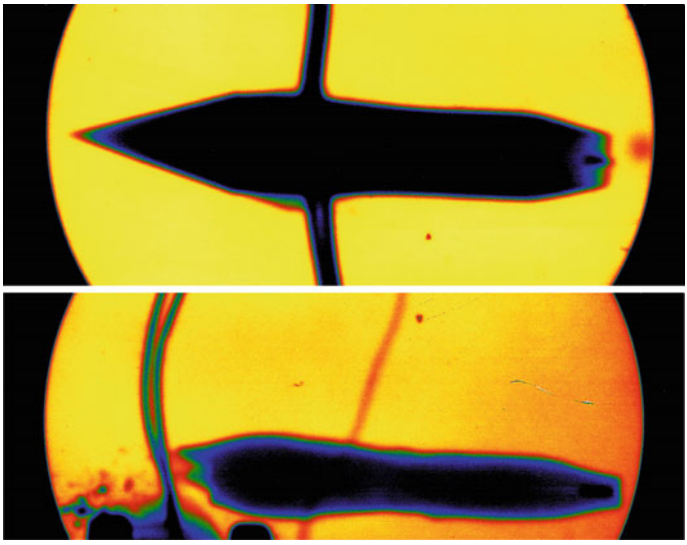

Fig. 21 X-ray photography of firings no. 170 (*top*) and no. 139 (*bottom*)

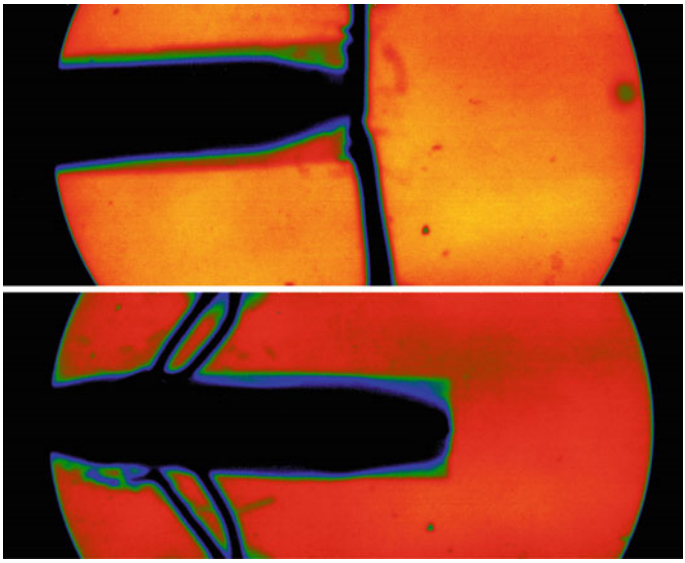

Fig. 22 X-ray photograph of inert firing no. 172 (*top*) and no. 178 (*bottom*)

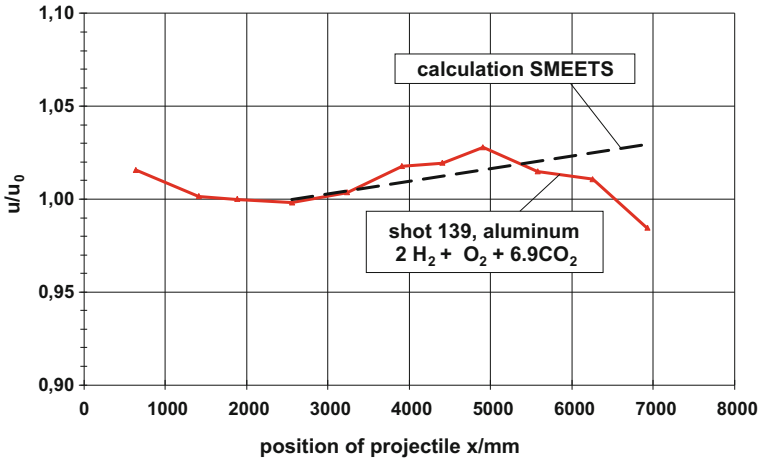

Fig. 23 Aluminum projectile firing no. 139 compared with calculation

In Fig. 25 a comparison is shown between shots fired with aluminum projectiles, either plasma coated with zirconium oxide ZrO_2 (no. 150) or with aluminum oxide Al_2O_3 (no. 151). Firing 178 was done with an aluminum projectile coated with a plastic steel layer. The coating thicknesses are in the range of about 200 µm. The protected aluminum projectiles endure longer in time than those of pure aluminum. The protection of the outer surface enabled these projectiles not to burn up completely after the 6 m tube length as also proved by the impact on the steel plates.

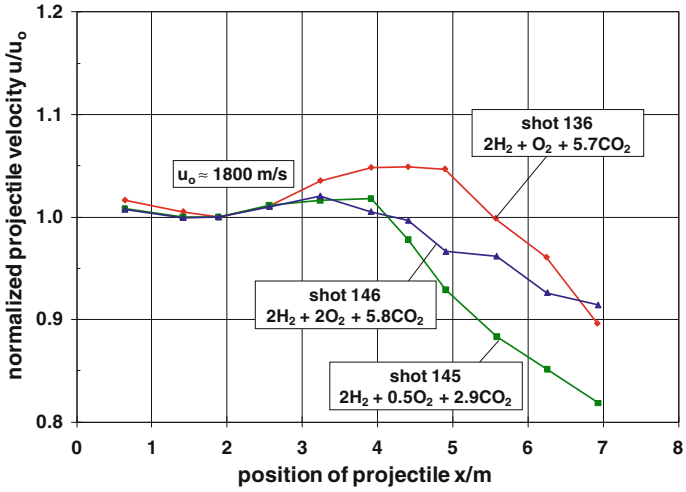

Fig. 24 Aluminum projectiles fired with fuel lean, rich and stoichiometric hydrogen based mixtures

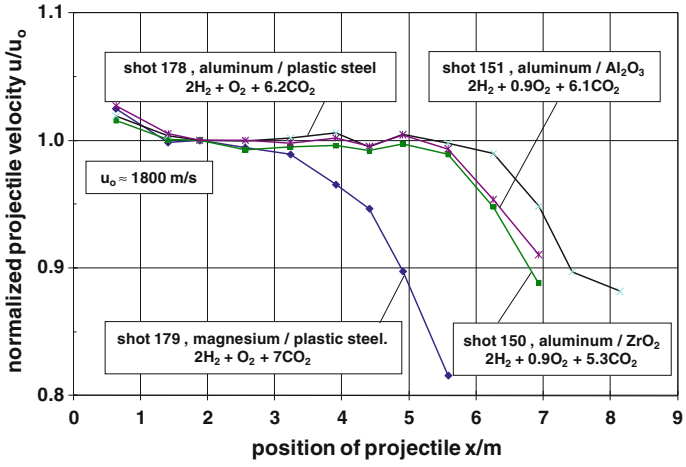

Fig. 25 Velocity distribution with coated projectiles

The non-coated aluminum projectile endures a flight of 3–4 m. After 6 m the aluminum projectile is almost vanished. Almost the same result was found with firing no. 179, a plastic coated magnesium projectile, with a lower heat release than no. 178.

Figure 26 shows the results of several firings into gas mixtures with nitrogen as diluent. The titanium projectiles show a rather good behavior whereas the shot with the aluminum projectile results in an unstart shortly after the beginning of the ram cycle. Figure 27 again shows the comparison between the experimental results in

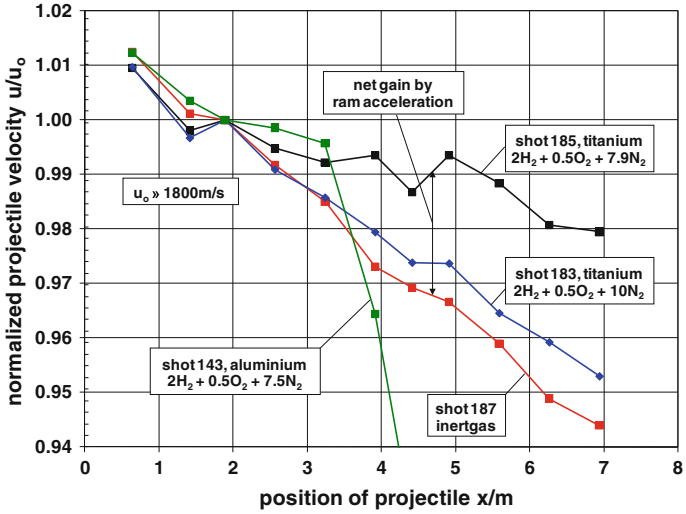

Fig. 26 Firings with nitrogen as diluent

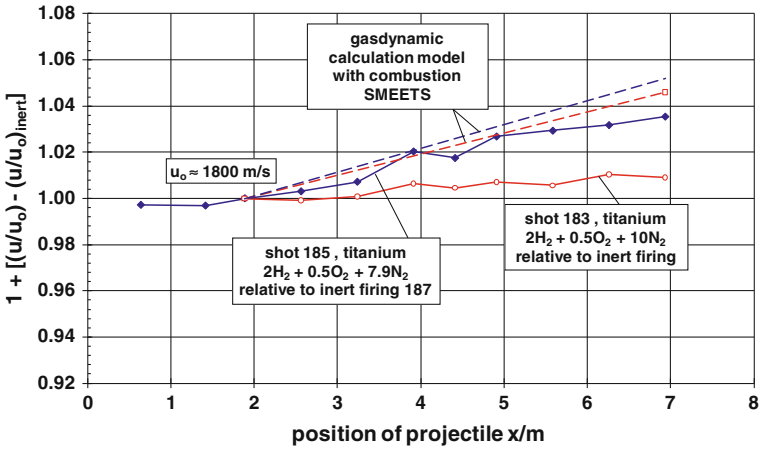

Fig. 27 Net gain compared with calculated velocity distributions

Fig. 26 with the corresponding calculations. The latter shows the projectile velocities of the several firings as compared with that of shot 187 fired in inert gas as net gain. This net gain by the ram cycle also increases with decreasing dilution with N_2. However, there is only a narrow possible N_2 dilution range between no ram acceleration at all and unstart by detonative reaction of the gas mixture.

3.3 Summary of the Smooth Bore Research

In conclusion, the firings carried out in ISL's RAMAC 30 with a smooth ram tube and fin guided projectiles demonstrate the following outcomes: (1) Controlled sabot separation in a sabot stripper tube; (2) Direct firing of fin guided projectiles into the superdetonative combustion mode was achieved with ignition and stable combustion at the projectile body and without unstart; (3) Weak acceleration with hydrogen and methane based combustible gas mixtures diluted with carbon dioxide was obtained; (4) Varying the fuel contents from fuel rich to fuel lean with hydrogen and methane based mixtures gave no better results in view of the previous points; (5) The strong heat flux causes aluminum and titanium projectile damage, especially melting and burning at the projectile fins due to chemical reactions of projectile material with oxygen and diluent (CO_2); (6) Results of zirconium oxide (ZrO_2) and aluminum oxide (AL_2O_3) coatings on aluminum have shown that the coating can lengthen the endurance time but not for the whole ram cycle; (7) The additional heat input by burning material is an unwelcome heat source and leads to an unstart with a detonation wave moving ahead of the projectile followed by projectile canting, and (8) Steel projectiles can endure the whole ram cycle but the ram acceleration is very small due to high projectile mass.

4 Heating and Erosion of Ram-Projectiles

4.1 Modeling of Surface Heating

4.1.1 Computational Requirements

Projectiles' heating estimates were carried out to understand the thermal behavior of the ram projectiles during their flight inside the ram tube. For calculating the temperature distribution at the surface and inside the projectile a flow model was developed, as shown e.g. in Fig. 28, for the fin stabilized projectile. Similar

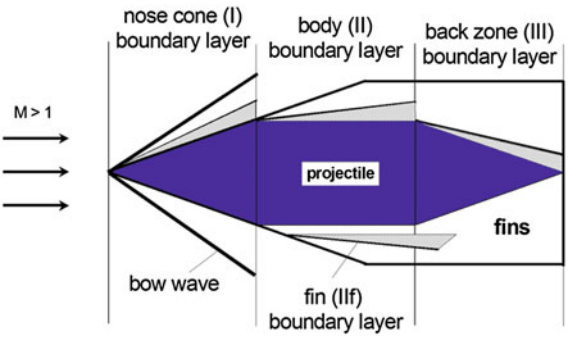

Fig. 28 Boundary layer formation at the fin stabilized projectile

derivations were also made for the rail tube versions, see Seiler [16] and Seiler and Mathieu [17]. In Fig. 28 the boundary layers are discussed in a projectile-fixed frame. It is assumed that compressible and turbulent boundary layers develop at the following projectile surface regions: (I) at the cylindrical nose cone, (II) in the combustion zone between projectile body and tube wall, (IIf) at the guiding fins in case of the smooth bore, and (III) in the expansion zone.

The flow between conical bow wave and projectile in region (I) is assumed to behave parallel to its surface, the same being assumed in regions (II), and (III). It is also assumed that at these surfaces, similar to that at a flat plate, a compressible and turbulent boundary layer develops that will be simulated in two dimensions in the flow model. This requirement is justified as long as the boundary layer thickness at the surface is much smaller than the radius of the projectile. Although this assumption fails near the cone tip, this small error is tolerated for obtaining an analytical solution for the description of the whole ram projectile heating.

4.1.2 Boundary Layer Solution

Beginning with Prandtl's boundary layer equations, the same differential equations were specified analytically for regions (I, II, and III) which were solved with the outer flow and surface boundary conditions given in these regions. As an analytical solution, the heat flux $\dot{q}_g$ from gas close to the projectile surface along the projectile's surface coordinate x is as follows for the three domains:

$$\dot{q}_g(x) = a_f \left(\frac{n+1}{n+3}\right)^{\frac{2}{n+3}} (B(n)\,\varphi)^{\frac{n+1}{n+3}} c_p\,(T_r - T_w)\,Pr^{-\frac{2}{3}} \rho_e \left(\frac{\delta^{**}}{\delta}\right)^{\frac{2}{n+3}} u_e^{\frac{n+1}{n+3}} \left(\frac{\nu_e}{x}\right)^{\frac{2}{n+3}}. \tag{2}$$

The parameter u_e in Eq. (2) is the flow velocity parallel to the surface in regions (I), (II) and (III) outside of the boundary layer. The other quantities used, as n, B(n), φ, δ, δ**, T_r, T_w, c_p, ρ_e and ν_e are explained by Heiser et al. [8].

4.1.3 Heat Conduction Solution

For taking into account the heat flux $\dot{q}_g$ into the sharp-cone geometry of the ram-projectile-nose in zone (I) the flat-plate heat flux of Eq. (2) is adjusted using the analogy factor a_f well known for this application. For determining the factor a_f the calculated heat flux $\dot{q}_g$ of (2) is fitted to the experimental heat transfer results of Chien [3] on a 5° sharp-cone. The best agreement, see [22], is found with $a_f = 1.07$ using n = 9 for the exponent of the u-velocity profile normal to the surface (y) inside

the turbulent boundary layer with thickness δ. In zone (II) and (III) the constant a_f is set equal to 1. The u-profile, u(y), chosen is the following one:

$$\frac{u}{u_e} = \left(\frac{y}{\delta}\right)^{\frac{1}{n}}. \tag{3}$$

The variation of the calculated heat flux along the x-coordinate at the surfaces in Eq. (2) is very small. Therefore, the heat flux $\dot{q}_g(x)$ into the projectile surface is treated to be approximately one-dimensional in depth y and the one-dimensional heat-conduction equation was applied for each x along the projectile surface:

$$\frac{\partial T}{\partial t} = k\frac{\partial^2 T}{\partial y^2} \qquad \text{with } k = \frac{\lambda}{\rho c} \tag{4}$$

Gatau [4] obtains by integration of Eq. (4) with the given boundary conditions analytical solutions for the temperature change ΔT inside the projectile material as a function of the heat flux $F = \dot{q}_g(x)$, for both, non-coated walls and coated walls up to three coating layers. In Eq. (5), a solution from Gatau [4] is presented for non-coated surfaces:

$$\Delta T(y,t) = \frac{F}{\sqrt{\lambda \rho c}}\left[2\frac{\sqrt{t}}{\sqrt{\pi}}\exp\left(\frac{y^2}{4kt}\right) - \frac{y}{\sqrt{k}}\operatorname{erfc}\left(\frac{y}{2\sqrt{kt}}\right)\right] \tag{5}$$

The instationary, time-dependent acceleration process was taken into account by a time-step-procedure as shown in Fig. 29. The real acceleration cycle expected and observed in the RAMAC 30 is approached by the successive time intervals $\Delta t_1, \Delta t_2, \ldots, \Delta t_n = t_n - t_{n-1}, \ldots$ with constant flow quantities during these individual steps, that are the parameters as needed for Eq. (2), but changing with ongoing time.

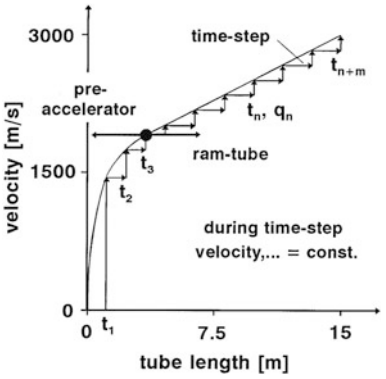

Fig. 29 Velocity time-step approach for RAMAC 30 operation up to 3 km/s

In this procedure the heat flux $\dot{q}_g(x)$ becomes additionally a function of time, i.e., of flow velocity u_e, which equals the projectile velocity. Introducing $\dot{q}_g\,(x,\ t\ =\ t_1, \ldots t_n)$ of Eq. (2) in (5) by assuming that the heat flux at the surface at $y = 0$ is equal on both the gas side (g) and the projectile surface (p), with stepwise constant $F\ =\ \dot{q}_g\,(x,\ t)\ =\ \dot{q}_p\,(x,\ y\ =\ 0, t)$ the temperature distribution $T(x, y, t) = T_0 + \Delta T(x, y, t)$ at the surface and inside the projectile can be calculated. The procedure is carried out for each time interval $\Delta t_1,\ \Delta t_2, \ldots, \Delta t_n, \ldots$ at all x along the surface for getting the temperature distribution T(x,y,t) with projectile displacement in time for the whole acceleration cycle. The projectile temperature increase ΔT is obtainable as:

$$
\begin{aligned}
&t = t_1 \colon \dot{q}_{p,1} = \dot{q}_{p,1} \\
&t = t_2 \colon \dot{q}_{p,2} = \dot{q}_{p,1} + \left(\dot{q}_{p,2} - \dot{q}_{p,1}\right) \\
&t = t_3 \colon \dot{q}_{p,3} = \dot{q}_{p,1} + \left(\dot{q}_{p,2} - \dot{q}_{p,1}\right) + \left(\dot{q}_{p,3} - \dot{q}_{p,2}\right) \\
&\ \ \vdots \\
&t = t_n \colon \dot{q}_{p,n} = \dot{q}_{p,1} + \left(\dot{q}_{p,2} - \dot{q}_{p,1}\right) + \left(\dot{q}_{p,3} - \dot{q}_{p,2}\right) + \cdots + \left(\dot{q}_{p,n} - \dot{q}_{p,n-1}\right) \\
&\qquad\quad \downarrow \qquad \downarrow \qquad\quad \downarrow \qquad\quad\ \downarrow \qquad\qquad\quad \downarrow \\
&\Delta T\ =\ \Delta T_1 + \quad \Delta T_2\ + \qquad \Delta T_3\ + \cdots \qquad\quad + \Delta T_n = \sum_{k=1}^{n} \Delta T_k
\end{aligned}
\tag{6}
$$

The procedure (6) can also be applied for the fin heating (IIf) with the assumption that the fins are thick enough to avoid the heat from arriving at the middle of the fin's width during heating cycle.

4.2 *Modeling of Melting Ablation*

4.2.1 Model Bases

It is assumed that ablation occurs only by melting erosion with no evaporation. Melting erosion often takes place when hot gas flows with a high stagnation temperature are in contact with colder walls. This process has been extensively treated by numerous authors, see [1]. Moreover, in the study herein an analytical ablation model for a ram-projectile is described, see [16–18]. A similar theory using a numerical model was developed in parallel by Naumann [13].

In the present analytical model it is assumed that the sharp-cone geometry (I), the body and fin contours (II, IIf) and the rear contour (III) remain approximately unchanged by heating and ablation, i.e., just a small amount of ablation occurs. Therefore, the boundary layer formation is considered to be uninfluenced. It is assumed that the strong shear stress present in the flow whips away the melting from the surfaces as soon as it is produced, when the wall temperature exceeds the

melting temperature. This means that no liquid layer remains on the solid surface. Heat addition from melt to gas flow is neglected.

4.2.2 Ablation Model

Heating and melting ablation are decoupled along the time-steps $\Delta t_1, \Delta t_2, \ldots, \Delta t_n, \ldots$ at each point x along the x-coordinate in each zone: (I), (II), and (III). For $t < t_n$ the surface temperature $T_{n-1}(x, y, t < t_n)$ is lower than the melting temperature T_m, see Fig. 30. For $t = t_n$ the temperature $T_n(x,y,t)$ exceeds the melting temperature T_m by the heat input $\dot{q}_{g,n}(x,t)$ of Eq. (2). Now melting occurs in the layer Δy_j (j = 1,…m) at time interval $\Delta t_n = t_n - t_{n-1}$ and the melting heat h_m of the projectile material has to be taken into account. The total heat flux input $\dot{q}_{g,n}$ must be divided into one part $\dot{q}_{c,n}(x, t)$ for heat conduction and one part for heat of melting:

$$\dot{q}_{g,n}(x)\ \Delta t_n = \dot{q}_{c,n}(x)\ \Delta t_n + \rho\ h_m\ \Delta y_j, \quad j = 1, \ldots m. \tag{7}$$

The molten layer Δy_j in time-step n is obtained from Eq. (7). For that $\dot{q}_{c,n}(x, t)$ is determined with the heat flux $\dot{q}_{g,n}(x,t)$ given from Eq. (2) and the heat lost by melting. From the temperature calculation using $F = \dot{q}_{c,n}(x,t)$ in Eq. (5) and procedure (6) as well as the assumption that

$$T_{n+1}(x, y = y_{n+1}) = T_m, \tag{8}$$

at the beginning of time-step t_{n+1}, the ablated layer Δy_j is found for time interval Δt_n.

At the end of time interval Δt_n the molten layer Δy_j is whipped away by the shearing forces exerted by the strong shear stress τ_p acting on the surface of the projectile. The described processes of melting and shearing are continued along the time-step approximation of the whole ram acceleration cycle, as:

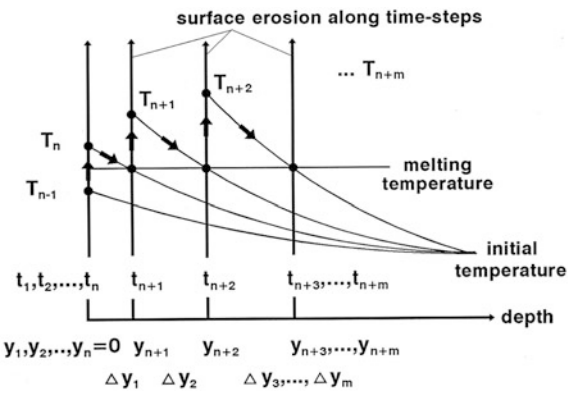

Fig. 30 Surface ablation along time-step procedure

$$
\begin{aligned}
&t < t_n : T_{n-1} < T_m \\
&t = t_n : T_n > T_m \xrightarrow{\Delta y_1 = y_{n+1} - y_n} T_{n+1} = T_m, \\
&t > t_n : T_{n+1} > T_m \xrightarrow{\Delta y_2 = y_{n+2} - y_{n+1}} T_{n+2} = T_m, \\
&\quad \vdots \\
&T_{n+m} > T_m \xrightarrow{\Delta y_m = y_{n+m} - y_{n+m-1}} T_{n+m} = T_m.
\end{aligned} \tag{9}
$$

Then, the total erosion e at position x along surfaces (I), (II), or (III) is given as:

$$e(x) = \sum_{j=1}^{m} \Delta y_j(x), \qquad j = 1, \ldots m. \tag{10}$$

4.3 Model Applied to Smooth Bore Firings

4.3.1 Surface Heating

Calculation results for the heating of the ram projectile nose are given for acceleration cycles obtained with the RAMAC 30 smooth bore ram accelerator (see Sect. 3) as shown in Fig. 31. The experiments are carried out with fin guided projectiles, see [14].

Figure 31 shows distinctive results obtained with the smooth bore version of RAMAC 30 depicted by firings: no. 139 (aluminum), no. 170 (titanium), no.

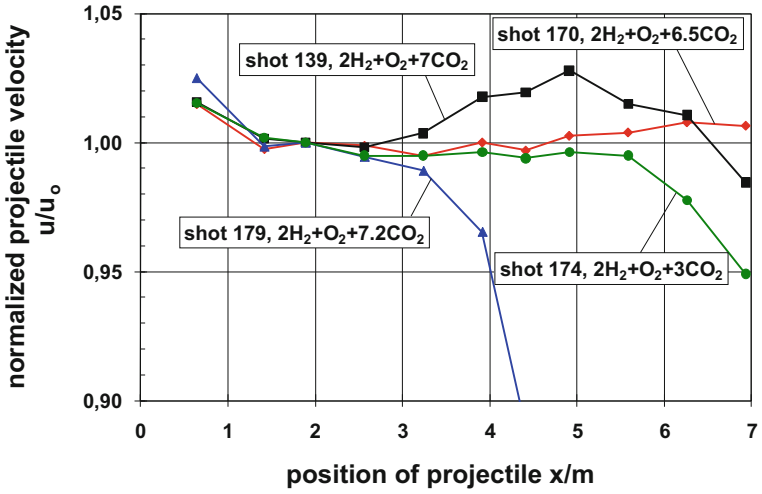

Fig. 31 Experimental velocity distributions from the smooth bore version

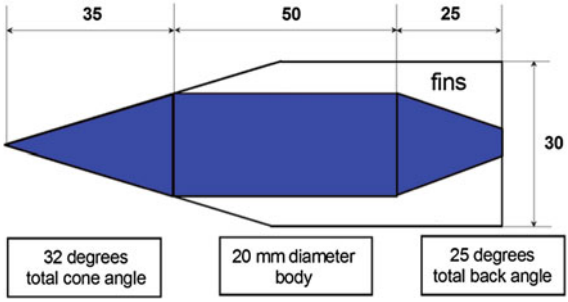

Fig. 32 Geometry of fin stabilized projectile

179 (magnesium) and no. 174 (steel). The fill pressure for each was about 20 bar. The projectiles used for firings no. 139, 170, and 179 had a half cone angle of 16 degrees and a cone length of 37 mm, measured along its surface, see Fig. 32. The constant diameter combustor region was 50 mm long and the divergent rear part surface 26 mm. A photo of the aluminum projectile of shot no. 139 is seen in Fig. 33 left hand side. The steel projectile of shot no. 174 had only three fins and a combustor length of 20 mm, to reduce mass (Fig. 33 right side). In these firings the initial velocity at the beginning of the ram-tube was u_p = 1863 m/s for shot no. 139, 1740 m/s for shot no. 170, 1857 m/s for shot no. 179 and 1726 m/s for shot no. 174.

With the aluminum projectile in firing no. 139, acceleration was achieved along the first 3 m of the total ram-tube length of 5.7 m, see Fig. 31. Then the acceleration turns into deceleration. Looking at shot no. 170 with a titanium projectile, the velocity increases, but very smoothly. In both firings the impact into the piston's steel plates placed in the decelerator tube, was weak. These weak impacts indicate that the projectiles have been damaged inside of the ram-tube with a huge mass loss during the ram accelerator cycle. With the projectile made of magnesium (no. 179), the projectile velocity drops immediately after entering the ram-tube, i.e., with a combustion unstart and no impact on the steel plates. From this observation we can deduce that the magnesium projectile melted and burned up completely as a result of its contact with the hot gases present in the combustion region (II). Good results regarding erosion resistance have been gathered with projectiles of steel (35 NCD

Fig. 33 Firing no. 139 (*left*) with aluminum, firing no. 174 (*right*) with steel

16). The projectile fired with shot no. 174 endured undamaged the ram cycle and made a massive impact on the steel plates.

X-ray pictures taken at the muzzle of the ram-tube support these outcomes, see [14]. The projectile fired in shot no. 139 (aluminum) lost its fins and erosion could be observed on the midbody. A similar result is present for no. 170 (titanium), i.e., the fins are burned up and cannot be recognized on the X-ray image (Fig. 21). The midbody erosion here is much smaller compared with that in shot no. 139 using aluminum as projectile material. The complete burning of the magnesium projectile in shot no. 179 is coupled with a strong unstart phenomenon and here no X-ray picture is available. For shot no. 174 (steel) the projectile is seen in good shape in the X-ray photograph, i.e., no melting and burning occurred.

To get an insight into the heating behavior of the four materials used (magnesium, aluminum, titanium and steel), a typical ram cycle was theoretically modeled with a constant projectile velocity of u_p = 1800 m/s along the whole ram-tube. The heat transfer calculations were done for a 20 bar fill pressure and the combustible gas mixture: $2H_2 + O_2 + 7CO_2$. This model firing represents quite well the real velocity distribution of most firings in smooth bore RAMAC 30. The data for the four projectile materials tested are sequentially listed hereunder for the density ρ (kg/m^3)/ the specific heat c_p (J/kg K)/the heat conduction λ (J/m s K)/the melting temperature T_m (K)/the melting heat h_m (J/kg) as: (1) magnesium: 1800/1046/96/923/2.13E5, (2) aluminum alloy (AlMgCu1): 2790/920/134/873/3.56E5, (3) titanium: 4540/471/16/1941/3.24E5 and (4) steel (35 NCD 16): 7830/460/38/1823/2.72E5.

The surface temperature calculated with procedure (6) as a function of flight time is given in Fig. 34 for the cone region (I). The cone surface temperature stays for x = 20 mm below melting temperature T_m during the whole modeled ram cycle beginning at t = 0 and ending at t = 2.75 ms.

The shape of the surface temperature distribution along the x-coordinate of the cone surface (I) is shown in Fig. 35 for t = 2.75 ms, at about the time point when the projectile passes the end cross-section of the ram–tube. No melting is present with titanium and steel projectiles. Magnesium and aluminum projectiles begin melting near the tip of the nose in the region where x approaches zero.

With the gas mixture $2H_2 + O_2 + 7CO_2$ at 20 bar fill pressure and constant u_p = 1800 m/s the following gas conditions were calculated for the midbody region (II) using the computer code of Smeets [26]: p = 252 bar, T_g = 1672 K,

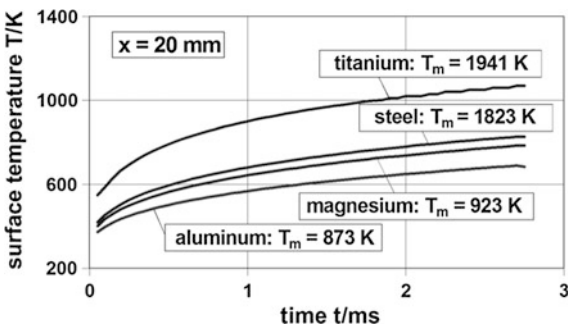

Fig. 34 Forebody (I) surface temperature increase for x = 20 mm for constant u_p = 1800 m/s

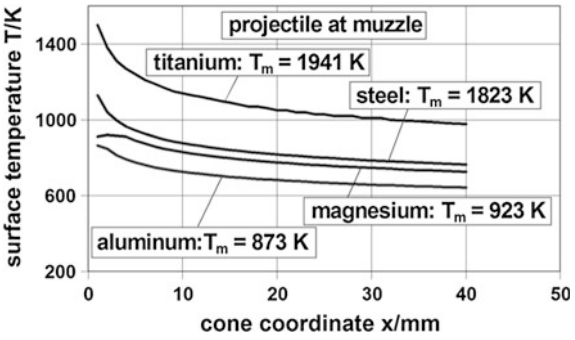

Fig. 35 Surface temperature along the x-coordinate of the cone forebody (I)

ρ = 69.2 kg/m^3, u = 1574 m/s. These flow quantities were taken as boundary conditions in region (II) at the border between the boundary layer and the outside flow. The calculated temperature increase at the midbody surface is shown as a function of time for x = 5 mm (Fig. 36) and 20 mm (Fig. 37) downstream of the inlet to the combustor region (II). Onset of melting is found for x = 5 mm for titanium, aluminum and magnesium. For steel projectiles melting temperature is not reached. Further downstream (x = 20 mm) the surface temperature is lower than at x = 5 mm. Therefore, besides steel, titanium does not melt either during the whole ram firing.

In Fig. 38 the time integrated heat history is shown for the time point t = 2.75 ms when the projectile leaves the ram-tube muzzle with surface temperature as a

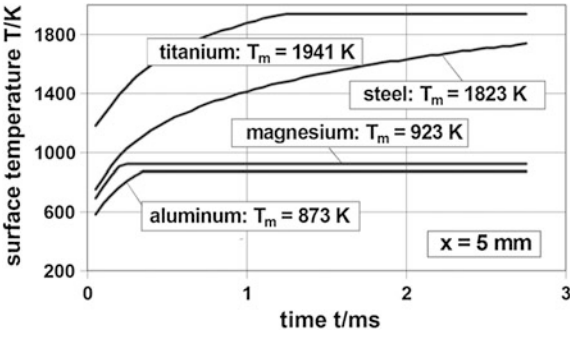

Fig. 36 Midbody (II) surface temperature for x = 5 mm versus projectile cycle

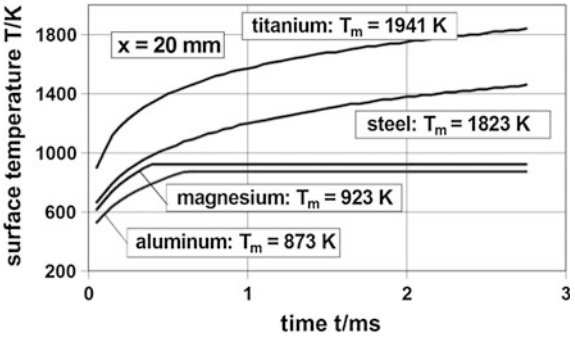

Fig. 37 Midbody (II) surface temperature for x = 20 mm versus projectile cycle

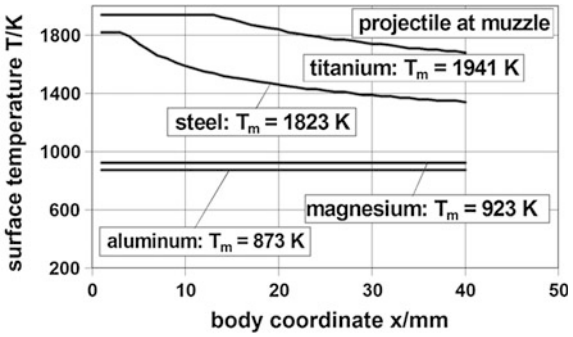

Fig. 38 Surface temperature along the x-coordinate of the midbody (II)

function of the x-coordinate. With magnesium and aluminum projectiles, the surface temperature as a function of the body's x-coordinate exceeds melting temperature. The whole midbody melts. Using titanium projectiles, melting is limited to about one third of the midbody surface.

4.3.2 Surface Ablation

For the four materials used (magnesium, aluminum, titanium and steel), no erosion occurs at the cone surface (I), because during the whole shooting cycle the surface temperature remains below melting temperature (Figs. 34 and 35).

For firings modeled with constant u_p = 1800 m/s along the entire flight inside the ram-tube, Figs. 39 and 40 show for the midbody surface (II) the total erosion e predicted with the sum procedure (10) as a function of time.

In Fig. 39 the calculated body erosion is seen for x = 5 mm behind the entry into the combustor region (II). Magnesium and aluminum show maximum erosion rates of 0.4 mm, resp., 0.2 mm at the time t = 2.75 ms when the projectile leaves the ram-tube. The calculations with titanium give less ablation. With steel as projectile material no surface erosion is present at all. Similar results are shown for x = 20 mm (Fig. 40).

Figure 41 shows the erosion predicted for the midbody surface (II) along the x-coordinate for a flight time t = 2.75 ms when the projectile leaves the muzzle of

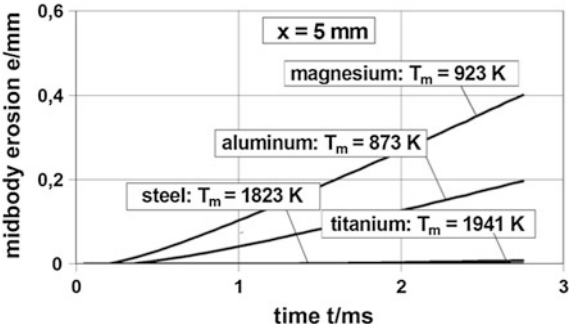

Fig. 39 Erosion at the midbody (II) for x = 5 mm along the projectile cycle

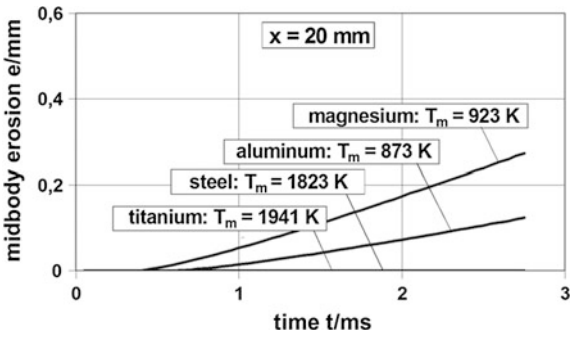

Fig. 40 Erosion at the midbody (II) for x = 20 mm along the projectile cycle

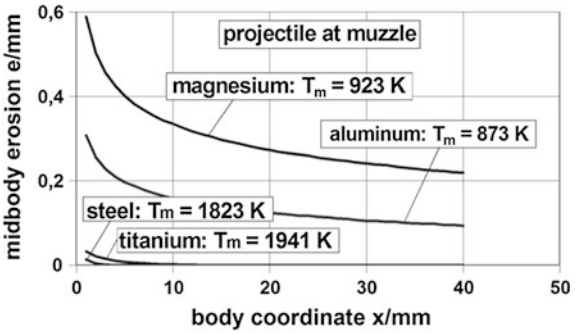

Fig. 41 Erosion along the x-coordinate of the midbody (II) surface

the accelerator tube. Magnesium and aluminum behave very erosive. Good results with just slight erosion at the beginning of the midbody can be obtained using titanium and steel as projectile material. The erosion for these two materials is in the range of less than a tenth of a millimeter.

Similar ablation as for the body (II) is expected at the projectile fins (IIf). Therefore, the results presented in Figs. 38 and 41 for the body region (II) can be extended to the erosion e along the x-coordinate at the fin's surface (IIf). The erosion e at x = 5 mm downstream of the front edge of the fins for the aluminum material is e = 0.2 mm, for a u_p = 1800 m/s at the end of the ram-tube, see Fig. 39.

For titanium material the erosion at the same position is nearly zero. Since melting occurs at both sides of the fins, the erosion e must be doubled to define the minimal thickness required by the guiding fins to endure the shot cycle when erosion is present. The fin thickness of 2.5 mm, e.g., present in experiment no. 139 (aluminum) proved enough to endure the ram-tube acceleration cycle. Notwithstanding this result, firing no. 139 failed and the fins vanished. Melting of surface material by heating seems therefore not to be the only process ablating both the fins and the body of the ram projectile. As discussed above, burning of aluminum (Fig. 31: shot no. 139) and maybe also titanium (Fig. 31: shot no. 170), i.e., reactions between surface material and oxygen, supported by surface melting, may play an important role in the failure reported.

4.4 Summary of Heat Considerations

At the cone (I) of projectiles made of magnesium, aluminum, titanium or steel, no significant deformations are expected, because the surface temperatures do not exceed melting temperature, see Figs. 34 and 35. At the midbody (II) for magnesium, aluminum and titanium projectiles, ablation by melting, due to high gas temperature and high gas pressure produced by combustion, is predicted. With steel almost no ablation is predicted for the velocity range (1800 m/s) and 20 bar fill pressure considered. The ablation at the fins (IIf) is of the same order as at the body (II). The calculated erosion e is smaller than the fin width in the velocity range of 1800 m/s. Notwithstanding, the projectiles lost their fins during ram firing. That means that other erosion mechanisms must additionally be present. It is assumed that chemical reactions between fin material and oxygen as well as the diluent (here CO_2) take place as erosion mechanisms for metals such as magnesium, aluminum and titanium, which easily form oxides (MgO, Al_2O_3, and TiO_2), especially at the high temperatures present in the combustion region. Such chemical reactions may also be present at the midbody surface (II).

To endure the acceleration process coupled with the melting and burning processes in the ram tube, other materials than magnesium, aluminum or titanium should be used for projectiles. Steel seems to be a good choice and possibly also special ceramics. An advantage could be the possibility of coating to protect the ground material against high temperatures and burning reactions. However, RAMAC 30 firings carried out in the smooth bore version with coated projectiles failed as did the firings with non-coated projectiles [14].

5 Conclusions

After the ram accelerator principle was successfully tested in 1986 in a 38-mm-device by Hertzberg et al. [10] at the University of Washington, the decision was taken at ISL to build two ram accelerators: a 30-mm-tube, called RAMAC 30, and a 90-mm-one, the RAMAC 90, see [7]. On the one hand, the RAMAC 90 was designed for accelerating projectiles of more than 1 kg in the subdetonative operation mode to velocities higher than 3 km/s. On the other, the RAMAC 30 concept directed towards basic research, sought to get a detailed insight into the gasdynamic phenomena present in a ram accelerator in superdetonative operation mode.

In the ram accelerator device at the University of Washington a smooth bore and a fin guided projectile were used. There the ram process starts with a subdetonative combustion. In the RAMAC 30, to overcome the gasdynamic problems of subdetonative ignition, the projectiles were directly fired into the superdetonative combustion mode at speeds higher than the Chapman-Jouguet (CJ) speed. The RAMAC

30 is used as a so-called scram accelerator. After having shown the applicability of the rail-equipped accelerator tube concept for ram acceleration in the RAMAC 30, see Seiler et al. [24], the smooth bore technique with a projectile guided by fins fixed at the body of the projectile was also investigated by Patz et al. [14].

The RAMAC 30 design follows in principle the prototype ram accelerator of the University of Washington. A conventional powder gun with a tube length of 1.8 m serves as pre-accelerator to accelerate the projectiles to about 1800 m/s muzzle velocity. The projectile is injected into the RAMAC 30 with superdetonative velocity relative to the Chapman-Jouget (CJ) speed of the combustible gas mixture. Ram tubes with four and five rails for guiding projectiles as well as the smooth bore tubes with fin guided projectiles have been tested. When firing directly into superdetonative mode, combustion takes place in the gap between projectile and tube wall (combustor channel), initiating at the beginning of this channel. "Thermal choking" must be avoided inside the combustor, because this phenomenon is followed by a failure in acceleration and an unstart. Therefore, the heat release must be adapted to the flow conditions, i.e., the flow Mach number ahead of combustion. If the energy input by combustion is properly managed, e.g., at 20 bar filling pressure and 1800 m/s input speed along several ram tube meters, a velocity increase of up to 200 m/s was measured. Despite all the achievements, the problems associated with melting processes and ablation caused by the overheating of the projectile seem currently insurmountable.

Since we achieved better results with aluminum projectiles in the rail tubes, it seems that melting and ablation in these tubes is not as significant as in smooth bores with fin-guided projectiles. This is mainly because in rail tubes melting of the rails is not present. All in all, however, future RAMAC research needs to find materials that can withstand the high heat loads. We are confident that future development of new compounds will again bring ram acceleration research into the spotlight. If one day the material problem was solved, an extrapolation from experiment no. 97 (Fig. 5) to a pipe length of, e.g., 300 m at constant acceleration, would result in a muzzle velocity of about 20 km/s. Summarizing, the ram accelerator is an outstanding acceleration system. Its theory allows to predict the acceleration of projectiles to speeds much higher than 10 km/s, which no other known acceleration system is capable of. Why not start a renaissance sometime?

References

1. Adams M.C.: Recent advances in ablation, ARS J. (1959)
2. Bruckner, A.P., Burnham, E.A., Knowlen, C., Hertzberg, A., Bogdanoff, D.W.: Initiation of combustion in the thermally choked Ram accelerator. In: 18th international symposium on shock waves. Sendai, Japan (1991)
3. Chien, K.-Y.: Hypersonic, turbulent skin-friction and heat-transfer measurements on a sharp-cone. AIAA J. **12**(11) (1974)

4. Gatau, F.: Conduction thermique dans un solide composé de plusieurs couches homogènes. ISL-report (1997)
5. Giraud, M., Legendre, J.F., Simon, G.: Ramac 90: experimental studies and results in 90 mm caliber, length 108 calibers. In: 1st International Workshop on Ram Accelerator, RAMAC I, ISL, France (1993)
6. Giraud, M., Legendre, J.F., Simon, G., Henner, M., Voisin, D.: RAMAC in 90 mm caliber or RAMAC 90: starting process, control of the ignition location and performance in the thermally chocked propulsion mode. In: 2nd International Workshop on Ram Accelerator, RAMAC II, University of Washington, Seattle, Washington, USA (1995)
7. Giraud, M., Legendre, J.F., Henner, M.: RAMAC in subdetonative propulsion mode—State of the ISL studies. In: 3rd International Workshop on Ram Accelerator, RAMAC III, Tohoku University, Sendai, Japan (1997)
8. Heiser, R., Seiler, F., Zimmermann, K.: Experimental and theoretical investigation of heat transfer in a gun barrel. In: 13th International Symposium on Ballistics, Stockholm (1992)
9. Hertzberg, A.: Thermodynamics of the Ram accelerator. In: 17th International Symposium on Shock Waves and Shock Tubes. Bethlehem, Pennsylvania, USA (1989)
10. Hertzberg, A., Bruckner, A.P., Bogdanoff, D.W.: The ram accelerator: a new chemical method of achieving ultra-high velocities. 37th ARA-meeting. Québec, Canada (1986)
11. Hertzberg, A., Bruckner, A.P., Knowlen, C.: Experimental investigation of Ram accelerator propulsion modes. In: 18th international symposium on shock waves, Sendai, Japan (1991)
12. Knowlen, C., Burnham, E.A., Kull, A.E., Bruckner, A.P., Hertzberg, A.: Ram accelerator performance in the transdetonative velocity regime. 41st ARA-meeting. San Diego, USA (1990)
13. Naumann, K.W.: Heating and ablation of projectiles during acceleration in a ram accelerator tube, AIAA/SAE/ASME/ASEE. In: 29th Joint Propulsion Conference and Exhibit, Monterey, CA, USA (1993)
14. Patz, G., Seiler, F., Smeets, G., Srulijes, J. : The behavior of fin-guided projectiles superdetonative accelerated in ISL's RAMAC 30. In: 3rd International Workshop on Ram Accelerator, RAMAC III, Tohoku University, Sendai, Japan (1997)
15. Patz, G., Seiler, F., Smeets, G., Srulijes, J.: Status of ISL's RAMAC 30 with fin guided projectiles accelerated in a smooth bore. In: 2nd International Workshop on Ram Accelerator, RAMAC II, University of Washington, Seattle, Washington, USA (1995)
16. Seiler, F.: Heating and ablation of a sharp-nosed body flying at hypersonic velocity through a tube filled with highly compressed gas mixture. In: IUTAM Symposium on Aerothermochemistry and Associated Hypersonic Flows, Marseille, France (1992)
17. Seiler, F., Mathieu, G.: Boundary layer model for calculating the heat transfer into a ram projectile fired in a ram accelerator. In: 2nd International Workshop on Ram Accelerator, RAMAC II, University of Washington, Seattle, Washington, USA (1995)
18. Seiler, F., Naumann, K.W.: Bow shock wave heating and ablation of a sharp-nosed projectile flying at supersonic velocity inside of a ram accelerator. In: 19th International Symposium on Shock Waves, Marseille, France (1993)
19. Seiler, F., Patz, G., Smeets, G., Srulijes, J.: Status of ISL's RAMAC 30 with rail stabilized projectiles. In: 1st International Workshop on Ram Accelerator, RAMAC I, ISL, France (1993)
20. Seiler, F., Patz, G., Smeets, G., Srulijes, J.: The rail tube in ram acceleration: feasibility study with ISL's RAMAC 30. In: 2nd International Workshop on Ram Accelerator, RAMAC II, University of Washington, Seattle, Washington, USA, (1995)
21. Seiler, F., Patz, G., Smeets, G., Srulijes, J.: Gasdynamic limits of ignition and combustion of a gas mixture in ISL's RAMAC 30 scram accelerator. In: 20th International Symposium on Shock Waves. California Institute of Technology, Pasadena, California, USA (1995)

22. Seiler, F., Gatau, F., Mathieu, G.: Prediction of surface heating of a projectile flying in RAMAC 30 of ISL. In: 3rd International Workshop on Ram Accelerator, RAMAC III, Tohoku University, Sendai, Japan (1997)
23. Seiler, F., Patz, G., Smeets, G., Srulijes, J.: Presentation of the rail tube version II of ISL's RAMAC 30. In: Third International Workshop on Ram Accelerator, RAMAC III, Tohoku University, Sendai, Japan (1997)
24. Seiler, F., Patz, G., Smeets, G., Srulijes, J.: Progress of ram acceleration with ISL's RAMAC 30. Journal de Physique. Proceedings RAMAC IV, vol. 10 (1999)
25. Smeets, G.: Ram-Nachbeschleuniger für aus konventionellen Kanonen verschossene Vollkaliber-Projectile. ISL-Report N 603/88 (1988)
26. Smeets, G., Gatau, F., Srulijes, J.: Rechenprogramm für Abschätzungen zur Ram-Rohrbeschleunigung. ISL-Report RT 507/92 (1992)
27. Zierep, J.: Strömungen mit Energiezufuhr. G. Braun Verlag, Karlsruhe, Germany (1990)

Author Biographies

Friedrich Seiler received his "Dipl.-Phys." degree and his "Dr.-Ing." degree from the University of Karlsruhe, Germany, now Karlsruhe Institute of Technology (KIT). His doctoral study dealt with the experimental investigation of the structure of a shock wave traveling along a wall, carried out in a low pressure shock tube, and compared with theoretical calculations, using the direct simulation Monte-Carlo method DSMC. From the year 1980 on, he worked at the French-German Research Institute of Saint-Louis (ISL), France, with shock tubes in the field of gasdynamics, hypersonics and measuring techniques. Additionally, he did a basic research in the field of ram acceleration. At the ISL he became in 1997 head of the Aerothermodynamics & Shock Tube Laboratory until his retirement in the year 2011. Since his "Habilitation" in 1992 and the upgrade to be "Professor for Fluid Mechanics" at the University of Karlsruhe, his student courses are dealing with the aerothermodynamic behavior of gases and with optical measuring techniques. Associated at KIT as "Lecturing Professor", he is in the editorial board of the "International Journal of Shock Waves" and member of the advisory committees of the "International Symposium on Shock Waves (ISSW)", the "International Shock Interaction Symposium (ISIS)" and the "International Symposium on Flow Visualization (ISFV)".

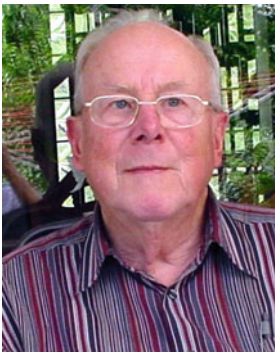

Günter Smeets born in 1935, got his doctoral degree of science in 1964 from the University of Freiburg/Breisgau. As one of the leading scientists within the French-German Research Institute in Saint-Louis (France) he has been working on fluid dynamics and gas dynamics. He developed numerous optical diagnostic techniques for shock tube research. In 1986 he was honored by the "Médaille de Aérodynamique en or" sponsored by the French Governement. Inspired by Abe Hertzberg from the University of Washington in Seattle, Ram Acceleration became one of the major research areas during the last decade before his retirement.

Gunther Patz has finished his education in aviation and spacecraft engineering at the Technical University of Stuttgart as Dipl.-Ing. After an activity of 2 years in the aircraft industry he joined the French-German-Research Institut of Saint-Louis in 1966. He received his Ph.D. degree as Dr.-Ing. at the Technical University of Karlsruhe at 1976 for the research of shock interaction with solid structures. Further activities have been the development of the hypersonic shock tube, research in hypersonic flow interaction and the development of a launcher for hypervelocity projectiles (RAMAC). He has been retired in 2002.

Julio Srulijes was born in Argentina in 1947. He received a degree in Mechanical Engineering from the Technological University, Buenos Aires, Argentina in 1972. After several years in the industry, in 1975 he took up Ph.D. work at the Institute of Fluid Mechanics of the University of Karlsruhe, Germany where in 1979 he obtained his Dr.-Ing. degree with his work on cellular convection in containers with horizontal temperature gradients. From 1980 to 1983 Chief Engineer at the Institute for Theoretical Mechanics of the University of Essen, Germany. There he was involved among other in planning a space experiment on thermocapillary migration of bubbles and drops flown successfully in the D-1 Space Shuttle mission. From 1983 to 2012 Scientist at the French-German Research Institute of Saint-Louis ISL, France, where he worked on gasdynamics of high enthalpy flows with and without reactive combustion at the Shock Tube Laboratory. He participated in the development of numerous optical measuring techniques. He retired in September 2012.

Gilbert Mathieu was born on 18.11.1942. In 1960 he graduated from industrial high school and in 1962 he obtained an Electronic Measurement Technician degree. He served in the French Army (Artillery) during the years 1962–1963. In 1964 he joined the French-German Research Institute of Saint-Louis in Saint-Louis, France, as scientific technician. Besides his work, he took postgraduate professional courses at CNAM (Conservatoire des Arts et Métiers). In 1971 he was promoted to Principal Engineer and in 1994 to Chief Engineer. He retired in 2005.

Berthold Sauerwein received his graduate mechanical design engineer (*Dipl. Ing.* (*Fh*)) in 1988 in Friedberg, Germany. At ISL, he was first working as engineer in planning and design of scientific installations for 10 years. After changing to the "Aerothermodynamics & Shock Tube" department of ISL, he was in charge of designing shock-tunnel models, of planning shock-tunnel operation and of the manufacturing and calibration of heat-flux probes used in shock-tunnel measurements. He mainly carries out shock-tunnel experiments with pressure and heat-flux measurements. Since 2008 he is responsible for operating the shock-tunnel facilities of ISL.

Jean-Luc Striby received his Baccalaureate in Mathematics and Technology certificate from the Lycée Mermoz in St. Louis, France in 1985. In 1988 he obtained his "diplôme universitaire de technologie" in mechanical engineering and industrial automation from the University of Haute Alsace in Mulhouse, France. In 1990 he joined the French-German Research Institute of Saint-Louis (ISL), France and has become Senior Technician there. His current work includes the study and instrumentation of aerodynamic models, the set-up of measurement chains and the measurement of pressures and heat fluxes in shock tubes and shock tunnels.

RAMAC in Subdetonative Propulsion Mode with Fin-Guided Projectile: Design, Modeling, Performance and Scale Effect

Marc Giraud and Pascal Bauer

1 Introduction

The successful development of the ram accelerator technology (RAMAC in short), an aero-thermo-chemical hypervelocity launcher, requires an adequate combination between aerodynamics, thermochemistry and technical conditions (see Fig. 1).

In the present contribution, two RAMAC demonstrators equipped with smooth bore only (in small caliber—30 mm, and in large caliber—90 mm) are essentially taken into consideration in the Sub-detonative propulsion mode.

Fundamental research together with a variety of experimental research works including analysis, calculations, modeling and simulation were conducted at the French-German Research Institute of Saint-Louis (ISL) within a strong collaboration with the Laboratory of Combustion and Detonation (LCD). Moreover, the research at ISL and LCD was also very much connected to that conducted throughout the world, as, for instance at the University of Washington, Seattle, USA [1], creator of the 1st RAMAC demonstrator, and at the Shock Wave Research Center, Sendai, Japan [2].

Based on the very many Ballistics and Aerodynamics applications aimed at reaching higher velocities in smooth conditions of acceleration, innovation in launching techniques were the key words of the hereabove mentioned collaboration.

M. Giraud
ISL and Exobal Consulting Office, 15 Rue de La Roselière, 68300 Saint-Louis, France

M. Giraud
ISL: French-German Research Institute of Saint-Louis, 5 Rue du Général Cassagnou, 68300 Saint-Louis, France

P. Bauer (✉)
PPRIME (LCD): Laboratoire de Combustion et de Détonique, ISAé-ENSMA, Rue Clément Ader, 86960 Poitiers, France
e-mail: pascal.bauer@ensma.fr

F. Seiler and O. Igra (eds.), *Hypervelocity Launchers*,
Shock Wave Science and Technology Reference Library 10,
DOI 10.1007/978-3-319-26018-1_6

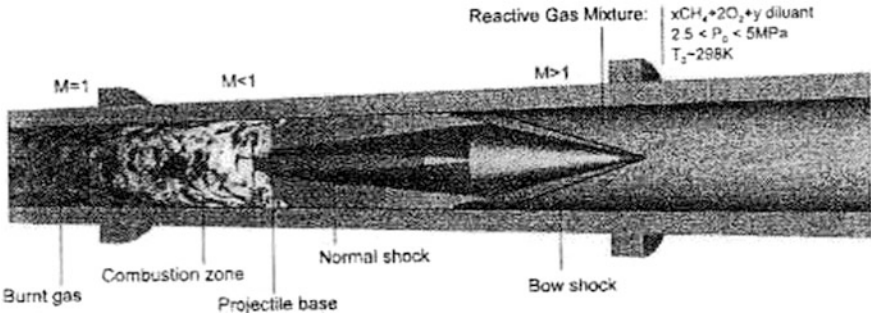

Fig. 1 Sketch of a typical ram accelerator (RAMAC) device

The basic feasibility of the RAMAC and its higher ability to accelerate a projectile than any conventional gun has been clearly demonstrated in several laboratories around the world and in different experimental conditions [1, 3–17]. This capability comes from the constant high pressure thrust at the rear of the projectile (see sketch of Fig. 2), contrary to the pressure distribution in a conventional powder gun barrel.

In the present investigation, the following points were addressed:

1. Appropriate design of the pre-accelerator: the projectile was equipped with a sabot and launched at a low supersonic velocity into the RAMAC using a classical powder gun. An efficient venting section was inserted in order to avoid any unstart in the 1st Ram bore filled with a reactive mixture.
2. Influence of the RAMAC smooth bore: two different calibers and several lengths were tested.
3. Nature of the reactive mixture: the compatibility with a Sub-detonative Propulsion Mode requires a careful adjustment of composition, initial pressure, and composition of the specific mixture in each of the stages.

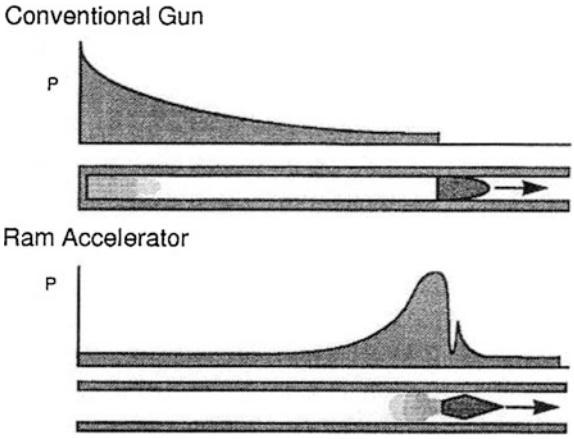

Fig. 2 Comparison of the pressure distribution between a ram accelerator and a conventional gun

4. Geometrical configuration of the projectile: profile, material, use of fins for its guiding in the tube and stabilization during the following free flight, if any. The geometry of the fins is a separate issue.
5. Initial velocity upon entering in the tube, i.e., at a Mach number slightly higher than 3.

In others words, the scale effect has been a major concern within the studies conducted at ISL. For this reason two different test facilities were developed, each of them including an appropriate methodology and a series of experimental diagnostics together with an "a priori" investigation of the reactive mixtures in terms of detonable areas and numerical analysis, using a new CFD code. This research has been conducted over a decade starting in the early 90's.

The present review clarifies the above-mentioned points by showing the main experimental results which are now available. The performance of the two smooth bore facilities with two different calibers and the corresponding scale effect are discussed.

2 Experimental Setup and Launch Tube Configuration

The general sketch including the geometrical characteristics of the tubes is shown on Fig. 3, together with the data acquisition system and related experimental equipment (Fig. 4). Moreover photos of the RAMAC 90 are presented, showing more specifically the pre-accelerator (Fig. 5) and the sequence of stages (Fig. 6).

3 Initial Investigation of the Main Elements of the RAMAC Process

3.1 Configuration and Design of the Projectile

The facilities in use at ISL included a 30 mm and a 90 mm diameter tubes, respectively named RAMAC 30 and RAMAC 90, see [15, 16, 18–32].

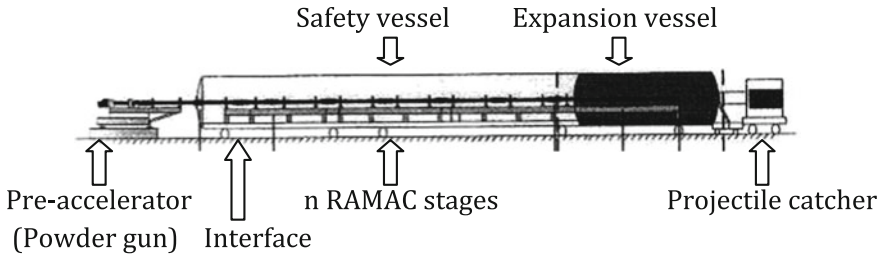

Fig. 3 Sketch of the 2 RAMAC facilities: RAMAC 30 with 2 stages: total length L = 18 m or 600 calibers RAMAC 90 with 3 stages: total length L = 46 m or 511 calibers

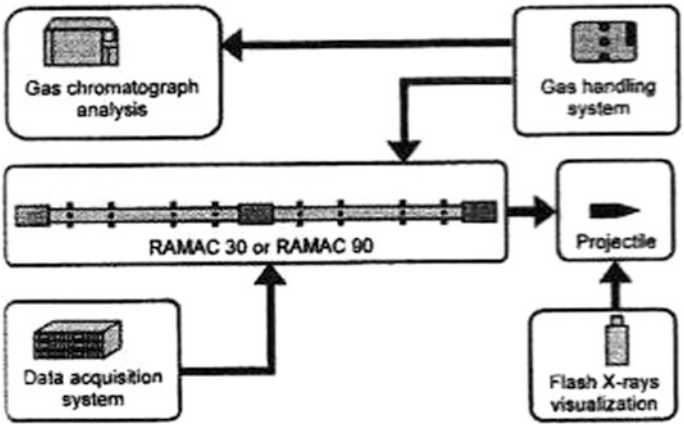

Fig. 4 Data acquisition system and equipments

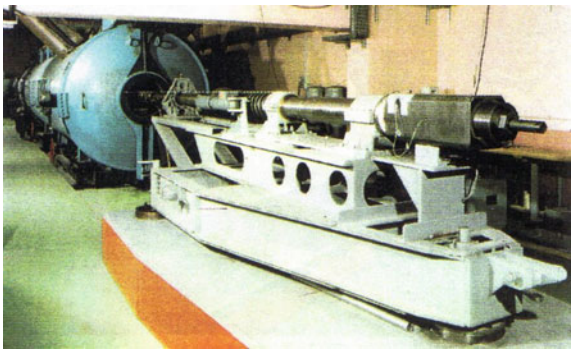

Fig. 5 RAMAC 90—photo of the pre-accelerator/powder gun

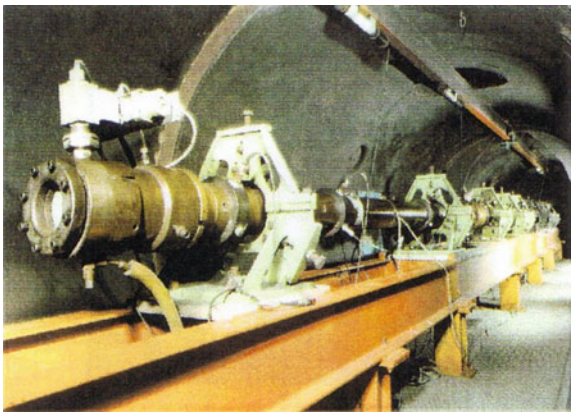

Fig. 6 RAMAC 90—photo of the sequence of 3 stages confined in a large expansion vessel (for safety concern)

The projectile was equipped with fins placed on its rear part. The fins (3, 4 or 5 fins) necessary for its guidance in the tubes were investigated. As an example, Fig. 7 shows a 4-fin-projectile used in smooth bores regardless the caliber, 30 and 90 mm.

The configuration of the projectile equipped with fins used in RAMAC 30 and RAMAC 90 is shown in Fig. 8. The projectile is composed of two main parts: the forebody, which is a cone with a length of 1.7 calibers and an angle of 25° and the afterbody which includes the fins with a length of 2.7 calibers. The material of this afterbody was aluminum and magnesium alloy. The overall diameter, including the fins was of a one-caliber size, i.e. 90 mm. This entire geometrical configuration was primarily optimized and patented [25, 33, 34].

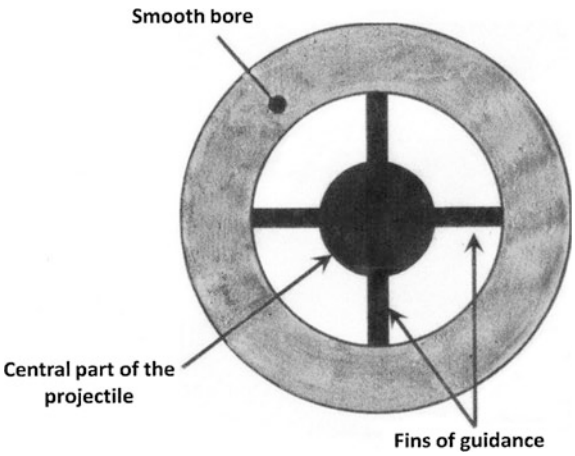

Fig. 7 4-fin guided projectile

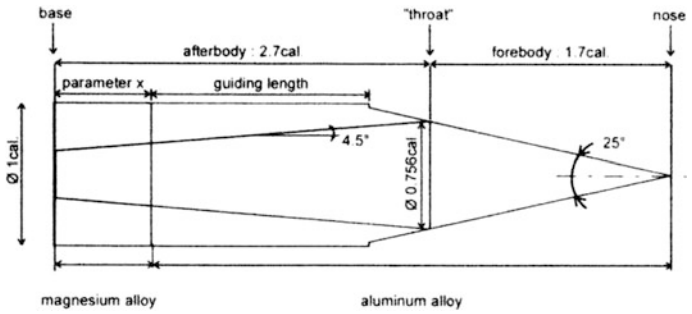

Fig. 8 Standard RAMAC projectile with semi-combustible afterbody of length x

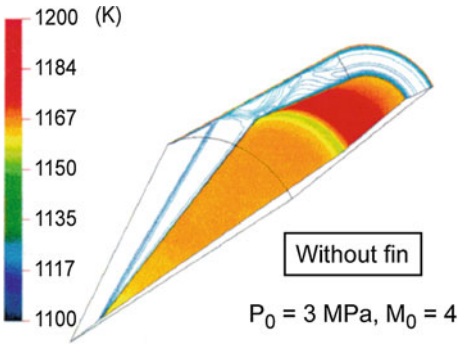

Fig. 9 Temperature distribution

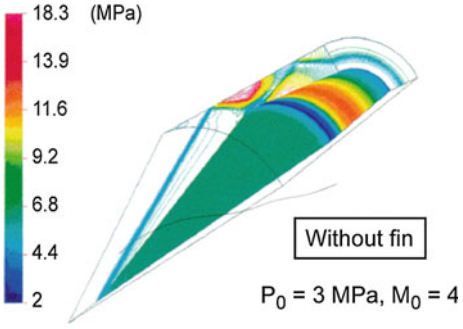

Fig. 10 Pressure distribution

3.2 Specific Investigation Related to the Fins

In order to show the influence of the geometry of the fins on the RAMAC performance a numerical simulation of the flow characteristics around the projectile with and without fins was undertaken [35–37]. Moreover, a better knowledge of the gas dynamics of the flow was expected in order to improve the ram accelerator operations by reducing the risk of unstart. A series of calculations were conducted using the 3D numerical code TascFlow^{TM} from ASC (Advanced Scientific Computing, Waterloo, Ontario, Canada), now ANSYS CFX (ANSYS, Cannsburg, Pennsylvania, USA), without fins (Figs. 9 and 10) and with fins (Fig. 11). Different types of fins, i.e., various shapes and number, were studied. The characteristics of the flow in terms of temperature, pressure and Mach number distributions were studied [38]. The data show a drastic role of the fin geometry on the maximum temperature of the flow. Moreover, the elevated value of the stagnation temperature at the leading edge of the fins, namely up to 1600 K at Mach number 5, may explain the combustion that locally takes place and eventually leads to an unstart. This phenomenon is the disgorging of a normal shock past the projectile throat, often resulting in an overdriven detonation wave, which rapidly decelerates the projectile. This process, which is a major obstacle to ram accelerator performance, has been addressed in other studies including numerical and experimental ones [18, 21, 22, 35, 39].

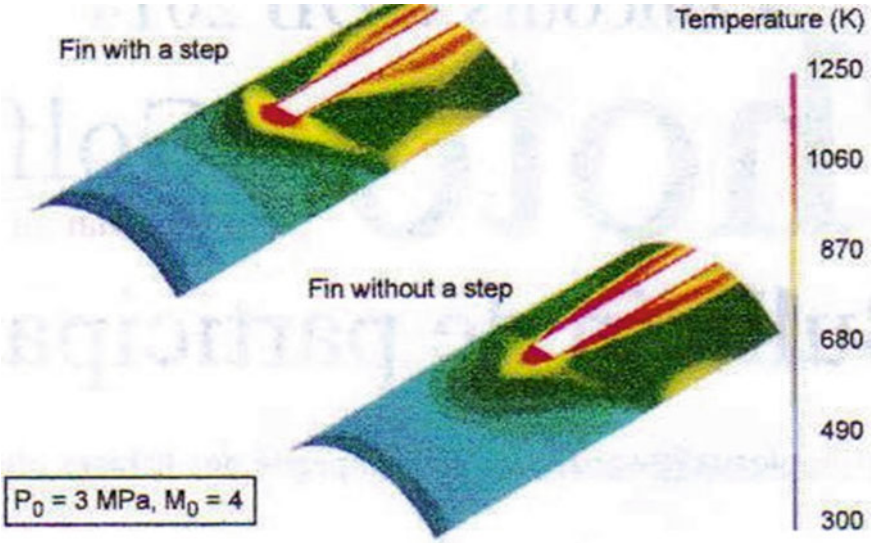

Fig. 11 Temperature distribution derived from the shock at the nose of the fin

In order to achieve the appropriate pressure and temperature conditions at the projectile base, the sabot design plays an important role in the initiation process of the mixture. Furthermore, the separation between the sabot and the projectile at the ignition time must be independent of the tube caliber. Depending on the reactive mixture (amount of heat release), this is a function of the initiation length and flame speed. Consequently, given similar initial conditions of projectile, design of the sabot and reactive mixture, the geometric scale is not rigorously respected in terms of mass ratio.

Although the geometrical configuration of the projectile of RAMAC 90 has been chosen once and for all following and optimization procedure, the main advantage of a fin-guided projectile is the flexibility of its 3D design and shape. Yet, some side effect related to the high degree of erosion of the fins was observed, as depicted in Fig. 12 showing X-ray records of the projectile exiting the tube [15, 38] .

This projectile erosion resulting principally from the fins ablation (both all over their length and at their leading edge) depends on the following parameters: the fin

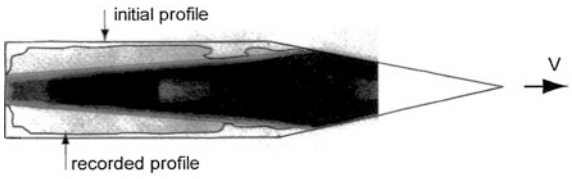

Fig. 12 Record of the projectile shape through X-ray photography

material, the RAMAC combustion duration, which is three times less in RAMAC 30 than in RAMAC 90, the fin geometry and dimensions and finally the projectile velocity. The X-Ray pictures [37] shown respectively in the 30 mm caliber (Fig. 13) and in the 90 mm caliber (Fig. 14) constitute an appropriate demonstration of the influence of these different factors.

To further enhance RAMAC performance, a most pertinent solution will be to protect the leading edge of the fins, in order to change the aerodynamic conditions in the diffuser, and to insure the necessary guiding length of the projectile. Several options have been proposed by Bogdanoff [40] and Veyssière [41].

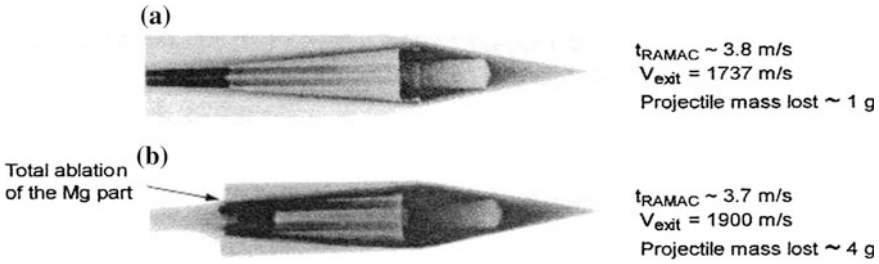

Fig. 13 Experiments in RAMAC 30L200 (1stage) thickness of the fins = 3 mm

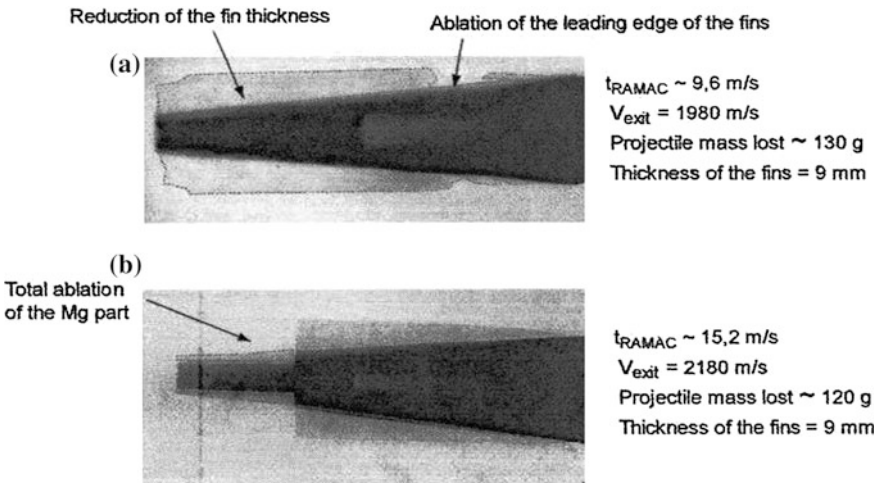

Fig. 14 Experiments in RAMAC 90: **a** tube 90L200 (1 ram stage), **b** tube 90L300 (3 ram stages)

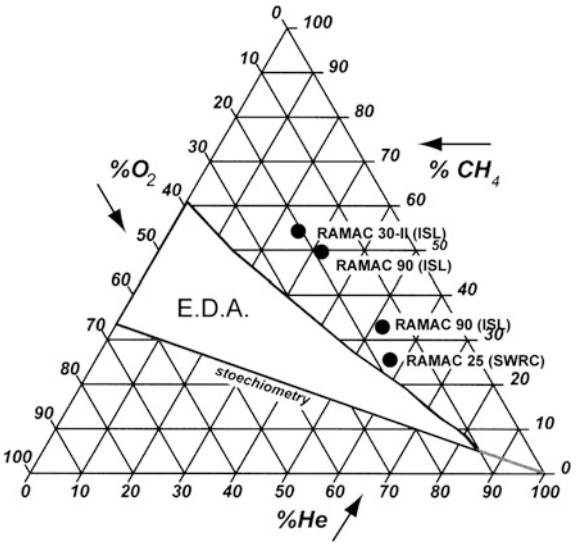

Fig. 15 CH_4–O_2–H_e mixtures (T_0 = 298 K, p_0 = 3.5 MPa, E.D.A. for Experimental Detonable Area)

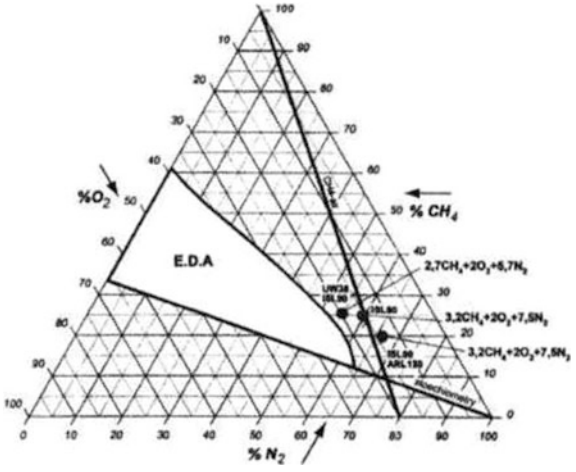

Fig. 16 CH_4–O_2–N_2 mixtures (T_0 = 298 K, p_0 = 2.5 MPa, E.D.A. for Experimental Detonable Area)

3.3 Selection of the Reactive Mixtures

The choice of the reactive mixture is a key parameter for the performance of the ram accelerator. The detonability of the mixture is one of the main characteristics that should be investigated because of the role played by the heat release in this process, as shown in others chapters. For this purpose, an important basic research has been conducted in 90 mm tubes by Legendre [42] in order to yield the best composition

of the reactants for a Sub-detonative propulsion mode. This studies included detonations experiments conducted in a 1.35 m long tube (15 calibers long) denoted 90L15 and a 3.15 m long tube (35 calibers long) denoted 90L35 [23, 26, 42–58]. The results are shown in Figs. 14 and 15 together with the composition of mixtures used at other facilities [1, 8, 17] (Fig. 16).

4 Some Significant Experimental RAMAC Results Obtained at ISL

Some typical experimental data collected in the RAMAC 90 [9, 12, 14, 24, 57, 59–61], i.e. in smooth tubes and in Sub-detonative Propulsion Mode, were obtained in a three stage configuration with a 1.608 kg projectile having a semi-combustible afterbody. The magnesium part (afterbody, as shown in Fig. 8) was 0.8 calibers long. The data, precise geometrical distribution of the stages, and mixture compositions are depicted in Fig. 17.

All along the RAMAC bore, the Mach number is maintained almost at the same level in order to obtain a better ballistic efficiency with the conservation of the organization sketch of the shock waves (efficiency of the diffuser). Moreover, in order to have some assessment on the scale effect, a series of experimental data corresponding to the two different bore diameters available at ISL are presented in Table 1.

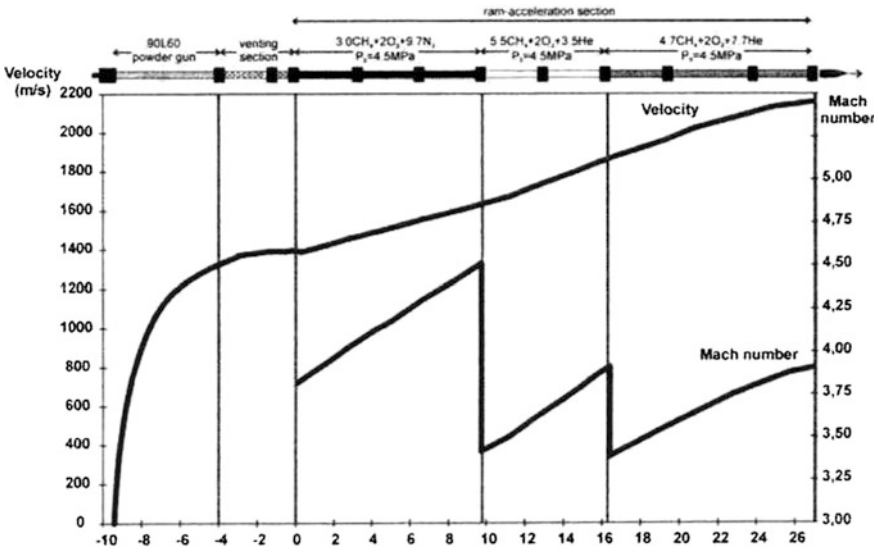

Fig. 17 Velocity of the projectile as a function of its axial position (m), entering at point 0 in the first stage of RAMAC 90 (3 stages filled with a reactive mixture, using a semi-combustible afterbody)

Table 1 Some data on respective performance of both facilities

RAMAC bore		
Caliber (mm)	30	90
Smooth RAMAC bore length (m)	30L300	90L300
	9	27
Total length (including the pre-accelerator) (m /cal)	14/475	37/410
Propulsion mode	Sub-detonative	Sub-detonative
Number of gaseous stages	2	3
Projectile		
Type	4 guiding fins	4 guiding fins
"Throat" area S/S_0 (%)	57.2	57.2
Length	4.4 cal, 132 mm	4.4 cal, 396 mm
Afterbody composition	Semi-combustible	Semi-combustible
Length x = 0.8 caliber	Al, Mg	Al, Mg
Initial mass (g)	69	1608
Entrance ram velocity (m/s)	1380	1360
Entrance ram mach number	3.8	3.75
Fusion temperature Al (K)	660	660
Fusion temperature Mg (K)	650	650
Premixed reactive mixture		
Composition (last stage)	5.0 CH_4 + 2O_2 + 2.2 He	4.7 CH_4 + 2 O_2 + 7.7 He
Initial pressure p_0 (MPa)	4.9	4.5
Detonation velocity (m/s)	2153	2287
Sound velocity (m/s)	452	552
Combustion zone		
Pressure P/Po	10 up to 20	10 up to 20
Temperature (K)	550 up to 850	550 up to 850
Duration of combustion (ms)	≈4.7	≈15
Lost of material (g)	≈4 (evaluated)	≈120 (evaluated)
RAMAC performance		
Exit velocity (m/s)	2380	2180
Increasing velocity factor	72 %	60 %
Acceleration (m/s/s)/gees)	209200/21325	55000/5600
Mach number@RAMAC bore exit	5.3	4
Mach number of projectile in free flight	7	6.4
Residual mass in free flight (g)	≈65	≈1488

5 Conclusion

The experiments that have been conducted at ISL using a RAMAC in Sub-detonative Propulsion Mode with a fin-guided projectile in two caliber size (ratio 3) are part of a worldwide contribution in this field. At least, they have clearly highlighted the important capability of accelerating a projectile compared to that obtained with a classical gun under almost the same launching conditions (caliber, accelerated mass and exit velocity).

The scientific objectives were primarily to provide a better understanding of the whole RAMAC phenomena, together with data that could be used for validation of ongoing modeling and simulations [15, 35, 36, 62, 63]. This goal has been partly reached, since the results obtained from the two facilities were used by number of researchers around the world.

Furthermore, the present research activities, and more specifically those concerning the different aspects of the scaling phenomena, provided additional information [15, 24, 59]. This can be regarded as a major issue in the RAMAC technology and consequently turn out to be useful milestones for these ballistics applications.

More research and experiments are still required. Yes the present one will still remain crucial in the databank for the ram accelerator development.

References

1. Hertzberg, A., Bruckner, AP., Bogdanoff, D.W.: A new chemical method of achieving ultrahigh velocities. In: Proceedings of 37th Meeting of the Aeroballistic Range Association (ARA), Québec, Canada (1986)
2. Sasoh, A., Hirakata, S., Maemura, J., Hamate, Y., Takayama, K.: Thermally choked operation in a 25-mm-bore ram accelerator. In: Takayama, K., Sasoh, A. (eds.) Proceedings of 3rd International RAMAC Workshop, pp. 111–118. Sendai SWRC-Japan (1997)
3. Bruckner, A.P., Bodganoff, D.W., Knowlen, C., Hertzberg, A.: Investigation of gasdynamic phenomena associated with the Ram accelerator concept, AIAA paper 87-1327 (1987)
4. Bruckner, A.P., Hertzberg, A., Kull, AE., Burnham, E.A., Knowlen, C., Yungster, S.: High velocity modes of the Ram accelerator. In: Proceedings of 40 Meeting of the Aeroballistic Range Association (ARA), Paris, France (1989)
5. Bruckner, A.P., Knowlen, C., Hertzberg, A., Bogdanoff, D.W.: Operational characteristics of the thermally choked ram accelerator. J. Prop Power **7**, 828–836 (1991)
6. Bruckner, A.P., Burnham, E.A., Knowlen, C., Hertzberg, A., Bogdanoff, D.W.: Initiation of combustion in the thermally choked Ram accelerator. In: Takayama, K (ed.), Ed Shock Waves, Springer, Heidelberg, pp. 623–630 (1992)
7. Bruckner, A.P.: The Ram accelerator, a technology overview. AIAA Survey paper, 2002-1014
8. Bruckner, A.P., Hinkey, J.B., Burnham, E.A., Knowlen, C.: Investigation of 3-D reacting Flow phenomena in a 38 mm Ram accelerator. In: Giraud, M., Smeets, G. (eds.) Proceedings of the 1st International Workshop on Ram Accelerators, Saint-Louis, France (1993)
9. Giraud, M., Legendre, JF., Simon, G.: RAM accelerator in 90 mm Caliber or RAMAC 90. Experimental results concerning the trans-detonative combustion mode. In: Proceedings of 14th International Symposium on Ballistics, Québec, Canada (1993)

10. Giraud, M., Legendre, JF., Simon, G.: RAMAC 90, experimental studies and results in 90 mm caliber, length 108 calibers. In: Giraud, M., Smeets, G. (eds.) Proceedings of the 1st International Workshop on Ram Accelerator, Saint-Louis, France (1993)
11. Giraud, M., Legendre, JF., Simon, G., Henner, M., Voisin, D.: RAMAC in 90 mm caliber or RAMAC 90. Starting process, control of the ignition location and performances in the thermally choked propulsion mode. In: Bruckner, A.P., Knowlen, C. (eds.) Proceedings of the 1st International Workshop on Ram Accelerators, Seattle, WA, USA (1995)
12. Giraud, M., Legendre, JF., Henner, M.: RAMAC in sub-detonative propulsion mode. State of ISL studies. In: Takayama, K., Sasoh, A. (eds.) Proceedings of the 3rd International Workshop on Ram Accelerators, pp. 65–78. Sendai, Japan, SWRC (1997)
13. Giraud, M., Legendre, J.F., Henner, M.: RAMAC in sub-detonative propulsion mode. In: Proceedings of 17th International Symposium on Ballistics, Midrand, South Africa (1998)
14. Giraud, M., Bruckner, A.P., Takayama, K., Bauer, P., Knowlen, C., Hamate, Y.: What about the Ram accelerator? History, principles, performances and applications. In: Proceedings of 55th ARA meeting in Freiburg, FRG (2004)
15. Henner, M.: Contribution à l'étude des Effets d'Echelle dans les Accélérateurs à Effet Stato en Mode de Combustion Sous-détonatif. Ph.D Dissertation, University of Poitiers, France (1998)
16. Hertzberg, A., Bruckner, A.P., Bogdanoff, D.W.: Ram accelerator, a new chemical method for accelerating projectiles to ultrahigh velocities. AIAA J **26**, 195–203 (1988)
17. Kruczynski, D.: Experiments in a 120-mm Ram accelerator. In: Murphy, M.J., Backofen, M.J. E. (eds.) Proceedings of the 14th International Symposium on Ballistics, Québec, Canada, p. 173 (1993). ISBN 0-9618156-9-8
18. Bauer, P., Henner, M., Legendre, J.F., Giraud, M.: Diameter effect in the initiation process of combustion in a ram accelerator in sub-detonative mode. Eur. Phys. J. Appl. Phys. **19**, 185–194 (2002)
19. Catoire, L., Dupre, G., Paillard, C., Giraud, M., Lecouvreur, P.: Study of the explosion hazard in the unburnt gas of the RAMAC 90. In: Giraud, M., Smeets, G. (eds.) Proceedings of 1st International RAMAC Workshop, on RAM Accelerators, Saint-Louis, France (1993)
20. Giraud, M., Legendre, J.F., Simon, G.: RAM accelerator at ISL. First experiments in 90 mm caliber. In: 42nd ARA meeting, Adelaide, Australia (1991)
21. Giraud, M., Legendre, J.F., Simon, G.: Ram accelerator studies in 90 mm caliber. In: 43rd ARA Meeting, Colombus OH, USA (1992)
22. Giraud, M., Legendre, J.F., Simon, G., Mangold, J.P., Simon, H.: RAMAC 90, facility and diagnostic methods. In: 44th ARA Meeting, Munich, FRG (1993)
23. Giraud, M., Catoire, L.: Secondary effects in a RAMAC firing. In: Proceedings of 1st International Meeting on Properties of Reactive Fluids and their Application to Propulsion, University of Poitiers, France (1993)
24. Giraud, M,: RAMAC, 1st Results concerning the Scale Effect in the Thermally Choked Propulsion Mode. In: Proceedings of 1st International Meeting on Properties of Reactive Fluids, University of Poitiers, France (1993)
25. Giraud, M., Simon, H.: Sabot for projectiles of Ram accelerators and projectiles equipped with such a sabot. US Patent Number 5, 394, 805 (1993)
26. Henner, M., Bauer, P., Legendre, J.F., Giraud, M.: Thrust prediction of a RAM accelerator projectile in the sub-detonative propulsion mode. In: Proceedings AIAA Joint Propulsion Conference, Cleveland, USA (1998)
27. Higgins, A.J., Knowlen, C., Bruckner, A.P.: Ram accelerator operating limits, identification of limits and nature of observed Limits. J Prop and Power, 1st part 14, pp. 951–958 and 2nd part 14, pp. 959–966 (1998)
28. Knowlen, C., Burnham, E.A., Kull, AE., Bruckner, A.P., Hertzberg, A.: Ram accelerator operation in the trans-detonative velocity regime. In: 41th Meeting of the Aeroballistic Range Association (ARA), San Diego, California, USA (1990)
29. Knowlen, C., Bruckner, A.P., Hertzberg, A.: Internal ballistics of the Ram accelerator. In: Proceedings of 13th International Symposium on Ballistics, Stockholm, Sweden (1992)

30. Knowlen, C., Higgins, A.J., Hinkey, JB., Burnham, E.A., Mattick, AT.: Diagnostic techniques for Ram accelerator phenomena. In: Proceedings of 43rd Meeting of the Aeroballistic Range Association (ARA), Colombus, Ohio, USA (1992)
31. Knowlen, C., Higgins, A.J., Bruckner, A.P., Bauer, P.: Ram accelerator operation in the super-detonative velocity regime. AIAA Paper 96-0098 (1996)
32. Knowlen, C., Bundy, C., Schwab, R., Bruckner, A.P.: University of Washington, high pressure Ram accelerator facility. In: 50th meeting of the Aeroballistic Range Association (ARA), Pleasanton, California, USA, 1999
33. Giraud, M.: Sabot et interface de projectile pour RAMAC. Brevet N°9211033, ISL N°F II 3/138 (1992)
34. Seiler, F., Lehr, H., Giraud, M.: Projectile conçu pour être lancé à partir d'un accélérateur à effet stato et accélérateur à effet stato mis au point à cette fin. Brevet N°P4120067,5 (RFA), (1991), et brevet N°9207356 (F), (1992), ISL F II 3/124
35. Bauer, P., Henner, M., Giraud, M.: Numerical investigation of the fin geometry of Ram accelerator projectiles in sub-detonative propulsion mode. Eur. Phys. J. App. Phys. **23**, 139–145 (2003)
36. Henner, M., Giraud, M.: Steady and non reactive flow around fin-guided RAM projectiles. Experiments and CFD computations. In: 48th ARA meeting, Austin TX, USA (1997)
37. Legendre, J.F., Giraud, M.: Enhanced RAMAC performances in sub-detonative propulsion mode with semi-combustible projectiles. In: Bauer, P. (ed.) Proceedings of the 4th International Workshop on Ram Accelerators, Poitiers, LCD, France. Journal de Physique, Vol. 10, Pr 11, ISSN 1155–4339, EDP Sciences Edition (2000)
38. Henner, M., Giraud, M., Legendre, J.F., Berner, C.: CFD computations of steady and non reactive flow around fin-guided RAM projectiles. In: Takayama, K., Sasoh, A. (eds.) Proceedings of the 3rd International Workshop on Ram Accelerator, Sendai, Japan, SWRC, pp. 325–332 (1997)
39. Bauer, P., Knowlen, C., Bruckner, A.P., Henner, M.: Determination of choke pressure of ram accelerator in sub-detonative mode. J. Phys. **10**, 59–67 (2000)
40. Bogdanoff, D.W.: Strategies to protect Ram accelerator projectiles from in-tube gasdynamic heating. In: Bauer, P. (ed.) Proceedings of the 4th International Workshop on Ram Accelerators, Poitiers, LCD, France. Journal de Physique, Vol. 10, Pr 11, ISSN 1155–4339, EDP Sciences Edition (2000)
41. Veyssière, B., Ingignoli, W., Khasainov, B.A.: On the possibility to modify the performance of propellant mixtures used in RAMAC by addition of metallic particles. In: Bauer, P. (ed.) Proceedings of the 4th International Workshop on Ram Accelerators, Poitiers, LCD, France. Journal de Physique, Vol. 10, Pr 11, ISSN 1155–4339, EDP Sciences Edition (2000)
42. Legendre, J.F.: Contribution à l'Etude de la Sensibilité et des Caractéristiques de Détonation de Mélanges Explosifs Gazeux Denses à Base de Méthane Utilisés pour la Propulsion dans les Accélérateurs à Effet Stato, Ph.D. Dissertation, University of Poitiers, France (1996)
43. Bauer, P., Giraud, M., Legendre, J.F., Catoire, L.: Detonability limits of methane-oxygen-nitrogen mixtures at elevated initial pressures. In: Proceedings of 18th International Pyrotechnics Seminar, Breckenridge, Colorado, USA (1992)
44. Bauer, P., Legendre, J.F.: Detonability limits of propellant mixtures used in the RAMAC. In: Murphy, M.J., Backofen, M.J.E. (eds.) Proceedings of the 14th International Symposium on Ballistics, Québec, Canada, p. 389 (1993). ISBN 0-9618156-9-8
45. Bauer, P., Legendre, J.F., Henner, M., Giraud, M.: Real gas effects in Ram accelerator propellant mixtures, theoretical concepts and applied thermochemical codes. In: Takayama, K., Sasoh, A. (eds.) Proceedings of 3rd International RAMAC Workshop, pp. 39–52. Sendai SWRC-Japan (1997)
46. Bauer, P., Knowlen, C., Higgins, A.J., Legendre, J.F.: Detonation initiation of insensitive dense gaseous mixtures by piston impact. In: Houwing, A.F.P. (ed) Proceedings of the 21st International Symposium on Shock Waves, Great Keppel Island, Australia, University of Queensland, p. 1609 (1997)

47. Bauer, P., Knowlen, C., Bruckner, A.P.: Real gas effects on the prediction of ram accelerator performance. Shock Waves **8**, 113–1118 (1998)
48. Bauer, P., Knowlen, C., Bruckner, A.P., Henner, M., Legendre, J.F., Giraud, M.: Determination of the choke pressure of a Ram accelerator. Projectile in sub-detonative regime. In: Bauer, P. (ed.) Proceedings of the 4th International Workshop on Ram Accelerators, Poitiers, LCD, France. Journal de Physique, Vol. 10, Pr 11, ISSN 1155–4339, EDP Sciences Edition (2000)
49. Henner, M., Legendre, J.F., Giraud, M., Bauer, P.: Initiation of reactive mixtures in a Ram accelerator. In: AIAA (ed.) Proceedings of the 33rd AIAA/ASME/ASEE Joint Propulsion Conference, p. 97, July 7–9 1997, Seattle, WA, USA (1997)
50. Leblanc, J.E., Nusca, M., Wang, X., Seiler, F., Sugihara, M., Fujiwara, T.: Numerical simulation of the RAMAC benchmark test. In: Bauer, P. (ed.) Proceedings of the 4th International Workshop on Ram Accelerators, Poitiers, LCD, France. Journal de Physique, Vol. 10, Pr 11, ISSN 1155–4339, EDP Sciences Edition (2000)
51. Legendre, J.F., Giraud, M., Bauer, P.: Effect of additives on the detonation properties of dense gazeous explosives. In: Giraud, M., Smeets, G. (eds.) Proceedings of the 1st International Workshop on Ram Accelerators, Saint-Louis, France (1993)
52. Legendre, J.F., Giraud, M., Bauer, P., Voisin, D.: 90L35 detonation tube experiments, influence of diluent nature on the detonation characteristics of dense methane based gaseous explosive mixtures. In: , edited by Bruckner, A.P., Knowlen, C. (eds.) Proceedings of the 2nd International Workshop on Ram Accelerators, Seattle, WA, USA (1995)
53. Legendre, J.F., Bauer, P., Giraud, M.: Influence of initiation modes on the detonability of dense gazeous explosives. In: Proceedings of 2nd International Meeting on Properties of Reactive Fluids, University of Poitiers, France (1996)
54. Legendre, J.F., Bauer, P., Giraud, M.: RAMAC 90, detonation initiation of insensitive dense methane-based mixtures by normal shock waves. In: Takayama, K., Sasoh, A. (eds.) Proceedings of the 3rd International Workshop on Ram Accelerators, Sendai, Japan, SWRC, pp. 223–231 (1997)
55. Legendre, J.F., Bauer, P., Giraud, M.: On the safety of dense methane-oxygen-nitrogen mixtures. In: 9th Symposium on Loss Prevention and Safety Promotion in the Process Industry, Barcelona, Spain (1998)
56. Legendre, J.F., Bauer, P., Giraud, M.: Detonation properties of helium-diluted dense methane-oxygen mixtures. Application to high performances in sub-detonative propulsion mode. In: Bauer, P. (ed.) Proceedings of the 4th International Workshop on Ram Accelerators, Poitiers, LCD, France (1999)
57. Legendre, J.F., Giraud, M.: Dual purpose launcher for ballistic research- RAMAC and SIBREF. In: Proceedings of 18th International Symposium on Ballistics, San Antonio, TX, USA (1999)
58. Legendre, J.F., Bauer, P., Giraud, M.: Helium dilution for Ram accelerator operation. Shock Waves **11**(5), 361–367 (2002)
59. Giraud, M., Legendre, J.F., Simon, G., Catoire, L.: RAM accelerator in 90 mm caliber. first results concerning the scale effect in the thermally choked propulsion mode. In: Proceedings of 13th International Symposium on Ballistics, Stockholm, Sweden (1992)
60. Legendre, J.F., Giraud, M., Henner, M.: Velocity performance in RAMAC 90 multistage experiments. In: AIAA Joint Propulsion Conference, Cleveland, USA (1998)
61. Legendre, J.F., Giraud, M., Henner, M.: Ram accelerator: a new hypervelocity launcher for ballistic studies. HVIS 98, Huntsville, USA (1998)
62. Bengherbia, T.: Contribution to numerical simulation analysis of the flow in the Ram accelerator in the sub-detonative propulsion mode. Ph.D. Dissertation, LCD, CNRS, ENSMA, Poitiers, France (2009)
63. Bengherbia, T., Yao, Y., Bauer, P., Giraud, M., Knowlen, C.: Improved 1-D unsteady modeling of the thermally choked RAMAC in the sub-detonative propulsion mode. J. Appl. Mech **78**, 150–167 (2011)

Author Biographies

Marc Giraud became successively in Strasbourg (France): Physicist at the University (1962), Engineer in Mechanical Engineering at ENSAIS (1962) and got his Ph.D. at the Laboratory of Fluid Mechanics (1971). His research areas and technical contributions are: Ballistics, Aeroballistics, Trans-Super-Hypersonic Flows, Launch Dynamics, Propulsion, RAM Accelerators, Scaling laws, Applications in Terminal Ballistics and Ballistics Instrumentation. As Research accomplishments he published almost 150 manuscripts as author/co-author in refereed Journals/Parts of Books/International Conference Proceedings. He served on 8 Ph.D. juries and filed 7 patents. His other activities in connection with the ballistic fields have been: Chairman of the Aeroballistic Range Association (ARA) (1995–97), Chairman of the International Ballistics Committee (IBC) (1999–2002), Co-founder member of the International Ballistics Society (IBS) (2010). Furthermore he received Ballistics Awards from the ARA (1999), from the Swedish Defense Research Agency Weapons and Protection (2002). He has been elected Chevalier de "l'Ordre National du Mérite" by the French Ministry of Defense (1993) and Ballistics Science Fellow Member of the IBS (2013).

Pascal Bauer After completing an engineer degree in Mech Eng. in 1972, he obtained a doctorate: Docteur es Sciences in 1985. He was Professor at University of Paris West in 1989, then, since 2002, he is now Professor at ENSMA. He is the author of over 150 papers and reports, including 50 archival papers on subjects related to detonation and its application to propulsion. The main aspects he addresses are those related to the equations of state of gaseous systems at extremely elevated pressure and, more recently, the propulsive properties of a novel propulsive technology. He is the author of three books respectively on (i) thermodynamics, (ii) propulsion, and (iii) shock waves and detonation. He is a Member of the research group on deflagrations, detonations and explosions at the Laboratory Pprime, CNRS, ENSMA. He is also Affiliate Professor at the University of Washington, Seattle, WA, USA and Professor at the Sino-european Institute of Aviation Engineering (SIAE), Tianjin, China. He is Associate Fellow of the American Institute of Aeronautics and Astronautics (AIAA). He was the former Chairman of the PEGASUS European network.

The Ram Accelerator in Subdetonative Propulsion Mode: Analytical and Numerical Modeling and Simulation

Pascal Bauer and Tarek Bengherbia

1 Introduction

The objective of the present chapter is to show the different steps that led to a better understanding of the dynamics of the flow and the ability to predict the performance of a ram accelerator. The study deals primarily with the thermally choked propulsive mode which operates in the sub-detonative velocity regime; i.e., below the Chapman-Jouguet (C-J) detonation speed of the propellant. In this mode, the thrust is generated by the high projectile base pressure resulting from a normal shock-wave system that is stabilized on the projectile aft-body, while downstream behind the projectile the flow is thermally choked at the full tube area (Fig. 1).

Moreover the investigation has been continued through a CFD analysis of the flow together with a series of improvements of the 1D modeling. Finally, a computer code was elaborated in order to provide data on the characteristics of the flow around the projectile, which ultimately predicts the performance, i.e., thrust of the ram accelerator. Most calculations were validated by experiments performed at the ram accelerator facility of the University of Washington (UW) at Seattle, Washington, USA, as it has been lengthily developed in Refs. [2, 46, 47].

The initiation of combustion around a projectile at a supersonic speed has been studied by several authors, including Lehr [65] who investigated a very simple geometry, namely, spheres entering mixtures at a low pressure. Higgins [53] further investigated this aspect and used the ram accelerator facility at University of Washington to perform this study. Investigations dealing with this type of

P. Bauer (✉)
PPRIME (ex LCD), UPR CNRS # 3346, ISAé-ENSMA, Rue Cl. Ader,
86960 Poitiers, France
e-mail: pascal.bauer@ensma.fr

T. Bengherbia
Det Norske Veritas, Palace House, 3 Cathedral Street, London SE1 9DE, UK

F. Seiler and O. Igra (eds.), *Hypervelocity Launchers*,
Shock Wave Science and Technology Reference Library 10,
DOI 10.1007/978-3-319-26018-1_7

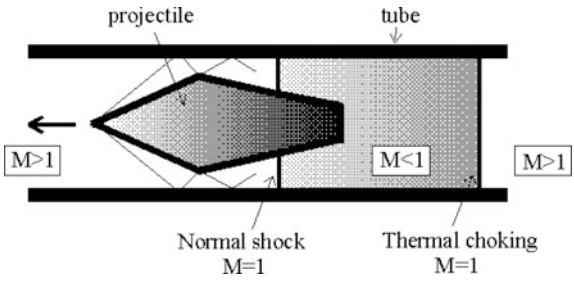

Fig. 1 Sketch of the flow in the subdetonative propulsion mode

combustion are numerous and they have often been used to validate numerical codes [1, 83].

Some contributions [1, 85] deal with the acceleration in a ram accelerator and include studies on initiation of premixed mixtures over edges or steps. These studies provide an analysis on initiation mechanisms due to aerodynamic phenomenon. These studies are mostly dealing with ram accelerators operations in a super-detonative regime with axi-symetrical projectiles [59].

Some ram accelerator operations remain unsuccessful when an unstart occurs. This phenomenon is the disgorging of a normal shock past the projectile throat, often resulting in an overdriven detonation wave, which rapidly decelerates the projectile. This process, which is a major obstacle to ram accelerator performance has been addressed in other studies including numerical and experimental ones [25, 63, 83]. Decreasing the sensitivity of the combustible mixture can be an issue to limit this unstart phenomenon. For this purpose, several studies were conducted on the detonation initiation of less detonable mixtures [5, 11, 14, 41, 62]. Some studies have also been dealing with the initiation mechanism behind an oblique shock wave and the transition from combustion to detonation [35–37, 82]. Another series of investigations were aimed at the characterization of the sensitivity of reactive mixtures, using a shock to initiate the high-pressure reactive mixture, which ultimately showed the effect of the shock dynamics on the initiation of the combustion and an eventual transition to detonation [12, 26, 44, 64, 78, 80, 81, 84, 85]. Nusca [72–74], proposed an extensive modeling of methane combustion at a high pressure, with calculations involving initial and boundary conditions that were close to those encountered during ram accelerator operations. The thorough analysis from Bruckner et al. [28], which takes into account the whole projectile, including the fins, was validated by experimental data. The predicted projectile acceleration and thermally choked pressure agreed well with the experimental data [15].

This chapter is arranged as follows. Firstly, the two-dimensional numerical simulation is described in Sect. 2 and the CFD results are validated against test data from a representative experiment at a University of Washington 38-mm-bore test facility. The early form of the 1D modeling based on a quasi-steady assumption of the flow and involving compressibility effects as well as a real gas equation of state

is then presented in Sect. 3. The modeling is further improved by using a real gas equation of state for the reactants to account for the compressibility effects when high initial pressures are involved. In order to further account for high acceleration rates, an unsteady modeling of the flow is then assumed. The corresponding calculation process is described in Sect. 4 and results are compared with quasi-steady predictions. In Sect. 5, the effectiveness of an improved 1D unsteady modelling applying the CFD predicted control volume length is demonstrated. The ram accelerator test data used for comparison with numerical predictions are from a University of Washington experiment in which the 16-m-long test section was pressurized with $2.95CH_4 + 2O_2 + 5.7N_2$ propellant at $p_o = 5.15$ MPa. In this experiment a titanium alloy projectile having mass of 109 g was launched into the ram accelerator test section with an entrance velocity of 1060 m/s and accelerated throughout its length to an exit velocity of 2050 m/s. Some conclusions on the state of the art in terms of modeling of the ram accelerator are drawn in Sect. 6.

2 Two-Dimensional CFD Modeling

2.1 On the Need of CFD Numerical Modeling of Reactive Flows

A preliminary numerical investigation of the fin geometry of ram accelerator projectiles in subdetonative propulsion mode was performed at ISL [16, 40, 42, 45]. It followed a previous investigation on the role of proper design of the sabot [38], which provided a series of data that highlight the influence of fins on the initiation process of combustion in a ram accelerator in subsonic propulsion mode. However, the calculations are based on a non-reactive numerical code for fluid dynamics simulation, namely TascFlow™ [16, 45], which provided a more simple calculation procedure, and the results were compared with available experimental data, showing that this numerical simulation could be regarded as fairly reliable. Yet, a further refinement of the simulation, involving the reactive behavior of the flow was required. This modeling is presented hereafter.

The numerical study that has been carried out here uses the Reynolds averaged Navier-Stokes (RANS) approach combined with different kinetic reaction mechanisms [19–21]. The reaction model approximation significantly influences the CFD prediction [18] for pressure distributions along the tube wall and the projectile centerline. Based on these investigations, it is concluded that minimally a five-step reaction model has to be adopted in order to replicate essential combustion details. Not surprisingly, the CFD predicted combustion length; i.e., the axial distance between the projectile base and the thermally choked location, is not a constant, but dependent on the Mach number of incoming flow.

2.2 Governing Equations

The governing equations for the chemically reacting viscous flows are the compressible Navier-Stokes equations with chemical source terms for mixture composed of 'N' gas species mixture, which are expressed in the following forms:

$$\frac{\partial Q}{\partial t}+\frac{\partial E}{\partial x}+\frac{\partial F}{\partial y}=\frac{\partial E_v}{\partial x}+\frac{\partial F_v}{\partial y}+H+H_v+S \tag{1}$$

$$Q=[\rho_1,\ldots,\rho_N,\rho u,\rho v,\rho e]^T \tag{2}$$

$$E=\left[\rho_1 u,\ldots,\rho_N u,\rho u^2,p,\rho uv,u(\rho e+p)\right]^T \tag{3}$$

$$F=\left[\rho_1 v,\ldots,\rho_N v,\rho uv,\rho v^2,p,v(\rho e+p)\right]^T \tag{4}$$

$$E_v=\left[\rho D_1\frac{\partial c_1}{\partial x},\ldots,\rho D_N\frac{\partial c_N}{\partial x},\tau_{xx},\tau_{xy},u\tau_{xx}+v\tau_{xy}+q_x\right]^T \tag{5}$$

$$F_v=\left[\rho D_1\frac{\partial c_1}{\partial y},\ldots,\rho D_N\frac{\partial c_N}{\partial y},\tau_{xy},\tau_{yy},u\tau_{xy}+v\tau_{yy}+q_y\right]^T \tag{6}$$

$$H=-\frac{m}{y}\left[\rho_1 v,\ldots,\rho_N v,\rho uv,\rho v^2,v(\rho e+p)\right]^T \tag{7}$$

$$H_v=-\frac{m}{y}\left[\rho D_1\frac{\partial c_1}{\partial y},\ldots,\rho D_N\frac{\partial c_N}{\partial y},\tau_{xy},\tau_{yy}-\tau_{\theta\theta},u\tau_{xy}+v\tau_{yy}+q_y\right]^T \tag{8}$$

$$S=[\dot{\omega}_1,\ldots,\dot{\omega}_N,0,0,0]^T \tag{9}$$

The transpose of a matrix is defined by the operator T. The shear stresses and heat fluxes are defined as:

$$\tau_{xx}=2\mu\frac{\partial u}{\partial x}-\frac{2}{3}\mu\nabla\cdot u=\frac{2}{3}\mu\left(2\frac{\partial u}{\partial x}-\frac{\partial v}{\partial y}-\frac{mv}{y}\right) \tag{10}$$

$$\tau_{yy}=2\mu\frac{\partial v}{\partial y}-\frac{2}{3}\mu\nabla\cdot u=\frac{2}{3}\mu\left(2\frac{\partial v}{\partial y}-\frac{\partial u}{\partial x}-\frac{mv}{y}\right) \tag{11}$$

$$\tau_{xy}=\mu\left(\frac{\partial u}{\partial y}-\frac{\partial v}{\partial x}\right) \tag{12}$$

$$\tau_{\theta\theta}=2\mu\left(\frac{\partial v}{\partial y}-\frac{2}{3}\mu\nabla\cdot u\right) \tag{13}$$

$$q_x = \lambda \frac{\partial T}{\partial x} + \rho \sum_{k=1}^{N} D_k h_k \frac{\partial c_k}{\partial x} \tag{14}$$

$$q_y = \lambda \frac{\partial T}{\partial y} + \rho \sum_{k=1}^{N} D_k h_k \frac{\partial c_k}{\partial y} \tag{15}$$

Here u and v are velocity components, p is the pressure, T is temperature, e is the total energy per unit mass, m = 0 for a planar flow and $m = 1$ for an axi-symmetric flow, ρ_k is the density of species k, with total density, $\rho = \sum_{k=1}^{N} \rho_k$, $c_k = \rho_k/\rho$ is the mass fraction, $\dot{\omega}_k$ is the mass production rate of species k due to chemical reactions, and h_k is the specific enthalpy. The mass diffusivity D_k of species k in the gas mixture is defined as:

$$D_k = (1 - X_k) / \sum_{j \neq k} \frac{X_j}{D_{kj}} \tag{16}$$

where D_{kj} is the binary diffusivity, X_k is the molar fraction, and μ, λ, are determined using viscosity and conductivity of the gas mixture, respectively. The equation of state for a mixture of ideal gases is:

$$p = \sum_{k=1}^{N} \frac{\rho_k}{M_k} RT \tag{17}$$

where M_k is the molecular weight of species k and R is the universal gas constant. The total energy per unit volume ρe is used for evaluating the temperature T implicitly by the Newton iteration method through the thermodynamic relationship $\rho e = \rho h - p$.

$$\rho e - \frac{1}{2}\rho u^2 = \sum_{k=1}^{N} \rho_k \left(\int_{T_0}^{T} \frac{c_{pk}}{M_k} dT + h_k^0 \right) - RT \sum_{k=1}^{N} \frac{\rho_k}{M_k} \tag{18}$$

where c_{pk} is the specific heat capacity for species k at constant pressure, and h_k^0 is the heat of formation at reference temperature T_0. The specific heat capacity for species k can be expressed as a function of temperature in polynomial fitting as:

$$\frac{c_{pk}}{R} = a_{1k} + a_{2k}T + a_{3k}T^2 + a_{4k}T^3 + a_{5k}T^4 \tag{19}$$

where the coefficients a_{ik} are the so-called NASA thermo-chemical polynomial data which are valid in a range of 300–5000 K.

2.3 Turbulent Combustion Model

In addition to the above-described governing equations, both turbulence model and combustion model are required. The shear-stress transport (SST) turbulence [67] is used for all simulations. This model takes advantage of both the Wilcox k-ω and the k-ε model; i.e., in the inner region of a boundary layer the standard k-ω model is used, while in the outer region of a boundary layer, a high-Reynolds-number version of the k-ε model applied. A blended function is used to make a smooth change at the interface between two models.

The chemical reaction source term in Eq. (9) is calculated using an eddy dissipation model (EDM) initially proposed by Magnussen and Hjertager [69] and later improved by Magnussen [68]. It is based on the same fundamental grounds as Spalding's model and relies on the idea that chemical reactions occur in the smallest turbulent eddies.

The reaction rate is calculated using the Arrhenius law, or if the flow is fully turbulent, then the EDM model is utilized. In other words, depending upon the Damköhler number D_a, either Arrhenius approach or the eddy dissipation model will be utilized. For $D_a \ll 1$, the chemical induction time is very short, then Arrhenius law is used. On the contrary, if the reaction rate is predominately influenced by turbulent flow, then the eddy dissipation model is selected. Bengherbia et al. [19–21] investigated more thoroughly the combustion process in the ram accelerator using the following reaction mechanisms: global one step, two steps, three steps, and five steps reaction mechanisms. Among these options tested, the five-step reaction mechanism yields better agreement with experimental data. Hence this reaction mechanism is considered in the present study:

$$CH_4 + 0.5O_2 \rightarrow CO + 2H_2 \tag{20}$$

$$H_2 + 0.5O_2 \rightarrow H_2O \tag{21}$$

$$CO + 0.5O_2 \rightarrow CO_2 \tag{22}$$

$$CO + H_2O \rightarrow CO_2 + H_2 \tag{23}$$

$$CO_2 + H_2 \rightarrow CO + H_2O \tag{24}$$

The reaction rate is defined using the law of mass fraction and a modified Arrhenius expression for these specific reaction rate constants is:

$$\dot{\omega}_{arrhenius} = AT^{\beta} e^{-\frac{E_a}{RT}} \sigma_{CH_4}^{a} \sigma_{O_2}^{b} \sigma_{CO}^{c} \sigma_{H_2}^{d} \sigma_{CO_2}^{e} \sigma_{H_2O}^{f} \tag{25}$$

where the AT^{β} is the collision frequency, T is the temperature, the exponent β is the Boltzmann factor, E_a is the activation energy with unit of kcal/mol, A is in (cm^3 mol s^{-1}) and gas constant R = 1.987 cal/(mol K), σ is the species mass fraction, and the coefficients a, b, c, d, e, f are the degrees of reaction for each

Table 1 Reaction rate equation data (β = 0)

Reaction	E_a	A	a	b	c	d	e	f
Equation (20)	30	2.3×10^7	−0.3	1.3	1	1	0	0
Equation (21)	37.6	1.0×10^5	0	0.5	0	1	0	1
Equation (22)	40	3.5×10^{14}	0	0.25	1	0	1	0

species. Note that the exponent is $\beta = 0$ for this mechanism. The key parameter is the activation energy E_a, and the coefficients *a, b, c, d, e, f* are shown in Table 1. The forward reaction for the Eq. (23) and the backward reaction of Eq. (24) will be calculated by:

$$\dot{\omega}_F = \frac{X_{\mathrm{CO}}}{W_{\mathrm{CO}}} X_{\mathrm{H_2O}} p_{abs}^2 \times 8.1 \times 10^{-9} \mathrm{e}^{\frac{-10926.5}{T}} \tag{26}$$

$$\dot{\omega}_B = \frac{X_{\mathrm{CO_2}}}{W_{\mathrm{CO_2}}} X_{H_2} p_{abs}^2 \times 3.3 \times 10^{-7} \mathrm{e}^{\frac{-15144}{T}} \tag{27}$$

where X_i is the molar fraction and W_i is the molecular weight of species i and p_{abs} is absolute pressure. The Eqs. (26) and (27) were previously developed by Kovacik [55] and have been validated against a wide range of experimental data.

In this five-step mechanism, the β exponent is set to be 0, because chemical reactions occur very fast. Therefore, the rate of combustion can be assumed to be determined by the rate of intermixing of the fuel and oxygen eddies at molecular scale, which, in turn, is given by the dissipation rate of eddies. The equation that yields a minimum reaction rate is the one that determines the local rate of combustion. The main advantage of the EDM model over the Spalding's model is that it is applicable for both non-premixed and premixed flames. Details of both the turbulence and combustion models are extensively described by Bengherbia [19].

2.4 Problem Configuration, Boundary Conditions and Computational Procedure

Numerical simulation using multi-step kinetics mechanisms has been carried out for an axis-symmetric projectile inside a 38-mm-diameter tube. The projectile body has a bi-conical shape with the nose cone having a half-angle of 10° and a length of 82 mm, whereas the aft-body is represented as a truncated cone having a convergence angle of 4.49° and a length of 71 mm, as shown in Fig. 2. The projectile throat has a maximum diameter of 29 mm situated at the joint of the two cones. The overall length of the projectile is 153 mm.

The computational domain begins 10 mm ahead of the projectile nose tip. For the present axi-symmetric modeling, the computational domain length is 563.23 mm; i.e., approximately 3.68 times the projectile length, L_p. Due to the

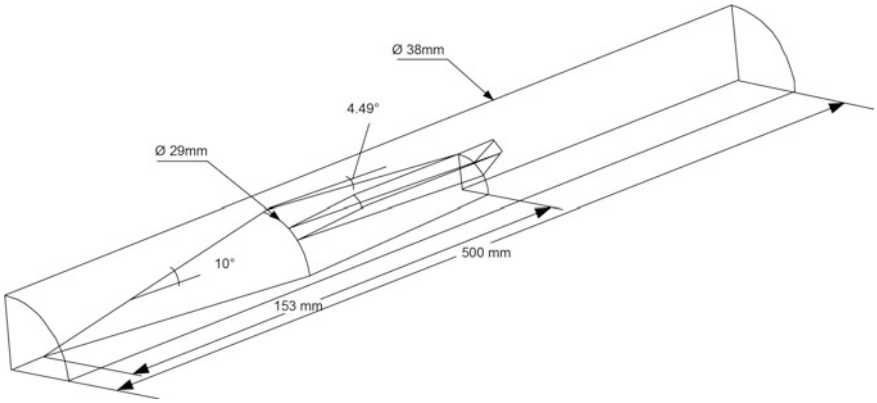

Fig. 2 CFD computational domain and geometry of the projectile. Note that the fin has not been included in present simulations

axis-symmetrical nature of the flow field, only one quarter of the complete domain is considered. A sequence of four meshes, from coarse to fine with the same topology, has been generated with the aim to identify the baseline grid with the appropriate grid resolution [19]. Of which, one grid mesh with the minimum grid spacing in the near wall region varies from 0.025 to 0.018 mm, resulting in a value between 2 to 8 in terms of wall units. This provided a fair resolution without consuming excessive computational time. Hence, this baseline mesh was used for the rest of the simulations. No-slip and adiabatic thermal boundary conditions are applied on the projectile surface. Moreover, the tube wall is assumed to be moving at same velocity as the incoming flow. The symmetric boundaries are used in the circumferential direction of the computational domain.

Figure 3 shows the pressure contours for three incoming velocities of 1091, 1173, and 1829 m/s, respectively. At a low velocity of 1091 m/s, oblique shock-waves around the projectile leading edge and inside the flow passage are clearly seen. Furthermore, there are several localized high and low pressure regions along the tube walls near the projectile trailing edge, indicating strong shock impingement there. Downstream in the near-wake region, shock reflection still exists, leading to an alternating high-low pressure pattern. However it does not survive for very long and decays gradually in the far field. By slightly increasing the inflow velocity to 1173 m/s, oblique shock-waves has been subsequently enhanced, and this 'pushes' the normal shock-wave position towards the projectile base. Subsequently, the alternating high-low pressure pattern has been moved to the near-wake region and similar to that observed with a velocity of 1091 m/s case, the magnitude of pressure gradually decreases in the far field while the flow re-accelerates. At a high velocity of 1829 m/s, the oblique shock-waves become predominant across the entire computational domain from the projectile leading edge until the exit plane. Oblique shock-shock interactions are clearly visible and there is no sign of alternating high-low pressure pattern.

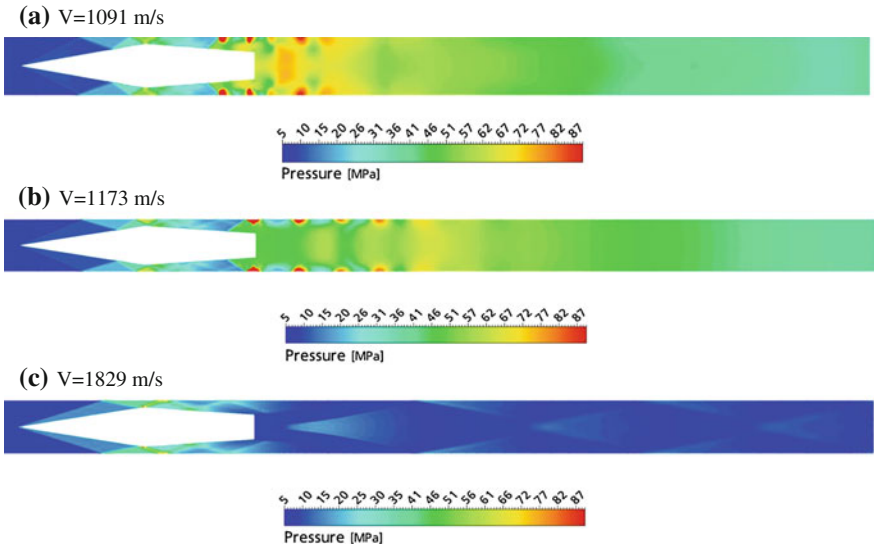

Fig. 3 CFD predicted static pressure contours at incoming velocity of 1091, 1173, and 1829 m/s, respectively

Figure 4 depicts the Mach number contours at three incoming velocities of 1091, 1173, and 1829 m/s, respectively. Same as that seen in Fig. 3, oblique shock-waves are clearly visible around the projectile leading edge and inside the flow passage between the projectile and the tube wall at incoming velocities of 1091 and 1173 m/s. At the aft-body of the projectile, the flow becomes subsonic due the existence of a normal shock-wave. Downstream in the near-wake region, low velocity region exists in the vicinity of the projectile base, similar to that seen in a bluff body flow, and the flow gradually accelerates up to the sonic speed in the far field of the projectile until then thermally choking the flow. It was found that the subsonic flow region decreases as the incoming Mach number increases. At incoming velocity higher than 1733 m/s, simulation results exhibit strong oblique shock-wave system and the shock-shock interactions are predominant in majority of the computational domain. At meantime, the subsonic flow region at the projectile base and downstream in wake region reduces very significantly.

Overall, good agreement has been achieved between the CFD predictions and the experimental measurements at an incoming velocity up to 1733 m/s.

Beyond this, the CFD calculation under-predicts the pressure magnitude slightly, and this is probably due to the fact that in this velocity range, the projectile is undergoing a transition procedure from a sub-detonative mode to a super-detonative mode.

In the present simulations, all the settings, in particular the turbulence model parameters were not suitable for a trans-detonative propulsive mode. Thus simulation is only valid up to $M \approx 5$. Another factor that might influence this under-prediction of thrust is that the simulation does not account for the

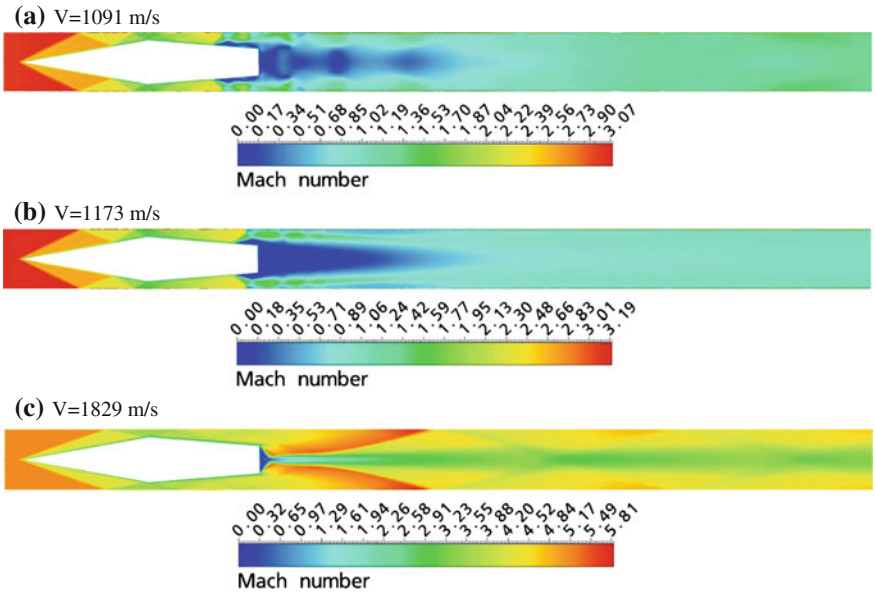

Fig. 4 CFD predicted Mach number contours at incoming velocity of 1091, 1173, and 1829 m/s, respectively

three-dimensional nature of the flow, due to the neglecting the guide fin effects in the modelling. Nevertheless, the normal shock-wave location tends to move towards the projectile aft-body, whilst the incoming velocity increases, as observed in Fig. 4. Further comparisons between the CFD predictions and the experimental measurements such as the tube wall pressure history at various probe locations and incoming velocities have been made with good agreements being achieved.

3 One-Dimensional Modeling

3.1 Real Gas Effect on the Prediction of Ram Accelerator Performance

3.1.1 Key Elements and Benefits of the 1D Modeling

Successful prediction of the ram accelerator thrust-Mach number relationship for a thermally choked propulsive mode is accomplished in a straightforward manner that yields the main parameters of acceleration process [19]. This analysis of subdetonative ram accelerator performance is based on one-dimensional modeling of the flow process that propels the projectile [27, 56]. The quasi-steady conservation equations are applied to a control volume attached to the projectile. The main

assumption that oversimplifies the actual physical process is using the ideal gas equation of state (EoS) for the combustion products. Since these products are at a substantially elevated pressure, i.e., on the order of several tens of MPa, the ideal EoS is no longer valid and a more realistic one should be used instead. This does not necessarily mean that an extremely sophisticated EoS is required, since there are a number of EoS such as the virial type that, despite their simplicity, may be regarded as totally appropriate [6, 7, 48, 49]. The effects of increasing the initial pressure beyond the 8 MPa value, thus yielding combustion products of the order of 100 MPa, may still be sufficiently modeled with a virial type EoS that includes more severe molecular interaction laws [48]. An equation of state with adjustable parameters such as those used in the case of high explosives may also be another issue [66] as will be shown later in this chapter.

The modeling of the performance of the ram accelerator, which was based on the ideal gas EOS, has been improved with the inclusion of real gas behavior [13, 32, 33]. This involves a correction of most of the thermodynamic parameters. The calculation was conducted on the basis of a virial EoS with relatively simple molecular interaction modeling. Independently, a general formulation of the relevant relationships was given in order to allow the use of any type of EoS for other applications. Implementing real gas corrections significantly improves the resulting non-dimensional thrust as a function of the flight Mach number.

3.1.2 General Equations

The main idea of this modeling (black box model) is to describe the aerothermodynamics of the flow around the projectile as a global process between its state as it enters the control volume and the state of the exit flow (Fig. 5).

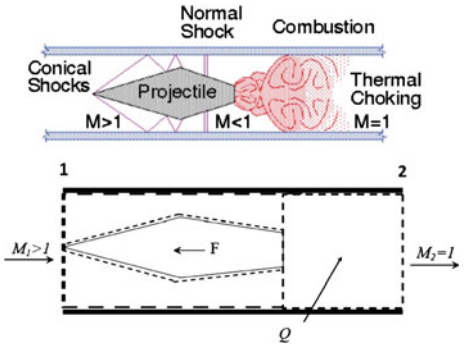

Fig. 5 One-dimensional model of the RAMAC thermally choked propulsive mode

This modeling is based on the set of one-dimensional conservation equations for quasi-steady flow:

- continuity:

$$\frac{u_1}{v_1} = \frac{u_2}{v_2} \tag{28}$$

- energy:

$$h_1 + h_{f1} + \frac{u_1^2}{2} = h_2 + h_{f2} + \frac{u_2^2}{2} \tag{29}$$

- momentum:

$$p_1 + \frac{u_1^2}{v_1} + \frac{F}{A} = p_2 + \frac{u_2^2}{v_2} \tag{30}$$

where the subscripts "1" and "2" refer to the flow properties entering and leaving the control volume respectively (Fig. 5). Subscript f refers to the heat of formation of species.

Furthermore, the following dimensionless parameters are defined:

$$Q = \frac{h_{f1} - h_{f2}}{c_{p1}\, T_1}; \quad I = \frac{F}{p_1 A}; \quad P = \frac{p_2}{p_1}; \quad V = \frac{v_2}{v_1} \tag{31}$$

which are the non-dimensional heat release, non-dimensional thrust, and the pressure and specific volume ratios between the initial and final states, respectively.

The parameters η and σ shown below denote a measure of caloric imperfection and non ideal gas behavior: $\eta = h/c_p T; pv = \sigma RT$. After some algebraic combination of these relationships, the following expression for the generalized Hugoniot results [57]:

$$P = \frac{\frac{2\, c_{p1}}{R_1}(Q + \eta_1) - (V+1)(I+1)}{V\left(\frac{2\, \eta_2\, c_{p2}}{\sigma R_2} - 1\right) - 1} \tag{32}$$

At this stage, the ideal gas EoS will be taken to describe the initial properties of the mixture, thus $\sigma_1 = 1$. The usual formulation for the used sound velocity is, $a2 = \Gamma RT$, where Γ, R, and T are the "adiabatic" heat capacity ratio (also named adiabatic gamma [34]), the gas constant, and temperature, respectively. One may express Γ in the form:

$$\Gamma = \left.\frac{\partial h}{\partial e}\right|_S = -\left.\frac{\partial Lnp}{\partial Lnv}\right|_S \tag{33}$$

where e and h are the specific internal energy and enthalpy, respectively.

This Γ, specifically used in the case of combustion products undergoing rapid phase or composition changes through compression or expansion processes, is readily correlated to the usual γ [49, 51]. Using the parameters described above, one can express the momentum equation in terms of Mach number as follows:

$$I = P - 1 + \frac{M_2^2 \Gamma_2 R_2 T_2}{p_1 v_2} - \frac{M_1^2 \gamma_1 R_1 T_1}{p_1 v_1} \tag{34}$$

Note that when dealing with the initial state of the mixture, i.e., the unburned gases, the classical relationship was used for the sound speed, namely, that involving γ_1. Hence, the non-dimensional thrust may be expressed as follows:

$$I = P\left(1 + \frac{\Gamma_2 M_2^2}{\sigma}\right) - \left(1 + M_1^2 \gamma_1\right) \tag{35}$$

Using the continuity equation, after some algebraic manipulation, yields:

$$P = \sigma \frac{M_1}{M_2} \sqrt{\frac{\gamma_1 R_2 T_2}{\Gamma_2 R_1 T_1}} \tag{36}$$

The temperature ratio may be derived from the energy balance in the form:

$$\frac{T_2}{T_1} = \frac{c_{p1}}{c_{p2}} \left(\frac{\eta_1 + \frac{\gamma_1 - 1}{2} M_1^2 + Q}{\eta_2 + \frac{M_2^2 \Gamma_2 R_2}{2 c_{p2}}} \right) \tag{37}$$

which yields:

$$P = \sigma \frac{M_1}{M_2} \sqrt{\frac{\gamma_1 R_2}{\Gamma_2 R_1} \frac{c_{p1}}{c_{p2}}} \sqrt{\frac{\eta_1 + \frac{\gamma_1 - 1}{2} M_1^2 + Q}{\eta_2 + \frac{M_2^2 \Gamma_2 R_2}{2 c_{p2}}}} \tag{38}$$

This, in turn, leads to the following final generalized relationship for non-dimensional thrust:

$$I = \sigma \frac{M_1}{M_2} \sqrt{\frac{\gamma_1 R_2}{\Gamma_2 R_1} \frac{c_{p1}}{c_{p2}}} \sqrt{\frac{\eta_1 + \frac{\gamma_1 - 1}{2} M_1^2 + Q}{\eta_2 + \frac{M_2^2 \Gamma_2 R_2}{2 c_{p2}}}} \left(1 + \frac{\Gamma_2 M_2^2}{\sigma}\right) - \left(1 + M_1^2 \gamma_1\right) \tag{39}$$

3.1.3 Real Gas Form of the Thermodynamic Parameters

The preceding equations require knowledge of several thermodynamic parameters, which can be provided by the classical thermodynamic functions. However, this

requires further numerical and analytical treatment which is detailed below. Enthalpy and internal energy may be expressed in the general following form:

$$\psi^{rg} = \psi^{ig} + \psi^{ex} \tag{40}$$

where Ψ is either the enthalpy or internal energy and ψ^{ex} is the excess (or correction) term of the corresponding parameter from ideal gas (ig) to real gas (rg). These correction terms may be expressed in the following differential forms [34] for enthalpy and internal energy, respectively:

$$h^{ex} = \left(v - T \left. \frac{\partial v}{\partial T} \right|_p \right) dp \tag{41}$$

$$e^{ex} = \left(T \left. \frac{\partial p}{\partial T} \right|_v - p \right) dp \tag{42}$$

A series of operators involving partial derivatives of σ introduced by Heuzé et al. [48] will be extensively used in the following calculations:

$$\sigma_v = T \left. \frac{\partial \sigma}{\partial v} \right|_T ; \quad \sigma_T = v \left. \frac{\partial \sigma}{\partial T} \right|_v \tag{43}$$

Using these operators in Eqs. (41) and (42) yields:

$$h^{ex} = RT(\sigma_v + \sigma_T) \frac{dv}{v} \tag{44}$$

$$e^{ex} = RT\sigma_T \frac{dv}{v} \tag{45}$$

The real gas corrections should also be applied to the so-called "adiabatic" gamma. It can be shown [51] that the generalized expression of this parameter is:

$$\Gamma = \gamma \left(1 - \frac{\sigma_v}{\sigma} - n_v \right); \quad n_v = \left. \frac{v}{n} \frac{\partial n}{\partial v} \right|_T \tag{46}$$

However, in the present form these parameters involve T and v and, therefore, they cannot be readily calculated. In order to perform such a calculation one can switch to p and T variables which are more representative of the actual inputs of the problem. On the basis of a set of finite difference relationships which can be obtained by a simple equilibrium calculation [50] for three distinct $\{p, T\}$ sets of values [51], the values of the dissociation rates, n_T and n_v may thus be derived from the preceding operators:

$$n_v = N_p \frac{v}{p}\frac{\partial p}{\partial v}\bigg|_T ; \quad N_p = \frac{p}{n}\frac{\delta n}{\delta p}\bigg|_T \tag{47}$$

It can be shown that the derivatives involved in these expressions can, in turn, be expressed as functions of the former operators (Eq. 43) as follows:

$$n_v = -\left(1 - \frac{\sigma_v}{\sigma}\right)\frac{N_p}{1 - N_p} \tag{48}$$

A comment can be made at this point: since n_v always has a positive value and $\sigma_v = 0$ in the case where an ideal gas is concerned, Γ for an ideal gas is always less than γ. The general expressions for the thermodynamic parameters, and more specifically those which appear in the generalized thrust relationship, namely Γ_2, can be expressed as a function of the operators: n_v, σ_v, σ_T. It should be noticed that all the preceding general formulation is not dependent on any type of EoS, apart from a general parameter σ and its derivatives. A more detailed expression of this σ used in the present case must now be given and its application to the thermodynamic parameters addressed. The next step of this modeling requires appropriate choice of an EoS.

3.1.4 Equation of State

The virial type EoS is very convenient, since analytical calculations can be easily handled and yet it is a very reliable EoS, as long as the pressure of the combustion products does not exceed 200 MPa [8]. In the present case, the EoS has the following form [3] (Boltzmann formulation):

$$\sigma = 1 + x + 0.625\,x^2 + 0.287\,x^3 + 1.93\,x^4 + O(x^n) \tag{49}$$

where $x = b/v$, and $O(x^n)$ indicates higher order terms which are not taken into account here. A simplified molecular interaction model was chosen which assumes that only like molecules interact: $b = \Sigma x_i b_i$.

This form of the EoS allows one to readily calculate all the corrections expressed above. These corrections happen to take a simple form, since one gets a simple representation for both σ_T and σ_v [49] as follows:

$$\sigma_T = 0 \tag{50}$$

$$\sigma_v = -x\frac{\partial \sigma}{\partial x} = -\left(x + 1.25\,x^2 + 0.861\,x^3 + 0.772\,x^4\right) \tag{51}$$

These rather straightforward expressions of the derivatives of σ, as well as σ itself, provide an easy way to calculate the pertinent real gas corrections that should be accounted for in the present situation:

$$h^{ex} = (\sigma - 1)RT \tag{52}$$

This can be easily derived since, in the present case:

$$e^{ex} = 0 \tag{53}$$

The generalized form of the one-dimensional thrust equation can thus be readily calculated on the basis of these analytical expressions. The effect of the real gas corrections on the non-dimensional thrust as a function of the inlet Mach was validated for the fuel-rich mixture: $2.8CH_4 + 2O_2 + 5.7N_2$. Calculations provided by the "black box" model of this propulsive mode showed that the real gas corrections tend to shift upward the thrust value; thus the propellant mixture is more effective at a higher initial pressure. In addition, the enhancement of thrust tends to increase as the Mach number increases.

Based on the fuel-rich mixture: $2.95CH_4 + 2O_2 + 5.7N_2$, the experimental velocity-distance profiles were in good agreement with the predictions for the thermally choked ram accelerator propulsive mode using a real gas EoS up to about 90 % of the detonation velocity D_{CJ}. In this velocity regime, the experiments start to deviate from theory as the projectile gets close to the CJ detonation velocity (Fig. 6).

It is believed that in this region, the propulsive cycle ceases to be thermally choked as the heat release process begins to move up onto the projectile body [47]. The real gas correction improvement was even more obvious for the experiments having a higher initial pressure value. Polynomials were fit to these *v*-*x* data and

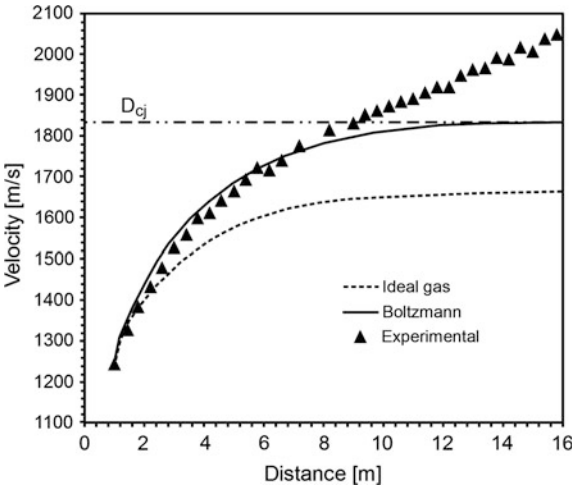

Fig. 6 Velocity versus distance, numerical and experimental results

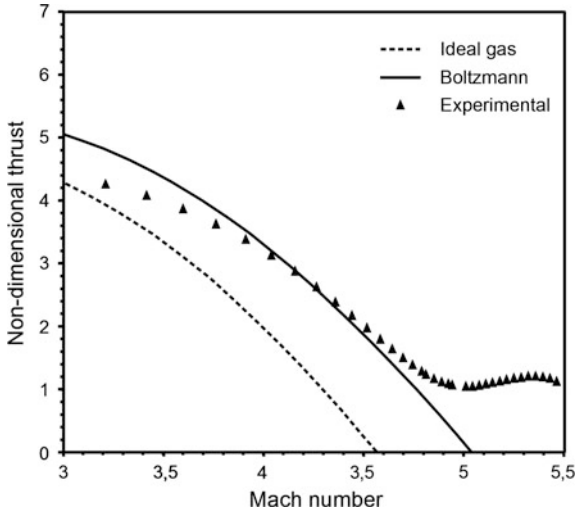

Fig. 7 Non-dimensional thrust versus Mach number, numerical and experimental results

then differentiated once to determine the experimental acceleration, and hence thrust (Fig. 7). Here again, the comparison with calculations based on both the ideal and real gas EOS shows that the corrections significantly improve the agreement between the "black box" calculations and experimental observations at velocities below D_{CJ}. As in the case of velocity-distance records, the experiments start to deviate from theory as the projectile gets close to the CJ detonation velocity. In this domain, the projectiles are believed to undergo a propulsive mode transition, which enables them to accelerate beyond CJ speed.

3.2 Influence of the Compressibility Effects of the Reactants

At initial pressures beyond the range of 10−12 MPa, a further model refinement was required in order to take into account real gas corrections for the initial state. Furthermore, the influence of the equation of state on the prediction of thermodynamic characteristics of the unreacted propellant can be demonstrated. Calculations of the ram accelerator performance in the subdetonative mode on the basis of a quasi-steady modeling of the process with compressible unreacted propellant are presented [4]. These yield a large deviation from the thrust-velocity performance calculations using the ideal gas EoS for the initial state. This modeling is most appropriate for ram accelerator applications where the projectile acceleration is less than 10,000 gees, e.g., direct space launch [58]. Previous studies dealing with detonation of relatively dense gaseous mixtures [8] showed that the two-constant Redlich-Kwong EoS [54], [71] predicts gaseous mixture properties at pressures in the range of 10–50 MPa more accurately than any other cubic EoS. This was further validated by thermochemical calculations that provided a very

accurate prediction of detonation properties of the mixtures [8]. The general analytical form of the non-dimensional thrust for the thermally choked ram accelerator propulsive mode, which has been presented in the first part of this section, was modified accordingly. The QUATUOR code [49, 52] was used in this investigation for determining the thermodynamic properties in the initial state, as well as for the calculation of the chemical equilibrium composition.

In addition, since the density of ram accelerator propellants begins to approach 20 % of water at fill pressures of 20 MPa, efforts were made to determine the sound speed of the reactants under these conditions [29–31]. To address these issues, a general approach for including the compressibility effects of the reactants in the thermally choked ram accelerator propulsive mode modeling, that can accommodate any EoS, is presented here. The upper limit of applicability of this approach, in terms of pressure, is that of the EoS.

Using the general expression of the compressibility factor, with the EoS inserted in the form: $pv/RT = \sigma(v, T)$, Eqs. (44) and (45) yield:

$$e^{ex} = \int_{\infty}^{v} RT^2 \left(\frac{\partial \sigma}{\partial T}\right)_v \frac{dv}{v} \tag{54}$$

The correction term for enthalpy is less readily accessible and requires a different analytical solution:

$$h^{ex} = \int_{\infty}^{v} \left(\frac{\partial h^{ex}}{\partial v}\right)_T dv \tag{55}$$

Or, after some algebraic re-arrangement:

$$h^{ex} = \int_{\infty}^{v} \left[v\left(\frac{\partial p}{\partial v}\right)_T + T\left(\frac{\partial p}{\partial T}\right)_v \right] dv \tag{56}$$

With the use of the compressibility factor:

$$\frac{h^{ex}}{RT} = T\int_{\infty}^{v} \left(\frac{\partial \sigma}{\partial T}\right)_v \frac{dv}{v} + \int_{\infty}^{v} \left(\frac{\partial \sigma}{\partial v}\right)_T dv = T\int_{\infty}^{v} \left(\frac{\partial \sigma}{\partial T}\right)_v \frac{dv}{v} + \sigma - 1 \tag{57}$$

Whereas the caloric imperfection term (η) becomes:

$$\eta = \frac{c_p T + h^{ex}}{c_p T} \tag{58}$$

The influence of real gas corrections to the combustion products on thermally choked ram accelerator performance using the Boltzmann EoS have just been presented as an introduction to this section. At this stage, the main difference of these formulations with that has been presented so far is the general analytical form of the thermodynamic parameters of the initial state. The present investigation is now dealing with the corrections that must be accounted for in the case of reactants at high pressure. At this point, a real gas equation of state is required that is applicable to mixtures of pure gases. It turns out, as it has just been noted that the Redlich–Kwong EoS [54, 71] is appropriate for non-reacting gaseous mixtures at initial pressures in the range of 10–50 MPa. This equation of state is given according to the following form:

$$\frac{pv}{RT} = \sigma(v,T) = \frac{v}{v-b} - \frac{aT^{-1.5}}{R(v+b)} \tag{59}$$

where a and b are physical constants depending on the critical pressure and temperature of the mixture. When dealing with a mixture of pure gases, these critical parameters are determined by a linear mixing rule of the corresponding critical values of each component.

The Redlich–Kwong EoS formulation provides:

$$e^{ex} = \frac{1.5aT^{-0.5}}{b}\ln\frac{v}{v+b} \tag{60}$$

Likewise, using the same equation of state one gets:

$$\frac{h^{ex}}{RT} = \frac{aT^{-1.5}}{Rb}\left(1.5\ln\frac{v}{v+b} - \frac{b}{v-b}\right) + \frac{v}{v-b} \tag{61}$$

Similarly, the constant volume heat capacity correction is readily calculated:

$$c_v^{ex} = \left(\frac{\partial e^{ex}}{\partial T}\right)_v = -\frac{0.75aT^{-1.5}}{b}\ln\frac{v}{v+b} \tag{62}$$

Furthermore, to obtain the correction for γ, one can use the relationship:

$$c_p - c_v = T\left(\frac{\partial v}{\partial T}\right)_p\left(\frac{\partial p}{\partial T}\right)_v \tag{63}$$

This yields:

$$\gamma = \frac{c_p(p,T)}{c_v(v,T)} = 1 + \frac{T}{c_v}\left(\frac{\partial v}{\partial T}\right)_p\left(\frac{\partial p}{\partial T}\right)_v \tag{64}$$

All partial derivatives used in this analysis can be obtained analytically from the formulation of the compressibility factor. Moreover:

$$\left(\frac{\partial p}{\partial T}\right)_v = \frac{\sigma R}{v} + \frac{RT}{v}\left(\frac{\partial \sigma}{\partial T}\right)_v$$
$$\left(\frac{\partial v}{\partial T}\right)_p = \frac{\frac{\sigma}{T} + \left(\frac{\partial \sigma}{\partial T}\right)_v}{\frac{\sigma}{v} - \left(\frac{\partial \sigma}{\partial v}\right)_T} \tag{65}$$

Substituting in the Redlich-Kwong expression for σ:

$$\left(\frac{\partial p}{\partial T}\right)_v = \frac{R}{v-b} + \frac{0.5aT^{-1.5}}{v(v+b)}$$
$$\left(\frac{\partial v}{\partial T}\right)_p = \frac{\frac{v}{T(v-b)} + \frac{0.5aT^{-2.5}}{R(v+b)}}{\frac{v}{(v-b)^2} - \frac{aT^{-1.5}}{R(v+b)}\left(\frac{1}{v} + \frac{1}{v+b}\right)} \tag{66}$$

The actual numerical calculation of all corrected variables requires the determination of both σ and the corrected value of v in the initial state of the propellant mixture. An iterative procedure is used until the Redlich-Kwong EoS is satisfied for the values of v_1 and σ_1 used.

Experiments were conducted at the 38-mm-bore ram accelerator facility of UW with propellants at initial pressures up to 20 MPa [29–31]. On the basis of the analytical procedure that has just been described, calculations were performed in order to show the influence of the compressibility effects on the non-dimensional thrust of the ram accelerator projectile as a function of its velocity. Several cases were computed, corresponding to pressures in the range of 5–20 MPa.

The more significant effect of the EoS for the non-reacting propellant on ram accelerator operation is the change in sound speed that occurs at elevated fill pressures. A plot of sound speed as a function of fill pressure based on the Redlich-Kwong EoS for $3CH_4 + 2O_2 + 5.7N_2$ propellant is shown in Fig. 8. This mixture has currently been used for ram accelerator operations at UW. The calculated sound speed increases by 15 % over that of an ideal gas at fill pressures of 20 MPa, thus it is likely that the minimum entrance velocity to initiate ram accelerator operation with this propellant may increase by nearly 150 m/s (nominal minimum entrance velocity has been determined by Schultz et al. [77] to be approximately 1050 m/s or Mach 2.9 at fill pressures less than 5 MPa). This increase in minimum entrance velocity requirement has indeed been observed in the high-pressure experiments [30]. Another observation in high pressure ram accelerator experiments reported by Bundy et al. [29] that may be due, in part, to reactant compressibility effects is the significant increase in the minimum velocity at which a projectile can maintain supersonic flow through its throat; i.e., the critical cross-section for having a maximum flow rate. Increased acoustic speed due to elevated fill pressure as well as rapid deceleration, are undoubtedly a factor in these results [31].

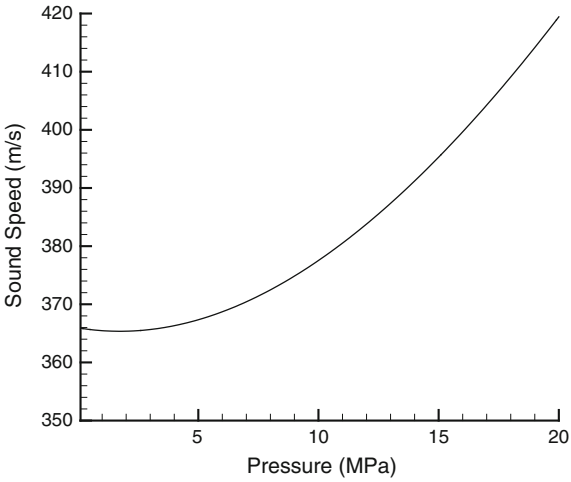

Fig. 8 Sound speed versus fill pressure for $3CH_4 + 2O_2 + 5.7N_2$

A computer code was developed in order to calculate the characteristics of the thermally choked ram accelerator thrust. The non-dimensional thrust was determined at various initial pressures, using the analytical procedure that has just been described. As a reference, the calculation includes the case where the unreacted propellant behaves like an ideal gas. All data related to the reacted state are derived from this computer code which is available at UW [32, 33]. The effect of the correction on the non-dimensional thrust vs. distance calculations are shown in Figs. 9, 10, and 11 for the current mixture used at UW; i.e., $3CH_4 + 2O_2 + 5.7N_2$

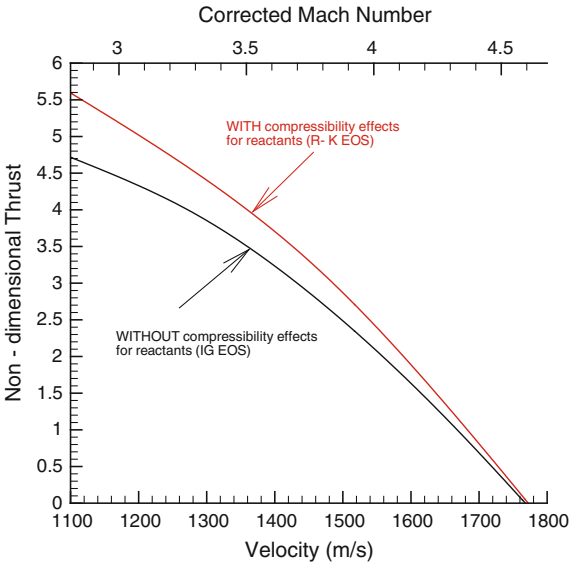

Fig. 9 Non-dimensional thrust versus velocity for $3CH_4 + 2O_2 + 5.7N_2$ at $p_0 = 5$ MPa (Boltzmann EOS used for the calculation of properties of combustion products)

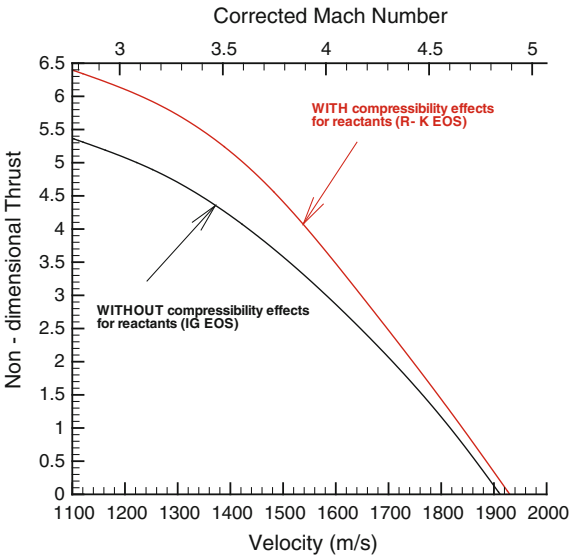

Fig. 10 Non-dimensional thrust versus velocity for $3CH_4 + 2O_2 + 5.7N_2$; $p_0 = 10$ MPa (Boltzmann EOS used for the calculation of properties of combustion products)

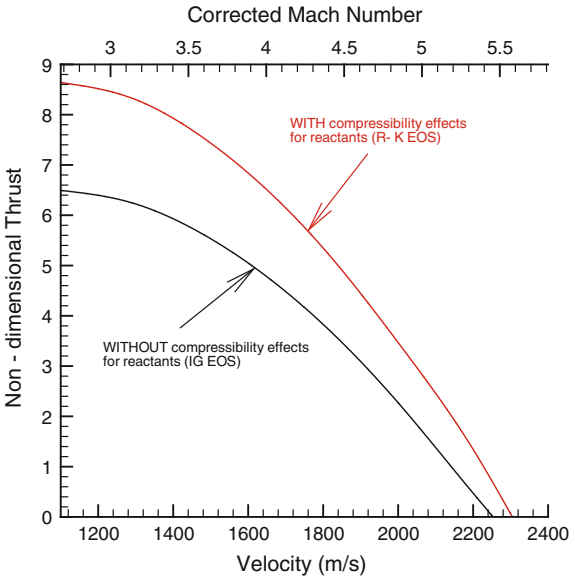

Fig. 11 Non-dimensional thrust versus velocity for $3CH_4 + 2O_2 + 5.7N_2$; $p_0 = 20$ MPa (Boltzmann EOS used for the calculation of properties of combustion products)

propellant at $p_0 = 5$, 10, and 20 MPa, respectively. The influence of the correction on the initial state is readily seen; the higher the pressure, the greater the correction. Thus the non-dimensional thrust is strongly shifted to higher values; i.e., of the order of 20–30 %, depending on the initial pressure of the mixture. Therefore, initial state corrections should be applied to correctly predict the velocity—distance profile of ram accelerator projectiles at velocities 60–80 % of CJ speed under these

conditions. A scale of the real Mach number that takes into account the corrected sound velocity at the corresponding initial pressure is indicated on these plots. It shows the required increase of projectile velocity for attaining a given thrust.

4 Modeling Acceleration Effects on Ram Accelerator Thrust at High Pressure

Prior analytical studies showed that at moderate accelerations; i.e., on the order of 15,000 gees, the unsteady terms in the conservation equations for the thermally choked propulsive mode scarcely exceed a few percent of the magnitudes of the steady convective terms, which allowed them to be neglected [25, 27]. At the high acceleration levels, which typically arise from operating the ram accelerator at elevated pressure, however, the quasi-steady one-dimensional model over-predicts the experimental acceleration when a real-gas equation of state (EoS) is used. Therefore, a revision to the quasi-steady model was made by Bundy et al. [29–31] to account for projectile acceleration on the thrust, the finite-length of the combustion zone, and the dependency of the real-gas heat release on the in-tube Mach number.

The unsteady performance model of Bundy et al. [31] used the ideal-gas EoS, together with a constant heat capacity for both the reactants and combustion products, and the real-gas heat release–Mach number profile calculated with the quasi-steady model. Because a sensitivity analysis had shown that the ram accelerator thrust was most affected by changes in heat release due to real-gas effects, the influence of the real-gas EoS on the sound speed and pressure at the thermal choking point were ignored in this previous modeling effort. It was found that the Mach number dependence of the non-dimensional thrust predicted by the unsteady model deviated considerably from that predicted by the quasi-steady model at high fill pressure, but it agreed more closely with experimental observations. As it has been previously demonstrated, improving the capability of this unsteady one-dimensional modeling by implementing it with more accurate real-gas corrections based on a virial-type EoS [13] was regarded as a pertinent additional step [17]. The influence of the control volume length–Mach number variations on the thrust characteristics of the thermally choked ram accelerator becomes another major issue.

A revised unsteady model that includes the effects of a real-gas EoS for the combustion products was developed for this purpose. It determines the effect of projectile acceleration on the net ram accelerator thrust, as a global process between the state of the propellant entering the control volume and the state of the thermally choked exit flow. In the reference frame of the projectile, the mass, energy, and momentum conservation equations were applied to the propellant flow entering and leaving the control volume, which has a length L_{CV}. Analysis of all the terms in these equations yields a readily applicable set of equations in the form expressed by Bundy et al. [31]. After some algebraic manipulation of these relationships, while

specifying the end state to be thermally choked, i.e., $M_2^2 = \Gamma_2 R_2 T_2 = 1$, and introducing a real-gas EoS [13, 32, 33, 49], namely, $pv/RT = \sigma(v, T)$, with $\alpha = L_{CV} a_p$ the following expressions are derived:

$$\frac{T_2}{T_1} = \frac{c_{p1}}{c_{p2}} \frac{\left(\eta_1 + \frac{M_1^2 \gamma_1 R_1}{2c_{p1}} + Q\right) - \frac{7}{2}\frac{\alpha}{c_{p_1} T_1}}{\left(\eta_2 + \frac{\Gamma_2 R_2}{2c_{p2}}\right)\left[1 - \frac{\alpha}{R_1 M_1^2 \gamma_1 T_1}\right]} \tag{67}$$

$$P = \frac{\sigma_2}{\sigma_1}\left[M_1\sqrt{\frac{\gamma_1 R_2}{\Gamma_2 R_1}} - \frac{\alpha}{R_1 M_1 T_1}\sqrt{\frac{R_2}{R_1 \gamma_1 \Gamma_2}}\right]\sqrt{\frac{T_2}{T_1}} \tag{68}$$

$$I = \frac{\alpha}{R_1 T_1} + \frac{\sigma_2}{\sigma_1}\left(M_1\sqrt{\frac{\gamma_1 R_2}{\Gamma_2 R_1}} - \frac{\alpha}{R_1 M_1 T_1}\sqrt{\frac{R_2}{R_1 \gamma_1 \Gamma_2}}\right)\sqrt{\frac{T_2}{T_1}}\left(1 + \frac{\Gamma_2}{\sigma_2}\right) - \left(1 + M_1^2 \frac{\gamma_1}{\sigma_1}\right) \tag{69}$$

For brevity, the steps required to justify the approximation of the integral terms of the unsteady conservation equations with algebraic expressions that lead to the above set are not included here; the reader is referred to the previous study of Bundy et al. [31] for details. As shown in that work, in the limit of infinite mass, the thrust predicted by the unsteady theory is exactly that predicted by the quasi-steady model for thermally choked ram accelerator operation; i.e., infinite mass results in no acceleration (Eqs. 37–39). For an accelerating projectile in a quiescent propellant, however, the projectile mass is coupled with the acceleration via $I = m_p a_p / p_1 A$ and an iterative approach is required to determine the unique I and a_p which satisfy the governing equations for a given projectile mass and Mach number.

For simplicity, throughout the present study, the ideal gas EoS is taken to describe the initial properties of the mixture; i.e., $\sigma_1 = 1$. For the combustion products, the value of σ_2 is derived from a virial EoS [13, 49]. The thermodynamic properties of the products were primarily determined from the ram accelerator computer code developed at the UW [32, 33]. In order to more accurately account for real gas effects, the c_p values at the thermal choking point determined from the UW code were corrected by the more exact calculations using the QUATUOR code and the virial EoS formulation [49, 52].

Unlike in the quasi-steady-state assumption, the preceding equations show that the non-dimensional thrust, I, is a direct function of both the length of the control volume and the acceleration. An iterative procedure was used to solve for the value of α in Eq. (69) for an arbitrarily chosen value for L_{CV}. The initial value for a_p was that of the steady state calculation. After the value for α converged, it was applied in Eqs. (67) and (68) to yield the values of T_2/T_1, and P, respectively. These values were then used to compute a new σ_2 and the iteration process was repeated until the α, σ_2, T_2/T_1, and P terms had all converged. This approach results in a slightly different heat release–Mach number profile than predicted from the quasi-steady model.

The parameter L_{CV} is a key element in the unsteady modeling because it appears in all the governing equations, i.e., Eqs. 67–69, via the term α. In experiments at fill pressures of 2.5 MPa, it was observed that the combustion during thermally choked ram accelerator operation at Mach 3.7 is typically completed within approximately one projectile length behind the projectile base [27]. Therefore, the value $L_{CV} = 2L_p$ was chosen in previous studies [27, 31]. Recent experiments were carried out at both 15 and 20 MPa fill pressure in a 4-m-long, 38-mm-bore ram accelerator test section, with 118 g titanium alloy projectiles [31]. The influence of L_{CV} on the theoretical non-dimensional thrust versus Mach number behavior is compared hereafter in Fig. 12 with the 15 MPa experiment. Based on signal distortion and sensor sampling rate (1 MHz) of center-differenced time-distance data, the experimental Mach-distance records were determined with a Mach number uncertainty of about ±3 %. The experimental acceleration was determined by double-differentiating time-distance data from instrumentation stations that are separated by 1.0–1.7 m; which results in uncertainties of ~70 % for the non-dimensional thrust. These uncertainties are indicated by the vertical error bars in Fig. 12.

One of the theoretical curves in Fig. 12 was calculated with the assumption that L_{CV} was fixed at twice the projectile length, as has been done previously [27, 31]. The length of the combustion zone, however, is expected to decrease with increasing Mach number since the static temperature increases, which, in turn, enhances the chemical kinetic rates. In order to examine the effects of a Mach number-dependent control volume length, the non-dimensional thrust versus Mach number behaviors were determined when L_{CV} varied linearly from both $4Lp$ to Lp and $6Lp$ to Lp over the Mach number range of 3 to M_{CJ}. The larger the value of L_{CV} at lower Mach number, the greater the reduction in thrust is from that of the

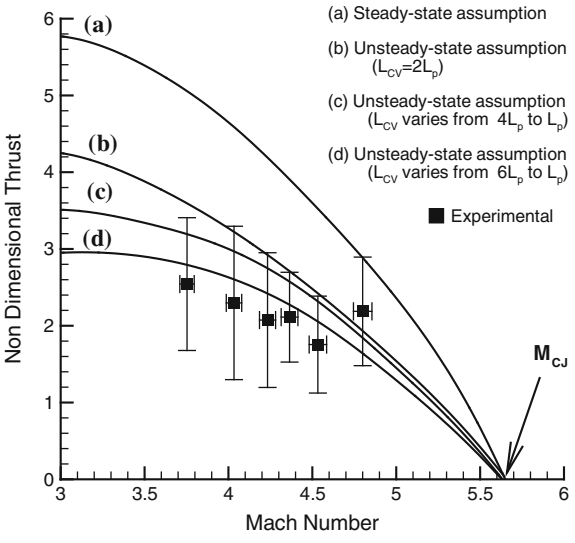

Fig. 12 Experimental thrust-Mach data with unsteady modeling (propellant: $2.6CH_4 + 2O_2 + 9.2N_2$ at $p_1 = 15$ MPa); projectile mass: $m_p = 118$ g

steady-state prediction. All of the thrust coefficient curves converge to zero at the same Mach number because the zero thrust condition for thermally choked flow at a given pressure is always that of a CJ detonation wave in the propellant. Consequently, the significance of the Mach number dependence for L_{CV} diminishes as the projectile velocity approaches that of M_{CJ}.

The control volume length that would be most appropriate in the unsteady ram accelerator model at a given projectile Mach number is very much related to the chemical kinetics of the process. Although it has been shown that the conical shock wave generated by the projectile nose tip and its multiple reflections prior to the combustion zone heat the flow in the ram accelerator [16, 75], only the effect of a single shock wave was examined here to determine the order of magnitude of the change in length of the combustion zone one may expect as the Mach number is increased. The Mach number dependence on the induction length behind an incident shock for the $2.6CH_4 + 2O_2 + 9.2N_2$ propellant, used in this study, was calculated with the CHEMKIN computer code [70], using the GRI kinetic scheme [79] for methane combustion under ideal-gas EoS conditions. The results are shown in Fig. 13. Although this kinetic scheme for fuel-rich propellants at high pressure has not been validated, these calculations do provide a qualitative description of the variation of L_{CV} with Mach number at velocities below M_{CJ}.

Figure 12 shows that in the Mach number range of 3.7–4, L_{CV} varies exponentially between $6L_p$ and L_p, where L_p is 125 mm. The goal of the present study, however, is not to determine the best fit for the Mach number dependence of L_{CV}, but rather to illustrate that performance predictions are very sensitive to the choice of these models.

Some of the other factors, which significantly influence the control volume length, are: real gas reaction kinetics, turbulence, shock-boundary layer interaction,

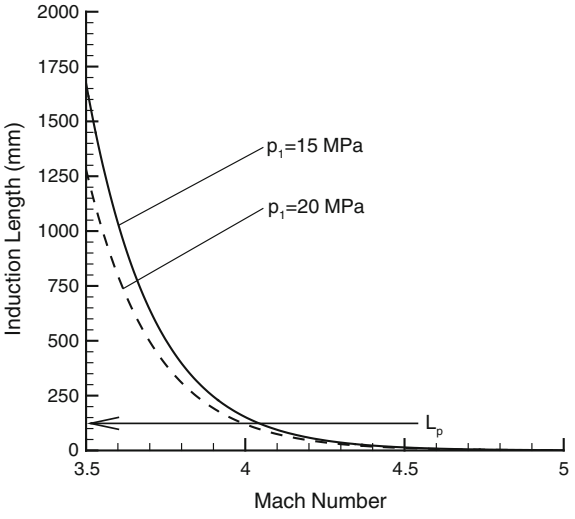

Fig. 13 Variation of the calculated induction length downstream of a normal shock wave

and heating of the flow by multiple shocks [76]. Consequently, a more refined analysis involving a detailed modeling of the flow field from the projectile nose tip to the choking point is needed to accurately determine the Mach number dependence of the control volume length. This can be achieved by means of the CFD modeling that has been presented in Sect. 2 of the present chapter.

5 Improved 1D Unsteady Modelling

5.1 CFD Data Input

Based on the developments that have just been presented, the implementation of a 1D modelling to predict the thrust in the thermally choked ram accelerator under conditions of high acceleration has now become a key issue. As it has just been shown, this modelling is strongly dependent on the control volume length, which is a representation of the distance within which the combustion process goes to completion, i.e., thermal choking. Furthermore, the influence of Mach number on the control volume length determined from CFD simulations using five-step kinetic reaction mechanisms can be used for improving this unsteady one-dimensional model calculation. Besides providing numerical results that show the Mach number influence on the control volume, these data can be used in the unsteady one-dimensional modeling.

In the light of previous data derived from CFD analysis, one can now focus on the improvement of 1D unsteady modelling [22–24] in order to provide more reliable thrust predictions for the thermally choked ram accelerator. It is known that the 1D modelling results will be dependent on an appropriate estimation of the control volume length, which is a representative length within which the combustion process is occurred and completed, as it has been explained in the previous section. As it has been expressed, most previous 1D models were using a unique control volume length that equals several times, which, in most cases was taken as exactly twice, the projectile length. While results have shown broad agreement with the measurement data, some discrepancies do exist particularly in the higher Mach number (>3.5) range corresponding to high velocity ram accelerator operation.

In order to improve the 1D unsteady model calculations, the aforementioned CFD simulation has been used to predict the control volume length variation at various incoming velocities. The calculation covers a wide range of incoming flow speeds over the projectile up to a fully established thermally choked propulsive mode. This is corresponding to a speed of about 1240 m/s. At this velocity speed, the CFD predicted the control volume length (L_{cv}) in which the combustion will be completed is about $2.8L_p$. As incoming velocity increases, it increases initially to maximum of about $3.6L_p$, then adversely decreases to about $1.1L_p$ at velocity 1829 m/s. After this velocity, it remains near constant.

By using the CFD predicted control volume length in the 1D unsteady modelling, the results have shown considerable improvements in comparison with

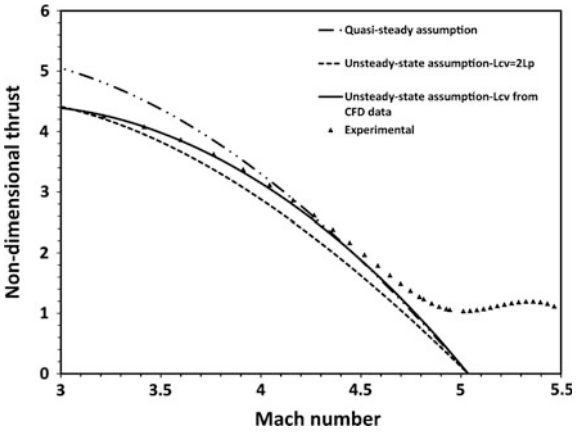

Fig. 14 Improvement of the 1D model of the RAMAC thermally choked propulsive mode based on ideal gas EoS and CFD data

experimental data (Fig. 14). At high Mach number of $M = 4.6$, a small deviation on the thrust curve is shown. This may be due to the fact that at this point, the projectile is approaching the Chapman-Jouguet detonation speed ($M \approx 5.05$), where a trans-detonative propulsive mode might occur. It is worth pointing that the present CFD modelling is merely based on the ideal gas assumption, which is actually unable to accurately describe the characteristics of combustion products at extremely high-pressure levels. Some suggestions for more appropriate EOS will be provided in the last part of this section.

Another observation is that, in the higher range of Mach numbers, in this case the quasi-steady 1D modelling has shown surprisingly good agreement with the experimental data and even slightly better than predicting while using the unsteady modelling. This is probably due to the fact that the acceleration effect is relatively low, i.e., the projectile having an acceleration of 2.5×10^5 m/s^2.

Based on these findings, the computer code, TARAM, which was elaborated earlier, has been implemented [22]. It now allows calculating the ram accelerator performance, using either a quasi-steady or unsteady assumption; in which case, the CFD data are included and used for the determination of L_{CV}. Moreover, it can incorporate any type of equation of state both for the propellant mixture and the combustion products, which turns this code into a very reliable and accurate tool for the prediction of ram acceleration performance. The next and final step now is to evaluate the applicability of other equations of state. The code will be used for this purpose.

5.2 *On the Selection of Equation of State with Reference to Scale Effect*

Even though the agreement between 1D modeling and experiment is very good, as shown in Fig. 14 when using the CFD-determined control volume length and

assuming the ideal gas EoS, it is of interest to develop ability to incorporate an EoS that would be more appropriate for RAMAC operation at fill pressures in the range of 7–30 MPa. Another issue is the validity of the improved 1D modeling for different projectile scales [39, 60, 61].

Computing the compressibility factor for a given EoS is the basis for incorporating real gas corrections. Numerous equations of state have been developed based on generalized empirical and theoretical considerations of Heuzé [48]. At this point several equations of state are suited to predict the thermochemical properties of combustion products. Depending on the pressure range some are more pertinent for use. In the present case, a virial type, namely the Boltzmann EoS [10] has been extensively used and its applicability to the RAMAC calculations has been widely demonstrated. It is currently running in the TARAM code. However, the use of other EoS, which have been previously validated for the detonation at high initial pressures, including high explosive cases can be considered [8, 9]. In this latter case, another EoS based on adjustable parameters that could be suited to fit the present use is worth investigating. For this purpose, the Becker, Kistiakowsky and Wilson (BKW) EoS [66] is investigated here. The main reason is its applicability to a wide range of temperatures and pressures of combustion products that cover the whole field of gaseous to condensed explosives, based on the appropriate choice of the adjustable parameters.

This EoS was introduced in 1921 by Becker, and later modified by Kistiakowsky and Wilson [66]. It can be presented as follows:

$$\frac{pv}{RT} = 1 + xe^{\beta x} \tag{70}$$

with:

$$x = \frac{\kappa B}{v(T+\theta)^{\alpha}}; \quad B = \sum_i x_i B_i \tag{71}$$

where α, κ, θ are semi-empirical constants that must be adjusted, B_i are the co-volumes with no link to the co-volume defined in Boltzmann equation of state. This form of EoS is mostly used for condensed explosives; however, a previous investigation [22, 48] showed that it could be used for the calculation of gaseous detonation characteristics at extremely elevated pressures. In this specific case, all the adjustable parameters must be set accordingly. In order to evaluate the ability of this code for predicting the performance for any size of facility, which would make it non scale-dependent, the results of calculation were compared with experimental data for both the UW ram accelerator facility and that of ISl, at a larger caliber tube [39, 40, 43].

The experimental data from the UW are plotted in Fig. 15, along with the 1D modelling results using the Boltzmann and the BKW EoS, and the CFD-determined control volume dependence on velocity. It is evident that the Boltzmann predictions

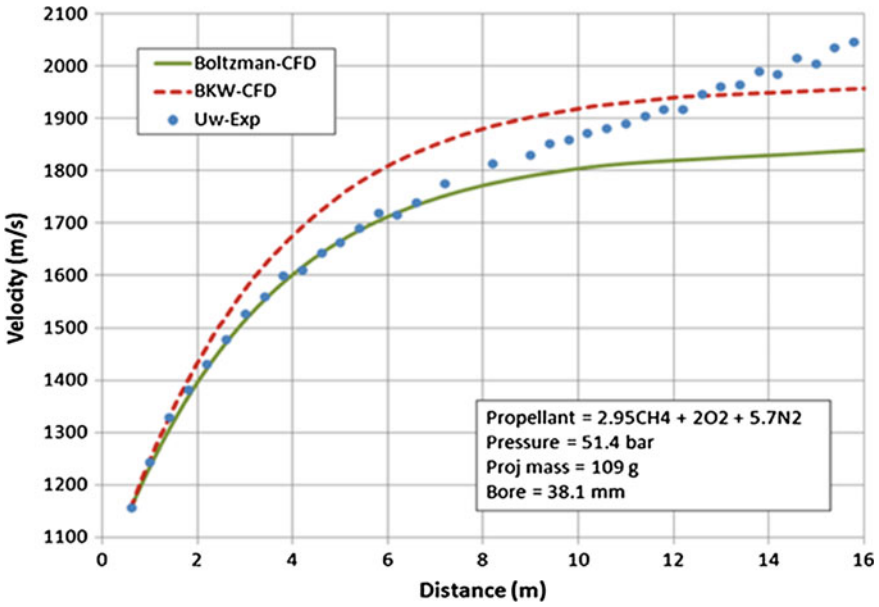

Fig. 15 Experimental and theoretical velocity-distance for RAMAC experiments in 38-mm-bore

agree very well up to a velocity of $\sim$1750 m/s, which is $\sim 0.95 D_{CJ}$, as predicted by this EoS, whereas the BKW results over-predict performance for this situation. The latter result is not unexpected since the CJ speed predicted for this propellant by the BKW EoS is about 10 % higher than that measured in experiments at this fill pressure.

The ISL experimental data are plotted in Fig. 16 along with the 1D modelling results using the Boltzmann and the BKW EoS, and the CFD-determined control volume dependence on velocity. Note that in this case the control volume length was geometrically scaled from CFD results for the 38-mm-bore and the ratio of propellant-to-projectile density ratio for the 90-mm experiment was less than that of the 38-mm experiment by more than an order of magnitude. The low propellant-to-projectile density ratio is consistent with the acceleration level being about 1/5th that of the 38-mm-bore experiment. In this case the BKW predictions agreed with experiment better than those based on the Boltzmann EoS.

The experimentally determined thrust data from the UW (38-mm-bore) are plotted along with the theoretical results using the ideal gas (Fig. 17), Boltzmann (Fig. 18), and BKW (Fig. 19) EoS and the CFD-determined control volume dependence on velocity. As previously demonstrated, the ideal gas EoS under-predicts the thrust in the region near the CJ detonation speed (Fig. 17). It is evident that the Boltzmann EoS modeled the thrust behavior within 3 % over the Mach range of 3.2–4.6, which is $\sim 0.95 D_{CJ}$ predicted by these EoS. Here again, the BKW

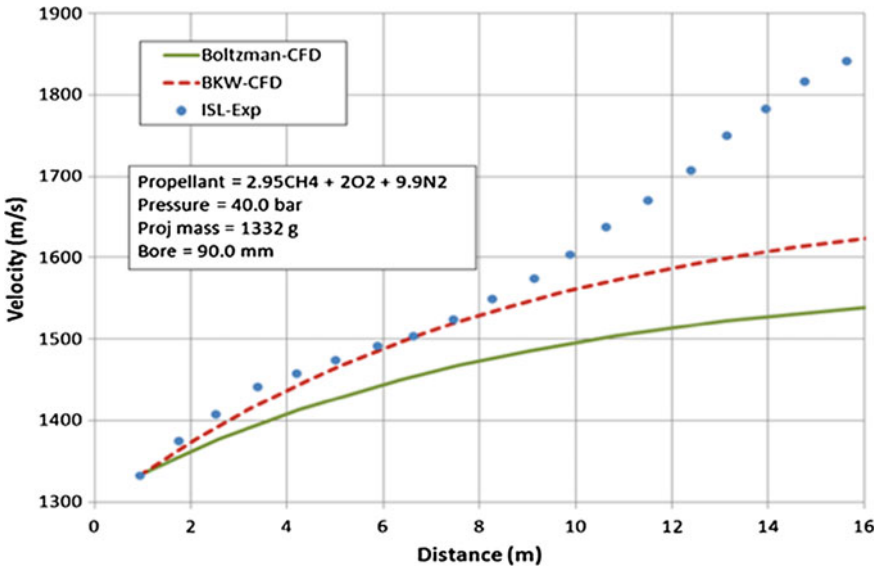

Fig. 16 Experimental and theoretical velocity-distance for RAMAC experiments in 90-mm-bore

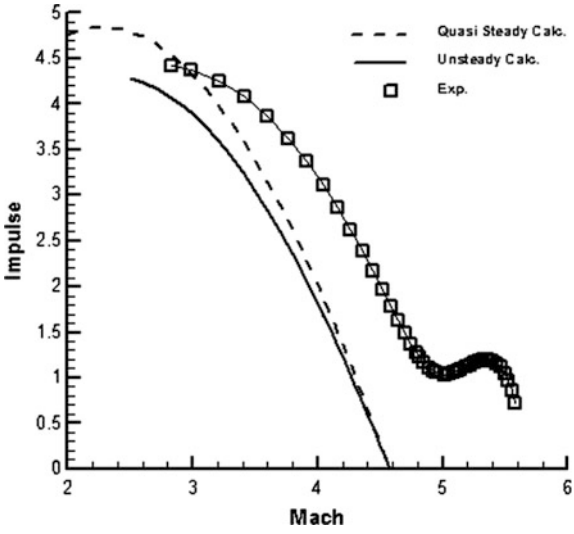

Fig. 17 Non-dimensional Thrust-Mach-Number plot for $2.95CH_4 + 2O_2 + 5.7N_2$ propellant, $p_0 = 5.0$ MPa (Ideal gas EoS was used both at station 1 and for the calculation of properties of combustion products)

results over predict performance for this situation, as observed with the velocity data.

The ISL experimental data (90-mm-bore) are plotted in Fig. 20 along with the theoretical results using the Boltzmann and the BKW EoS and the CFD- determined

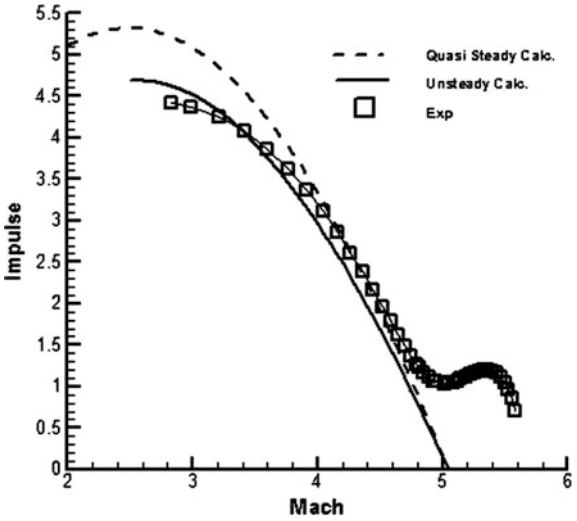

Fig. 18 Non-dimensional Thrust-Mach-number plot for $2.95CH_4 + 2O_2 + 5.7N_2$ propellant, $p_0 = 5.0$ MPa (Ideal gas EoS was used at station 1 and Boltzmann EoS was used for the calculation of properties of combustion products)

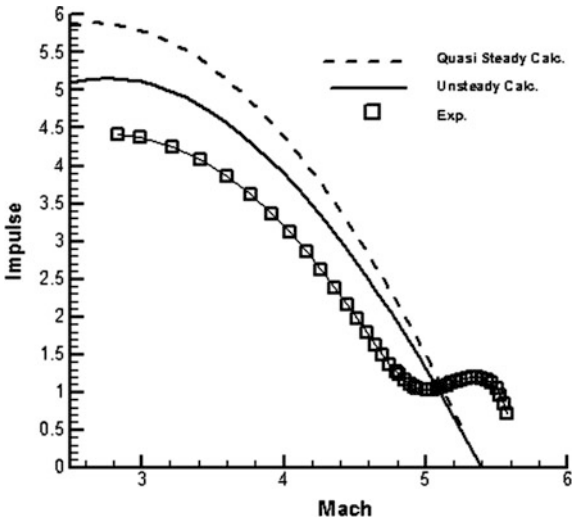

Fig. 19 Non-dimensional Thrust-Mach-number plot for $2.95CH_4 + 2O_2 + 5.7N_2$ propellant, $p_0 = 5.0$ MPa (Ideal gas EoS was used at station 1 and BKW EoS was used for the calculation of properties of combustion products)

control volume dependence on velocity. The discrepancy in the thrust-velocity predictions of the TARAM code when using Boltzmann and BKW EoS for the 38-mm-bore and 90-mm-bore may be due to the control volume length scaling used in these computations. This matter must be investigated in more detail with large-scale CFD modeling, which may improve the slight disagreement that remains in the lower range of Mach numbers.

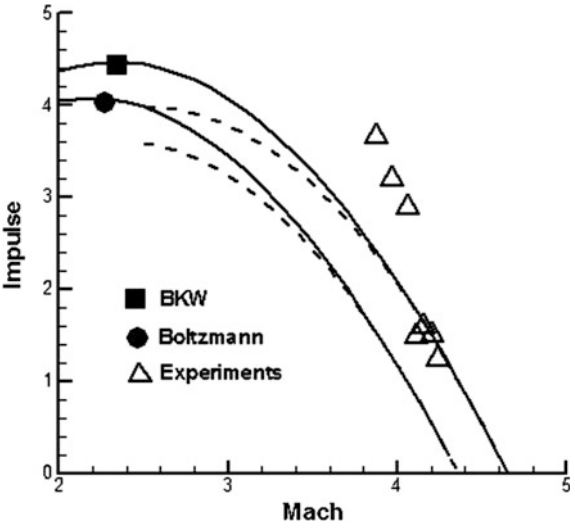

Fig. 20 Non-dimensional Thrust-Mach-number plot for $2.95CH_4 + 2O_2 + 9.9N_2$ propellant, $p_0 = 4.0$ MPa (Ideal gas EoS was used at station 1 and Boltzmann and BKW EoS's were used for the calculation of properties of combustion products; solid and dashed lines are quasi-steady and unsteady assumption, respectively)

6 Conclusion and Perspectives

This chapter is intended to show the various steps taken for modeling the flow around projectile in the ram accelerator in subdetonative propulsion mode. The early 1D modeling is shown and the steps that now lead to the final form of this 1D modeling are shown in details. This required a more sophisticated analysis of the hypothesis that prevail in this 1D modeling, including the use of more pertinent equations of state to account for compressibility effects of both the combustion products and the unreacted propellants. The quasi-steady approach of the phenomena was further improved by an unsteady assumption, and, furthermore, a CFD modeling of the reactive flow turned out to provide an additional improvement tool. This finally led to the 1D unsteady assumption which is now totally derived form CFD calculation and makes this simple 1D modeling a fairly reliable tool for predicting the ram accelerator performance.

The calculations were successfully validated by numerous experiments, most of them being conducted at the ram accelerator facility of University of Washington. However, besides the quality of such agreement, the applicability to larger projectile scales of this modeling, together with the versatility of the computer code, TARAM, that was developed, remains a key issue. Some calculations turned out to be satisfactorily validated by experiments performed with the 90-mm ram accelerator at the French-German Research Institute of Saint-Louis (ISL), i.e., at a slightly larger scale. However, the recent results show that, for instance, a further analysis of the EoS, in this larger scale environment, may be an additional interesting investigation route. In the long run, further experiments together with more refined analysis of this 1D modeling are still needed. The kinetic approach that prevailed in the CFD modeling is one major element of this analysis.

Yet, at this time, the contour of the main issues of this modeling begins to be more clearly defined. The present findings provide appropriate tools, both in terms of understanding the process and its obstacles, and in terms of numerical and analytical procedures.

References

1. Ahuja, J.K., Tiwari, S.N.: Effect of various flow and physical parameters on stability of shock-induced combustion. In: AIAA (ed.) Proceedings of the 34th Aerospace Sciences Meeting, Reno, NV, USA, paper 96-0732 (1996)
2. Auzias De Turenne, J., Chew, G., Bruckner, A.P.: Recent results from the University of Washington's 38 mm ram accelerator. In: AIAA (ed.) Proceedings of the 28th Joint Propulsion Conference, Nashville, TN, USA, paper 92-3782 (1992)
3. Bauer, P., Brochet, C.: Properties of detonation waves in hydrocarbon-oxygen-nitrogen mixtures at high initial pressures. In: AIAA (ed.) Progress in Aeronautics and Astronautics, vol. 87, pp. 231–243. AIAA, New York (1983)
4. Bauer, P., Knowlen, C.: Compressibility effects of unreacted propellant on thermally choked ram accelerator performance. Eur. Phys. J. Appl. Phys. **21**, 233–238 (2003)
5. Bauer, P., Legendre, J.F.: Detonability limits of propellant mixtures used in the ramac. In: Murphy, M.J., Backofen, M.J.E. (eds.) Proceedings of the 14th International Symposium on Ballistics, Québec, Canada, p. 389 (ISBN 0-9618156-9-8) (1993)
6. Bauer, P., Brochet, C., Krishnan, S.: Detonation characteristics of gaseous ethylene, oxygen and nitrogen mixtures at high initial pressures. In: AIAA (ed.) Progress in Aeronautics and Astronautics, vol. 75, pp. 408–422. AIAA, New York (1981)
7. Bauer, P., Presles, H.N., Heuzé, O., Brochet, C.: Equation of state for dense gases. Arch. Combust. **5**(1), 315–320 (1985)
8. Bauer, P., Dunand, M., Presles, H.N.: Detonation characteristics of methane oxygen and nitrogen at extremely high initial pressures. In: AIAA (ed.) Progress in Aeronautics and Astronautics, vol. 133, pp. 56–62. AIAA, New York (1991)
9. Bauer, P., Dunand, M., Presles, H.N., Heuzé, O.: Investigation on extremely dense gaseous explosives. In: Proceedings of 17th International Symposium on Pyrotechnics and Explosives, pp. 551–556. China Academic Publishers, Beijing, China, (1991)
10. Bauer, P., Presles, H.N., Heuzé, O., Legendre, J.F.: Prediction of detonation characteristics of dense gaseous explosives on the basis of virial equation of state. In: Proceedings of the 20th International Pyrotechnics Seminar, Colorado Springs, CO, USA (1994)
11. Bauer, P., Legendre, J.F., Knowlen, C., Higgins, A.J.: Detonation of insensitive dense gaseous mixtures in tubes. In: AIAA (ed.) Proceedings of the 32nd Joint Propulsion Conference, Lake Buena Vista, FL, USA, paper 96-2682 (1996)
12. Bauer, P., Knowlen, C., Higgins, A.J., Legendre, J.F.: Detonation initiation of insensitive dense gaseous mixtures by piston impact. In: Houwing, A.F.P. (ed.) Proceedings of the 21st International Symposium on Shock Waves, Great Keppel Island, Australia, p. 1609. University of Queensland (1997)
13. Bauer, P., Knowlen, C., Bruckner, A.P.: Real gas effects on the prediction of ram accelerator performance. Shock Waves **8**, 113–118 (1998)
14. Bauer, P., Legendre, J.F., Knowlen, C., Higgins, A.J.: A review of detonation initiation techniques for insensitive dense methane-oxygen-nitrogen mixtures. Eur. Phys. J. Appl. Phys. **2**, 183 (1998)
15. Bauer, P., Knowlen, C., Bruckner, A.P., Henner, M.: Determination of choke pressure of ram accelerator in sub-detonative mode. J. Phys. **10**, 59–67 (2000)

16. Bauer, P., Henner, M., Giraud, M.: Numerical investigation of the fin geometry of ram accelerator projectiles in subdetonative propulsion mode. Eur. Phys. J. Appl. Phys. **23**, 136–145 (2003)
17. Bauer, P., Knowlen, C., Bruckner, A.P.: Modeling acceleration effects on ram accelerator thrust at high pressures. AIAA J. Propul. Power **21**, 955–995 (2005)
18. Bender, R., Menter, F.R.: Coupling of large Eddy simulation with Eddy dissipation model. The 5th Framework Programme, Progress Report, ANSYS-CFX Ltd (1998–2002)
19. Bengherbia, T.: Contribution to numerical simulation analysis of the flow in the ram accelerator in the sub-detonative propulsion mode. Ph.D. Dissertation, Laboratoire de Combustion et de Détonique (LCD), CNRS, ENSMA, Poitiers, France (2009)
20. Bengherbia, T., Yao, Y.F., Bauer, P.: Computational Investigation of Transitional Viscous Flow over a Ram Accelerator Projectile in Sub-detonative Propulsion Mode. AIAA 2006-0558 (2006)
21. Bengherbia, T., Yao, Y.F., Bauer, P., Knowlen, C.: Numerical Investigation of Thermally Choked Ram Accelerator in Sub-detonative Regime. AIAA 2009-0635 (2009)
22. Bengherbia, T., Yao, Y., Bauer, P., Knowlen, C.: One-dimensional performance modeling of the RAMAC in subdetonative regime. Aerotecnica J. Aerospace Sci. Tech. Syst. **89**, 3–13 (2010)
23. Bengherbia, T., Yao, Y., Bauer, P., Giraud, M., Knowlen, C.: Improved 1D unsteady modeling of the thermally choked RAMAC in the sub-detonative propulsion mode. J. Appl. Mech. **78**, 150–167 (2011)
24. Bengherbia, T., Yao, Y., Bauer, P., Knowlen, C.: CFD-based 1D modeling of the thermally choked ram accelerator. In: Proceedings of the 50th AIAA Aerospace Sciences Meeting and Exhibit, Nashville, TN, AIAA 2012-982 (2012)
25. Brouillette, M., Frost, D.L., Zhang, F., Chue, R.S., Lee, J.H.S., Thibault, P., Yee, C.: Limitations of the ram accelerator. In: Brun, R., Dumitrescu, L.Z.: Shock Waves at Marseille Vol. 1: Hypersonics, Shock Tube and Shock Tunnel Flow, pp. 171–176. Springer, Berlin (1995)
26. Bruckner, A.P., Burnham, E.A., Knowlen, C., Hertzberg, A., Bogdanoff, D.W.: Initiation of combustion in the thermally choked ram accelerator. In: Takayama, K. (ed.) Shock Waves Proceedings, Sendai, Japan, vol. II. Springer, Heidelberg (1991)
27. Bruckner, A.P., Knowlen, C., Hertzberg, A., Bogdanoff, D.W.: operational characteristics of the thermally choked ram accelerator. J. Propul. Power **7**(5), 828–836 (1991)
28. Bruckner, A.P., Hinkey, J.B., Burnham, E.A., Knowlen, C.: Investigation of 3-D reacting flow phenomena in a 38 mm ram accelerator. In: Giraud, M., Smeets, G. (eds.) Proceedings of the 1st International Workshop on Ram Accelerators, Seattle, Saint-Louis, France (1993)
29. Bundy, C., Knowlen, C., Bruckner, A.P.: Ram Accelerator Operating Characteristics at Fill Pressures Greater than 10 MPa. AIAA Paper 99-2261 (1999)
30. Bundy, C., Knowlen, C., Bruckner, A.P.: Investigation of Ram Accelerator Operation at Fill Pressures up to 20 MPa. AIAA Paper 2000-3231 (2000)
31. Bundy, C., Knowlen, C., Bruckner, A.P.: Unsteady effects on ram accelerator operation at elevated fill pressures. J. Propul. Power **20**, 801–810 (2004)
32. Buckwalter, D.L., Knowlen, C., Bruckner, A.P.: Ram Accelerator Performance Code Incorporating Real Gas Effects. AIAA paper 96-2945 (1996)
33. Buckwalter, D.L., Knowlen, C., Bruckner, A.P.: Real Gas Effects on Ram Accelerator Analysis. AIAA paper 97-2894 (1997)
34. Byers Brown, W., Amaee, A.: Review of equations of state of fluids valid to high densities. Report # 39/1992. Dept of Chemistry, University of Manchester, U.K. (1992)
35. Chiping, L., Kailasanath, K., Oran, E.S., Landsberg, A.M., Boris, J.P.: Dynamics of oblique detonations in ram accelerators. Shock Waves **5**, 97 (1995)
36. Dabora, E.K., Desbordes, D., Guerraud, C., Wagner, H.G.: Oblique detonation at hypersonic velocities. Progress Astronaut. Aeronaut. AIAA J. **133**, 187 (1991)
37. Desbordes, D., Hamada, L., Guerraud, C.: Supersonic H_2-air combustion behind oblique shock waves. Shock Waves **4**, 339 (1995)
38. Giraud, M., Simon, G.: Sabot for Projectiles of Ram Accelerators and Projectiles Equipped with such a Sabot. United States Patent No 5, 394, 805

39. Giraud, M., Legendre, J.F., Simon, G., Catoire, L.: Ram accelerator in 90 mm caliber. First results concerning the scale effect in the thermally choked propulsion mode. In: Proceedings of the 13th International Symposium on Ballistics, Stockholm, Sweden (1992)
40. Giraud, M., Legendre, J.F., Simon, G.: RAMAC 90: experimental studies and results in 90 mm caliber, length 108 caliber. In: Giraud, M., Smeets, G. (eds.) Proceedings of the 1st International Workshop on Ram Accelerators, Saint-Louis, France (1993)
41. Giraud, M., Legendre, J.F., Simon, G., Henner, M., Voisin, D.: RAMAC in 90 mm caliber or RAMAC 90. Starting process, control of the ignition location and performances in the thermally choked propulsion mode. In: Bruckner, A.P., Knowlen, C. (eds.) Proceedings of the 2nd International Workshop on Ram Accelerators, Seattle, WA, USA. University of Washington (1995)
42. Giraud, M., Legendre, J.F., Henner, M.: RAMAC in subdetonative propulsion mode: state of ISL studies. In: Takayama, K., Sasoh, A. (eds.) Ram Accelerators. Springer, Berlin (1997)
43. Giraud, M., Legendre, J.F., Henner, M.: RAMAC in subdetonative propulsion mode: state of the ISL studies. In: Takayama, K., Sasoh, A. (eds.) Ram Accelerators, pp. 65–78. Springer, Heidelberg (1998)
44. Henner, M., Giraud, M., Legendre, J.F., Berner, C.: Initiation of reactive mixtures in a ram accelerator. In: AIAA (ed.) Proceedings of the 33rd Joint Propulsion Conference, July 7–9, Seattle, WA, USA, pp. 97–3173 (1997)
45. Henner, M., Giraud, M., Legendre, J.F., Berner, C.: CFD computations of steady and non-reactive flow around fin-guided ram projectiles. In: Takayama, K., Sasoh, A. (eds.) Ram Accelerators. Springer, Berlin (1997)
46. Hertzberg, A., Bruckner, A.P., Bogdanoff, D.W.: Ram accelerator: a new chemical method for accelerating projectiles to ultrahigh velocities. AIAA J. **26**(2), 195–203 (1988)
47. Hertzberg, A., Bruckner, A.P., Knowlen, C.: Experimental investigation of ram accelerator propulsion modes. Shock Waves **1**(1), 17–25 (1991)
48. Heuzé, O.: Equations of state of detonation products. Phys. Rev. A **34**, 428–432 (1986)
49. Heuzé, O., Bauer, P., Presles, H.N., Brochet, C.: Equations of state for detonation products and their incorporation into the QUATUOR Code. In: Proceedings of the 8th Symposium (Int.) on Detonation, pp. 762–769 (1986)
50. Heuzé, O., Presles, H.N., Bauer, P.: Computation of chemical equilibrium. J. Chem Phys. **38**, 4734–4737 (1987)
51. Heuzé, O., Bauer, P., Presles, H.N.: Compressibility and thermal properties of gaseous mixtures at a high temperature and high pressure. High Temperatures, High Pressures, no 19, pp. 611–620 (1987)
52. Heuzé, O., Bauer, P., Presles, H.N.: QUATUOR: A Code for Computing Thermodynamic Properties of Detonation and Combustion Products, Seriep Ed., Paris, pp. 91–96 (1987)
53. Higgins, A.J.: Detonation initiation by supersonic blunt bodies. Ph.D. Dissertation, University of Washington, Seattle, WA, USA (1996)
54. Kemp, M.K., Thompson, R.E., Zigrang, D.J.: Equations of state with two constants. J. Chem. Educ. **49**, 802–803 (1975)
55. Kovacik, G.J., Knill, K.J. (1994) Numerical simulation of coal gasification reactors. In: International Joint Power Generation Conference and Exposition, Phoenix, USA (1994)
56. Knowlen, C.: Theoretical and experimental investigation of the thermodynamics of the thermally choked ram accelerator. Ph.D. Dissertation, University of Washington, Seattle, WA, USA (1991)
57. Knowlen, C., Bruckner, A.P.: A Hugoniot analysis of the ram accelerator. In: Takayama, K. (ed.) Shock Waves Proceedings, Sendai, Japan, vol. I. Springer, Heidelberg (1991)
58. Knowlen, C., Bruckner, A.P.: Direct Launch Using Ram Accelerator Technology, Space Technology an Applications. In: El-Genk, M.S. (ed.) Int. Forum, pp. 583–588. American Institute of Physics (2001)
59. Knowlen, C., Higgins, A.J., Bruckner, A.P., Bauer, P.: Ram Accelerator Operation in the Superdetonative Velocity Regime. AIAA paper 96-0098 (1996)

60. Kruczynski, D.L.: New experiments in a 120-mm ram accelerator at high pressures. In: 29th AIAA, SAE, ASME, and ASEE Joint Propulsion Conference and Exhibit, Monterey, CA (1993)
61. Kruczynski, D.: Experiments in a 120-mm ram accelerator. In: Murphy, M.J., Backofen, M.J. E. (eds.) Proceedings of the 14th International Symposium on Ballistics, Québec, Canada (ISBN 0-9618156-9-8), p. 173 (1993)
62. Lefebvre, M.H.: Modeling of unstarts in ram accelerator. In: Bruckner, A.P., Knowlen, C. (eds.) Proceedings of the 2nd International Workshop on Ram Accelerators, Seattle, WA, USA. University of Washington (1995)
63. Legendre, J.F., Giraud, M., Bauer, P., Voisin, D.: 90L35 detonation tube experiments: influence of diluent nature on the detonation characteristics of dense methane-based gaseous explosives. In: Bruckner, A.P., Knowlen, C. (eds.) Proceedings of the 2nd International Workshop on Ram Accelerators, Seattle, WA, USA. University of Washington (1995)
64. Legendre, J.F., Bauer, P., Giraud, M.: RAMAC 90: detonation initiation of insensitive dense methane-based mixtures by normal shock waves. In: Takayama, K., Sasoh, A. (eds.) Ram Accelerators. Springer, Berlin (1997)
65. Lehr, H.F.: Experiments on shock-induced combustion. Astronaut. Acta **17**, 589 (1972)
66. Mader, C.L.: Detonation Properties of Condensed Explosives Computed Using the Becker–Kistiakowsky–Wilson Equation of State. Report-LA-2900. Los Alamos Scientific Laboratory, NM, USA (1963)
67. Menter, F.R.: Zonal two Equation k-ω Turbulence Models for Aerodynamic Flows. AIAA paper 93-2906 (1993)
68. Magnussen, B.R.F.: On the structure of turbulence and a generalized eddy dissipation concept for chemical reaction in turbulent flow. In: 19th Aerospace Sciences Meeting, St. Louis, Mo., 1981, AIAA paper 1981-42 (1981)
69. Magnussen, B.F, Hjertager, B.H.: Eddy dissipation in turbulent reacting flows. In: 16th International Symposium on Combustion, p. 719. The Combustion Institute, Pittsburgh, Pennsylvania (1977)
70. Mitchell, R.E., Kee, R.J.: A General-Purpose Computer Code for Predicting Chemical Kinetic Behavior Behind Incident and Reflected shocks. Report SAND82-8205 (1992)
71. Morris, R.W., Turek, E.A.: Optimal temperature-dependence parameters for the Redlich-Kwong equation of state. In: Chao, R. (ed.) Equations of State, pp. 389–397. Am. Chem. Soc., Washington, DC
72. Nusca, M.J.: Numerical simulation of reacting flow in a thermally choked ram accelerator projectile launch system. In: AIAA (ed.) Proceedings of the 27th Joint Propulsion Conference, Sacramento, CA, USA, pp. 91–1915 (1991)
73. Nusca, M.J.: Reacting flow simulation of transient, multi-stage ram accelerator operation and design studies. In: Bruckner, A.P., Knowlen, C. (eds.) Proceedings of the 2nd International Workshop on Ram Accelerators, Seattle, WA, USA. University of Washington (1995)
74. Nusca, M.J., Kruczynski, D.L.: Reacting flow simulation for large-scale RAMAC. J. Propul. Power **12**(1), 61–69 (1991)
75. Patz, G., Seiler, F., Smeets, G., Srulijes, J.: Status of ISL's RAMAC 30 with Fin guided projectiles accelerated in a smooth bore. In: Bruckner, A.P., Knowlen, C. (eds.) Proceedings of the 2nd International Workshop on Ram Accelerators, Seattle, WA, USA. University of Washington (1995)
76. Petersen, E.L., Davidson, D.F., Hanson, R.K.: Ignition delay times of ram accelerator mixtures. In: AIAA (ed.) Proceedings of the 32nd Joint Propulsion Conference, Lake Buena Vista, FL, USA, pp. 96–2681 (1996)
77. Schultz, E., Knowlen, C., Bruckner, A.P.: Obturator and detonation experiments in the subdetonative ram accelerator. Shock Waves **9**, 181 (1999)
78. Schultz, E., Knowlen, C., Bruckner, A.P.: Starting envelope of the subdetonative ram accelerator. J. Propul. Power **16**(6), 1040–1052 (2000)
79. Smith, G., Golden, D., Frenklach, M., Moriarty, N., Eiteneer, B., Goldenberg, M., Bowman, T., Hanson, R., Song, S., Gardiner, W., Lissianski, V., Qin, Z.: GRI-Mech 3.0. http://www.me.berkeley.edu/gri_mech (2000)

80. Stewart, J.F., Bruckner, A.P., Knowlen, C.: Effects of launch tube shock dynamics on initiation of ram accelerator operation. In: Takayama, K., Sasoh, A. (eds.) Ram Accelerators. Springer, Berlin (1997)
81. Stewart, J.F., Knowlen, C., Bruckner, A.P.: Effects of launch tube gases on starting of the ram accelerator. In: AIAA (ed.) Proceedings of the 33rd Joint Propulsion Conference, Seattle, WA, USA, pp. 97–2652 (1997)
82. Viguier, C., Guerraud, C., Desbordes, D.: H_2-air and CH_4-air detonations and combustion behind oblique shock waves. In: Proceedings of the 25th Symposium (Int.) on Combustion, p. 53. The Combustion Institute Ed. (1994)
83. Weirs, V.G., Candler, G.V.: Simulation of ram accelerator flowfields using elemental conservation equations. In: Proceedings of the 30th Joint Propulsion Conference, Indianapolis, IN, USA, AIAA paper 94-2966 (1994)
84. Yungster, S., Rabinowitz, M.J.: Numerical study of shock induced combustion using a detailed methane-air mechanism. J. Prop. Power **10**, 609 (1994)
85. Yungster, S., Eberhardt, S., Bruckner, A.P.: Numerical simulation of hypervelocity projectiles in detonable gases. AIAA J. **29**, 238 (1991)

Author Biographies

Pascal Bauer After completing an engineer degree in Mech Eng. in 1972, he obtained a doctorate: Docteur es Sciences in 1985. He was Professor at University of Paris West in 1989, then, since 2002, he is now Professor at ENSMA. He is the author of over 150 papers and reports, including 50 archival papers on subjects related to detonation and its application to propulsion. The main aspects he addresses are those related to the equations of state of gaseous systems at extremely elevated pressure and, more recently, the propulsive properties of novel propulsive technology. He is the author of three books respectively on (i) thermodynamics, (ii) propulsion, and (ii) shock waves and detonation. He is a Member of the research group on deflagrations, detonations and explosions at the Laboratory Pprime, CNRS, ENSMA. He is also Affiliate Professor at the University of Washington, Seattle, WA, USA and Professor at the Sino-european Institute of Aviation Engineering (SIAE), Tianjin, China. He is Associate Fellow of the American Institute of Aeronautics and Astronautics (AIAA). He was the former Chairman of the PEGASUS European network.

Tarek Bengherbia is a Senior Consultant at Det Norske Veritas London. He received his Ph.D. in Aeronautical engineering from the Laboratory of Combustion and Detonation at the Ecole Nationale Supérieure de Mécanique et d'Aérotechnique (ENSMA), Poitiers-France. He has 11 years of professional experience which covers a range of engineering fields; mechanical, automotive and aeronautical engineering with strong emphasis on computational fluid dynamics, fire and explosion modeling. During his career, he has had experience in onshore and offshore safety analysis using CFD for gas dispersion of heavy gases, explosions, fire and smoke modeling. He is a senior member at the American Institute of Aeronautics and Astronautics and a member at the International Conference on

Computational Fluid Dynamics. He is active in research and research supervision related to green propellant for ICE engines, mechanics of gaseous reacting systems, explosion modeling and detonations at elevated pressures. He is the author of over 15 papers and reports, including 6 archival papers on subjects related to Computational Fluid Dynamics, turbulent combustion and detonation. He has 10 years of experience in using commercial software for CFD such as CFX and Fluent. In his current position, he has been the project manager and technical lead for explosion risk analyses, for projects such as BP Ula platform, Britannia platform and INPEX Ichthys FPSO for different design stages.

RAMAC25

Akihiro Sasoh

1 Background

With the increasing interests in ram accelerators [5] throughout the world, the Shock Wave Research Center (SWRC), Institute of Fluid Science (IFS), Tohoku University, Sendai, Japan, decided to construct their own ram accelerator. With limited resources, at first the bore diameter was determined from existing unused tubes made of stainless steel. The name 'RAMAC25' came from its bore diameter as was done in other institutes. The first publication appeared as an institute internal report in 1996 [7]. Even before installing RAMAC25 and also thereafter, SWRC received valuable support from the group of University of Washington through researcher exchanges by Abe Hertzberg, Adam P. Bruckner, Carl Knowlen, realized by the funds from Ministry of Education, Japan, via their technical advice and collaboration projects.

Using RAMAC25, we conducted experimental examination of its propulsion performance, obtaining a muzzle speed of a projectile of 2.3 km/s and a world-highest acceleration averaged over the ram acceleration section of 4×10^5 m/s^2 by using an 'open-base' projectile. Also, the building-up processes of a high-temperature slug in the transition region to the ram acceleration section were visualized.

A. Sasoh (✉)
Department of Aerospace Engineering, Nagoya University, Nagoya 464-8601, Japan
e-mail: sasoh@nuae.nagoya-u.ac.jp

F. Seiler and O. Igra (eds.), *Hypervelocity Launchers*,
Shock Wave Science and Technology Reference Library 10,
DOI 10.1007/978-3-319-26018-1_8

2 Apparatus

The schematic illustration of RAMAC25 in its final configuration is shown in Fig. 1 [3, 10]. A powder gun (Fig. 2) was used as the pre-launcher to the ram acceleration section, where the projectile was accelerated to a maximum velocity of 1.3 km/s. Smokeless power (NY500, Nippon Oil and Fats Cooperation) was used as the pre-launcher propellant. In the pre-launcher, the projectile was backed by a perforated obturator, which in turn was backed by a back plate that plugged the perforation [1, 7, 8]. The obturator assists the initiation of the ram acceleration by moderately compressing and heating the mixture on the entry to the ram acceleration section. Before the ram acceleration section, the burnt gas of the smokeless

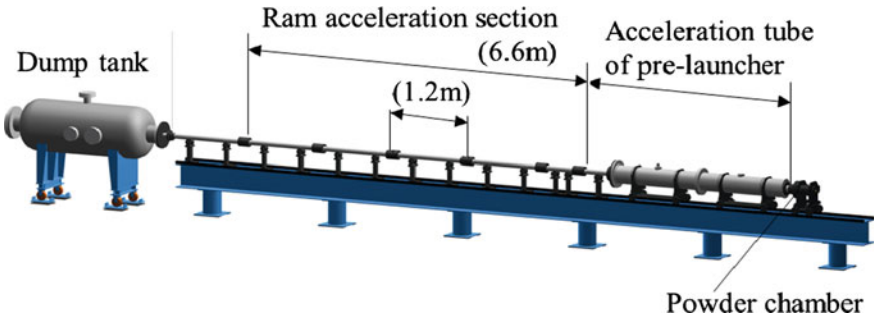

Fig. 1 25-mm-bore ram accelerator (RAMAC25)

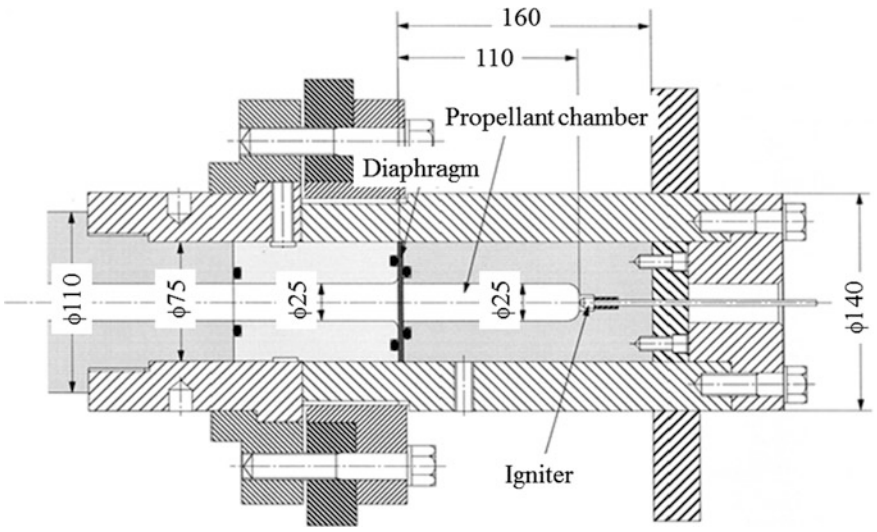

Fig. 2 Propellant chamber

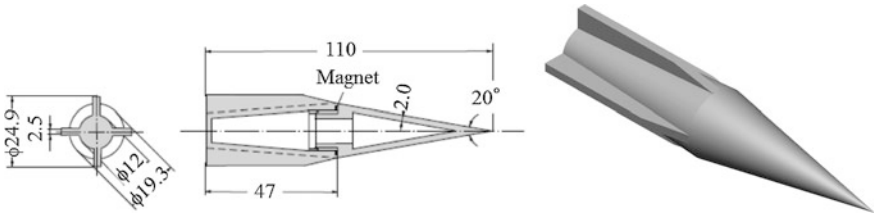

Fig. 3 Conventional-type projectile with fins

powder was vented through ventilation holes fabricated along the acceleration tube of the prelauncher.

The ram acceleration section consists of a 0.6-m-long entrance tube followed by five 1.2-m-long tubes. The inner diameter of the ram acceleration tubes is 25 mm. The instrumentation units, composed of a pickup coil and a piezoelectric pressure transducer, were placed with a separation distance of 0.3 m. When the projectile passage is sensed using the pick-up coils, the projectile velocity is determined by the method of time-of-flight. There is a projectile catcher in the dump tank.

Figure 3 schematically illustrates the conventional-type projectile used in RAMAC25. It comprises two pieces, a nose and an after-body, which are hollowed and threaded together. The projectile is made of the magnesium alloy and weighs 18.5 g.

3 Visualization of Starting Processes

Since RAMAC25 was the world-smallest-circular-bore ram accelerator, the effect of finite-rate chemical reactions under a modest fill pressure could lead to difficulties in igniting the propellant mixture. This problem was solved after careful investigation of the starting processes with optical visualization of a high-temperature slug built-up by repeated shock wave reflections [2, 9]. The visualization was done using an aspherical lens (Fig. 4, [9]) through which the in-tube flow image was radially magnified with a uniform magnification. The slug was built up before a projectile entered the ram acceleration section (Fig. 5). Then, during the transition, the propellant mixture was successfully ignited. Figure 5 shows high-speed framing photography of projectile entry process observed through the aspherical lens. The images are vertically magnified by a factor of 2.06. Frame interval; 10 μs. The initial pressure of the upstream (air), 240 Pa; downstream (N_2), 0.8 MPa, single layer of 50-μm-thick Mylar diaphragm, projectile speed, 1120 m/s. A shock heated region is observed as an illuminating slug. This visualization was backed up by the pressure measurement, see Fig. 6 [9].

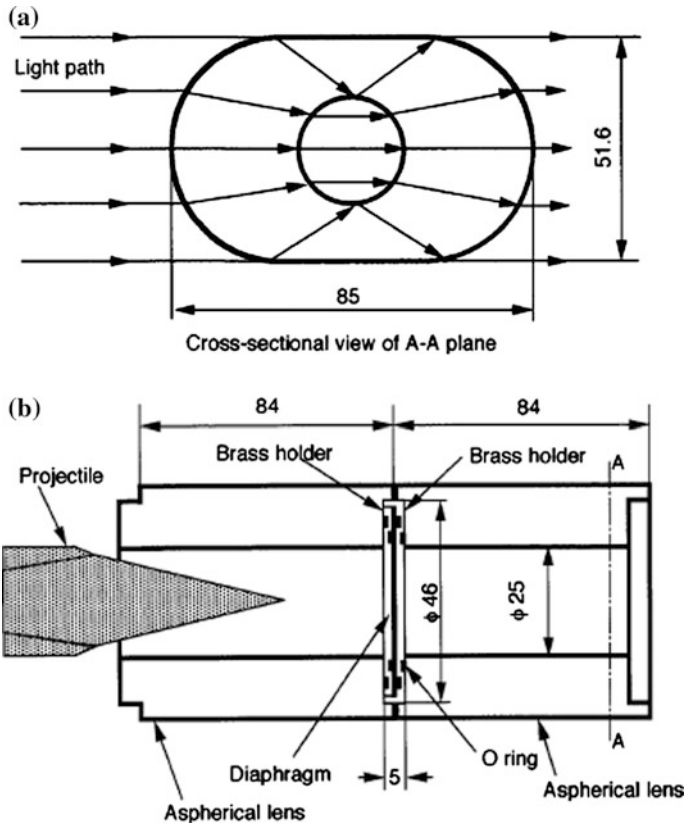

Fig. 4 Visualization experiment showing projectile transition using aspherical lenses. **a** Light path through aspherical lens, **b** test section

Using a holographic interferometer, the transition processes of the projectile entering the high-pressure section filled with inert gas are visualized in Figs. 7 and 8. Upon piercing of the Mylar diaphragm by the projectile conical nose, a conical shock wave is attached to the sharp nose. Then the shock wave repeats reflection between the acceleration tube and projectile walls. With this configuration, the pressure and the temperature of the gas around the conical nose are not excessively increased. Even if the gas on the right-hand side of the diaphragm was a propellant mixture, the ignition would be delayed and occur behind the projectile base. In this way, the ram acceleration can be successfully started.

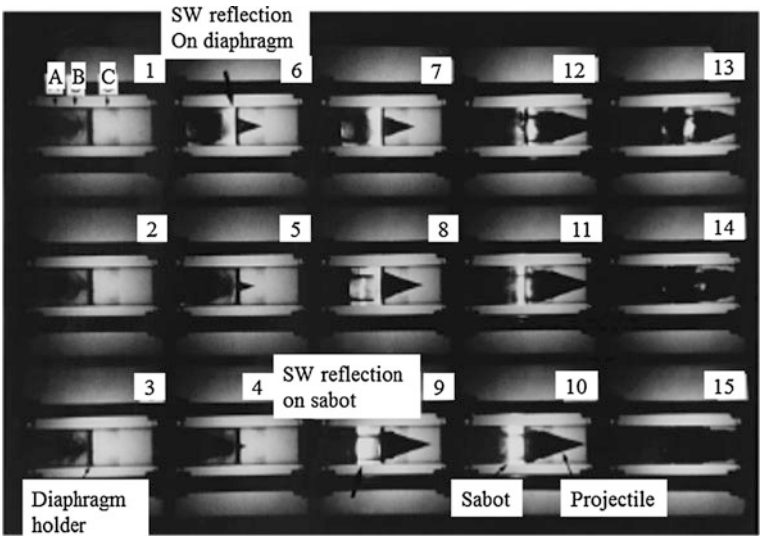

Fig. 5 Visualized shock wave refection processes during the transition with the impingement against the diaphragm

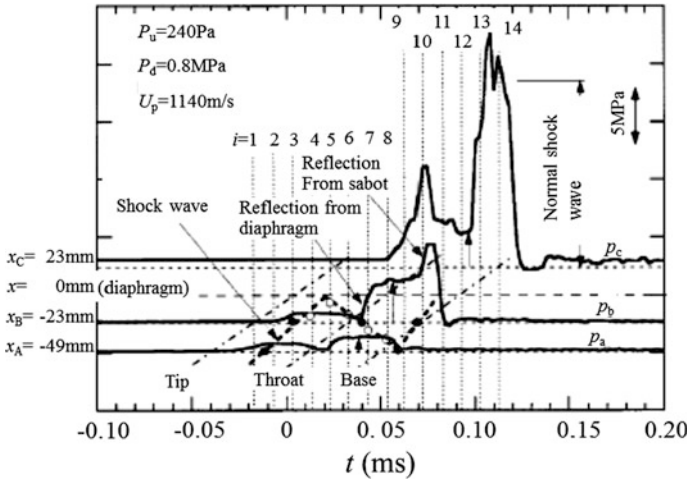

Fig. 6 In-tube pressure histories near the diaphragm. Pressure histories in projectile entry process under the same fill condition as of Fig. 5. Projectile speed of 1140 m/s. The labels '*i*' indicate the moment in Fig. 5. *x*, distance from the diaphragm; labels 'A', 'B', 'C' correspond to the locations shown in Fig. 5

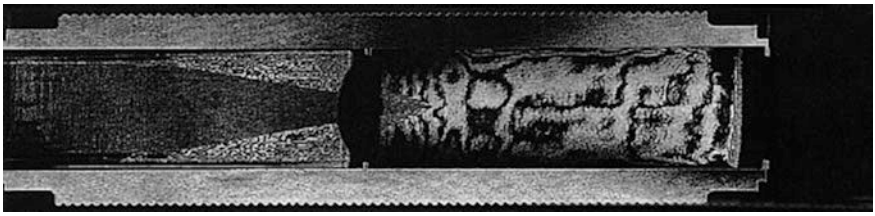

Fig. 7 Reconstructed interferogram of projectile entry process by piercing Mylar diaphragm, fill pressures, 0.1 MPa (*left*) and 1.0 MPa (*right*) of the Mylar diaphragm, single layer diaphragm (thickness, 100 μm), projectile speed, 1051 m/s

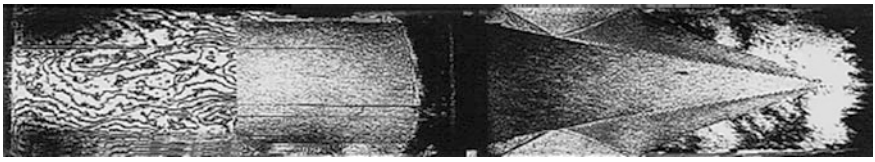

Fig. 8 Reconstructed interferogram of projectile entry process by piercing Mylar diaphragm, fill pressures, 0.1 MPa (*left*) and 1.0 MPa (*right*) of the Mylar diaphragm, two-layer diaphragm (thickness, 188 μm), projectile speed, 1105 m/s

4 High Acceleration Operation Using Open-Base Projectile

The small facility had the advantage to obtain a high acceleration owing to the square-cubic law; in principle the mass of a projectile scales with the cube of its dimension whereas the acceleration with an area that scales with its square. With this background, the high acceleration operation, which may not be relevant for tactical purposes, was investigated in RAMAC25.

Most projectiles used in ram accelerators have a centerbody, which is supported either by fins or rails. For the projectile to keep its integrity during the prelaunch with a high-acceleration level of the order of 10^4 *g* (gravitational acceleration) or higher, it was manufactured as a single piece. Moreover, for thermally-choked operation [1, 5, 6], the required entrance velocity is about 1.2 km/s, and the projectile experiences an acceleration level higher than 10^4 g also in the prelaunch processes. In order to obtain this high acceleration level, the mass of the projectile needs to be as small as possible. In order to reduce mass, the center-body of a projectile is often hollowed. Usually the hollow is machined by dividing a projectile into two pieces, a nose and an after-body. After machining a hollow in each piece, the two pieces are threaded together. In this way, the mass of the projectile is decreased. However, while the pressure outside of the center-body becomes 20 times as high as the fill pressure or even higher, the inside pressure remains unchanged. The projectile experiences a large compressive load from the outside.

Table 1 Experimental conditions of the third stage in three-stage operation with conventional projectile; fill pressure, 3.5 MPa; propellant mixture, $X CH_4 + 2O_2 + Y He$

Shot no.	X	Y	Speed of sound $\times 10^2$ (m/s)	Specific heat ratio	CJ detonation speed (km/s)	Dimensionless heat release	M_3	Unstart Mach number
H194	2.4	12.0	6.4	1.54	2.9	4.4	2.9	3.0
H199	3.2	13.2	6.4	1.53	2.5	3.1	2.9	3.0
H200	3.6	11.8	6.2	1.51	2.4	3.1	3.0	3.1
H195	3.0	9.6	6.0	1.50	2.6	3.8	3.1	3.2
H198	4.0	9.3	5.8	1.48	2.3	3.4	3.2	3.7
H197	5.0	10.2	5.8	1.47	2.2	3.2	3.2	3.4

Table 1, Figs. 9 and 10 show the experimental conditions, the acceleration tube wall pressure histories and the projectile velocity profiles obtained with the conventional type projectile. In first and second stage, the propellant mixtures are $2.8CH_4 + 2O_2 + 5.7N_2$ and $4.6CH_4 + 2O_2 + 2He$, respectively. The initial fill pressure is 3.5 MPa all through. In the third stage, except for the case of $M_{CJ} = 3.4$, where M_{CJ} denotes the Chapman-Jouguet detonation speed, unstart occur right after the transition and the projectile is decelerated right away.

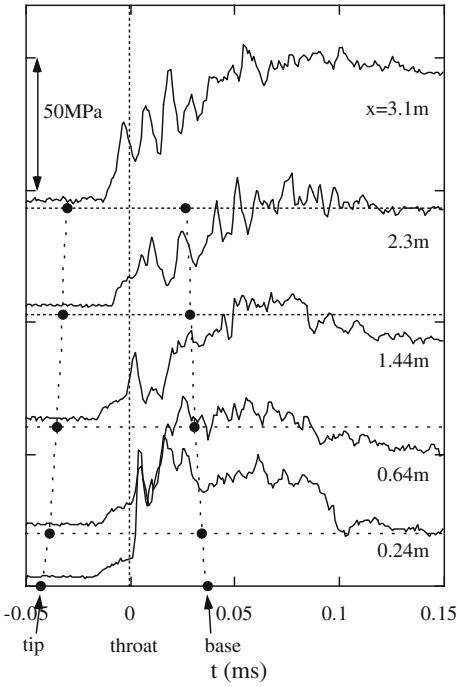

Fig. 9 Inner wall pressure histories during the passage of the conventional type projectile, the time, t, corresponds to the moment of the throat

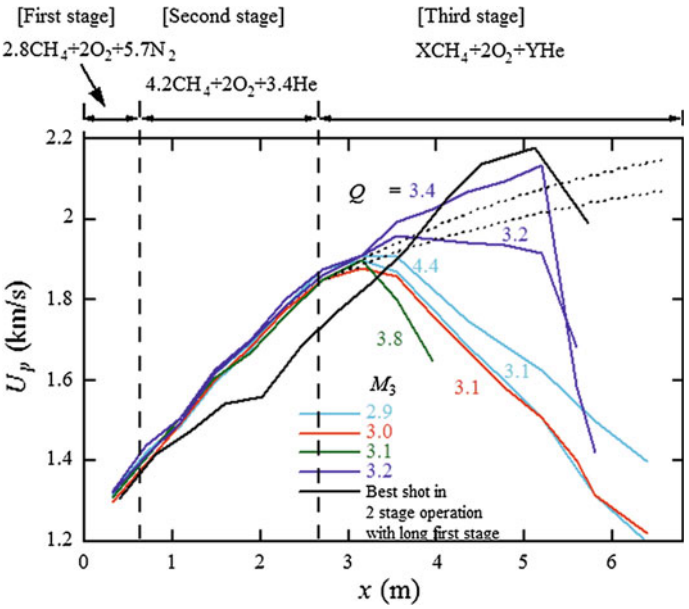

Fig. 10 Velocity profiles of three-stage operation using the conventional projectile with fins, fill pressure; 3.5 MPa

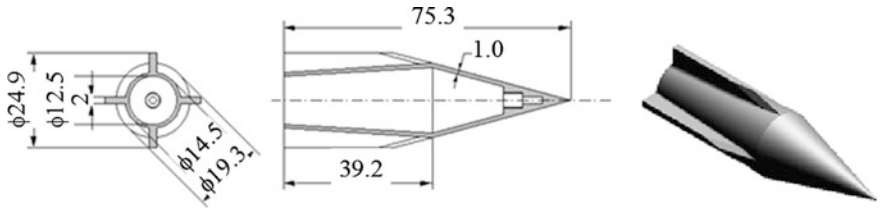

Fig. 11 Open-base projectile

Utilizing RAMAC 25, another type, that is an open-base projectile (Fig. 11, [4]), was also used to increase the acceleration with a limited operation pressure. They are made as a single piece, of aluminum alloy, A7075-T6. Since the base of the projectile center-body is hollow, pressure inside and outside the projectile is almost balanced. Its wall thickness could be significantly reduced. A thread to connect two center-body pieces is not necessary. The minimum body thickness is 1 mm. Four fins support the center-body. The mass is about 12 g. Table 2 contains the experimental conditions. The propellant mixture of the first and second stages are the same as those of the Table 1.

Figure 12 shows inner wall pressure histories measured during the passage of a projectile. A high pressure was maintained around the projectile after-body, corresponding to thermally choked operation.

Table 2 Experimental conditions of the third stage in three-stage operation with the open-base projectile; fill pressure: 3.5 MPa

Shot no.	X	Y	Speed of sound × 10^2 (m/s)	Specific heat ratio	CJ detonation speed (km/s)	Dimensionless heat release	M_3	Unstart Mach number
H223	3.2	4.2	5.0	1.43	2.4	5.0	3.5	4.1
H225	3.3	4.3	5.0	1.43	2.4	4.8	3.5	4.0
H226	3.5	4.4	5.0	1.43	2.3	4.6	3.5	4.2
H224	4.4	4.6	5.0	1.42	2.2	4.2	3.4	Exit test section
H222	8.0	6.0	5.0	1.40	1.8	3.4	3.4	WF
H230	2.9	6.3	5.4	1.47	2.6	4.8	3.2	4.2
H227	3.0	6.5	5.5	1.47	2.5	4.5	3.1	4.2

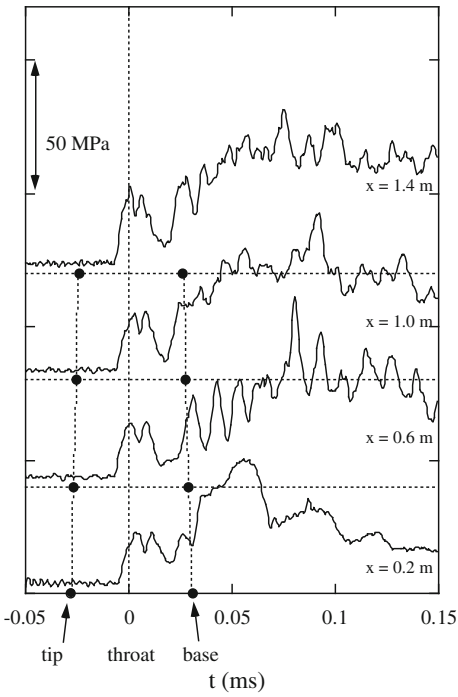

Fig. 12 Inner wall pressure histories during the passage of the open-base projectile

Figure 13 shows projectile velocity histories measured with the open-base projectile. The operation has three stages. Various fuel mixture ratios are investigated in the third stage (4.8 m in length). Hereafter the ratio of a heat release from the combustion to the initial static enthalpy will be designated by Q. The entrance Mach number in the third stage, M_3, was varied from 3.1 to 3.5. For Q = 3.4, wave

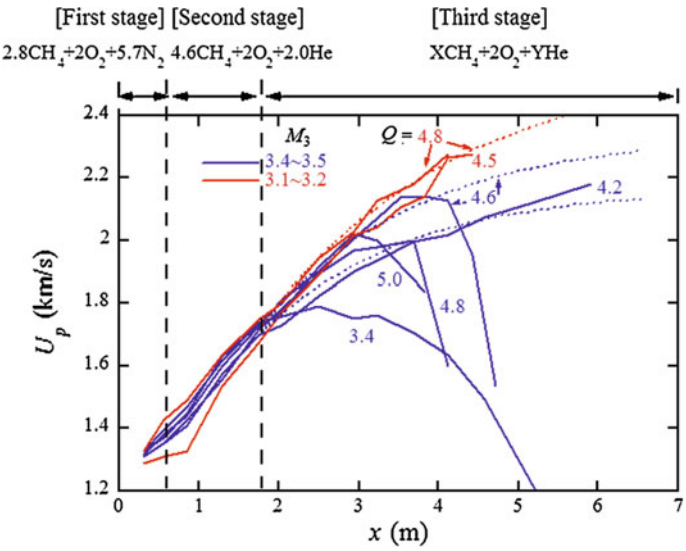

Fig. 13 Velocity profiles of three-stage operation using the open-base projectile, fill pressure; 3.5 MPa

fall-off occurs right after entering the third stage. With Q = 4.2, ram acceleration lasted for the longest distance. However, the average acceleration was lower than that with Q = 4.6. With Q larger than this value, wave un-start occurs before reaching the achievable velocity. However, when M_3 was decreased from 3.5 to 3.2, the effective acceleration length increased, and a higher velocity was achieved. With this decreased value of M_3, not only the maximum velocity but also the maximum Mach number became higher. Although the lower M_3 operation was superior to that in the earlier mentioned acceleration performance, usually starting reliability was improved with increasing the entrance Mach number. The value of 3.2 for the entrance Mach number was close to this critical condition.

Operation of the system at M_3 = 3.2 yielded the highest performance: Through the 6.6-m-long, three-stage-ram-acceleration section, a velocity increment from 1.3 to 2.3 km/s and an average acceleration of 4×10^4 g was achieved.

5 Summary

The investigations of RAMAC25 were conducted with a global collaboration, exchange of personal, know-how, data and information. Using this world-smallest-circular-bore ram accelerator, understanding the initiation processes of ram acceleration was improved by the visualization of starting processes. Also, the high ram acceleration with a modest fill pressure was demonstrated using the open-base projectile.

References

1. Bruckner, A.P., Knowlen, C., Hertzberg, A., Bogdanoff, D.W.: Operational characteristics of the thermally choked ram accelerator. J. Propul. Power **7**(5), 828–836 (1991)
2. Burnham, E.: Investigation of starting and ignition transients in the thermally choked ram accelerator. Ph.D. Dissertation, University of Washington (1993)
3. Hamate, Y., Sasoh, A., Takayama, K.: Ram accelerator operations at acceleration level up to 6×10^4 g. J. Phys. IV **10**(Pr11), 3–9 (2000)
4. Hamate, Y., Sasoh, A., Takayama, K.: High ram acceleration using open-base projectile. J. Propul. Power **19**(2), 190–195 (2003)
5. Hertzberg, A., Bruckner, A.P., Bogdanoff, D.W.: Ram accelerator: a new chemical method for accelerating projectiles to ultrahigh velocities. AIAA J. **26**(2), 195–203 (1988)
6. Knowlen, C., Sasoh, A.: Ram Accelerator Performance Modeling. Ram Accelerators, pp. 25–37. Springer, Heidelberg (1998)
7. Sasoh, A., Hirakata, S., Ujigawa, Y., Takayama, K.: RAMAC25, the ram accelerator at Shock Wave Research Center, Institute of Fluid Science, Tohoku University (in Japanese), pp. 161–190. Institute of Fluid Science Report, No. 7 (1996)
8. Sasoh, A., Hirakata, S., Maemura, J., Hamate, Y., Takayama, K.: Thermally Choked Operation in a 25-mm-Bore Ram Accelerator. Ram Accelerators, pp. 111–118. Springer, Heidelberg (1998)
9. Sasoh, A., Maemura, J., Hirakata, S., Takayama, K., Falcovitz, J.: Diaphragm rupture. Impingement by a conically-nosed, ram-accelerator projectile. Shock Waves **9**, 19–30 (1999)
10. Sasoh, A., Hamate, Y., Takayama, K.: Small-bore ram accelerator operation. J. Propul. Power **17**(3), 622–628 (2001)

Author Biography

Akihiro Sasoh continues shock wave studies in particular on ram accelerator, laser blast wave, sonic boom and aerodynamic impact of laser energy deposition. After his receiving doctoral degree in engineering from Department of Aeronautics, University of Tokyo, he worked as a research associate at Nagoya University, associate and full professors at Shock Wave Research Center, Institute of Fluid Science, Tohoku University. From 2008 to present, he is a professor of Department of Aerospace Engineering, Nagoya University, Nagoya, Japan.

Curriculum Vitae
Professor, Department of Aerospace Engineering, Graduate School of Engineering, Nagoya University

Specialization: Compressible fluid dynamics, Non-chemical space propulsion

Education:
1984 Bachelor, Department of Aeronautics, University of Tokyo
1986 Master, Department of Aeronautics, University of Tokyo
1989 Doctor, Department of Aeronautics, University of Tokyo

Academic carrier:
1989 Research Associate, Department of Aeronautics, Nagoya University
1991 Associate Professor, Institute of Fluid Science, Tohoku University
2003 Professor, Institute of Fluid Science, Tohoku University
2006 Professor, Department of Aerospace Engineering, Nagoya University.

Numerical Simulation of Super-Detonative Ram Accelerator; Its Shock-Induced Combustion and Oblique Detonation

Jeong-Yeol Choi and In-Seuck Jeung

Abbreviations

HR	Heat Release Parameter
ID	Induction Distance
ODW	Oblique Detonation Wave
OSW	Oblique Shock Wave
NDW	Normal Detonation Wave
SCRamAc	Super detonative Combustion Ram Accelerator
SBLI	Shock Boundary Layer Interaction
SCRamAc	Super detonative Combustion Ram Accelerator
SD	Shock Standoff Distance
SIC	Shock-Induced Combustion
TC	Thrust Coefficient
ZND	Zeldovich, von Neumann and Döring Model

1 Introduction

Hypersonic propulsion has been subjected to an intense research for the future propulsion. Various techniques have been proposed to replace the existing techniques. Most of them are chemical propulsion system, in which combustion plays a vital role in heat addition and its conversion to kinetic energy. The Ram Accelerator [1, 2], (referred to as RamAc), a ramjet-in-tube concept, is a propulsion concept based on using the Shock-Induced Combustion (SIC) to accelerate the projectile to

J.-Y. Choi (✉)
Department of Aerospace Engineering, Pusan National University,
609-735 Busan, South Korea
e-mail: jaywaichoi@nrf.re.kr; aerochoi@pusan.ac.kr

I.-S. Jeung
Department of Aerospace Engineering, Seoul National University,
151-744 Seoul, South Korea
e-mail: enjis@snu.ac.kr

F. Seiler and O. Igra (eds.), *Hypervelocity Launchers*,
Shock Wave Science and Technology Reference Library 10,
DOI 10.1007/978-3-319-26018-1_9

a very high velocity. In a Ram accelerator, a projectile travels at supersonic speed in a launch tube, filled with a premixed fuel-oxidizer mixture. The combustible gas mixture is compressed by a series of shocks which generates the thrust by a high-speed combustion mechanism such as an oblique detonation wave (ODW). The RamAc shares the principle with oblique detonation wave engine (ODWE), but only the RamAc has been realized.

Different forms of SIC produce high pressure on the projectile depending on the composition of mixture, speed and configuration of the projectile. Since the flight time involved in the shock induced combustion is in the order of few milliseconds, it is hard to analyze the flow experimentally so numerical study plays a vital role in analyzing the characteristics of the combustion.

Present literature is the compilation of the previous works by the authors on RamAc and its combustion mechanism, SIC and ODW, reside in the RamAc operation. Chapter 2 introduces the mathematical models and numerical method used for these studies. Chapter 3 handles the RamAc performance with the combustion mechanisms inside. Chapter 4 goes further on the viscous effects in RamAc with more emphasis on the ODW evolution by the SBLI. Chapter 5 deals with the scaling effect of the fluid dynamic parameters on SIC. Chapter 6 seeks for the evolution of cellular instabilities of the ODW. Finally in Chap. 7, a new type on instability in oblique SIC at non-attaching condition of ODW.

2 Validation Studies

A CFD code [3, 4] has been developed for the study of propulsion performance and the combustion dynamics in RamAc. The code has been validated over the unsteady SIC phenomena and the unsteady ignition phenomena in RamAc experiment carried out using an expansion tube.

2.1 Mathematical Formulations and Numerical Methods

2.1.1 Governing Equations

Fully coupled form of species conservation equations and Reynolds averaged Navier-Stokes equations is considered over axisymmetric geometry to analyze the chemically reacting supersonic viscous flow in Ram accelerator. The governing equations for a number of N species are summarized in a conservative vector form in general curvilinear (ξ, η) coordinates.

$$\frac{1}{J}\frac{\partial \mathbf{Q}}{\partial t} + \frac{\partial \mathbf{F}}{\partial \xi} + \frac{\partial \mathbf{G}}{\partial \eta} + \frac{1}{J}\mathbf{H} = \frac{1}{J}\mathbf{W} + \frac{\partial \mathbf{F}_v}{\partial \xi} + \frac{\partial \mathbf{G}_v}{\partial \eta} + \frac{1}{J}\mathbf{H}_v \tag{1}$$

where,

$$\mathbf{Q}=\begin{bmatrix}\rho_1\\ \rho_2\\ \vdots\\ \rho_N\\ \rho u\\ \rho v\\ e\end{bmatrix},\mathbf{F}=\frac{1}{J}\begin{bmatrix}\rho_1 U\\ \rho_2 U\\ \vdots\\ \rho_N U\\ \rho uU+\xi_x p\\ \rho vU+\xi_y p\\ U(e+p)\end{bmatrix},\mathbf{G}=\frac{1}{J}\begin{bmatrix}\rho_1 V\\ \rho_2 V\\ \vdots\\ \rho_N V\\ \rho uV+\eta_x p\\ \rho vV+\eta_y p\\ V(e+p)\end{bmatrix},\mathbf{H}=\frac{1}{y}\begin{bmatrix}\rho_1 v\\ \rho_2 v\\ \vdots\\ \rho_N v\\ \rho uv\\ \rho v^2\\ (e+p)v\end{bmatrix},$$

$$\mathbf{W}=\begin{bmatrix}w_1\\ w_2\\ \vdots\\ w_N\\ 0\\ 0\\ 0\end{bmatrix},\mathbf{F_v}=\frac{1}{JRa}\begin{bmatrix}-\rho_1 U_1^d\\ -\rho_2 U_2^d\\ \vdots\\ -\rho_N U_N^d\\ \xi_x\tau_{xx}+\xi_y\tau_{xy}\\ \xi_x\tau_{xy}+\xi_y\tau_{yy}\\ \xi_x\beta_x+\xi_y\beta_y\end{bmatrix},\mathbf{G_v}=\frac{1}{JRa}\begin{bmatrix}-\rho_1 V_1^d\\ -\rho_2 V_2^d\\ \vdots\\ -\rho_N V_N^d\\ \eta_x\tau_{xx}+\eta_y\tau_{xy}\\ \eta_x\tau_{xy}+\eta_y\tau_{yy}\\ \eta_x\beta_x+\eta_y\beta_y\end{bmatrix},$$

$$\mathbf{H_v}=\frac{1}{yRa}\begin{bmatrix}-\rho_1 v_1^d\\ -\rho_2 v_2^d\\ \vdots\\ \rho_N v_N^d\\ \tau_{xy}\\ \tau_{yy}-\tau_{\theta\theta}\\ \beta_y\end{bmatrix} \tag{2}$$

Here, total density ρ is expressed as a sum of the partial density ρ_k of each species ($\rho=\sum_{k=1}^{N}\rho_k$), u and v are velocity components in Cartesian coordinates (x, y), and total energy per unit volume e is defined as a sum of kinetic energy and internal energy. U and V are the contravariant velocity components in generalized coordinates. Coordinate transformation metrics ξ_x, ξ_y, η_x, η_y and metric Jacobian J are obtained from coordinate transform relation. Pressure p is evaluated from the ideal gas law for a mixture of thermally perfect gases.

$$p=\sum_{k=1}^{N}\frac{\rho_k}{M_k}\boldsymbol{R}T \tag{3}$$

Here, M_k is the molecular weight for kth species and $\boldsymbol{R}$ is the universal gas constant. Temperature T is evaluated implicitly by the Newton-Raphson iteration method with the definition of total energy and the specific heats of each species which are obtained as function of temperatures from NASA thermochemical polynomial data. Although the ideal gas law may introduce some errors at high temperature and pressure conditions, it is not considered to change the overall flow structures significantly. Fick's law is used for the convenient evaluation of diffusion velocity components of u_k^d and v_k^d. Contravariant diffusion velocity components of U_k^d and V_k^d are defined in similar way to contravariant velocities in generalized coordinates. *Ra* in viscous terms is the Reynolds number based on inflow sonic velocity. By applying the Stokes' hypothesis, viscous momentum and heat flux terms are reconstructed in generalized coordinates by chain rule. The laminar values of dynamic viscosity and thermal conductivity of each species are determined by forth-order polynomials of temperature. Once the viscosity and the conductivity of each species have been determined, the conductivity and the viscosity of the mixture are calculated using Wilke's mixing rule.

2.1.2 Chemistry and Turbulence Models

Reaction source term w_k in Eq. (2) is the mass production rate of kth species by N_r chemical reaction steps.

$$w_k = M_k \sum_{r=1}^{N_r} \left(\nu''_{k,r} - \nu'_{k,r} \right) \left[k_{fr} \prod_{k=1}^{N} \left(\frac{\rho_k}{M_k} \right)^{\nu'_{k,r}} - k_{br} \prod_{k=1}^{N} \left(\frac{\rho_k}{M_k} \right)^{\nu''_{k,r}} \right] \tag{4}$$

The forward and backward reaction rate constants k_{fr} and k_{br} for rth reaction step are expressed in Arrhenius form, $k_r = A_r T^{B_r} \exp\left(-E_r^* / T\right)$, where $\nu'_{k,r}$ and $\nu''_{k,r}$ are the stoichiometric coefficients.

As Reynolds number in a Ram accelerator is very high, a fully turbulent flow can be assumed. In the present study, turbulence eddy viscosity is calculated by the Baldwin-Lomax algebraic turbulence model. This model is chosen for its simplicity and the lack of a sufficiently accurate model for this kind of flow. The mixture viscosity and thermal conductivity, as well as the binary diffusivity of species in the gas mixture are expressed as sums of the laminar and turbulent values. The constant turbulent Prandtl and Schmidt numbers of 0.9 are assumed to evaluate turbulent thermal conductivity and mass diffusivity. The combustion process in a Scram accelerator is mainly accomplished by the oblique detonation and the major viscous effects are observed at the burned gas region in which the chemical reaction is already completed. Therefore, the interactions between turbulence and chemistry are not considered in the present study since its analysis requires the direct numerical simulation or the complex closure of reaction source term using the pdf models. Further details are included in the previous literature [5].

2.1.3 Numerical Methods

Equation (1) is discretized by a finite volume approach. The numerical schemes for the discretization are documented well in the Refs. [3, 4], and summarized here for brevity. The convective fluxes are formulated using Roe's FDS (Flux Difference Splitting) method derived for multi-species reactive flow. MUSCL (Monotone Upstream-centered Schemes for Conservation Laws) type variable extrapolation approach is used to get a high order spatial accuracy, and differentiable limiter is used to preserve the TVD (Total Variation Diminishing) property. Central difference method is used for viscous fluxes. For the case of the steady state solution, first order accurate implicit scheme is utilized for the temporal integration of the governing equations. LU (Lower-Upper) relaxation scheme is used for the implicit analysis with approximate splitting of flux Jacobian matrix.

In case of unsteady simulation, the second-order accurate implicit method is applied for time integration. Newton sub-iteration method is of use to preserve the time accuracy and solution stability at large time step. The implicit part of Eq. (3) is inverted by the following lower and upper symmetric Gauss-Seidel sweeps at every sub-iteration level. Split flux Jacobian matrices are obtained by the Steger-Warming method and approximate Jacobian Splitting method.

2.2 Unsteady SIC

For the purpose of validating the developed computational fluid dynamics code, Lehr's experiments [6] of periodically oscillating shock-induced combustion were numerically simulated. Stoichiometric hydrogen/air mixture was used in the experiment at 320 mm Hg and 403 m/s of sonic velocity. This sonic velocity corresponds to the temperature of 293 K. Diameter of the hemispherical projectile used in the experiment is 15 mm. The considered cases are oscillating results at Mach number 4.18, 4.48, and 4.79. Experimentally observed oscillation frequencies are 148, 425, and 712 kHz, respectively. Figure 1 is the experimental shadowgraph for the cases of Mach number 4.18 and 4.79.

For the present study, Jachimowski's [7] 9 species detailed hydrogen-oxygen combustion mechanism was used and inviscid flow is assumed. A constant time step is used equivalent to CFL number of 3 for incoming flow and 4 sub-iterations are performed. The computational domain is composed of a grid system with 200 grid points along the projectile surface and 300 grid points normal to the surface. The inflow boundary is set some distance in front of the oscillating bow shock. Figures 2, 3 and 4 show the local Mach number distribution of the flow field and the temporal variation of density along the stagnation streamline for three Mach numbers.

The Mach number distribution is selected for plotting since it shows most of the important flow characteristics of shock-induced combustion very clearly. The plots of Mach number distribution agrees well with the experimental results and the

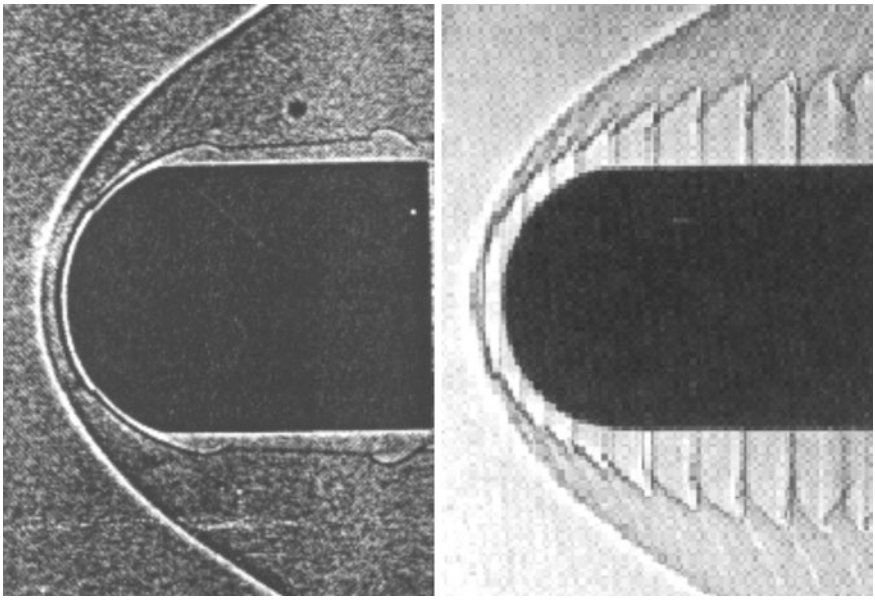

Fig. 1 Experimental shadowgraph of periodically oscillating shock-induced combustion at Mach number 4.18 and 4.79. Taken from Lehr [6]

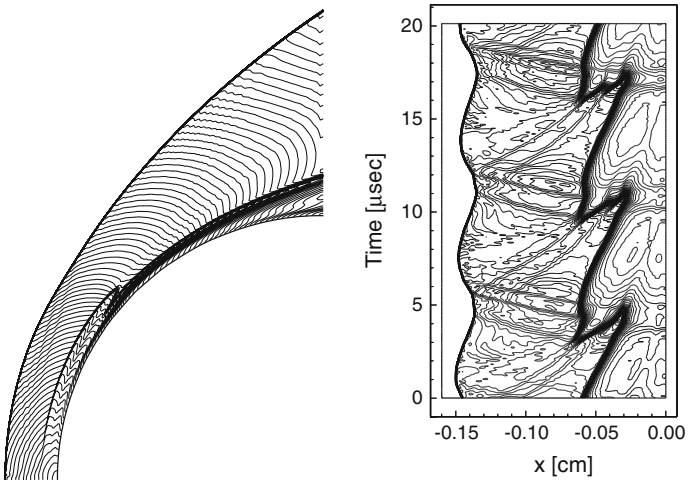

Fig. 2 Local Mach number distribution and the temporal variation of density along stagnation line for the case of M = 4.18

density history show all the details of the instability mechanism. The chemistry mechanism used in this study is same to the one used by Yungster and Radhakrishnan [8] and Matsuo et al. [9] and the different choice of the chemistry

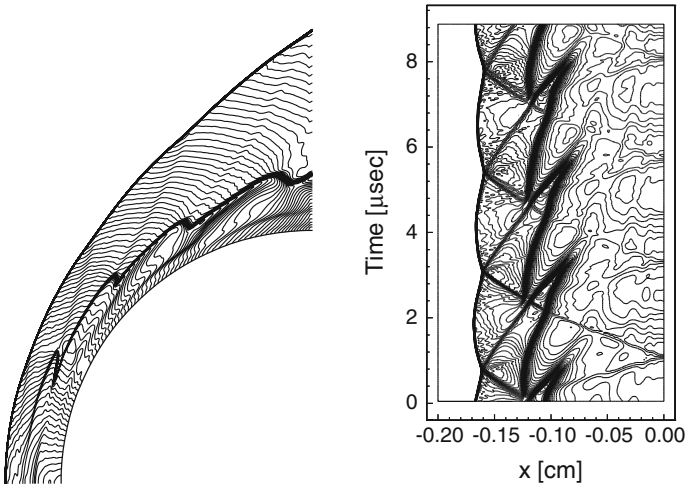

Fig. 3 Local Mach number distribution and the temporal variation of density along stagnation line for the case of M = 4.48

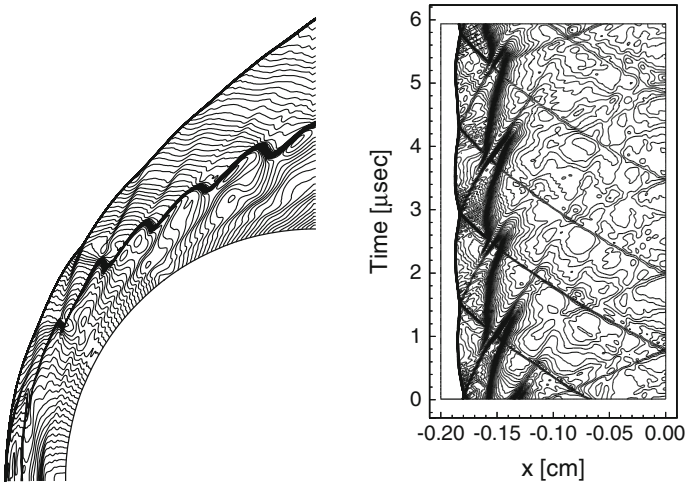

Fig. 4 Local Mach number distribution and the temporal variation of density along stagnation line for the case of M = 4.79

mechanism has been known to be responsible for the frequency disagreement of the result by Wilson and Sussman [10] and Hosangadi et al. [11]. The frequency of oscillation is obtained from these results and compared in Table 1 with experimental and numerical values obtained by previous researchers. The results of the simulation showed satisfactory agreement with experimental results even though they do not exactly agree.

Table 1 Comparison of oscillation frequency of unstable shock-induced combustion

kHz	M = 4.18	M = 4.48	M = 4.79
Experiment	148	425	712
Present result	155	426	707
Yungster and Radhakrishnan [8]	163	431	701
Matsuo et al. [9]	160	–	725
Wilson and Sussman [10]	–	–	530
Hosangadi et al. [11]	–	–	450

2.3 *Numerical Simulation of RamAc in an Expansion Tube*

An expansion tube facility, a laboratory facility to study the hypersonic flows, is an impulse flow device used to generate short duration, high velocity gas flows. Morris et al. [12] visualized the stationary Ram accelerator flow field using a model RamAc and investigated the combustion phenomena in less energetic mixtures using the expansion tube facility. But a clear explanation on combustion involved in the reaction was not given. The experimental images are plotted in Fig. 5 compared with steady-state CFD results by Choi et al. [13, 14] for the experimental conditions. They reported that for the mixture with m = 12, there exists only a near wall combustion in the flow field whereas for m = 17 there exists a combustion also in the central region. The parameter m is the amount of gas dilution added to the combustible mixture. By using steady state the near wall combustion was predicted

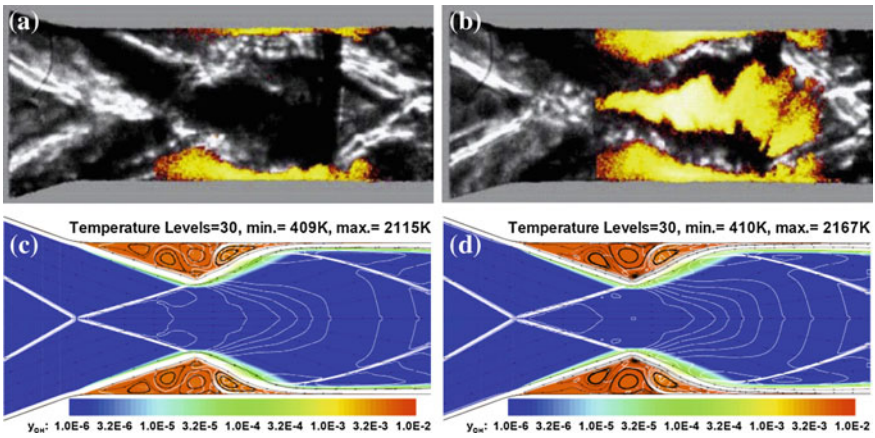

Fig. 5 Comparison of experimental results and numerical results with steady state assumption. Courtesy of Morris et al. for the experimental results [12]. **a** Overlaid Schlieren and OH PLIF image for $2H_2 + O_2 + 17N_2$ mixture. **b** Overlaid Schlieren and OH PLIF image for $2H_2 + O_2 + 12N_2$ mixture. **c** Overlaid OH mass fraction distribution, temperature contours and streamlines for $2H_2 + O_2 + 17N_2$ mixture. **d** Overlaid OH mass fraction distribution, temperature contours and streamlines for $2H_2 + O_2 + 12N_2$ mixture

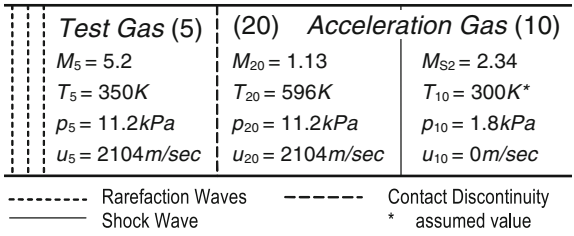

Fig. 6 Deduced flow conditions of the acceleration gas with conditions of the test gas and assumed acceleration gas temperature of 300 K. Numbers (*5*), (*10*) and (*20*) designate the flow regions in expansion tube [15]

but the combustion along the centerline in the case for lesser energetic mixture could not be studied using steady state and hence unsteady simulation was performed for both mixture conditions. The detailed flow conditions of the unsteady simulation was deduced from the operating condition of the expansion tube facility [12] and summarized in Fig. 6.

The unsteady combustion process for $2H_2 + O_2 + 12N_2$ mixture condition is plotted in Fig. 7 by the distribution of OH mass fraction and temperature contours. Just after the beginning of the reaction, a fast and weak normal shock wave, a contact surface, and a slow and strong normal shock wave are observed as a result of the intersection between the contact surface and the forward running normal shock wave. As the contact surface and strong normal shock rush into the test section, dual-angled oblique shock waves are formed at the nose of the RamAc model. Between the oblique shock waves of different angles, the small angled one is a weak oblique shock wave and the large angled one is a strong shock wave formed by the influence of the high-density region between the strong normal shock wave and contact surface. Mach waves and slip lines are formed at the intersection point.

As the time passes, the cross-sectional area of the normal shock wave is getting smaller and upper and lower strong oblique shock waves intersect with each other. The intersection of the strong oblique shock waves forms a new strong normal shock wave or a Mach stem at the center of the test section. Complex wave intersections are noticed during this process, but they do not seem to be important from the viewpoint of major combustion phenomena. The strength of the new Mach stem seems to be greater than the previous normal shock, and the mixture flow ignites by the shock heating behind the Mach stem. After the ignition, the combustion proceeds very rapidly, and the Mach stem transits to a normal SIC or a normal detonation wave. As a result of the presence of a strong normal detonation, the large value of the entropy fixing parameter was needed in the computation, because the small value of it results in carbuncle and even–odd decoupling phenomena. The normal detonation is maintained with a configuration of a triple-point interaction mechanism for a long time after the disappearance of strong oblique shock waves. An oblique shock wave originating from the triple interaction point reflects at the wall surface, and a contact surface (slip line) is formed parallel to the wall, which acts as a flame boundary. The flame boundary is represented as a thick temperature gradient across which the

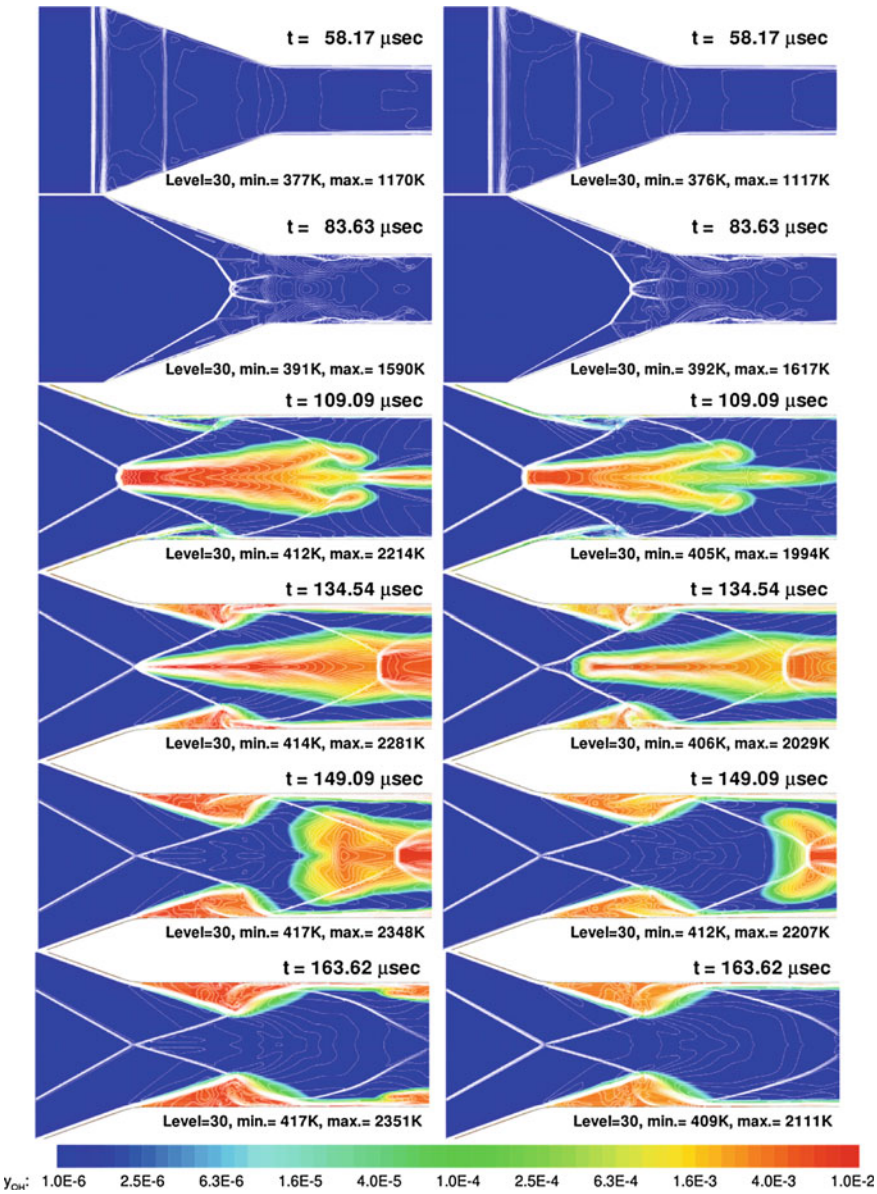

Fig. 7 Overlaid temperature contours and OH mass fraction distributions showing unsteady combustion process of $2H_2 + O_2 + 12N_2$ mixture in right column and $2H_2 + O_2 + 17N_2$ mixture in left column; combustion region is magnified after t = 94.54 μs

burned gas and the unburned gas are segregated. The combustion initiated by the normal detonation wave forms a long burned gas core that extends to the exit along the centerline of the test section. This transient result is comparable to the

experimental result in Fig. 7. Meanwhile, the intersection of the reflected oblique shock waves makes a secondary Mach stem in the rear part of the test section, which enhances the combustion and forms a secondary combustion zone.

The burned gas core is maintained for a sufficiently long time as long as the Mach stem (normal detonation wave) exists. However, the cross section of the normal detonation is getting smaller and finally disappears. After the disappearance of the normal detonation, two oblique shock waves intersect with each other at the center of the test section. Behind the regular shock intersection, the flow speed increases to supersonic speed, and the shock heating is not high enough to ignite the mixture. In accordance with the disappearance of the normal detonation wave, the ignition source in the core of test section, the burned gas region detaches at the intersection point of the oblique shock wave and flashes downstream. Thus, the central burned gas region completely disappears after some time.

On the other hand, combustion progresses in the separated flow region that originates from the oblique shock wave/boundary-layer interaction and the adverse pressure gradient. The separated flow region expands with the progress of combustion but is bounded by the tail of the expansion fan, the reflected oblique shock wave, and the wall. The combustion of this separated flow region is ignited by the aerodynamic heating of stagnated flow and is maintained to the end of the computation. Although there could be a question about the structure of vortex in the separated flow region due to the assumption of laminar flow, it would not be an important problem in view of the global combustion mechanism because the separated flow region is bounded by inviscid flow characteristics and does not have a great influence on the global flow features. According to these inviscid and viscous combustion characteristics, the transient solution shows reasonable agreement with the experimental result in Fig. 5b, and the final solution of the unsteady simulation agrees with the result of steady-state simulation in Fig. 5d.

The unsteady combustion process for $2H_2 + O_2 + 17N_2$ mixture condition is simulated too, and the summarized results are compared in Fig. 8. The unsteady combustion is processed very similarly except the timing and level of OH intensity. The OH level of $2H_2 + O_2 + 17N_2$ mixture shows late ignition and earlier extinction with about 40 % lower OH intensity. However the location of the primary combustion is almost same, because it is determined fluid dynamically by the intersection of the oblique shock waves and the Mach stem. The combustion zone is maintained for 30 μs for $2H_2 + O_2 + 17N_2$ and 40 μs for $2H_2 + O_2 + 12N_2$. Admitting that the heat addition behind the Mach stem could sustain the combustion region for a time, the combustion region finally extinguishes for the present cases. After extinction of the primary combustion zone, the transient secondary combustion appears around the second intersection point of the reflected waves. However, the secondary Mach stem is not strong enough for flame holding, and the combustion zone finally disappears. In summary, the centerline flame duration time is about 70 μs for $2H_2 + O_2 + 12N_2$ and 60 μs for $2H_2 + O_2 + 17N_2$. This difference in flame duration seems to be critical for the different observation in the experiment as shown in Fig. 5, since the operation time of the expansion tube is around 150 μs, which allows very little chance for the observation.

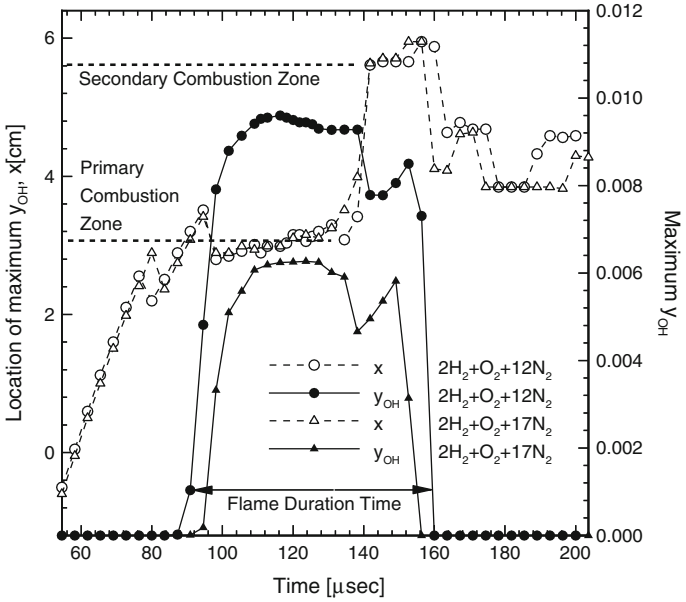

Fig. 8 Maximum value of OH mass fraction and its location along combustor center line. The location x designates the distance from the leading edge of test section in cm

The experimentally observed combustion region near wall surfaces agrees well with this simulated result. The separated flow region is originated by SBLI and this region is bounded by the tail of expansion fan, reflected oblique shock wave and projectile walls and the combustion in the separated region is initiated by the aerodynamic heating in stagnated flow. Thus there could be two kinds of ignition mechanisms in RamAc flow field. The one is shock heating and the other is viscous heating. The ignition by shock heating seems to be explosive but somewhat unstable, and the ignition by viscous heating is stable but restricted to solid surface.

3 Numerical Studies of Ram Accelerators

The combustion phenomena in a Ram Accelerator cannot be studied completely by experiments since the reaction time involved in the whole process is only a few milliseconds and hence a numerical study plays a vital role in understanding the physical characteristics in such high speed complex combustions. In a RamAc operation, the high speed flow aerodynamically compresses the propellant mixture behind the shock wave and raises the temperature behind the shock wave which is sufficient enough to ignite the propellant mixture depending on the aerodynamic compression from the oblique shock. The combustion taking place in such a complex flowfield, as stated above, cannot be studied completely by experiments.

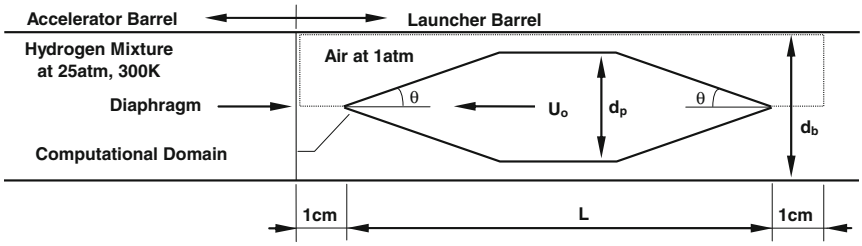

Fig. 9 Schematics of the computational domain of Ram accelerator

The computational domain depicted in Fig. 9 was used for this study. The propellants are loaded in acceleration barrel at very high pressure. A conical body and blunt body projectile was used in most cases to study the combustion flowfield.

3.1 Unstart in an Energetic Mixture

Initially, combustion mechanism involved in H_2 + air mixtures, which is more energetic and highly reactive, is considered 5. For this mixture, the initial condition was assumed to be the flight flying at an initial Mach of 6.1 and the overdrive factor[1] at such speed is 1.22. At x_p[2] = −0.5 cm, i.e. when the projectile haven't started its flight in a physical domain, as shown in Fig. 10a, the diaphragm is marked as a stiff pressure gradient in front of the projectile nose. As the projectile marches only 0.5 cm from the initial state, the result is nearly same as that of steady state. A thin thermal boundary layer is formed on the body surface, and a high-temperature and high-pressure region exists at the shock wave impinging point on the middle of the body surface.

Just after the breakdown of the diaphragm (x_p = 2.0 cm as in Fig. 10c), a normal shock system is developed and moves towards the downstream. At the projectile nose a bubble of detonation is appeared after the passage of the normal shock system comprising a normal shock, the contact discontinuity, and the expansion waves. Then, the bubble of detonation grows very rapidly in the radial and downstream directions. Finally, the detonation catches up with the non-reacting normal shock, although it cannot expand upstream because the projectile velocity is 22 % higher than that of C–J detonation velocity. At this stage, the high drag force (reverse thrust force) begins to act on the body due to the high-pressure region inside the bubble even though the drag force is limited to a small value because it

[1]Overdrive factor—ratio of projectile velocity to that of the C-J detonation velocity: the velocity at which the detonation propagates at the same velocity at which the reacting gas reaches sonic velocity as the reaction ceases.

[2]x_p—Distance traveled by the projectile in laboratory frame.

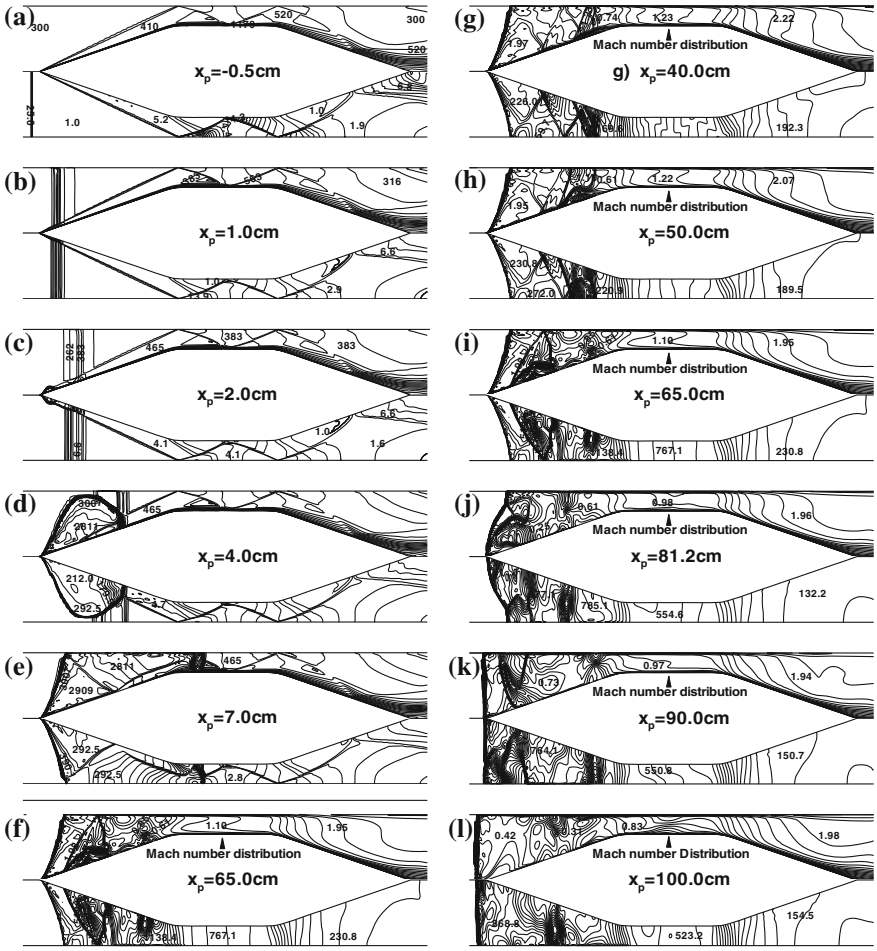

Fig. 10 Temperature distributions (upper half of each figure) and pressure distributions (lower half of each figure) in marching sequence for $2H_2 + O_2 + 3.76N_2$ mixture; Mach number distributions are plotted for cases after $x_p = 40.0$ cm

acts only on the nose tip of the body. This spontaneous ignition may be due to the interaction between the normal shock system (a normal shock followed by a contact surface and expansion waves) and the oblique shock wave.

As the bubble of detonation ($x_p = 7.0$ cm as in Fig. 10e), a bow shock is reflected on the barrel wall and the reflection procedure is repeated on the body surface. After the aforementioned shock–shock interaction, the preceding normal shock is left as a following contact surface while the normal detonation moves downstream. A drag force, which acts as a reverse thrust, increases enormously, and the projectile velocity begins to drop sharply because the high-pressure of burned gas occupies all

of the frontal area of the body. Thereafter, the shock reflection procedure is repeated several times until the regular pattern of the shock train is formed (x_p = 24 cm as in Fig. 10f). During this shock-train formation period, the acceleration is maintained at a value of about −15,000 G (refer to Fig. 13) for a sufficiently long time, although the acceleration shows an oscillatory behavior because of the variation of the shock-impinging points on the conical nose and tail. Even though the numerical results correspond to the earlier stage of their experimental result, this sharp decrease can be compared to that of the experimental result of Seiler et al. [16]. The slope of the oblique shock in the burned gas region is much steeper than that in the air because the Mach number is low due to the high sonic velocity in this region, even though the low velocity is kept in the same order of magnitude.

On the other hand, the strong shock/boundary layer interactions (denoted as SBLI hereafter) are observed at the three shock-impinging points on the conical nose. No severe SBLI is observed after these impinging points. Significantly, the interaction is strongest at the second impinging point and is enough to generate the separation bubble and a pair of the oblique shocks around the impinging point. Such a strong SBLI is very important because the separation bubble grows in the burned gas region because of severe aerodynamic heating. The growth of the bubble leads to a large subsonic high-temperature region and separates a pair of the oblique shocks that interact. As time goes on, the severe shock–shock interactions and shockwave/boundary-layer interactions are repeated and form the strong oblique shock ahead of the large separation bubble. As a result, thermal choking is provided by a strong shock at the back of the separation bubble (x_p = 40 cm as in Fig. 10g). The thermal choking produces a severe drag force and makes the velocity of the projectile drop rapidly. The oblique shock moves forward continuously and interacts with the incident oblique detonation. The triple-shock interaction point is shown when the projectile marches to 81.2 cm as shown in Fig. 10j. Finally, a normal detonation is formed ahead of the projectile and propagates upstream with the support of thermal choking. This unstart behavior coincides with the experimental observation of Seiler et al. [16]. Although, the flow conditions are different, the acceleration of −30,000 G is nearly same as the experimental results.

The direct ignition of detonation by the rush of a high-speed body into a reactive mixture as explained above could be expected to exist and considered as a cause of *Super-detonative Combustion Ram Accelerator (SCRamAc) unstart*. The reason for the spontaneous ignition can be explained as follows. When the normal shock propagates downstream followed by contact discontinuity and expansion waves, the temperature of the region between the shock and the contact discontinuity rises up to about 60 % higher than that of initial states. The temperature increases again after the interaction between the normal shock and the oblique shock attached on the conical body, even though the pressure rise is not significant. As a result, the chemical kinetic reaction rate increases, and the mixture detonates when the pressure at the nose is increased after the passage of the expansion wave for the cases of reactive mixtures such as the $2H_2$ + Air mixture.

3.2 *Starting in Less-Energetic Mixtures*

Similarly the combustion study was explained for a less energetic mixture as well. Combustion phenomena for another case with $2H_2 + O_2 + 5N_2$ were explained (as depicted in Fig. 11) as follows: when the projectile breaks through the diaphragm; at this moment, the interaction between the oblique shock and the normal shock system is shown clearly. When the projectile moves 10 cm from the diaphragm, as shown in Fig. 11b, the normal shock system passes the SBLI region and then ignition occurs in the boundary layer. After this stage, the low-pressure burned

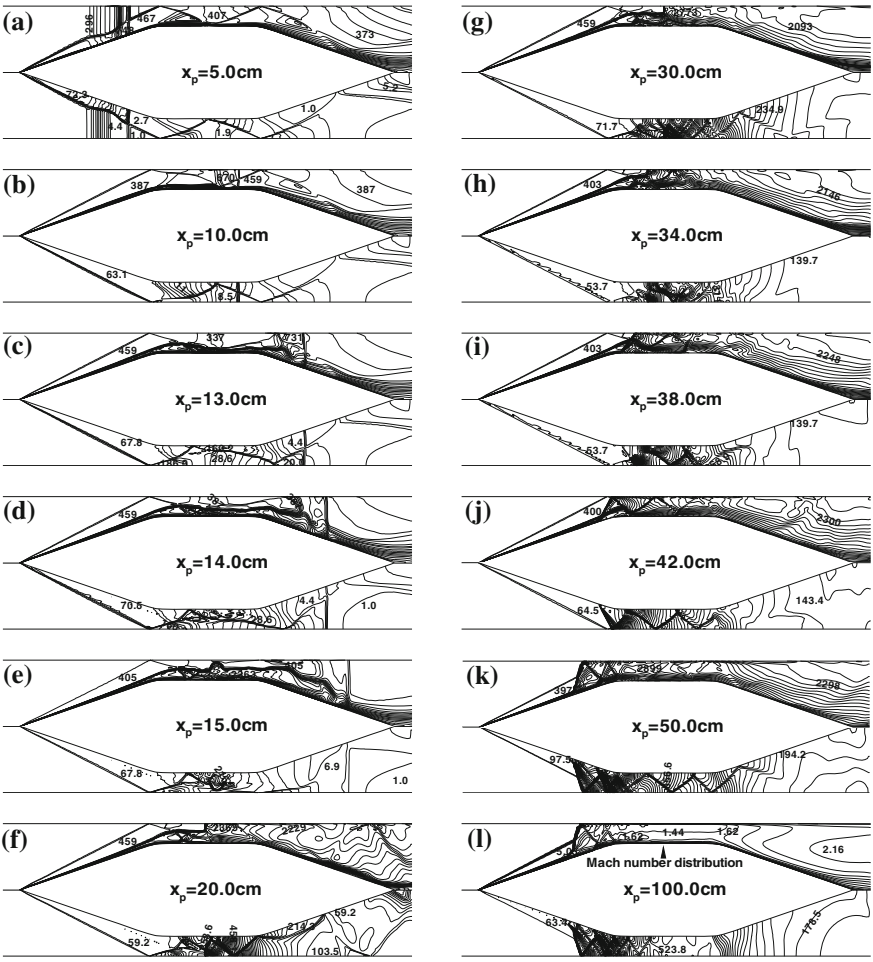

Fig. 11 Temperature distributions (upper half of each figure) and pressure distributions (lower half of each figure) in marching sequence for $2H_2 + O_2 + 5N_2$ mixture; Mach number distributions are plotted for cases x_p = 100.0 cm

gas generated in the boundary layer expands downstream with the expansion wave while the normal shock passes through the projectile tail cone. The reflected shock from the barrel wall deflects with a larger angle when it crosses the expanding burned gas boundary. The deflection causes the forward movement of the shock impinging point. Moreover, the mixture downstream of the impinging point burns more quickly than that in the nose boundary layer because of its compressed condition. The strong shock impingement forms a new oblique shock at the body surface. The oblique shock interacts with the burned gas boundary to form a normal detonation to the barrel wall, and a strong oblique shock is reflected to the body at the interaction point. At this moment, the expanding burned gas boundary acts as a strong contact discontinuity across which the temperature and density vary severely but the pressure changes negligibly.

Although the reaction front downstream of the previous impinging point expands and pushes up the oblique shock, it no longer exists as a reaction front because of the development of the new detonation front. During the separation of the growth bubble, the thrust is generated in a regular manner and the projectile velocity increases linearly. Also, the high-temperature and high-pressure burned gas expands through the conical nozzle and generates the high thrust force that corresponds to more than 5,000 G. The Thrust Coefficient (TC)[3] showed a peak value of about 9 when the SCRamAc operates in a regular manner.

When the separation bubble is large enough to generate the oblique shock outside the burned gas boundary, the oblique shock is transformed to the oblique detonation and moves forward to the conical nose. Finally, the oblique detonation loads high pressure force to the conical nose and results in the severe reduction of acceleration of about zero. The oblique detonation settles down at a specific point on the conical nose after a sufficient March. After this, there exists a regular pattern of shock train, even though there exists a SBLI. The flowfield shows a choked like behavior, even though the choking has not occurred, the acceleration shows an oscillatory behavior resulting in constant velocity. After some time the flowfield seems to be stabilized as shown in the acceleration curve in Fig. 13 and the SCRamAc accelerates in a steady manner. In the previous case, the interaction between the normal shock and oblique shock wave is the possible cause for the initiation of the oblique detonation but at the final stage, the thermal choking is attained at the back of the separation bubble, which causes the severe deceleration of the projectiles. Thus the experimentally investigated lower dilution limit unstart phenomena might be the result of the formation of oblique detonation wave at the nose and the thermal choking conditions provided there by the strong SBLI. For a lesser energetic mixture, regular ignition is observed, which involves complex flow field interactions. However the projectile moves at a quasi-state manner at the final stage with balanced force acting on the body, which is caused by the forward movement of the oblique detonation generated by the separation bubble. Thus, for a

[3]Thrust Coefficient is defined here as the ration of the thrust acting on the body and the initial pressure on the projectile cross section.

regular operation of SCRamAc, the thermal choking condition must be avoided which moves the oblique detonation to the nose of the projectile and decelerates the projectile.

3.3 Performance Comparison

Similarly various studies has been done with various energetic level and the overdriven factor varying from 20 to 50 % for $2H_2 + O_2 + mN_2$ where m is the amount of dilution gas added to the stoichiometric mixture of the propellants and it ranges from 3.76 to 9 to study the combustion process taking place in it as shown in Fig. 12. In the case of m as 7 and the overdriven factor as 1.42, the shock impingement on the middle of the body leads to the gradual growth of the separation bubble that induces a leading oblique shock ahead of it. As time goes on, the separation bubble is getting larger and the leading oblique shock is getting stronger. The new oblique detonation moves forward with the support of the separation bubble and settles down on the conical ramp. This movement of oblique detonation

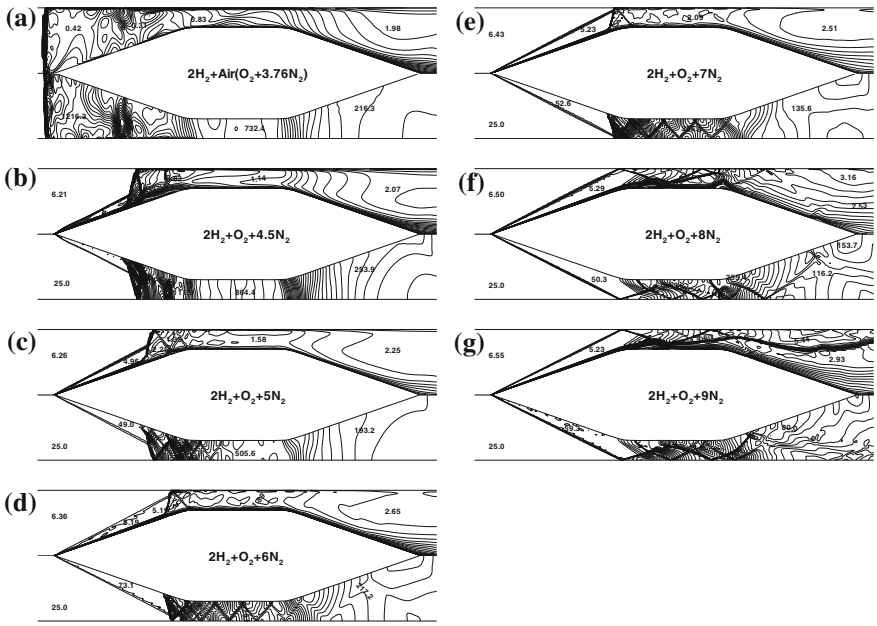

Fig. 12 Mach number distributions (upper half of each figure) and pressure distributions (lower half of each figure) for $2H_2 + O_2 + mN_2$ mixtures varying *m* from 3.76 to 9

results in a reduction of thrust as in the case of m as 5. After moving a considerable distance the flow-field seems to be stabilized and shows a quasi-steady state solution. At the final stage the projectile acceleration is about 6,500 G and the velocity gain of about 15 m/s is attained.

For reactive mixture with m as 5–7, the stabilized oblique detonation is observed at the nose. The flowfield is stabilized at the final stage and thermal choking is not observed. The lesser energetic mixture, the larger is the thrust because the position of oblique detonation is important in view of the force balance along the axisymmetric projectile surface because the post detonation pressure is high enough to cause a severe reduction of thrust. Among the cases considered in this study, the reacting flowfield configuration for reactive mixture with m = 8 predicts maximum performance because the main combustion region is maintained at the midsection of the RamAc projectile. The force acting on the body is evaluated by integrating the pressure and shear wall stress over the projectile surface and the acceleration of the projectile is obtained from the force divided by the projectile mass.

At m = 4.5 the acceleration is about −10,000 G and the velocity decreases about 16 m/s at the final stage. And this result is considered as the lower dilution limit unstart while for m = 9, the velocity increases and the acceleration shows the values of nearly zero because the heat release is not enough to generate a thrust force. And this result is considered as the upper dilution limit start which was observed experimentally. Thus for a regular operation of RamAc, the oblique detonation at the nose must be avoided, which may lead to thermal choking conditions and decelerates the whole projectile and at the same time there must be sufficient heat release to generate the thrust (Fig. 13).

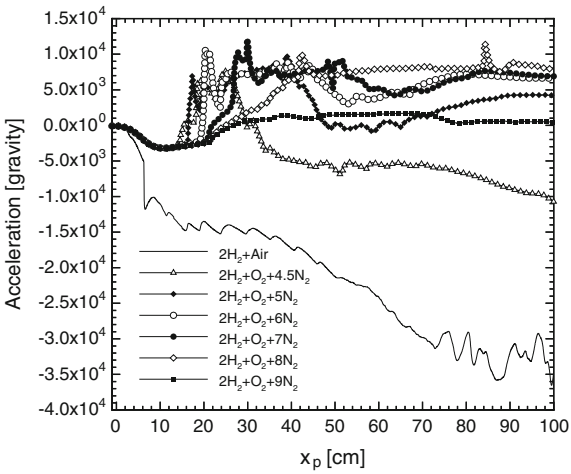

Fig. 13 Acceleration curve for different mixtures with respect to projectile distance from diaphragm

3.4 *Effect of Ignition Source*

A research conducted in RAMAC 30, a facility in ISL[4] which operate directly at superdetonative mode without transition from the thermally choked mode, showed material dependency, in which the material used in the shot was found melted and eroded resulting in 25 % loss in the initial mass [16]. Acceleration was successful with an aluminum projectile while there was no combustion in the case of steel projectile. Choi et al. [17] further improved their code for high pressure combustion analysis of RamAc by modifying the code with real gas equation of state and using a high pressure combustion mechanism. Moon et al. [18] numerically studied the artificial ignition of the projectile along different location along the combustor section and studied the material dependency in a SIC and explained the importance of the location of ignition source for evolution of detonation.

In that study, they performed different case studies by varying the effect of amount and position of the external ignition source as:

Case 1: Provision of ignition source, 1Q at (a + b + c + d + e) section
Case 2: Provision of ignition source, 1/2Q at (a + b + c + d) section
Case 3: Provision of ignition source, 1/2Q at (e) section
Case 4: Provision of ignition source, 1/4Q at (a + b) section
Case 5: Provision of ignition source, 1/4Q at (b + c) section
Case 6: Provision of ignition source, 1/4Q at (c + d) section

where (1/4Q or 1,383 J) is defined as the minimum ignition energy for this simulation. As a result, stable combustion was possible in case 1, case 2 and case 4 whereas the remaining cases did not show detonation and resulted in upper dilution unstart limit.

From Fig. 14a, we can find that the major difference in these cases were the location of the ignition source. When the ignition source is located on the frontal part of the projectile, the coupled shock and reaction front creates a severe pressure gradient across the boundary layer along the projectile's surface and a large separation bubble. This 'Blockage effect' becomes larger as the separation bubble grows and the induced shock wave has more strength which leads a smooth condition for the detonation wave evolution. But when having the ignition source on the rear part of the combustor, the interaction between the shock wave and reaction front was weak and hence the separation bubble was not fully developed for a condition of detonation wave evolution. Thus the initiation of detonation is not only sensitive to the flow field but also to the location of the position of ignition source.

[4]French-German Research Institute of Saint Louis, France.

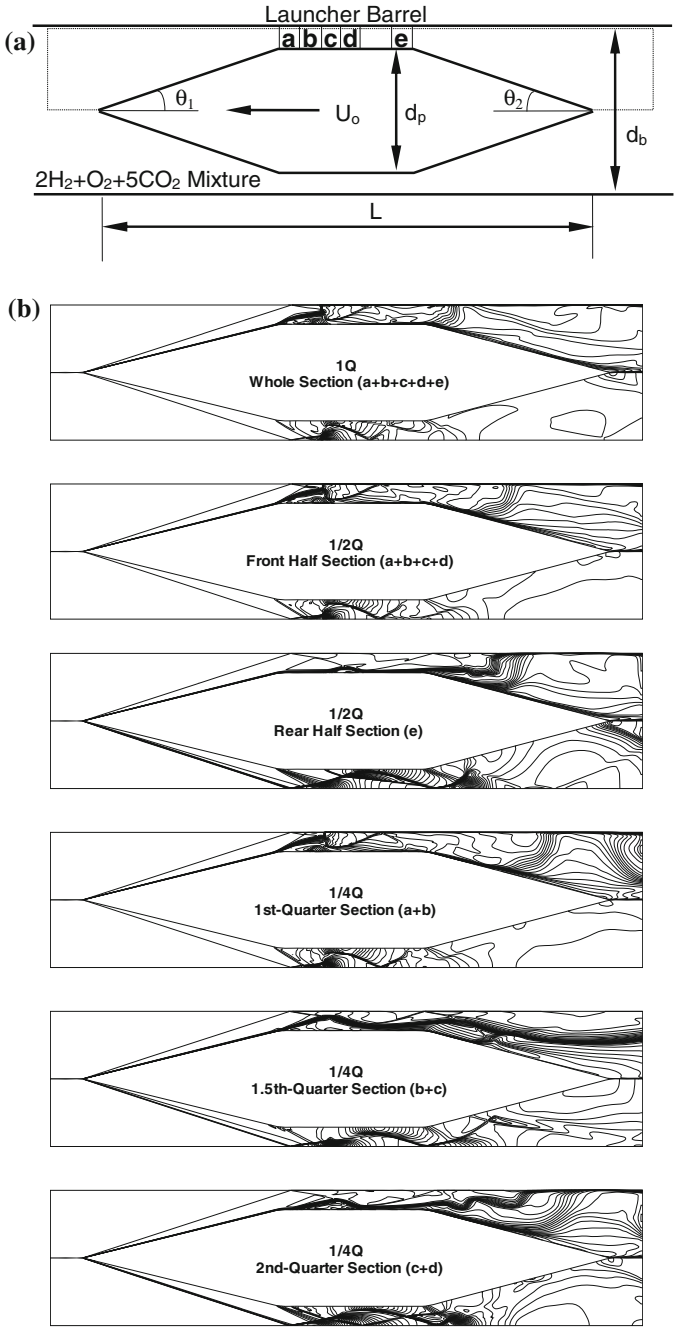

Fig. 14 **a** Configuration of a SCRamAc and Combustor sub-section [a], [b], [c], [d] and [e]. (U_0 = 1800 m/s; mass = 130 g; L = 163.1 cm; d_p = 3.0 cm; d_b = 4.2 cm and $\theta_1 = 14^{\circ}$; $\theta_2 = 15^{\circ}$). **b** The effect of the position of external ignition source

3.5 *Effect of Cone Angle*

Similarly numerical studies were performed to investigate the effect of nose cone angle with the ignition source imposed on the frontal part of the projectile for half-cone angles varying from 12.5˚ to 20˚. The temperature and pressure profiles in Fig. 15 depict the combustion at various considered conditions.

In the case of 12.5˚, the flame did not remain stable and was forced to move backwards because of the strong incident and reflected shock was weak. Accordingly, only the flame in the boundary layer remained and an unstart process

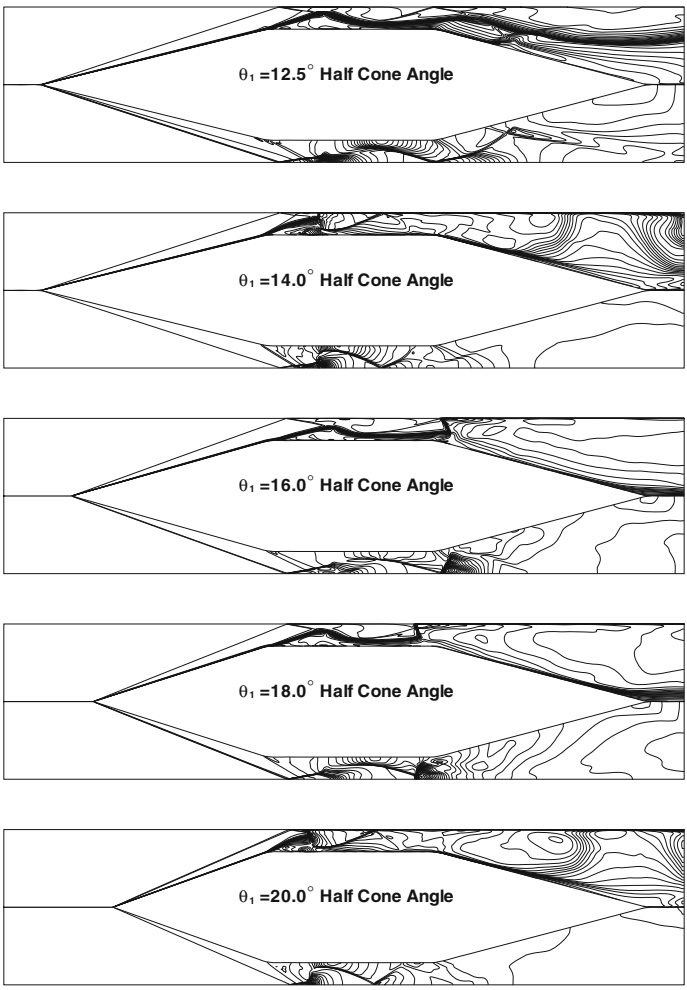

Fig. 15 Effect of nose cone angle provided ignition along the frontal part of the combustor, (1/4Q, Combustor Front Section a + b): *Upper* Temperature Contours, *Lower* Pressure Contours

followed due to the failure of detonation initiation. For 16° and 18°, the reaction front initially formed seemed to remain stable as time proceeded, because the incident and reflected shock wave did not form a strong shock focusing with the induced shock. The reaction front blown off downstream seemed to be stable by strong reattached shock at the tube wall but it was not sustained by something like separation bubble near the projectile surface. For 20°, strong oblique detonation wave was created but the separation bubble tended to grow and move forward. Shock focus between the reflected shock and induced shock waves varies according to the cone angle of projectile and hence nose cone angle influences the reaction front stability.

4 Viscous Effects in Ram Accelerators

4.1 Viscous Effects on RamAc in the Expansion Tube

The calculation was done for $2H_2 + O_2 + 12N_2$ mixture to estimate the effect of boundary layer combustion using a half-computational domain used before with non-reflecting boundary condition at upper surface. Figure 16a is a result of the calculation showing overlaid pressure and OH mass fraction contours. Figure 16b is the plot near the wedge shoulder with overlaid streamlines. It is noted that the combustion is confined to thin boundary layer but recirculation is not present due to the smooth flow turning angle. Expansion waves are present but have negligible effect on combustion. On the contrary, the boundary layer (colored OH distribution) beyond the wedge shoulder is slightly thicker than on the wedge slope. However,

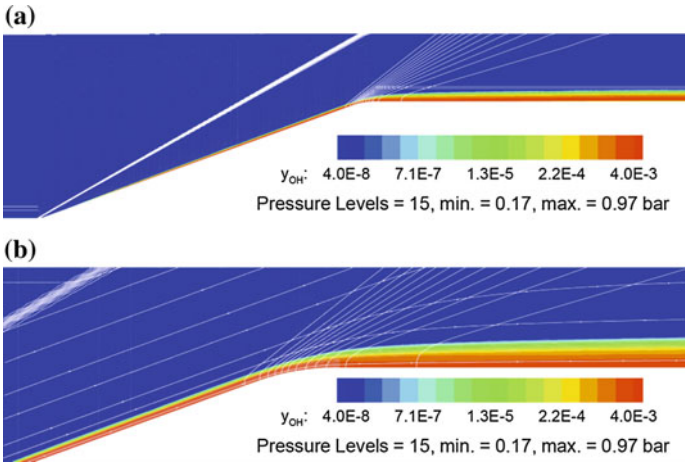

Fig. 16 Steady state results $2H_2 + O_2 + 12N_2$ case without shock wave reflection **a** Over pressure contours and OH distribution, **b** magnified view near wedge shoulder overlaid with streamlines

the boundary layer thickness is still much thinner than the size of recirculation region. Also the maximum level of OH in the recirculation zone is 0.01, it is hard to think that the OH in the recirculation zone is only a residual effect of boundary layer combustion without combustion in recirculation zone itself. Even though the reflected shock wave itself is not strong enough to ignite the mixture, the boundary layer flow stagnates in front of the shock wave and forms a recirculation zone. If the flow stagnates, the temperature rises up beyond the ignition temperature and combustion initiates.

Simulation was done for the $2H_2 + O_2 + 12N_2$ mixture without viscous terms and the result shows nearly same evolution process shown in the Fig. 17, except for the boundary layer combustion and recirculation region. It is also noted that combustion occurs locally behind the impinging oblique shock wave at time of around 160 μs, but finally disappears. This is considered as a local and temporal effect of shock heating, and similar results are shown in Fig. 7 combined with the influence of boundary layer. With the result of inviscid calculation, it becomes manifest that the formation of recirculation zone and the combustion in it are the effect of viscosity.

4.2 Viscous Effects During RamAc Operation

As already mentioned the viscous effect plays a very important role in a SCRamAc operation because the viscous effect induces complex flow interactions even though the viscous drag is negligible. In a regular operating condition, the ignition of the mixture initiates at the shockwave/boundary-layer interaction point, where the temperature is very high due to the aerodynamic heating, as shown in the previous study of super-detonative [19] and trans-detonative mode [20] operations. A numerical study was performed with the dilution amount m = 8 and Fig. 18 depicts the stabilized flow field of the mixture at the final stage. The main combustion front is composed of the oblique SIC behind the reattachment shock and the normal detonation to the barrel wall. A large separation bubble is shown at the shock impinging region at the projectile surface and the separation bubble induces a strong oblique shock ahead of it. A similar result of the large separated flow region is also found from the experimental result of Morris et al. [12] and from the numerical simulations [12]. In the burned gas boundary layer of more energetic mixtures, the growing process of the separation bubble has a very close relation with the RamAc performance. The oblique shock ahead of the separation bubble can be changed into a new oblique detonation that reduces thrust by settling down on the conical nose. Sometimes the large separation bubble blocks most of the combustor section and causes the thermal choking that results in the lower dilution limit unstart.

After the burning of the mixture, local temperature increases whereas local density decreases. Therefore, the local values of sonic velocity and viscosity of burned gas increase. Because of this, local values of Mach number and Reynolds

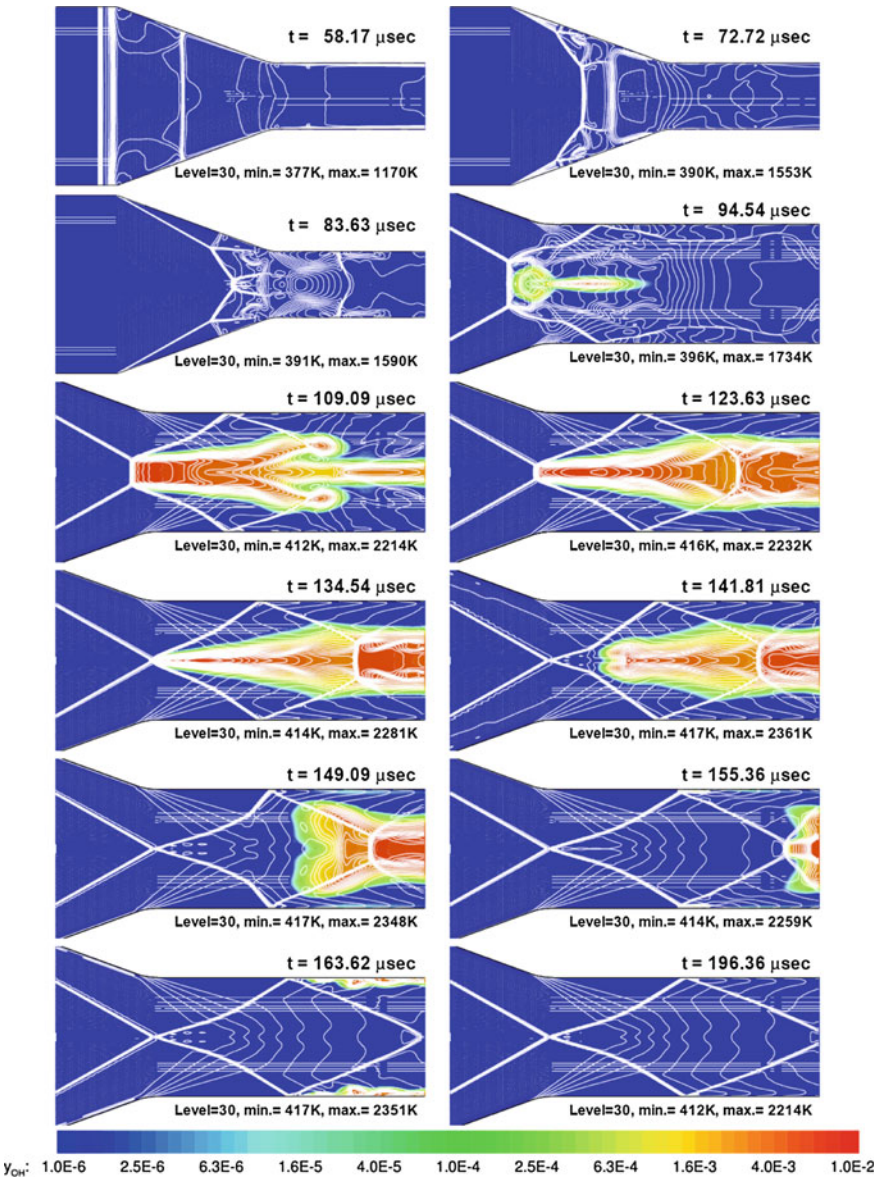

Fig. 17 Result of inviscid computation using slip-wall boundary condition: Overlaid temperature contours and OH mass fraction distributions showing unsteady combustion process of $2H_2 + O_2 + 12N_2$ mixture. Combustion region is magnified after t = 94.54 μs

number are maintained at order of 2 and 1×10^6, respectively, which are considered to be small values in comparison with the values for the non-reacting flow. Thus, the effect of viscosity is shown to be more enhanced than that in the non-reacting

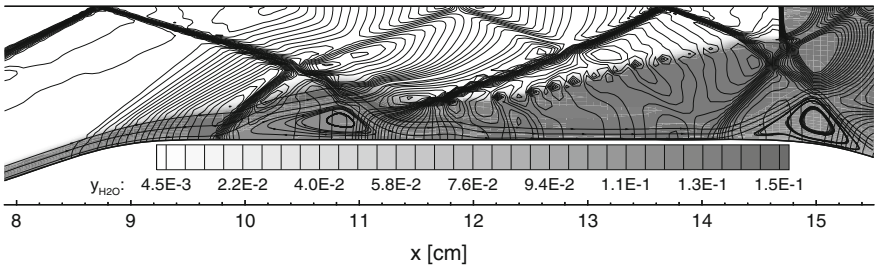

Fig. 18 Magnified view of internal combustion flow field for case of $2H_2 + O_2 + 8N_2$ mixture; overlaid plot of the distribution of H_2O mass fraction, pressure contours, and streamlines in boundary layer

flow. Such a strong viscosity effect influences not only the regular ignition or initiation process but also the stabilization of oblique detonation at the final stage.

For the cases considered in this study, the oblique detonation wave is formed at the conical ramp for mixtures with various dilution amount ranging m = 5−7. In the summarized plots in Fig. 12, it is readily found that the location of the oblique detonation wave moves downstream as the quantity of diluent gas increases. However, the structure of the stabilized oblique detonation waves looks similar, and complex shock trains are shown downstream.

To investigate the flow structure closely near the oblique detonation wave, the result of the case of m as 6 is plotted in Fig. 19 (with magnification). A separation bubble is shown at the origin of oblique detonation, and compression waves are formed ahead of this separation bubble. The compression waves and the deflagration wave, i.e., an edge of the thermal boundary layer, merge and form an oblique detonation. Meanwhile, expansion waves are present after the oblique detonation wave that was generated around the separation bubble. Recompression

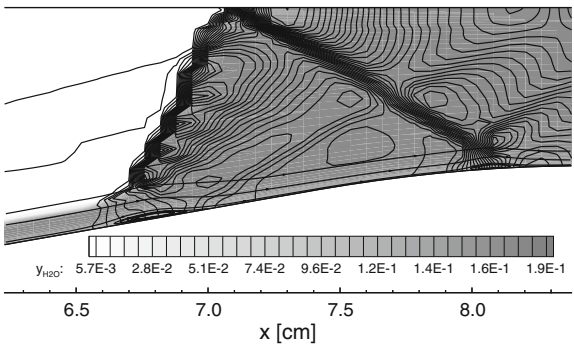

Fig. 19 Magnified view of flow-field near oblique detonation for case of $2H_2 + O_2 + 6N_2$ mixture; overlaid plot of the distribution of H_2O mass fraction, pressure contours, and streamlines in boundary layer

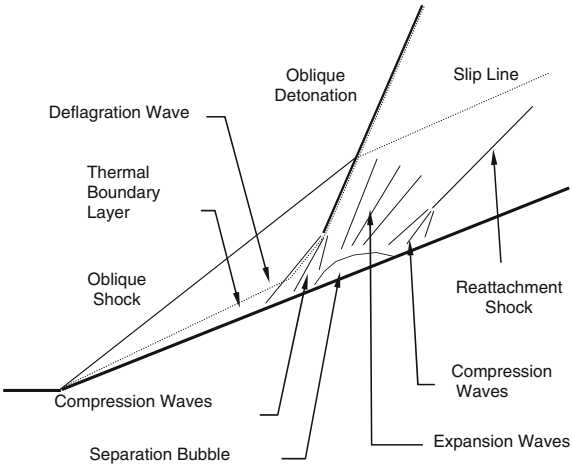

Fig. 20 Schematic of flow structure of stabilized oblique detonation supported by strong shock wave/boundary-layer interaction

waves are found downstream of the separation bubble and form a reattachment shock in the burned gas region. After the collision of incidence shock and the detonation front, a slip line is present downstream, as shown in Fig. 19 by the wiggles of the pressure contours. Similar flow features are also found in other cases and are summarized as a schematic plot in Fig. 20.

4.3 Evolution of ODW in Boundary Layers

In the previous study of SCRamAc operation, SBLI is found to have a critical role in the evolution and stabilization of the detonation wave. Hence, another case study on RamAc operations, with the inflow temperature, pressure, Mach number and incidence shock angle were fixed at 293 K, 1 bar, 5 and 20° respectively, were performed for different length scale [21]. The length scale L of the plate is defined as the distance from the nose to the impinging point of the incidence shock wave. For this study,

Case 1: L as 1.0 cm with Reynolds numbers as 8.9×10^5
Case 2: L as 2.0 cm with Reynolds numbers as 1.8×10^6
Case 3: L as 5.0 cm with Reynolds numbers as 4.5×10^6
Case 4: L as 10.0 cm with Reynolds numbers as 8.9×10^6

However, it will not be fair to attribute the reason only to different Reynolds numbers, even though the Reynolds numbers of each case are different to the order of magnitude. Even with the different Reynolds numbers, the dimensionless thickness of boundary layer is not significantly different. Therefore, it will be fair to attribute the reason to the fluid dynamic length scale of each case, such as absolute thickness of the boundary layer.

The combustion is considered to be most actively going on in the case 1 while for the case 2, the situation is similar but quite different, and the flame region is thicker than for the case 1. The burned gas region is not confined in the boundary layer but is expanding to the outer region. The expanding burned gas region makes new compression waves between the reflecting oblique shock wave and the flame front and pushes the oblique shock wave to have a steeper wave angle and the separation bubble occupies a much larger area than the case 1. The most active combustion region is the separation bubble itself, differently to the case 1. These differences are due only to the different scale, because all other flow conditions are exactly the same. Quantitative comparison of these two cases to that of skin friction coefficient is shown in Fig. 21 where the location of the impinging point is marked as a vertical solid line, and the location of the zero-friction coefficient, where velocity changes are present, is marked as a horizontal solid line. The distance between the locations of the zero-friction coefficient may be defined as the maximum length of separating bubble. In case of the frozen flow solution, both cases show nearly the same size of separation bubble in dimensionless sense. However, case 2 shows about a two times larger separation bubble in reactive simulation. The actual size may be three to four times larger than in case 1. The concave bumps of the skin friction curves in the frontal part are the locations of turbulence transition, and Reynolds number is responsible for the difference between the bump locations.

The cases are different for 3 and 4. These cases show an unsteady evolution process of oblique detonation wave, and the detonation wave does not settle down at a specific location. Figure 22 shows snapshots of the evolution process of the oblique detonation wave for case 3. At the beginning, a gas mixture detonates at some distance behind the shock impinging point. The detonation wave just expands downstream due to the overdriven flow velocity and forms an oblique detonation wave. Along with the expansion of the detonation wave, the separation bubble grows and shows the structure of the oblique detonation wave. Even though this

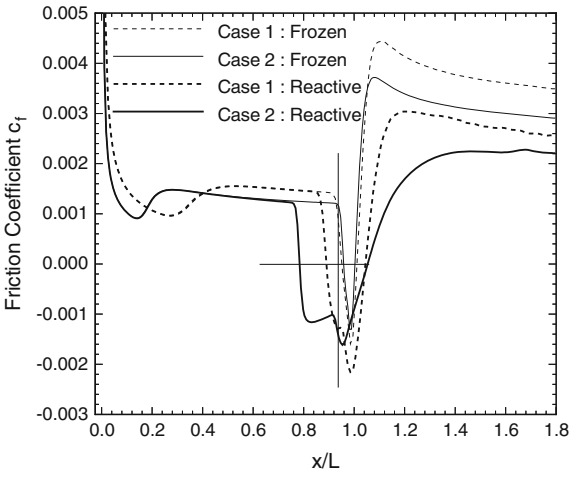

Fig. 21 Distribution of skin friction coefficient along the wall for cases 1 and 2

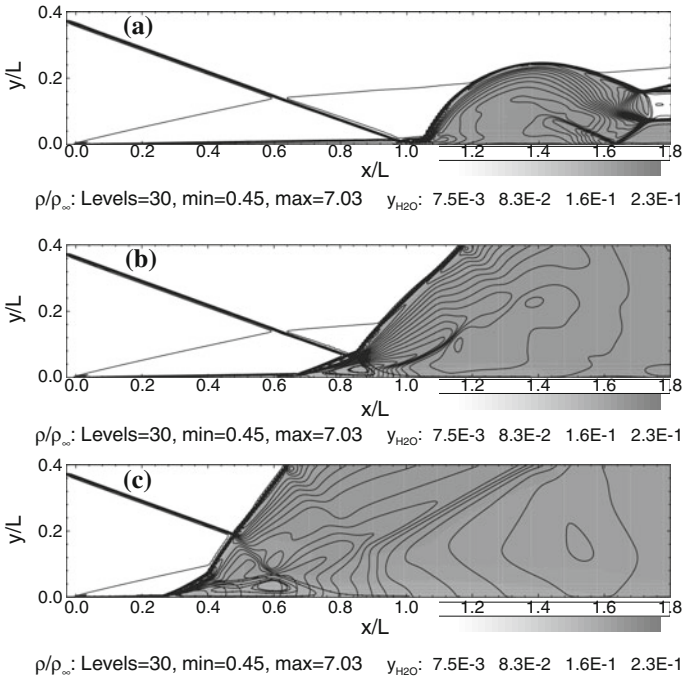

Fig. 22 Result of case 3 where L = 5.0 cm. Overlaid plot of density contours and distribution of water vapor mass fraction at different instances. **a** t = 2.32 μs. **b** t = 7.72 μs. **c** t = 23.15 μs

process is considered as an unphysical one due to the ideal initial condition, it takes about only 1/10 of the time of the total process. Once the oblique detonation wave is formed, the detonation wave moves forward at relatively slow speed. The separation bubble does not grow more than a certain height and breaks up into two parts during the forward movement. The breakup of the separation bubble is considered owing to the crossed structure of the incidence shock wave and the oblique detonation wave. At the final stage, the oblique detonation wave moves to the leading edge and the transient calculation was terminated, because the primary investigation point of this study is the combustion characteristics near the shock impinging point.

More detailed time-dependent processes are plotted in Fig. 23 for cases 3 and 4. The result for cases 3 and 4 show nearly the same trend. However, in case 4, with the length scale two times larger than in case 3, the detonation originates at a closer distance behind the incidence shock impinging point. The absolute time needed for the evolution of the oblique detonation wave seems to have the same order of magnitude. However, more than two times the absolute time is needed for case 4 to reach the leading edge due to the length is two times as large of case 4. This means that the forward running speed of the oblique detonation wave is nearly the same for both cases, and it is estimated at 1,200 m/s.

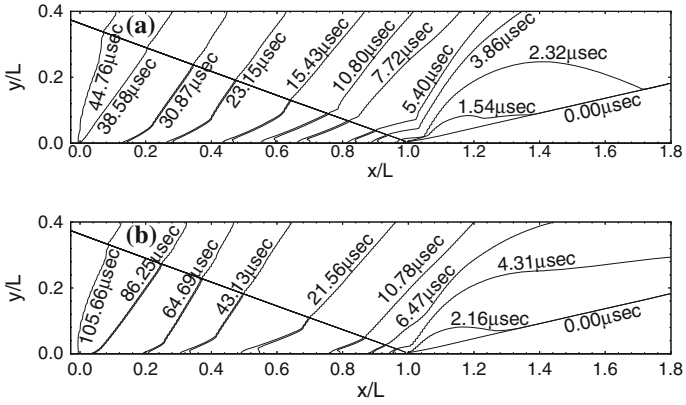

Fig. 23 Time-dependent plot of propagating oblique detonation wave. Only the incidence shock wave and the oblique detonation wave are plotted. **a** Case 3 where L = 5.0 cm. **b** Case 4 where L = 10.0 cm

Case 1 with the smallest length scale, shows an active combustion region behind the separation bubble. In case the length scale increases, the flame is getting thicker, and combustion is accomplished in the separation bubble. If the length scale exceeds a certain value, the mixture detonates through the edge of the boundary layer, and the forward running oblique detonation wave evolves. The behavior with respect to the fluid dynamic length scale may be attributed to the different values of the Damköhler number, defined as a ratio of flow residence time to the chemical induction time. If the flow residence time is sufficiently long to accommodate the complete combustion, the detonative explosion is possible, and the oblique detonation may be observed. If not, the combustion is restricted as boundary layer flame or oblique shock-induced combustion.

5 Effect of Fluid Dynamic Parameters on SIC

5.1 Effect of Physical Size

A parametric study [22] has been done with respect to body size ranging from 0.1 R^* to 1.0 R^* with an increment of 0.1 R^*, where the reference radius R = 1.0 R^* corresponds to the body radius used in the Lehr Experiment [6], to investigate the effect of fluid dynamic length scale while inflow pressure and temperature from the experiments are kept constant. From the study it was found that the regime of SIC gradually changes from decoupled shock-deflagration to overdriven detonation. This is due to the ID decreasing relatively as the body radius increases, even though the

absolute value of ID may not be affected by the change of body radius. Therefore, the reaction front gets closer to the shock front in the overall flow field, and the burned gas takes a larger portion of the post-shock region and expands more quickly to push the shock and the reaction front itself forward. The shock SD increases as the radius of the body increases while the ID relatively decreases.

The shock SD and the ID are plotted with respect to body radius in a relative (non-dimensional) length scale in Fig. 24 and in an absolute (dimensional) length scale in Fig. 25. In a relative coordinate, SD increases rapidly as the body size increases. However, ID gradually decreases while the absolute value of ID remains nearly constant.

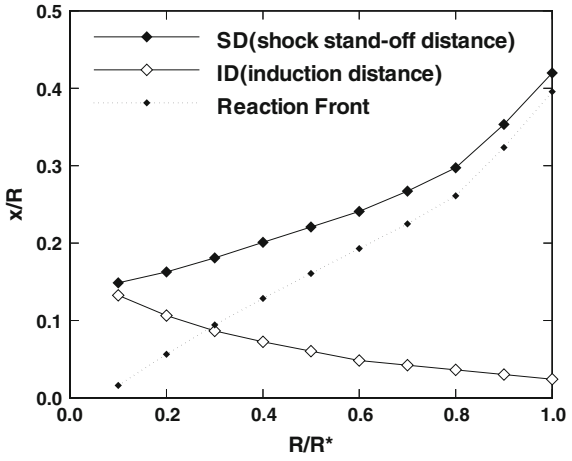

Fig. 24 Shock SD and ID with respect to body radius in a relative length scale

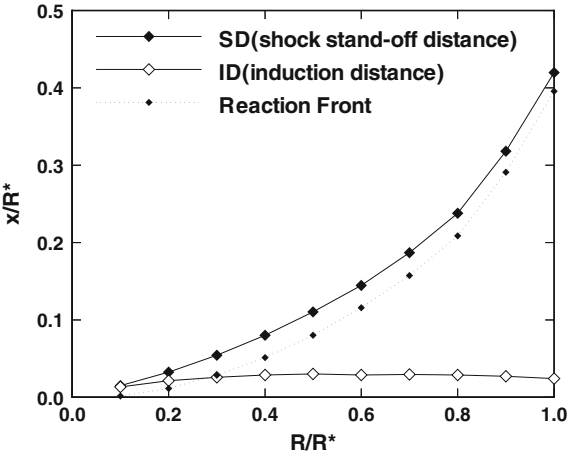

Fig. 25 Shock SD and ID with respect to body radius in an absolute length scale

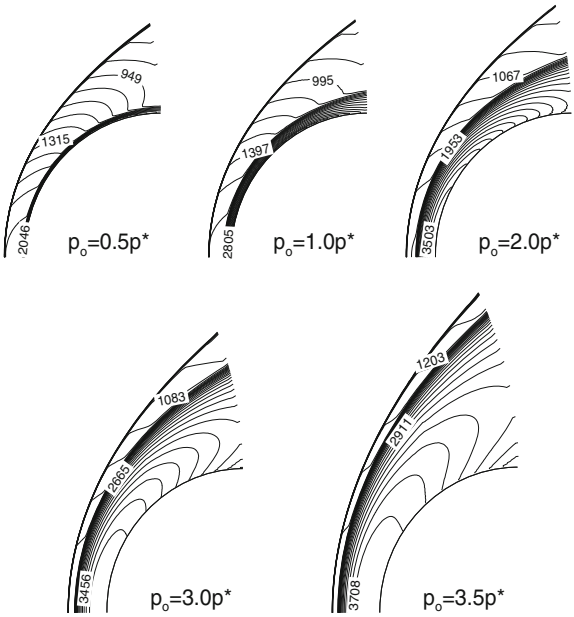

Fig. 26 Effect of inflow Pressure for T_0 = 292 K and R = 0.2 R*

5.2 *Effect of Inflow Pressure*

The effect of inflow pressure is studied with a physical body size of 0.2 R and inflow temperature from the experiment are kept as constant where p* corresponds to the pressure used by Lehr [6]. As the inflow pressure increases, the regime of SIC changes from decoupled shock-deflagration to overdriven detonation, which is very similar to the results for body size variation. It is worth noting that the maximum temperature increases as the inflow pressure increases as shown in Fig. 26, and the approximate maximum value of heat release shows slightly larger values than those for the body size variation. The variation of the overdrive parameter ranges from 1.07 to 1.03 with the inflow pressure variation, and the maximum deviation is limited to about 4 %, which is introduced by the slight increase of heat release.

Therefore, this case is also considered as Damköhler number[5]—dominated phenomenon and not as Heat Release parameter (HR) or overdrive parameter-dominated phenomenon. Consequently, a very similar tendency is obtained as for body radius variation. The global kinetic mechanism of SIC may seem to be a second order reaction. The increase of body size or inflow pressure mainly leads to an increase of the shock SD and a decrease of the ID, which means a transition from decoupled shock-deflagration to overdriven detonation.

[5]More detailed discussion on the effect of Damköhler number (Da_1) and Heat Release parameter are discussed by Choi et al. in Ref. [22].

5.3 *Effect of Inflow Temperature*

Series of calculations were performed for different inflow temperatures varying from 292 to 900 K, with a physical body radius of with a physical body size of 0.2 R and inflow pressure from the experiment are kept as constant. The result in Fig. 27 shows very different features than the results with variation of body radius and inflow pressure. Even though an increase of inflow temperatures causes the regime transition of SIC from decoupled shock-deflagration to a coupled system, no solution is observed that can be considered as overdriven detonation. With an increase of inflow temperature, the Damköhler parameter slowly increases but shows a maximum value of about 150, which is small in comparison to the results of the effect of body size or inflow pressure increase. The HR decreases rapidly and shows negative values for the cases of high inflow temperatures; that is, the chemical reaction is endothermic due to the dissociation of the combustion product.

5.4 *Effect of Fluidic Dynamic Parameters on SIC*

With a variation of inflow temperature, the overdrive parameter monotonically increases from 1.06 to 1.79, which is readily understood from the decrease of HR. As a result, the increase of inflow temperature causes the slight increase of local Damköhler number but dilutes the effect of heat addition. This is true for the whole flowfield and is not restricted to the stagnation line. The variation of Da_1 and HR are summarized in Fig. 28 for the variation of temperature. Therefore, the burned gas region cannot expand or push the shock front, and the reaction front is decoupled downstream.

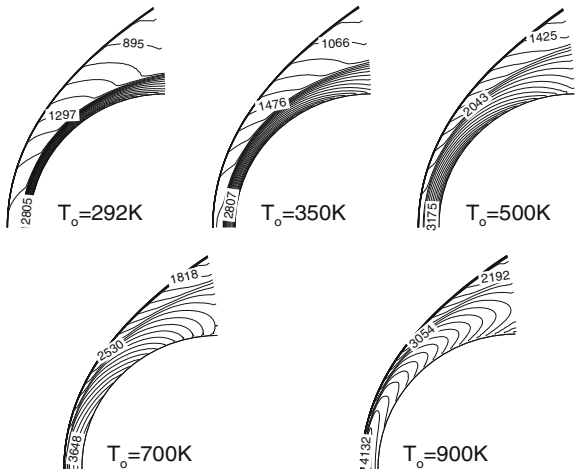

Fig. 27 Effect of inflow Temperature for $P_0 = 1.0\ P^*$ and $R = 0.2\ R^*$

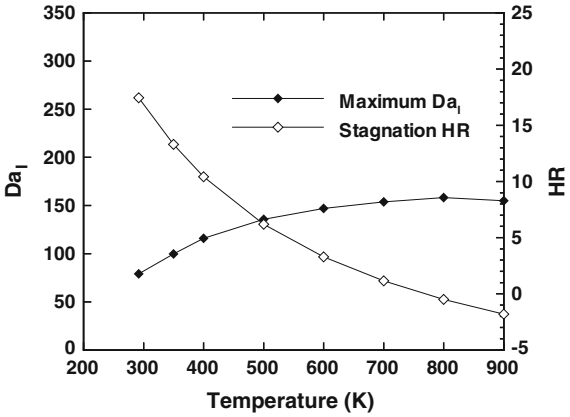

Fig. 28 Maximum Da_I for H_2O production and stagnation HR with respect to inflow temperature

6 Evolution of Cellular Instabilities of the Oblique Detonation Wave

Oblique detonation waves (ODWs) stabilized over inclined walls has long been considered as a promising combustion means for hypersonic propulsion systems such as ODW engines and RamAc. A number of studies [23] were carried out to examine the fundamental characteristics of an ODW and its implementation for propulsion systems. Pratt et al. [23] applied classical detonation theories by assuming immediate heat addition behind an oblique shock wave (OSW). Shepherd [24] reported the state of knowledge about ODW for propulsion applications as of 1994. The ODW phenomena have been observed by using the two-layer detonation tubes for two-dimensional configurations [23, 25] and the ballistic range facilities for axi-symmetric configurations [26, 27]. Morris et al. [28] used the expansion tube to study oblique SIC. A number of numerical studies have been carried out to understand the physics of the ODW for more than a decade [29, 30]. These studies have provided much insight into the ODW dynamics and structures, but they need much more proof, such as detonation cell structure, to convince that the ODW is a class of detonation phenomena, neither the experiments nor the numerical simulations provided yet. Choi et al. conducted a series of fine scale numerical studies to pursue the answer for the stability of the ODW wave structures [31].

6.1 Numerical Model for the Fine Scale Analysis of ODW

An analysis was done based on the Euler equations for an inviscid compressible flow, and conservation of a reaction progress variable was taken into account. A governing equation in a two-dimensional coordinate system was taken into account where the pressure, p, at any instant is obtained through the equation of state as follows.

$$p = (\gamma - 1)\rho\left\{e - \frac{1}{2}\left(u^2 + v^2\right) + Zq\right\} \tag{5}$$

where

γ—Specific Heat Ratio
ρ—Density of the mixture
e—Total energy of the mixture
u, v—Velocity in the 2 dimensional plane
Z—Reaction Progress variable
q—Heat addition

The reaction progress variable, Z, characterizes the mass fraction of product species, and varies from 0 to 1. The dimensionless heat addition is denoted by q and a one-step Arrhenius type reaction model was used to simulate the various regimes of detonation phenomena without the complexity and large computing time associated with multiple chemical species and reaction steps. Thus the reaction rate depends only on the mixture concentration as:

$$w = (1 - Z)k\exp(-E_a\rho/p) \tag{6}$$

where,

k—Pre-exponential factor
E_a—Activation energy.

Thorough description of the fluid dynamic model and numerical methods are included in Choi et al. [32] with detailed numerical studies on the detonation structure.

In a study [31], with a Mach number 7 flow with a specific heat ratio $\gamma = 1.3$ over a 30° wedge is treated as shown in Fig. 29 with a relatively small value of dimensionless heat addition, q, of 10.0 is assumed to render the difference between Oblique Shock Wave (OSW) and Oblique Detonation Wave(ODW). The resultant wave angles are 37.6° for OSW and 48.6° for ODW. Five different levels of numerical grid resolution are considered with the corresponding grid sizes as $\Delta x = \Delta y = 1/250$, 1/500, 1/1000, 1/2000, 1/4000 respectively with a non-dimensional length of 1 unit. To study the influence of dimensionless activation energy on **the** wave instability characteristics, different values of activation energy, $E_a = 10$, 20, 25 and 30 were considered. The pre-exponential factor, k, is adjusted to capture the primary triple point over the wedge surface at the dimensionless distance of $x \approx 0.2$.

Figure 30 shows the distribution of the reaction progress variable along the wave normal direction behind the OSW and ODW from the steady ZND[6] calculations,

[6]ZND—the flow in which a high speed flow causes a thin reactionless shock wave followed by the reaction zone because of high temperature and aerodynamic compression of the mixture.

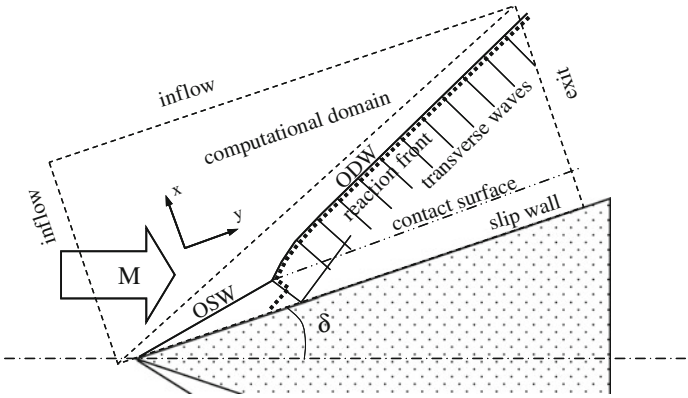

Fig. 29 Schematics of flow configuration and coordinate systems

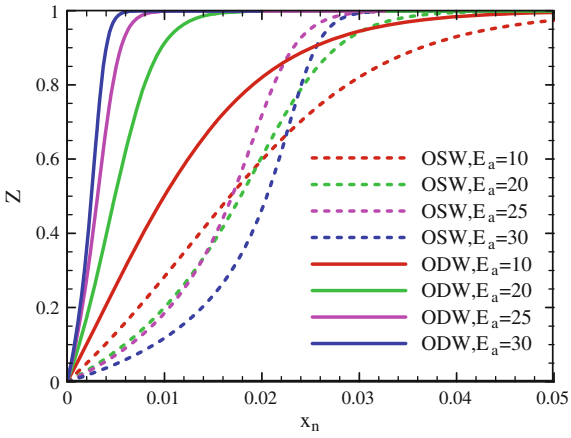

Fig. 30 Effect of activation energy on the distribution of reaction progress variable along the wave normal direction. Obtained from the calculated ZND structure behind OSW and ODW

where Z is the reaction progress variable calculated along the dimensionless distance x_n. A higher activation energy leads to a higher ratio of half reaction length $L_{1/2}^{OSW}$ to $L_{1/2}^{ODW}$, suggesting a more refined grid is required to capture the ZND structure behind the ODW.

6.2 *Regularly Unstable ODW*

In the case of E_a = 10.0, no coupling between the shock and reaction front occurs, and the OSW transits to the ODW very smoothly. The pressure profiles comparison at the exit of the computational domain with different grid resolutions shows that all the results coincide to a single distribution. Thus, for E_a = 10, a stable ODW is obtained without any oscillations at the wave front. The calculated OSW and ODW

angles are 38° and 49°, respectively, agreeing well with the theoretical values of 37.6° and 48.6°.

In the case of $E_a = 20.0$, the coupling between the shock wave and reaction front is clearly observed, although the interaction is not strong enough and the OSW smoothly transits to a detonation wave. The results with different grids agree well with each other and the numerical-convergence characteristics are similar to those for $E_a = 10$. Therefore, the case of $E_a = 20$ is also considered as a stable ODW. It is worth noting that those stable ODWs with low activation energies have not been observed in experiments, and must be treated as theoretically limiting cases.

For $E_a = 25.0$, a coarser grid shows a smooth wave front. But with finer grids, the situation gets completely changed. For $\Delta x = \Delta y = 1/500$, instability starts which gets revealed by the variation of the wave-front thickness. The situation becomes more obvious for the $\Delta x = \Delta y = 1/1000$ especially near the end of the computational domain. Shock wave, generated at the primary triple point and reflected from the wedge surface, passes across the slip surface and interacts with the ODW. It is generally believed that the instability at the wave front grows out of reinforcement between the disturbances inherent in the flowfield and shock waves. A small disturbance initially produced by numerical errors propagates downstream along the wave's tangential direction and then amplifies to interact with the ODW structure. With $\Delta x = \Delta y = 1/2000$ grid system, the ODW front instability is clearly observed as well-organized cell-like structures.

A comparative study of different grids with snapshots of temperature is shown in Fig. 31. A close-up view is given in Fig. 32, along with a schematic diagram of the wave-front structure (as shown in Fig. 33) illustrating features distinct from those of a NDW front. Under current flow conditions, all the transverse waves propagate in the same direction behind the ODW. The situation bears a close resemblance to the numerically produced x–t diagram 4 for Lehr's experiment [6] of oscillating SIC around a blunt body. The cell structure of an ordinary NDW may not be expected to

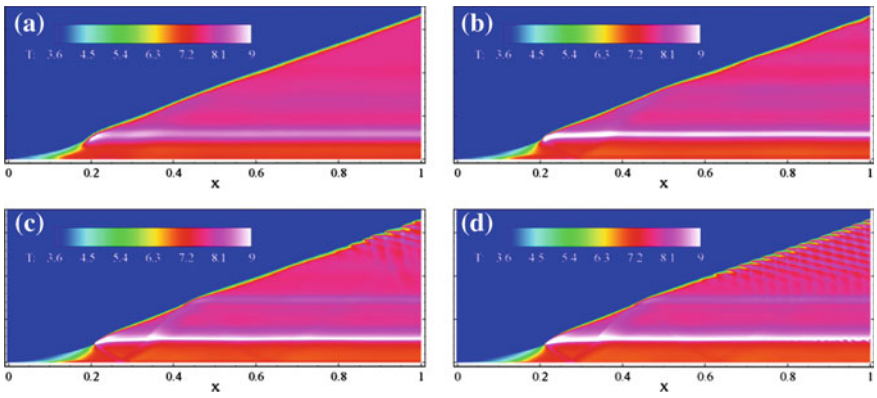

Fig. 31 Snapshots of temperature field for the case of $E_a = 25$ with different grids: **a** $\Delta x = \Delta y = 1/250$, **b** $\Delta x = \Delta y = 1/500$, **c** $\Delta x = \Delta y = 1/1000$, **d** $\Delta x = \Delta y = 1/2000$

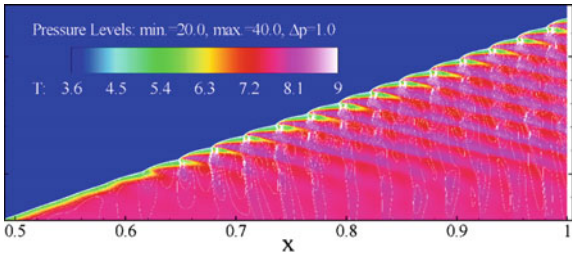

Fig. 32 Regularly unstable ODW front structure for the case of $E_a = 25$ with $\Delta x = \Delta y = 1/2000$ with a close view of pressure and temperature fields

Fig. 33 Schematic of wave front structure

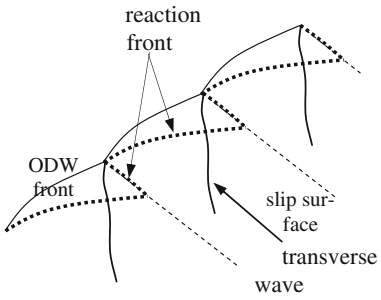

occur for an unstable ODW on a smoke-foil record. Thus, we refer the unstable ODW front structure to a cell-like structure instead of a cell structure.

Figure 34a shows a more refined result with $\Delta x = \Delta y = 1/4000$. The wave instability begins at a location where the reflected shock from the wall interacts with the ODW. Strong vorticity generation occurs at the slip surface originating from the primary triple point. The vortical field interacts with transverse waves from the unstable ODW front. The resultant reflected waves further interact with the ODW front. The highly refined numerical grid resolves many sources of flow disturbances that make the unstable ODW front irregular. Figure 34b shows instantaneous exit pressure profiles with different grids. A finer grid gives rise to stronger pressure unsteadiness. Nonetheless, all the calculations lead to the same ODW angle in the time-averaged sense, and agree well with the theoretical value of 48.6°.

6.3 Irregularly Unstable ODW

For higher activation energy, even in the coarser grids, flow unsteadiness was found whereas for slightly finer grids results in an unstable ODW structure, as shown in Fig. 35. With a grid cell size of $\Delta x = \Delta y = 1/500$, a regular pattern of an unstable ODW structure is obtained, whereas a $\Delta x = \Delta y = 1/1000$ cell sized grid systems

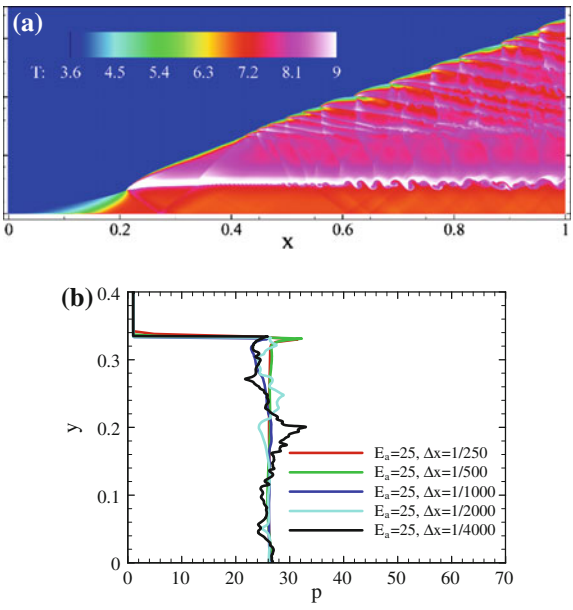

Fig. 34 Unstable ODW for the case of $E_a = 25$, **a** snapshot of temperature field with $\Delta x = \Delta y = 1/4000$, **b** exit pressure profiles with different grids

leads to an irregular pattern. In the latter two cases, the location where the unstable ODW structure begins is almost at the same location.

An even finer solution results in a very complex structure consisting of a strong vorticity generating mechanism from the primary triple point, as shown in Fig. 36. The vortical field appears quite regular in this case. The unstable ODW structure starts to occur when the reflected shock wave interacts with the ODW front, though some instability phenomena are already present upstream of the interaction point. Also, a secondary vorticity is observed at the slip surface originating from the triple point of an unstable ODW front. With a finer grid, the flow unsteadiness becomes quite strong, and the instability appears at a very early position around the primary triple point.

As Viguier et al. [25] observed in their experiment, the unstable ODW structure is small at the initial position and becomes larger as it moves downstream. The various sources of flow disturbances interact with each other, and consequently cause a complex flow structure. The flame front is disturbed accordingly and presents such an irregular wavy pattern. Although the flow-field behind the primary triple point is very complex, the preheat zone ahead of that point remains steady and nearly unchanged. The dominant peak in the wall pressure is caused by the reflected shock wave from the primary triple point. The calculated pressure profiles tend to converge as the grid becomes finer. The pressure distribution is relatively smooth upstream of the peak, but becomes oscillatory in the downstream region. The angle of the triple point trace is determined by the vector sum of the triple point and flow velocities. As discussed before, no noticeable cell structure is observed because all transverse waves move in the same direction, although with slightly different speeds. The wiggles in the smoke foil result from the misalignment of the computational grid line with the flow direction.

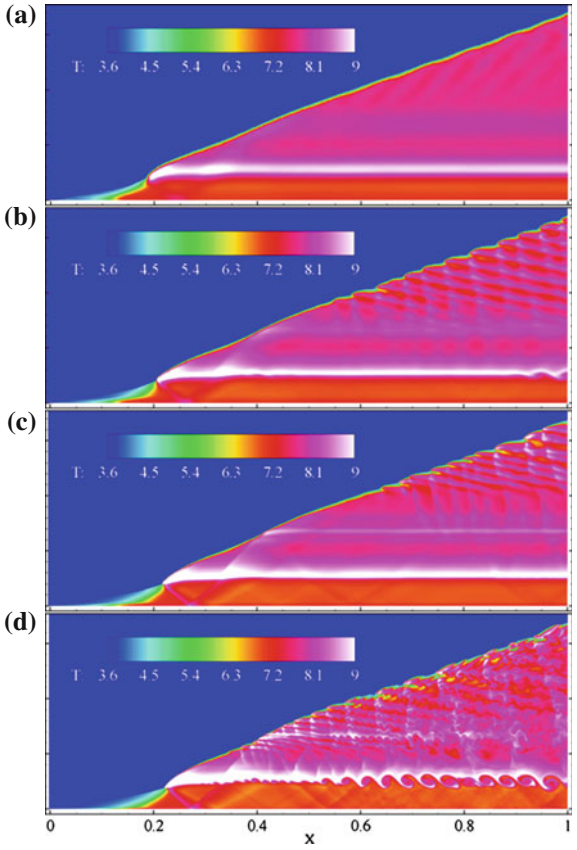

Fig. 35 Snapshots of temperature field for the case of $E_a = 30$,
a $\Delta x = \Delta y = 1/250$,
b $\Delta x = \Delta y = 1/500$,
c $\Delta x = \Delta y = 1/1000$,
d $\Delta x = \Delta y = 1/2000$

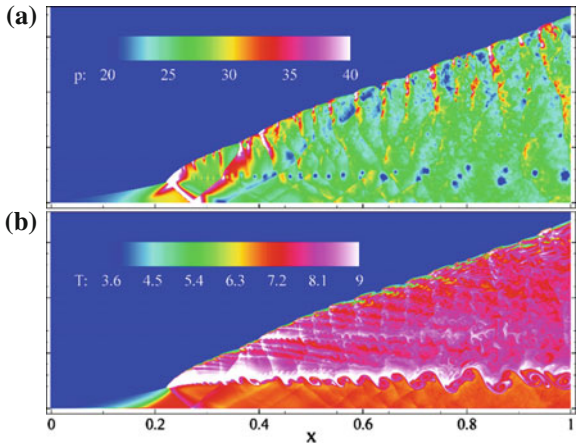

Fig. 36 Unstable ODW for the case of $E_a = 30$, **a** pressure field with $\Delta x = 1/4000$, **b** temperature field with $\Delta x = 1/4000$

7 Non-attaching Instability of Oblique SIC

7.1 Non-attaching Conditions of ODW

It is known that there is a range of the flow turning angle for a given Mach number where the ODW may be stabilized, although it is narrower than that of a frozen OSW [12]. The stabilized structure of the ODW was numerically studied by Li et al. [29], and the structure has been observed in many experiments using a two layer detonation tube [23, 24]. The chemical kinetic effect induces a preheating zone behind an OSW, and combustion initiates at some distance behind the wedge nose in the stabilized ODW. Coupling of the reaction front and the OSW results in a triple-point structure, and an ODW is formed behind the triple point with a wave angle greater than that of the OSW. Figure 37 depicts a polar diagram of the OSW and ODW assuming frozen flow and equilibrium chemistry. Here, β is the shock wave angle, θ_{CJ} is the physically possible minimum turning angle above which the attached oblique detonation solutions are possible till θ_{ODW}^{max}, maximum allowable turning angle. If β is further increased, a detached detonation solution is obtained. Beyond the maximum turning angle θ_{ODW}^{max}, referred to here as an off-attaching condition, the overdriven detonation may be detached similar to a frozen shock wave. Kasahara et al. [27] presented an example of the detached overdriven detonation wave over a conical projectile. Another interesting result is the experiment by Morris et al. [12] at the off-attaching condition of an ODW [12]. They carried out an experiment of a SIC over a wedge angle of 40°, which is greater than θ_{ODW}^{max} for their experimental condition. The attached SIC results were observed in the experiment, which differs from the theoretical expectation in equilibrium theory.

There was a debate in Morris et al.'s experiment [12] whether the flow is stabilized or not, due to the experimental time in the expansion tube facility.

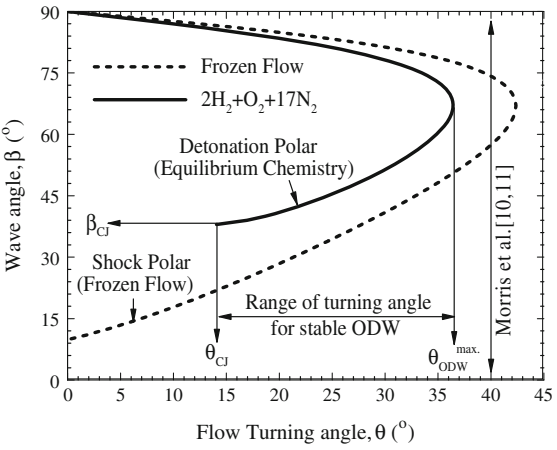

Fig. 37 Shock-polar diagram showing the range of the wave angle and flow turning angles for the experimental condition by Morris et al. [28]: $2H_2 + O_2 + 17N_2$ mixture, $M_\infty = 5.85$, $T_\infty = 292$ K and $P_\infty = 0.12$ bar

Following the first computational results by Li et al. [29], that showed the two-dimensional detailed structure and different regimes of the ODW, various CFD studies were carried out for the ODW itself and for ODW propulsion systems. Most of all the previous computations, however, were done for the flow turning angles where the Rankine–Hugoniot theory gave a stable ODW. They are therefore not suitable for the explanation of the experimental observation by Morris et al. Choi et al. [33] studied various regimes of ODW and reported that the attached solutions are transient phenomena and that the detached overdriven detonation waves are the final solutions after a sufficiently long time period beyond the experimental test time. However, an SIC was still observed at the off-attaching condition for the case of a less sensitive mixture, which is unstable and oscillates periodically.

For this study, a coupled form of the species conservation equations and compressible inviscid Euler equations were employed with the detailed combustion mechanism of $H_2/O_2/N_2$ for the simulation of the oblique SIC/detonation phenomena over a two-dimensional wedge. The chemical reactions were modeled using Jachimowski's nine-species and 19 steps detailed chemistry model including both HO_2 and H_2O_2 and the same computation condition was selected to that of the experiment [28].

7.2 *Periodically Oscillating Oblique SIC*

The gas mixture ignites behind the oblique shock with an ID behind the shock wave. The burnt gas expands after the ignition and couples with the oblique shock front forming a triple point structure, but a long ignition delay causes the triple point to be positioned far above the wedge surface. The combustion flow field may therefore be mistaken for decoupled SIC if the frame of view is confined to near the wedge surface. The interaction between the expansion wave and the transverse wave from the triple point slows down the progress of the triple point toward the wedge nose since the triple point is formed far above the wedge surface. Therefore, the flowfield looks stabilized for a long time in comparison to the experimental test time of 150 μs. The triple point moves forward very slowly, taking more than 1200 μs to reach the wedge nose. The coupled waves, however, do not detach from the wedge after the arrival of the triple point at the nose. The reaction front instead retreats backward and decouples with the incident OSW. After the decoupling, a new coupling of the OSW and the reaction front forms a new triple point. The new triple point moves forward again, and the periodic motion of repeated coupling and de-coupling of the shock and reaction front begins. A wedge length of 2.44 cm is selected as a reference case for the discussion of the characteristics of the periodically oscillating combustion because this case clearly shows the basic characteristics of the periodic oscillation.

7.2.1 Mechanism of the Periodically Oscillating Combustion

The unsteady motion becomes a regular oscillation after several transitional periods. Figure 38a is a partial history of the density variation showing periodically oscillating features from the beginning of the oscillation, and a single oscillation is depicted in Fig. 38b which is a magnified view of a period showing a 45 μs duration that is equivalent to an oscillation frequency of about 220 kHz. The coupling between the shock wave and reaction front becomes weaker as the triple point moves forward to nose and the decoupled waves finally move backward. An oblique shock and a reaction front in the middle of the wedge forms a new coupling and the same periodic motion is repeated after the formation of a new triple point above the middle of the wedge.

The pressure field was investigated in detail to obtain an understanding of the decay-down process of the triple point. Figure 39 shows the locations of the shock wave and reaction fronts and the maximum pressure behind the OSW along the wedge surface. During the forward-moving phase, the transverse wave originating from the triple point reflects at the wedge surface as a Mach reflection and the mixture ignites behind it. The triple point structure is therefore considered to be supported by the high-pressure region behind the Mach reflection waves. However, the Mach reflection breaks down as the triple point moves forward, and the pressure level goes down accordingly. Thus the triple point structure cannot be sustained any

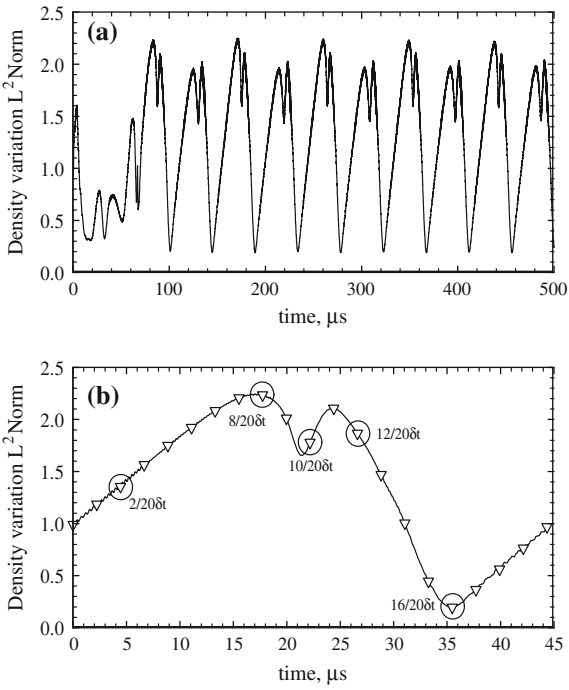

Fig. 38 **a** Part of a density variation L_2 norm history showing periodic oscillation. **b** Magnified view of a period of oscillation

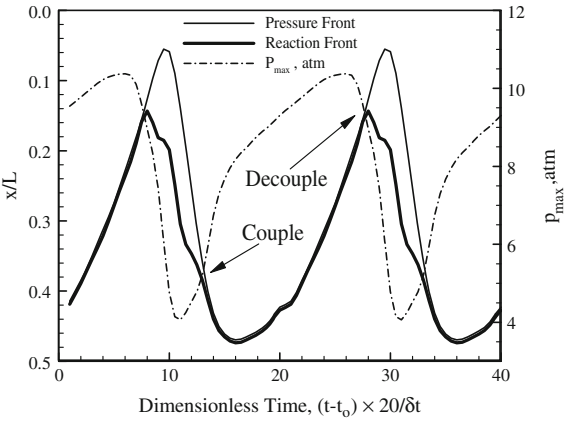

Fig. 39 Temporal variations of the locations of the pressure wave front and reaction wave front, and the maximum pressure along the wedge surface

longer and the reaction front moves backward. The chemical kinetic effect is one of the reasons for the breakdown of the triple point structure. As the triple point moves forward, the induction region is getting smaller and there is not enough time for heat to be generated behind the Mach reflection wave. The pressure level then goes down and the reaction front moves backward. The wave structure cannot be sustained any longer without sufficient heat generation, and the Mach reflection that supports the triple point structure breaks down. Then both the pressure and reaction front move backward until the new coupling is formed behind a sufficient ID. Therefore, the oscillatory motion along the wedge surface is considered to be very similar to that of a one-dimensional detonation wave.

The oscillatory behavior is presumed to have originated as a result of the low heat content of the mixture, but the chemical kinetic induction time needed for complete combustion plays a much more crucial role, since the oscillating case corresponds to the off-attaching condition predicted by the Rankine–Hugoniot theory with equilibrium chemistry that assumes prompt heat addition behind a shock wave. This indicates that the time needed for heat addition is more important than the amount of the final heat addition, and the non-equilibrium chemical kinetic effect that introduces a chemical induction time for a sufficient amount of heat addition is considered to play a crucial role in the oscillatory behavior of the ODW.

7.2.2 Scaling Law

Numerical calculations were carried out to gain an understanding of the scaling effects between the fluid dynamic time scale and chemical time scale by simply adjusting the length of the wedge with the other flow conditions fixed. The wedge lengths were changed from 1.16 to 384 cm. The following wedge lengths were considered: L = 1.16, 1.74, 2.44, 3.84, 5.76, 6.96, 11.5, 38.4 and 384 cm. The converged results for selected cases are plotted in Fig. 40 and an intermediate solution of the regular oscillation is plotted for unstable cases.

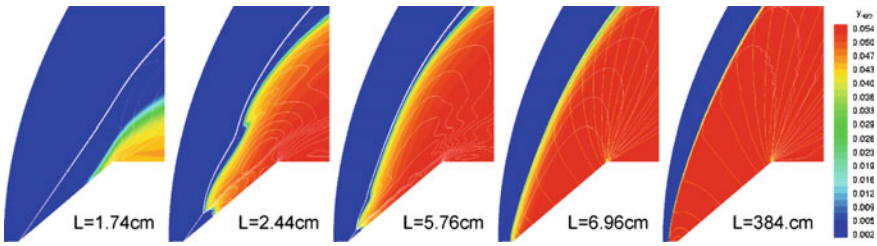

Fig. 40 Overlaid dimensionless density contours (number of levels = 30, minimum = 1.20 and maximum = 12.2) and the OH mass fraction distribution showing various regimes of oblique SIC with respect to the wedge length

Combustion is not observed for the wedge length of 1.16 cm and the induction length needed for the combustion is considered to be much longer than the wedge length. The case of L = 1.74 cm shows a stationary decoupled shock-induced combustion. The solution was fully converged for this case but this case is considered to be a quasi-stable solution since a slight change of the fluid dynamic length scale may result in different regimes of combustion. Numerical results show the oscillatory combustion regime for the wedges with lengths between L = 2.44 cm and L = 5.76 cm. The basic characteristics of the oscillatory combustion are considered similar for all cases, but it is noticed that the oscillating location of the triple point is getting closer to the wedge nose for larger wedges. It is also shown that there are two triple points for these cases, which occurs from repeating the process of merging and collapsing.

The shock wave is detached from wedge nose beyond the wedge length of 6.96 cm. As the size of the wedge is getting larger, the shock SD is also getting larger but gradually converges to an equilibrium condition in a dimensionless sense. The case of 384 cm can practically be considered to be a case corresponding to the equilibrium combustion of a very fast reaction. From the numerical experiments for the fluid dynamic length scales it is discovered that the scaling effect is the major criterion for determining the combustion regimes between the unstable attached SIC and the detached combustion at the off-attaching condition, since the time needed for heat addition is more important than the amount of the final heat addition with the equilibrium assumption. The chemical and fluid dynamic time scale was computed to quantify the chemical kinetic effect and this was then compared with the combustion regimes. In order to measure the scaling effects quantitatively, flow time scales and chemistry scales are compared for each case. The time scales can be explained as:

τ_f^o: Flow residence time behind an OSW.

τ_f^n: Flow residence time behind a detached shock wave.

τ_c^n: Chemical characteristic time behind an OSW.

τ_c^n: Chemical characteristic time behind a detached shock wave.

The flow residence time scales were defined as the fluid dynamic length scale divided by the speeds of the gas behind the shock waves. The flow residence time

therefore unmistakably varies case by case. The fluid dynamic length scale is defined as a distance from the wedge nose to the expansion corner along the wedge surface for an OSW, and is defined as the shock SD of a detached wave with equilibrium chemistry for the detached shock wave. The speed of gas is calculated by the Rankine–Hugoniot theory and the detached shock wave is considered to be locally normal to the flow direction. The chemical characteristic time on the other hand is defined from the ignition transient with the fluid dynamic condition behind the shock waves obtained from the Rankine–Hugoniot relation. The ignition transient behind the shock wave was considered to be a constant volume process. The chemical characteristic time is typically defined as the induction time behind a shock wave. The induction time, however, is too short for the present conditions due to the high temperature behind the shock waves and a heat release that takes much longer than the induction period. The chemical characteristic time is therefore considered here as the time needed for an amount of the heat release to take place. The flow residence time is estimated from the flow speed behind the shock wave and maximum allowable fluid dynamic length scale.

The time scaling effect on the SIC mode around a wedge at the off-attaching condition is summarized in this listing as follows: (1) No ignition or decoupled combustion was observed if a fluid dynamic time is shorter than a chemical time behind an OSW. (2) Oscillatory combustion was observed behind an OSW if a fluid dynamic time is longer than a chemical time behind an OSW and the fluid dynamic time is shorter than the chemical time behind a normal shock wave (NSW) at same Mach number. (3) Detached bow SIC (or detached overdriven detonation wave) was observed if a fluid dynamic time is longer than a chemical time behind a NSW.

The results suggest that two sets of Damköhler number should be considered; one based on normal shock, to determine SIC and the other based on oblique shock, to determine shock-combustion coupling.

7.3 Non-attaching Instability of OSIC in Larger Domains

By expanding the computational domain with appropriate actions, computations were carried out for a wide range of body sizes. The surface length of the cone is selected in between 0.7 and 1.5 cm by trial and error to capture the unstable nature since the flow condition is different for the axi-symmetric configuration. The results for the two-dimensional wedges are essentially the same as the previous results except for the capturing of the vortex structure behind the expansion corner. The vortex structure is generated from the contact surface originating from the triple point. The vortex structure is too small above the wedge surface, but the larger computational domain made it possible to capture the structure getting larger as it moved downstream. The results for the axi-symmetric configuration exhibit a stronger dependency on the length scale. The combustion was observed for the length scale greater than 0.7 cm. The characteristics of the axi-symmetric cases were shown to be non-homogeneous behind the shock wave since the shock

strength and flow residence time are not uniform along the flow turning angle. Due to this axi-symmetric effect, the oscillatory motion of the shock and the combustion waves were much greater than the two-dimensional cases.

The combustion characteristics become quite irregular, explosive and unpredictable for the intermediate length scales. The shock wave and the combustion wave coupled and turned out to be an oblique detonation at the outer region of the body for the length scale greater than 1.2 cm, although the unstable SIC is maintained around the nose. The oblique detonation wave front shows a periodic wave motion, which generates the detonation cell structures. Figure 41 displays the instantaneous density gradient plots for the selected cases in Sect. 3.5. The attached SIC may be possible at the off-attaching condition, but is unstable and oscillates similar to a one-dimensional detonation wave. The mechanism of the periodic instability is a two-dimensional interaction of both the shock and reaction waves coupled with chemical kinetic effects. Through the above studies, the stability of the SIC at the off-attaching conditions over a two- dimensional wedge were reported with the combustion regimes being classified into three categories as follows:

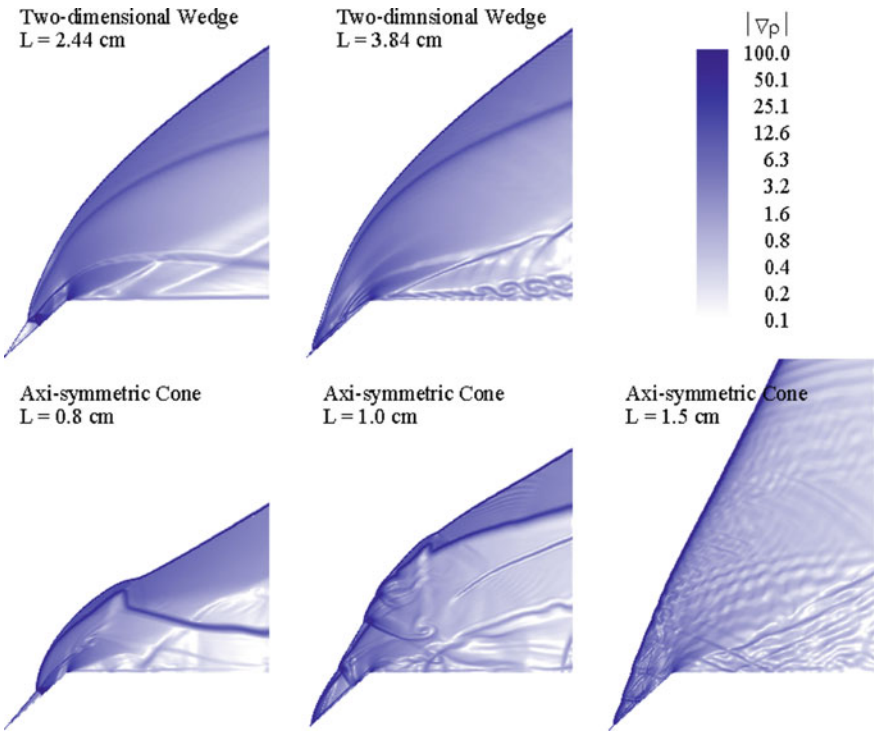

Fig. 41 Instantaneous density gradient plots for the SIC over two-dimensional wedges and axi-symmetric cones. (L is the length of the inclined portion of the wedge)

1. No combustion or de-coupled SIC is found if the chemical characteristic time is longer than flow residence time behind an OSW.
2. At the other extreme, detached combustion is found in case where the chemical characteristic time is shorter than flow residence time behind a detached normal shock wave.
3. At an intermediate condition, the unsteady numerical analysis reveals the ODW or SIC still attached at a wedge, but shows a periodic motion.

8 Concluding Remarks

Starting from the motivation to understand the performance and combustion characteristics in a novel propulsion device, RamAc, variety of numerical studies have been carried out for SIC, ODW and viscous effects in RamAc for the last 20 years. Original works have been published as separate papers and listed in the references. Those gave a detailed understanding of each physics, but the compilation of those works could provide better insight on the high speed combustion physics by the combined understanding of each other. Yet, further topics remain and those should be sought for deeper understanding of the physics. One of them would be the surface melting and evaporation, eventually adding more heat to the flow field by the metallic combustion. Geometrical changes should be considered further by the surface erosion. Another topic would be the understanding on the role of fine scale turbulence on entire flow physics including the combustion process and the evolution and stabilization of detonation. Authors expect that those topics could be covered in the near future by the development of computational environment and techniques.

Acknowledgements Authors appreciate greatly P. Pradeep Kumar for editing the manuscript with great care. Authors also thank to F. Seiler and O. Igra and for suggesting this great opportunity, reading the manuscript and giving corrections.

References

1. Hertzberg, A., Bruckner, A.P., Bogdanoff, D.W.: Ram accelerator: a new chemical method for accelerating projectiles to ultrahigh velocities. AIAA J. **26**(2), 195–203 (1988)
2. Bogdanoff, D.W.: Ram accelerator direct space launch system: new concepts. J. Propul. Power **8**(2), 481–490 (1992)
3. Choi, J.-Y., Jeung, I.-S., Yoon, Y.: Computational fluid dynamics algorithms for unsteady shock-induced combustion, part 1: validation. AIAA J. **38**(7), 1179–1187 (2000)
4. Choi, J.-Y., Jeung, I.-S., Yoon, Y.: Computational fluid dynamics algorithms for unsteady shock-induced combustion, part 2: comparison. AIAA J. **38**(7), 1188–1195 (2000)
5. Choi, J.-Y., Jeung, I.-S., Yoon, Y.: Numerical study of scram accelerator starting characteristics. AIAA J. **36**(6), 1029–1038 (1998)

6. Lehr, H.F.: Experiments on shock-induced combustion. Astronaut. Acta **17**(4, 5), 589–597 (1972)
7. Jachimowski, C.J.: An analytical study of the hydrogen-air reaction mechanism with application to scramjet combustion. NASA TP-2791 (1988)
8. Yungster, S., Radhakrishnan, K.: A fully implicit time accurate method for hypersonic combustion: application to shock-induced combustion instability. AIAA Pap. 94–2965 (1994)
9. Matsuo, A., Fujiwara, T.: Numerical simulation of shock-induced combustion around an axisymmetric blunt body. In: AIAA Paper 91–1414, AIAA 26th Thermophysics Conference, Honolulu (1991)
10. Wilson, G.J., Sussman, M.A.: Computation of unsteady shock-induced combustion using logarithmic species conservation equations. AIAA J. **31**(2), 294–301 (1993)
11. Hosangadi, A., York, B.J., Sinha, N., Dash, S.M.: Progress in transient interia ballistic flowfield simulation using multi-dimensional upwind/implicit numerics. AIAA Pap. 93–1915 (1993)
12. Morris, C.I., Kamel, M.R., Hanson, R.K.: Expansion tube investigation of Ram-accelerator projectile flow fields. AIAA 1996–2680
13. Choi, J.-Y., Jeung, I.-S., Yoon, Y.: Unsteady-state simulation of model Ram accelerator in expansion tube. AIAA J. **37**(5), 537–543 (1999)
14. Choi, J.-Y., Jeung, I.-S., Yoon, Y.: Transient simulation of the superdetonative mode initiation process in SCRam accelerator. In: Proceedings of the Combustion Institute, vol. 26, pp. 2957–2963 (1996)
15. Trimpi, R.L.: A preliminary theoretical study of expansion tube, a new device for producing high-enthalpy short duration hypersonic gas flows. NASA TR-R-133 (1962)
16. Seiler, F., Patz, G., Smeets, G., Srulijes, J.: The rail tube in a Ram acceleration: feasibility study with ISL's RAMAC 30. In: Second International Workshop on Ram Accelerators, RAMAC II, Seattle, WA, July 1995; also Inst. of Saint-Louis, ISL Rept. PU366/95, St. Louis, France, 1995
17. Choi, J.-Y., Lee, B.J., Jeung, I.-S., Yoon, Y.: Computational investigation of high pressure combustion mechanism in scram accelerator. J. Phys. IV **10**(11), 131–142 (2000)
18. Moon, G.-W., Jeung, I.-S., Choi, J.-Y., Seiler, F., Patz, G., Smeets, G., Srulijes, J.: Numerical modelling and simulation of RAMAC 30 experiment carried out at the French-German research institute of Saint—Louis. J. Phys. IV **10**, 143–153 (2000)
19. Yungster, S.: Numerical study of shock-wave/boundary-layer interactions in premixed combustible gases. AIAA J. **30**(10), 2379–2387 (1992)
20. Nusca, M.J., Kruczynski, D.L.: Reacting flow simulation for a large-scale Ram accelerator. J. Propul. Power **12**(1), 61–69 (1996)
21. Choi, J.-Y., Jeung, I.-S., Yoon, Y.: Scaling effect of the combustion induced by shock-wave boundary-layer interaction in premixed gas. Proc. Combust. Inst. **27**, 2181–2188 (1998)
22. Choi, J.-Y., Jeung, I.-S., Lee, S.: Dimensional analysis of the effect of flow conditions on shock-induced combustion. Proc. Combust. Inst. **26**, 2925–2935 (1996)
23. Pratt, D.T., Humphrey, J.W., Glenn, D.E.: Morphology of standing oblique detonation waves. J. Propul. Power **7**(5), 837–845 (1991)
24. Shepherd, J.E.: In: Buckmaster, J., Jackson, T.L., Kumar, A. (eds.) Detonation Waves and Propulsion, pp. 373–420. Combustion in High-Speed Flows, Kluwer Academic Pub, Dordrecht (1994)
25. Viguier, C., Gourara, A., Desbordes, D., Deshaies, B.: Three dimensional structure of stabilization of oblique detonation wave in a hypersonic flow. Proc. Combust. Inst. **27**, 2207–2214 (1998)

26. Kaneshige, M.J., Shepherd, J.E.: Oblique detonations stabilized on a hypervelocity projectile. Proc. Combust. Inst. **26**, 3015–3022 (1996)
27. Kasahara, J., Fujiwara, T., Endo, T., Arai, T.: Chapman–Jouguet oblique detonation structure around hypersonic projectiles. AIAA J. **39**(8), 1553–1561 (2001)
28. Morris, C.I., Kamel, M.R., Hanson, R.K.: Shock-induced combustion in high-speed wedge flows. Proc. Combust. Inst. **27**, 2157–2164 (1998)
29. Li, C., Kailasanath, K., Oran, E.S.: Detonation structures behind oblique shocks. Phys. Fluids **6**(4), 1600–1611 (1994)
30. Fusina, G., Sislian, JP., Parent, B.: Formation and stability of near Chapman-Jouguet standing oblique detonation waves. AIAA J. **43**(7), 1591–1604 (2005)
31. Choi, J.-Y., Kim, D.-W., Jeung, I.-S., Ma, F., Yang, V.: Cell-like structure of unstable oblique detonation wave from high-resolution numerical simulation. Proc. Combust. Inst. **31**, 2473–2480 (2007)
32. Choi, J.-Y., Ma, F., Yang, V.: Some numerical issues on simulation of detonation cell structures. Combust. Explos. Shock Waves **44**(5), 560–578 (2008)
33. Choi, J.-Y., Shin, E.J.-R., Jeung, I.-S.: Unstable combustion induced by oblique shock wave at non-attaching condition of oblique detonation wave., Proc. Combust. Inst. **32**, 2387–2396 (2009) (See also, Proc. 22nd Int. Symp. Shock Waves, 1999, pp.333-337 (ISBN 085432-706-1))

Author Biographies

Jeong-Yeol Choi is a Professor of Aerospace Engineering, Pusan National University, Republic of Korea. He received his Ph.D. from the Seoul National University in 1997. His research interests include Dynamics of Energetics flows, High Pressure Combustion, Detonation, Reaction Kinetics, Multi-Phase/Particle flows, Turbulence-Chemistry interaction in Propulsion systems. He has published more than 100 archival papers and more than 300 conference papers in these areas. He is an Associate Fellow of the AIAA and his other professional activities include The Combustion Institute, IDERS, KSAS, KSPE, KOSCO, KSCFE.

Currently, he is serving as the Program Manager of Space R&D, National Research Foundation of Korea. His duty encompasses the monitoring and evaluation of Space R&D programs sponsored by the Ministry of Science, ICT and Future Planning, Republic of Korea Government, including the development of space launch vehicle, micro- to GEO satellites, space exploration, basic space R&Ds, space utilizations and industrializations.

In-Seuck Jeung has been a professor at Seoul National University since 1984. While he completed all of his degrees from Seoul National University he has also served as a visiting scientist, honorary fellow and professor at Hosei University, University of Minnesota and University of California, Irvine during his career. And, his research interests include scramjet and ramjet combustion and the design of the test facility. He also participates in work on gas turbine combustors, ram accelerators, ramjet intake test, hydrogen leak explosion, laser propulsion, laser plasma flow control, aero-optics and hypersonic aerothermodynamics.

In addition to serving as an associate editor of *The Proceedings of the Combustion Institute, Transactions of Japan Society for Aeronautical and Space Sciences/Aerospace Technology Japan*, and *The Scientific World Journal,* also serves as a member of the editorial board of *Progress in Energy and Combustion Science.* Prof. Jeung has served as a member of the international advisory committee of the International Symposium on Shock Waves Colloquium, Colloquium Co-Chair of the International Symposium on Combustion, Asia-Pacific Conference on Combustion, Asian-Pacific International Symposium on Aerospace Technology and the Asian Joint Conference on Propulsion & Power.

RAMAC37 Activities at CARDC

Sen Liu, Zhiyong Bai and Hexiang Jian

1 Introduction

The RAMAC, short for ram accelerator, is a relatively new concept of hypervelocity launcher. It was first proposed by Prof. A. Hertzberg of the University of Washington (UW) in 1980s [1]. The principle of a ram accelerator is similar to that of a ramjet/scramjet engine. The projectile, similar in shape to the center-body of a ramjet, is launched by an initial launcher such as a powder gun or gas gun, at a certain velocity and then enters a stationary tube filled with premixed gaseous propellant (typically combustible gas, oxygen and diluents). The combustion or detonation of the propellant gas creates high pressure around the projectile base to further accelerate it to higher velocities (comparison of ram accelerator and ramjet engine is shown in Figs. 1 and 2 [2]).

Experiments were first conducted at the University of Washington with the ram accelerator. In 1985, the first ram accelerator device, a 38 mm ram accelerator, was designed and built at UW and progress has been made since then [2–7]. A 85 g projectile was accelerated to 2.7 km/s [2] with maximum filling pressure of 20 MPa [8]. In the 1990s, experimental and numerical investigations were carried out in other institutions and countries, including the US Army Research Laboratory, French-Germany Institute of Saint Louis (France) [9, 10], in Japan, Korea, UK, Brazil and Israel. Much encouraging results were obtained [2].

S. Liu (✉) · Z. Bai · H. Jian
Hypervelocity Aerodynamics Institute (HAI), China Aerodynamics Research and Development Center (CARDC), Mianyang 621000, Sichuan Province, People's Republic of China
e-mail: liusen@cardc.cn

Z. Bai
e-mail: hawkwhite@sina.com

H. Jian
e-mail: jianhx@sina.com

F. Seiler and O. Igra (eds.), *Hypervelocity Launchers*,
Shock Wave Science and Technology Reference Library 10,
DOI 10.1007/978-3-319-26018-1_10

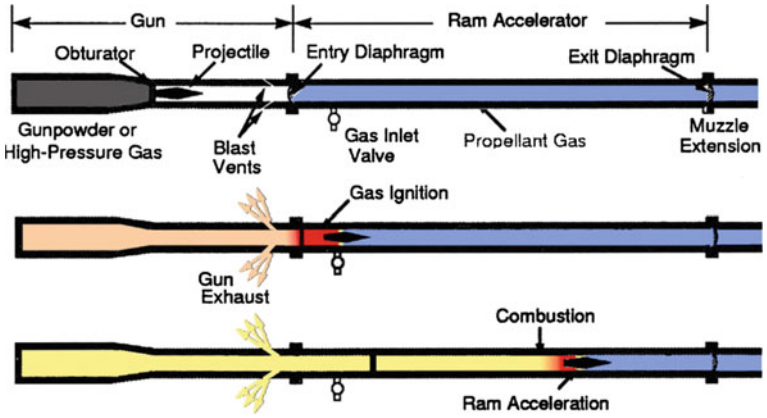

Fig. 1 Operational sequence of ram acceleration [2]

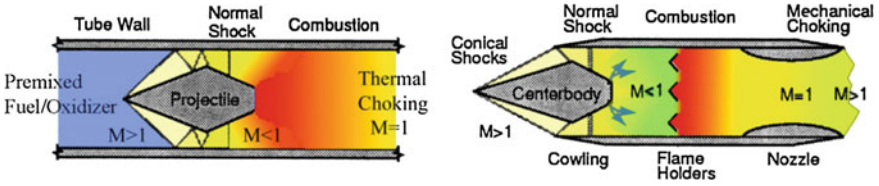

Fig. 2 Comparison of ram accelerator and ramjet [2]

In 1992, Prof. ZHANG Zhicheng, then the Chief Engineer of Hypervelocity Aerodynamics Institute (HAI) of China Aerodynamics Research and Development Center (CARDC), proposed conducting research in RAMAC. Dr. Sen Liu and his group at HAI started their work on RAMAC in 1994. After a year of design, fabrication, and installation, they set up the only ram accelerator in China (RAMAC37, with acceleration tube bore diameter of 37 mm) in the beginning of 1996. The first cold shot test was successfully conducted in August, 1996. In December of the same year, a 110 g projectile was successfully accelerated from 1085 to 1400 m/s in sub-detonation mode. In 1998, the acceleration tube was lengthened from its previous 4.8 m length to 9.6 m. In 1999, a 115 g projectile was successfully accelerated up to 2090 m/s.

As for numerical simulations, the following researchers carried out various work on the in-bore combustion/detonation flow fields around ram accelerator projectiles: Dr. LIU Sen, BAI Zhiyong, JIAN Hexian, and Dr. CHEN Jianqiang [11] from CARDC; Prof. WENG Chunsheng [12], Prof. ZHANG Guoqiang [13], and Prof. SUN Xiaohui [14], from Nanjing University of Science and Technology.

In this chapter, RAMAC37, as the only ram accelerator that has been built and functioned successfully in China, is introduced with results of cold shot and hot shot tests conducted from 1995 to 2001.

2 RAMAC37

RAMAC37 of CARDC consists of 5 subsystems [15]: The initial launcher-projectile system, acceleration tube and venting section, gas handling system, measurement system, and a recovery system, as shown in Fig. 3. After the projectile leaves the muzzle of the initial launcher (4), the high pressure gas is dumped in the venting section (3) before the projectile enters the acceleration tube (2). The projectile is then accelerated by high pressure from propellant gas combustion or detonation in the acceleration tube, and finally recovered by the recovery system if needed.

2.1 Initial Launcher/Projectile

The initial launcher-projectile system consists of the initial launcher and projectiles. The launcher is a 37 mm antiaircraft gun, shown in Fig. 4. However, the rifled gun tube is replaced by a smooth bore tube. A 400 g projectile can be launched at 1000 m/s, and the highest muzzle velocity of the gun is about 1.5 km/s.

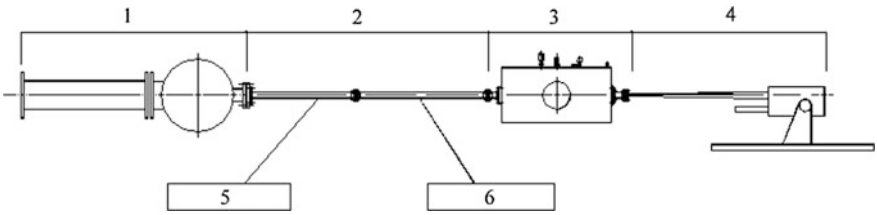

Fig. 3 Subsystems of the RAMAC37 at CARDC. (*1*) Recovery system (*2*) acceleration tube (*3*) Venting section (*4*) initial launcher (*5*) gas handling system (*6*) measurement system

Fig. 4 Initial launcher of RAMAC37

A typical four-finned projectile, made of aluminum alloy (LC4-CS) is shown in Fig. 5. The length of the nose cone is 80 mm and the tail is 70 mm. These two parts are joined together by screw thread. At the conjunction, a piece of rubber magnetic ring is placed for projectile velocity measurement.

The area ratio of this configuration (ratio of flow area between the projectile's largest cross section and tube wall to the total cross section area of the acceleration tube) is 0.42. At the throat entrance, the Mach number must be greater than 2.6, which means that the initial velocity should be over 900 m/s.

A pressure relief support is used in tests, which consists of an obturator and baffle. The obturator is made of aluminum alloy with 19 holes, as shown in Fig. 6. The baffle material is polycarbonate.

2.2 Acceleration Tube/Venting Section

The venting section is the connection between the initial launcher and the acceleration tube. It guarantees that the projectile will fly directly into the acceleration tube at a desired high velocity. Meanwhile, the high pressure gunpowder gas from the initial launcher is released here, in order to avoid undesired influence on the acceleration tube. It is not necessary that the venting section will bear a heavy load, but it is important that it is able to withstand the impact from the initial launcher gas pressure. $PCrN_{11}Mo$ is used for the venting section, which is of the same bore

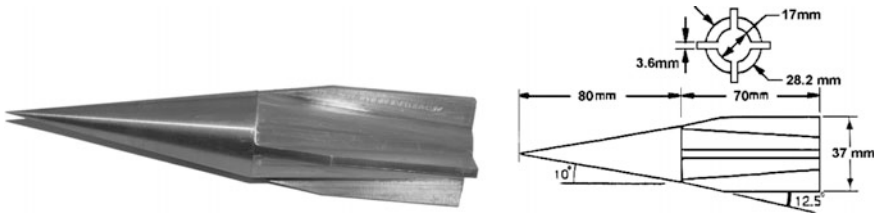

Fig. 5 Typical projectile configuration of RAMAC37

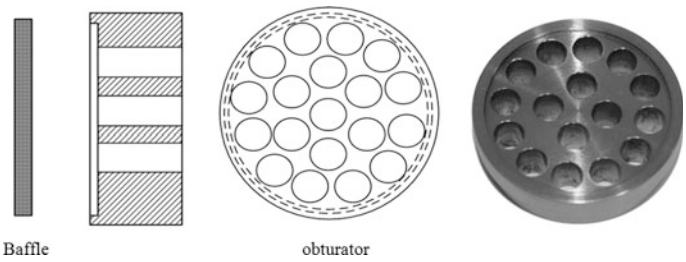

Fig. 6 Projectile support of RAMAC37

diameter as the acceleration tube. Totally 264 holes are machined in the venting section.

Since the pressure generated by the propellant gas combustion or detonation could be as high as 200 MPa and the temperature over 2000 K, the acceleration tube is made of $PCrN_{11}Mo$ to withstand such high pressure and temperature gas corrosion. The inner and outer diameters of the acceleration tube are 37 and 100 mm, respectively. At first, there were four sections having a total length of 4.8 m. After upgrade in 1998, the acceleration tube was lengthened to 9.6 m, consisting of 8 sections. There are five measurement stations with four vertical measurement holes at each station on any acceleration tube section, each consisting of two pressure sensors and two electromagnetic sensors. The 20 measurement stations on the acceleration tube are numbered from 1# to 20#. In addition, there is one air supply inlet station equipped with a pressure gauge mounting hole on each of the acceleration tube sections.

2.3 Gas Handling System

The gas handling system consists of a high pressure air supply, mixing/filling line and gas chromatographer. Its main function is to fill propellant composition (for example, H_2, CH_4 and N_2) safely into the acceleration tube in a short time with expected mixing ratio and pressure. Propellant gas sample is analyzed by a GC-9560II gas chromatograph. The chromatographer takes high purity hydrogen as the carrier gas. The stationary phase in the chromatographic column is a 4 Å molecular sieve, and the contents of CH_4, O_2, N_2 and He are directly measured at operation temperatures ranging from 8 to 450 ^{o}C and a precision of $\pm 0.1^{o}$. The volume fraction measurement precision is 0.5 %.

The composition of the propellant gas mixture has great influence on the propulsion performance of RAMAC. Thus, one of the key factors of the gas handling system is to control gas composition concentration precisely.

An example of a gas handling system for O_2, N_2 and CH_4 mixtures is shown in Fig. 7. Pure O_2, N_2 and CH_4 are filled into a mixing tank according to pre-calculated proportion, and then the mixed gas is sampled. After analysis of the sampled gas mixture composition by a gas chromatographer, the propellant mixture composition is adjusted if needed. After several adjustment-mixing-analyzing cycles, the propellant gas mixture is properly prepared and then filled into the acceleration tube.

2.4 Measurement System

The measurement system is an important part of the RAMAC37. It consists of electromagnetic sensors, pressure sensors, a multi-channel data acquisition system,

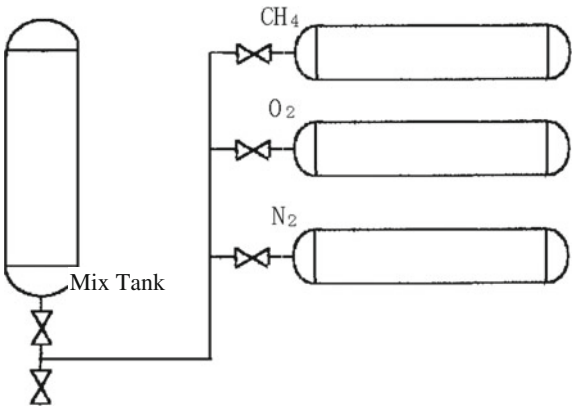

Fig. 7 Sketch of gas handling system

etc. Internal ballistic parameters can be obtained, such as projectile velocity and combustion pressure, in the acceleration tube. The velocity measurement system of RAMAC37 is shown in Fig. 8.

2.4.1 Electromagnetic Sensor

The projectile velocity in RAMAC37 acceleration tube is measured using an electromagnetic method. A rubber magnetic ring is placed inside the projectile. Electromagnetic sensors are installed in measurement holes of the acceleration tube. The velocity range is from 100 to 5000 m/s with an error of ±1 %. Positioning error is less than ±0.16 mm when the sample rate set at 10 MHz.

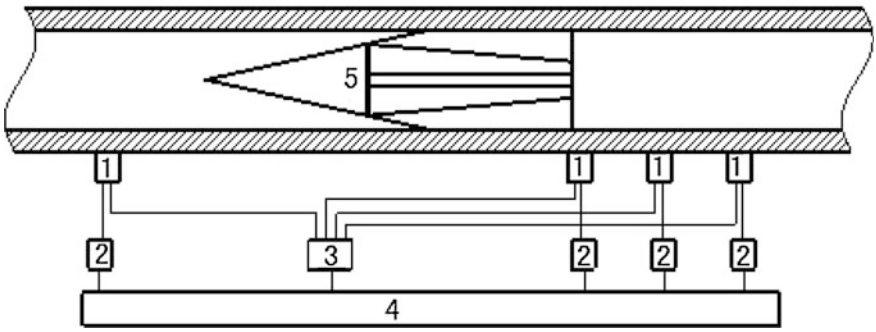

Fig. 8 Projectile velocity measurement system of RAMAC37. *1* Electromagnetic sensor/pressure sensor, *2* load amplifier, *3* summing amplifier, *4* data collection and *5* rubber magnetic ring

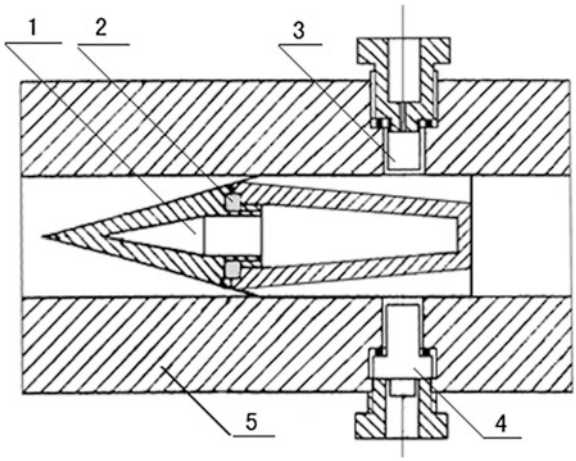

Fig. 9 A typical measurement station in the RAMAC37. *1* Projectile, *2* rubber magnetic ring, *3* electromagnetic sensor, *4* pressure sensor and *5* acceleration tube

An electromagnetic sensor consists of base, induction coil and coil cap. The coil is a winding of a fine enameled wire. The base and coil cap are made of austenitic stainless steel and sealed with copper. The magnetic ring is made of SoCo, a type of permanent magnetic rubber. The magnetic rubber is of large residual magnetic flux density, high Curie temperature, and has the capability of generating strong electromagnetic signals. Configuration of a typical measurement station is shown in Fig. 9 equipped with an electromagnetic sensor and a pressure sensor.

2.4.2 Pressure Sensor

The burning or detonating gas pressure around the projectile is measured using pressure sensors installed in the acceleration tube wall. The range of pressure measured by the sensor is from 100 to 200 MPa with an error of 3 %; the frequency response is 100–110 kHz.

2.4.3 Data Acquisition System

A 16 channel data acquisition system having a resolution of 8 bits is used in the RAMAC37 experiments. The highest sample rate is 20 MHz with a sample size of 128 kb. Time precision is 7×10^{-6} s. The DC and AC accuracy is ±0.2 and ±1 % respectively.

With this data acquisition system, the pressure variation versus time at each measurement station is recorded, and the electromagnetic signals of the rubber ring are processed to give projectile velocity.

3 Cold Shot Tests

Cold shot test means to launch a projectile into the acceleration tube filled with incombustible gas (such as N_2, Ar, etc.) instead of combustible propellant gas. There are two main purposes for cold shot tests:

(1) to verify the design and function of all the subsystems of RAMAC37, except propellant ignition;
(2) to solve the problem of "unstart".

If there are flaws in the projectile design, or if the projectile velocity is too low to establish a supersonic flow field at the projectile throat, a normal shock would be generated upstream of the projectile throat. High pressure of the normal shock would decelerate projectile, and this phenomenon is called cold shot unstart, or sonic diffuser unstart.

If an unstrat occurs in the cold shot test, hot shot tests could never be successful.

3.1 Cold Shot Test Results

A series of cold shot tests was carried out after the construction and debugging of the 37 mm RAMAC37 in early 1996 [15], with 2.0 MPa nitrogen in the acceleration tube.

Figure 10 shows the projectile velocity versus distance during cold shot test CS019. The projectile enters the acceleration tube at 1130 m/s and the velocity reached 1150 m/s at station 2, finally, it exits the acceleration tube at 1000 m/s. Figure 11 shows the pressure signal recorded at the second measurement station.

The first pressure peak of about 10 MPa is caused by the projectile nose-tip shock wave striking the acceleration tube wall. The second, of about 18 MPa

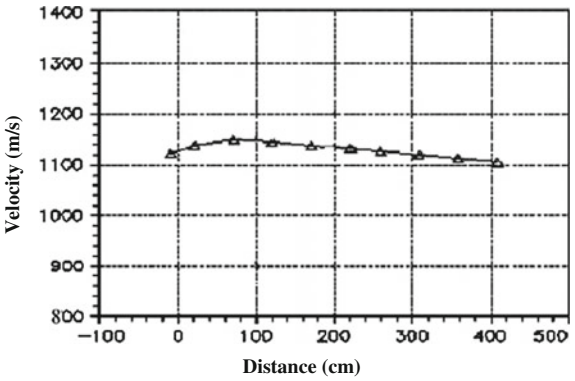

Fig. 10 Projectile velocity versus distance in CS019

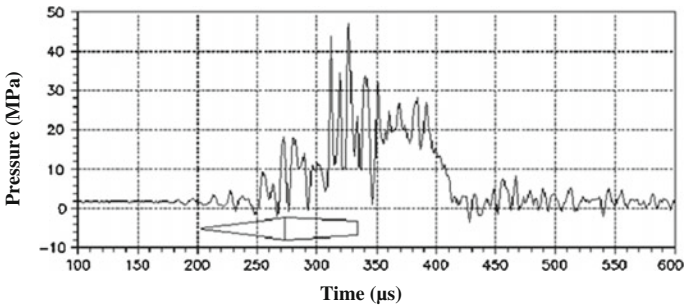

Fig. 11 Acceleration tube wall pressure versus time in CS019

appears at the position of the throat, with even higher pressure downstream. This pressure profile indicates that there is no normal shock upstream of the throat, which means that the throat is started and the cold shot test succeeds.

The cold shot tests indicate that the system design is reliable, and parameters such as velocity and pressure can be measured accurately.

3.2 Flow Field Numerical Simulation

3.2.1 Numerical Simulation Cold Shot Flow Field [16]

Liu's [17] implicitly time-marching solver of unsteady Navier-Stokes equations, which had been used to simulate unsteady flow over a transonic dynamic airfoil [18], was adopted for cold shot flow field numerical analysis after simple modification. Axisymmetric/3-D Navier-Stokes equations are solved by LU (Lower-Uper decomposition) [19] implicit decomposition and the Gauss-Seidel iteration method (SGS), with the inviscid spatial derivatives discretized by second or third order NND scheme (Non-oscillatory and Non-free-parameter Dissipation Difference Scheme) [20], and with viscosity terms by using second order central difference scheme.

For example, numerical simulation is used to analyze the flow at one station of cold shot CS014, for which T_∞ = 293.5 K, M_∞ = 3.14, P_∞ = 2.0 MPa, Re = 3.0 × 10^6. Figure 12 shows pressure contours with different space discretization precision. A complex wave system observed in vicinity and in the wake of the projectile is obtained by using a second-order or higher scheme. Figure 13 shows the comparison of calculated and measured pressure distribution on the acceleration tube wall. The reason for the difference between calculated and measured results might be that the four fins of the projectile are not taken into account.

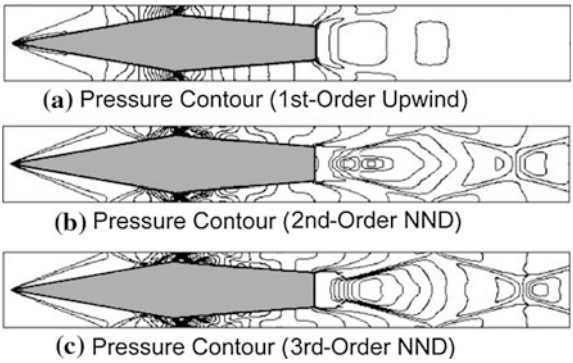

Fig. 12 Pressure contours with different space discretization precision

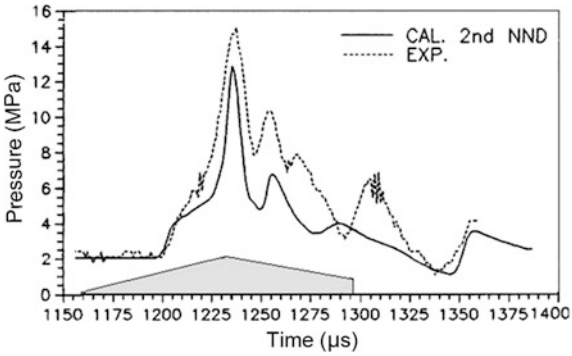

Fig. 13 Comparison of pressure distribution of second-order calculation and experiment

3.2.2 Stability Analysis of Projectile in a Free-Flight [21]

To investigate the stability of projectile with four-fin sections the implicit time-marching solution of unsteady Navier-Stokes equations software is used for calculating aerodynamic forces, with algebraic meshes (41 × 51 × 81, 41 × 71 × 73) as shown in Fig. 14.

The following initial conditions were used: V_∞ = 1,760 m/s (M_∞ = 5.18), T_∞ = 294 K, Re = 5.0 × 10^6. Computation is conducted for different angles-of-attack. Figure 15 shows flow field pressure contours at 10° angle-of-attack. The analysis shows that the RAMAC37 projectile gravity center is downstream of its pressure center. Static stability of the projectile is −9 %, which means that it is unstable. This matches the experimental results.

3.2.3 Stability Analysis of Projectile in Motion Inside the Acceleration Tube [22, 23]

Friction between the projectile fins and the acceleration tube wall could cause damage to the projectile fins. There are two possibilities, namely the projectile

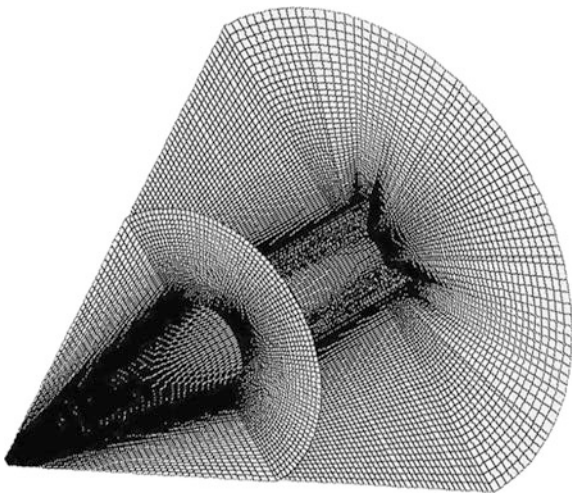

Fig. 14 Projectile calculation meshes

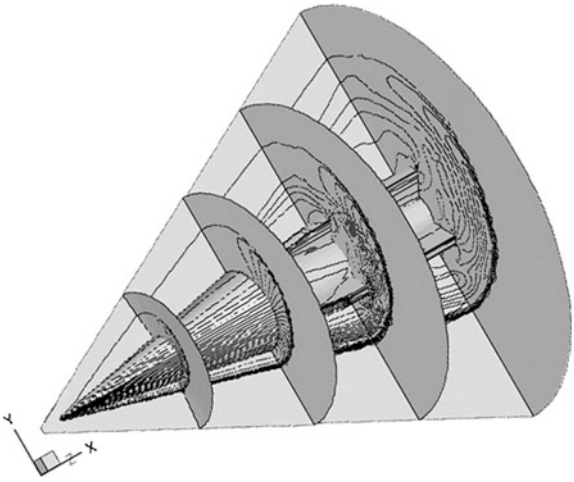

Fig. 15 Flow field pressure distribution at 10° angle

offsets its acceleration with respect to the tube axis, or it moves at an angle-of-attack. Numerical simulations were carried out for these two situations while using the following intial condition: $Ma_\infty = 4$, $P_\infty = 3.5$ MPa, $T_\infty = 288.15$ K, $Re = 2.89 \times 10^8$. Test gas in the acceleration tube is N_2.

Figure 16 shows flow field pressure contours for the cold shot calculation, when the projectile pitches at 1° angle-of-attack with respect to the gravity center (no parallel movement), and when it moves parallel to, but with 1 mm displacement from the tube axis. The analysis indicates that if the projectile moves parallel to, but with 1 mm displacement, from tube axis aerodynamic force tends to push the projectile back to the tube axis and generate an angle-of-attack; if there exists an

(a) Projectile flow field with 1° angle-of-attack

(b) Projectile flow field with 1mm displacement from tube axis

Fig. 16 Pressure contours of projectile flow field

angle-of-attack, aerodynamic forces tends to reduce it. It is then concluded that the projectile is aerodynamically stable in the acceleration tube for cold shot tests.

In the RAMAC hot shot test, the propellant burns or detonates inside the acceleration tube. Complicated chemical reactions happen, which is not easy to be simulated numerically. A simplified model is considered here. Assume a throat-like structure (virtual throat) moving with the projectile at a certain downstream position (Fig. 17). If suitable shape and position are chosen for the virtual throat, an aerodynamic choking similar to heat choking appears somewhere between projectile and the virtual throat. It is attempted to simulate the real thermo-choking by using this artificial aerodynamic choking.

Figure 18 shows calculated pressure contours around projectiles pitching off their gravity center at two different angles-of-attack (no displacement from tube axis), and a projectile displaced of 1 mm from the tube axis (with zero degree angle-of-attack).

Analysis indicates that, with 1 mm displacement downwards, oblique shock wave could be stablized somewhere downstream from the projectile throat, and the projectile is forced to recover to the acceleration tube axis while pitching upwards. At 1° angle-of-attack, oblique shock wave could also be stabilize somewhere downstream from the throat, however, the projectile is forced to pitch up further while moving back to the tube axis. At greater angles-of-attack such as 2.5 and 5°, oblique shock waves are distorted gradually and normal shock appears upstream from the projectile throat, slowing down the projectile and resulting in a hot shot unstart. In summary, projectiles with angle-of-attack or parallel displacement are aerodynamically unstable in the acceleration tube. Thus, in a hot shot test of

Fig. 17 Thermo choking simulated by an virtual throat

(a) Projectile flow field at 1°angle-of-attack

(b) Projectile flow field at 5°angle-of-attack

(c) Projectile flow field with 1mm displacement from tube axis (downwards)

Fig. 18 Pressure contours of projectile flow field with artificial aerodynamic choking

RAMAC37, if a projectile moves with an angle-of-attack or parallel displacement in the tube because of its fabrication quality or other causal factors, it is forced to pitch up further, resulting in severe wearing of the projectile fins, which in turn further increases the possibility of pitching up to greater angle-of-attack. When the angle-of-attack is larger than a certain value, hot shot unstart occurs. Details of the artificial choking by a virtual throat can be found in Ref. [23].

4 Hot Shot Test with Different Fill Pressures

After conducting cold shot tests in the RAMAC37, the problem of hot shot unstart was solved and the desired ignition of propellant gas mixture was realized. The first ram acceleration of RAMAC37 was achieved in December 1996. Fill pressures in the hot tests since then are set to 2, 3.5 and 4.5 MPa.

4.1 The First Successful Ram Acceleration

Since the flow area ratio is 0.42 for RAMAC37, Mach number 2.6 is required for the projectile throat to start. The propellant gas mixture composition, $3CH_4 + 2O_2 + 5N_2$ used in the low pressure hot shot tests of the University of Washington [1], is selected as the propellant, with fill pressure of 2.0 MPa. The sonic speed of the propellant, at room temperature is 360 m/s, so the projectile

should enter the acceleration tube at a speed higher than 940 m/s. The initial launcher muzzle velocity is set at 1100 m/s in most of the RAMAC37 tests, except in the study of low entrance velocity.

Unstart occurred in the early hot shot tests, slowing down the projectile rapidly with a strong normal shock/detonation wave upstream of the projectile throat. Figure 19 shows measured pressure history at the second measurement station on the acceleration tube in Test HS019 (the propellant was $3CH_4 + 2O_2 + 5.5N_2$). As seen in Fig. 19, high pressure detonation wave exists upstream of the projectile, resulting in rapid deceleration of projectile. This quick deceleration is clearly visible in Fig. 20. While the projectile entrance velocity is 1120 m/s, its exit velocity reduced to about 503 m/s after passing through the 4.8 m-long acceleration tube.

Several factors could lead to hot shot unstart, including improper temporal process of propellant gas ignition, too much propellant gas energy, improper obturator structure, etc.

Modifications of the propellant gas composition and obturator structure were made, leading to the success of ram acceleration. In the first successful hot shot, the propellant gas mixture was $3CH_4 + 2O_2 + 5.8N_2$ at 2.3 MPa, and the mass of the projectile was 107 g. Figure 21 shows the tube wall pressure recorded at the third measurement station of the acceleration tube. High pressure appears downstream of the projectile throat and it propels the projectile to higher speed. Figure 22 shows

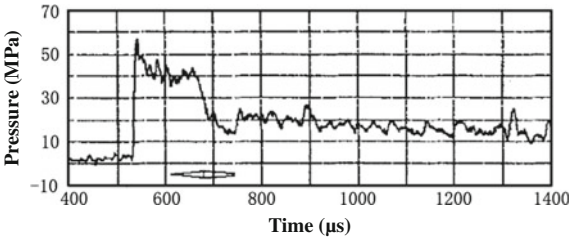

Fig. 19 Tube wall pressure-time *curve* in hot shot unstart (HS019, station #2)

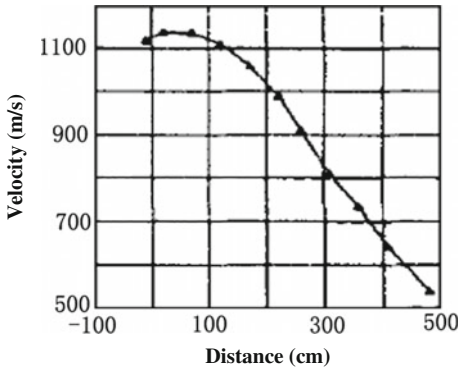

Fig. 20 Projectile velocity-distance *curve* in hot shot unstart (HS019)

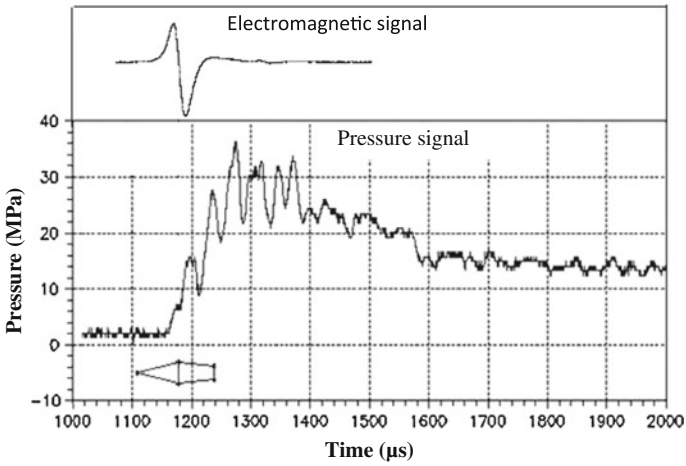

Fig. 21 Tube wall pressure in the first successful hot shot (HS022, station #3)

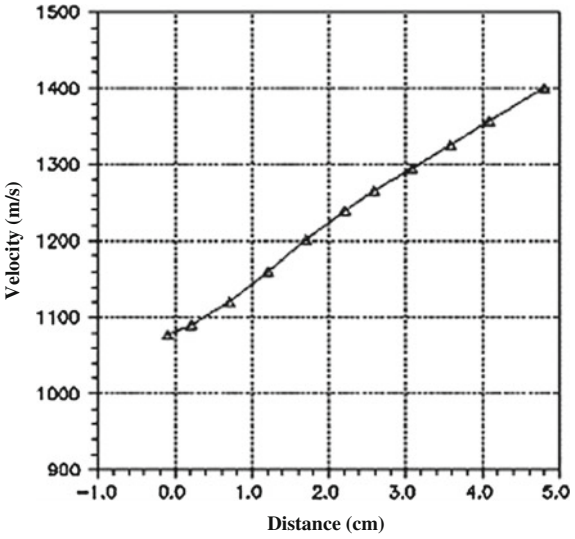

Fig. 22 Variation of projectile velocity in the first successful test, HS022

variations in the projectile velocity while propagating inside the acceleration tube (test HS022). After entering at 1100 m/s, the projectile is accelerated to 1400 m/s in the 4.8 m acceleration tube, with an average acceleration of 8000 G (G refers to gravity acceleration).

After the first successful ram acceleration, it was confirmed that:

(1) It was feasible for RAMAC37 to accelerate a projectile;
(2) The problems of wave fall-off and hot shot unstart could be solved by adjusting the propellant gas composition.

In another successful hot shot (test HS031), the propellant gas composition was $3CH_4 + 2O_2 + 5.8N_2$, and the fill pressure was 2.2 MPa. The tube wall pressure at the third measurement station is shown in Fig. 23. Variations in the projectile velocity are shown in Fig. 24.

In test HS031, the projectile initial velocity when entering the acceleration tube was 1120 m/s. After being accelerated through the 4.8 m acceleration tube, the projectile reached 1460 m/s, having an average acceleration of 9300 G.

By comparing test HS022 with HS031 it could be seen that the propellant gas compositions are identical. The fill pressure in HS031 is 4.5 % lower than in HS022, and a small difference of 2 % in the entrance velocity of projectile exists. However, the average acceleration and the muzzle velocity of test HS031 is 1300G and 4.2 % higher than those observed in HS022, respectively.

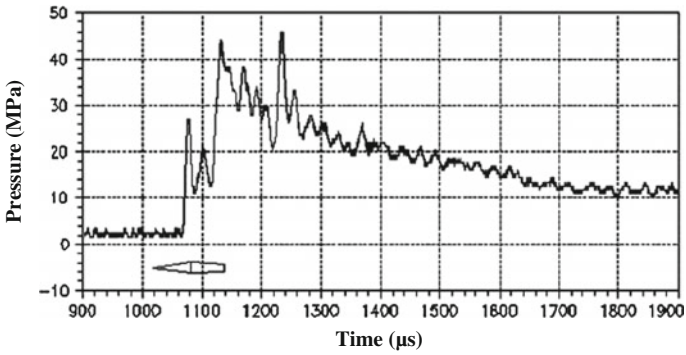

Fig. 23 Tube wall pressure in test HS031, station #3

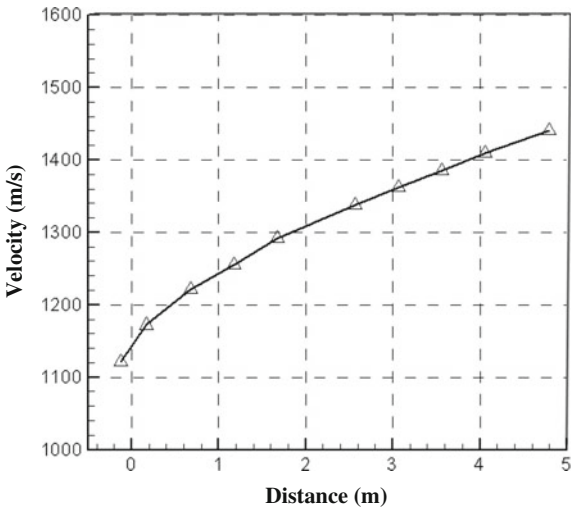

Fig. 24 Variation of projectile velocity in test HS031

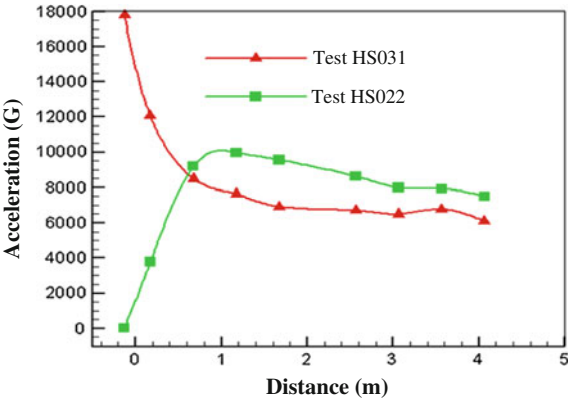

Fig. 25 Variation of in-tube acceleration in test HS022 and HS031

The in-tube acceleration in the two shots is examined, as shown in Fig. 25. In the first half meter of the acceleration tube, the acceleration in HS022 is much lower than that of HS031. A possible reason is the difference in ignition time or ignition location. It is supposed that, the ignition in HS031 is just in time (or the location is good), and high pressure of the combusting gas immediately acts on the projectile, resulting in very high acceleration. In HS022, the ignition time might be a little bit late (or the ignition location is slightly downstream), so the combustion wave takes a while to catch up with the projectile, and the acceleration is slowly built up during this period. The cause of this ignition difference has not been well understood. It might be some tiny difference between the two shots, such as the projectile entrance velocity, fill pressure, the venting of gun powder gas, etc. It is realized that little difference in shot conditions might result in relatively great influence on the ignition of the propellant gas mixture for RAMAC37, and increase the difficulty in hot shot tests.

From the following expression for the dimensionless thrust coefficient τ [1],

$$\tau = \frac{F}{p_1 A} = \frac{k_1 Ma_1}{k_2}\sqrt{\frac{2\left(k_6^2-1\right)}{k_1-1}\left[1+\frac{k_1-1}{2}Ma_1^2+Q\right]} - \left(1+k_1 Ma_1^2\right) \quad (1)$$

The thrust of projectile can be obtained as,

$$F = p_1 A \tau \quad (2)$$

Thus the acceleration of projectile can be expressed as,

$$a = \frac{F}{mass} = \frac{p_1 A \tau}{mass} \quad (3)$$

Observing a control volume in front of the projectile and behind it, the index (1) refers to fill conditions, and index (6) refers to the thermal choking point behind the combustion zone with $M_{a6} = 1$.

Resulting in,

$$a = \frac{p_1 A}{mass}\left\{\frac{k_1 Ma_1}{k_2}\sqrt{\frac{2\left(k_6^2-1\right)}{k_1-1}\left[1+\frac{k_1-1}{2}Ma_1^2+Q\right]}-\left(1+k_1 Ma_1^2\right)\right\} \quad (4)$$

where *mass* is the projectile mass, P_1 is the tube gas fill pressure, A is the tube cross-section area, M_{a1} is the projectile velocity, k_1 and k_6 are the adiabatic coefficients at control volume sections (1) and (6).

Equation (4) is the expression for the projectile's acceleration in the subdetonative mode of ram accelerator.

In test HS031, the dimensionless propellant heat release is $Q = 4.1$ [24], so the acceleration is calculated by using expression (4), and the result is compared to test results in Fig. 26.

In Fig. 26, it can be seen that the calculated result is in relatively good agreement with the test result. This also indicates that in HS031, RAMAC37 works in the subdetonative mode.

4.2 Hot Shot Test with 3.5 MPa Fill Pressure

According to Eq. (3), it can be seen that the acceleration of the projectile increases with the propellant gas fill pressure. The unit volume energy of propellant gas, as well as the dimensionless heat release $Q = \Delta q/(c_{p1}T_1)$ and the dimensionless thrust coefficient, increases with fill pressure. Thus, a greater acceleration is expected by increasing the propellant gas fill pressure. Δq is released heat, c_{p1} is specific heat, and T_1 is fill gas temperature.

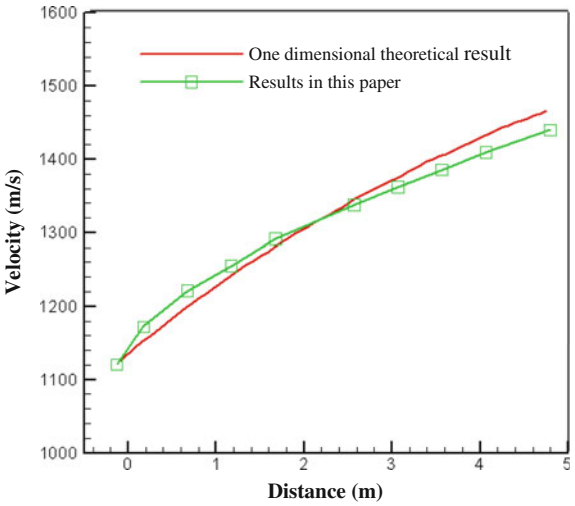

Fig. 26 Calculated and test results of subdetonative acceleration (HS031)

As mentioned above, the RAMAC37 succeeded in the hot shot with the $3CH_4 + 2O_2 + 5.8N_2$ propellant mixture and 2.2 MPa fill pressure. Then the propellant gas composition was maintained unchanged, while the fill pressure was increased to 3.5 MPa. This time however, the throat failed to start and projectile velocity decreased rapidly. Then the propellant composition was adjusted to $3CH_4 + 2O_2 + 6.4N_2$, and RAMAC37 worked. The tube wall pressure of HS046 is shown in Fig. 27. In HS046, the projectile enters the acceleration tube at 1110 m/s and exits at 1590 m/s, with average acceleration of about 14,180 G. The variation of in-tube projectile velocity is shown in Fig. 28.

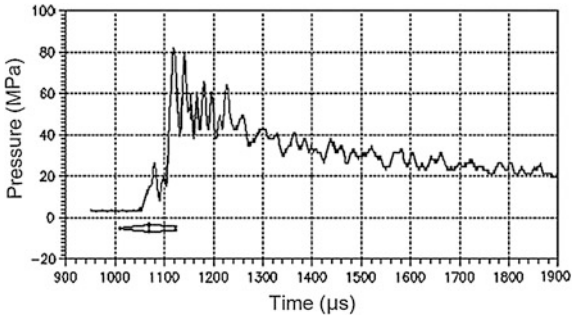

Fig. 27 Tube wall pressure at 3.5 MPa fill pressure (HS046, station #3)

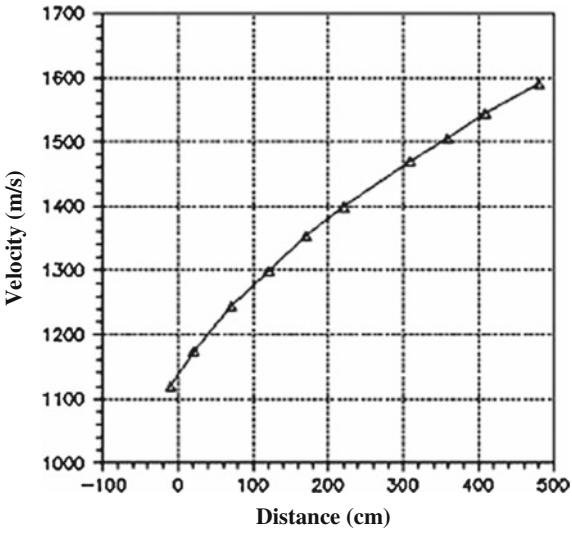

Fig. 28 In-tube projectile velocity at 3.5 MPa fill pressure(HS046)

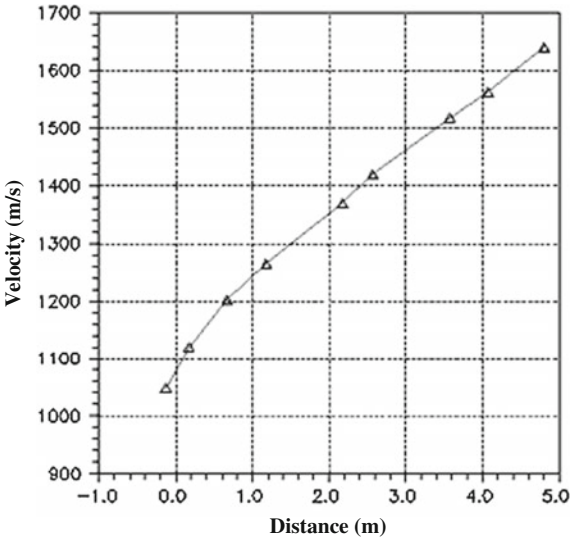

Fig. 29 In-tube projectile velocity at fill pressure of 4.5 MPa (HS061)

4.3 Hot Shot Test at 4.5 MPa Fill Pressure

The fill pressure was further increased. In test HS061, the ram acceleration was accomplished with the propellant gas $3CH_4 + 2O_2 + 6.8N_2$ at 4.5 MPa fill pressure. In this case, the projectile was accelerated from 1048 to 1640 m/s with an average acceleration of 16,400 G. The variation of projectile velocity is shown in Fig. 29.

4.4 Analysis of the Effect Associated with Increase in the Fill Pressure

4.4.1 Influence of Propellant Constituents

When the fill pressure is 2.2 MPa, the propellant composition which can realize ram acceleration is $3CH_4 + 2O_2 + 5.8N_2$. At 3.5 and 4.5 MPa, the propellant compositions which can realize ram acceleration are $3CH_4 + 2O_2 + 6.4N_2$ and $3CH_4 + 2O_2 + 6.8N_2$, respectively. The propellant energy per unit volume and the heat released during the combustion process increases with increase in the fill pressure, resulting in a faster heat release process. Because of this faster heat release process, if we keep the projectile entrance velocity unchanged while increasing the fill pressure, the combustion wave might pass over the throat of projectile from downstream, causing hot shot unstart and decelerating the projectile. To get well-matched projectile velocity and combustion heat release, when the fill pressure is increased more diluent (such as N_2) should be added to decrease the heat release coefficient of the propellant gas.

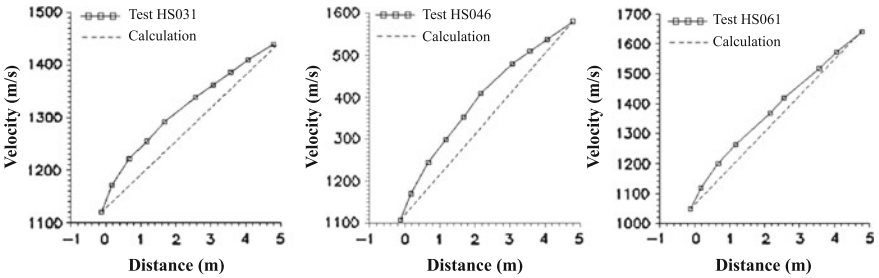

(a) $3CH_4+2O_2+5.8N_2$, 2.2 MPa **(b)** $3CH_4+2O_2+6.4N_2$, 3.5 MPa **(c)** $3CH_4+2O_2+6.8N_2$, 4.5 MPa

Fig. 30 Comparison of test and calculation results with different fill pressures

4.4.2 Propulsion Efficiency of the Propellant

The influence of the fill pressure on the average acceleration can be expressed by the following equation

$$\overline{a} = K_a \frac{P_0 A}{mass} \tag{5}$$

Comparison of three test results having different fill pressures with the calculated results from Eq. (5) is shown in Fig. 30. K_a = 5.7 in the calculations. P_0 is fill pressures.

K_a is regarded as the propulsion efficiency of the propellant gas mixture, which can be derived from Eq. (5) as

$$K_a = \overline{a}/(P_0 A/mass) \tag{6}$$

Statistical results from all successful tests of RAMAC37 give a K_a of 6.1, 5.7 and 5.4 when the fill pressures are 2.2, 3.5 and 4.5 MPa, respectively. The higher the fill pressure is, the lower the unit propulsion efficiency of the propellant gas will be.

5 Hot Shot Test with Different Propellant Compositions

To study the propulsion efficiency and optimize the choice of propellant composition, the acceleration tube of the RAMAC was lengthened from 4.8 to 9.6 m in 1998.

5.1 Hot Shot Test with Longer Acceleration Tube

Figure 31 shows the results calculated with Eq. (4), which indicates that the exit velocity of the projectile will be increased to 1630 m/s when the acceleration tube

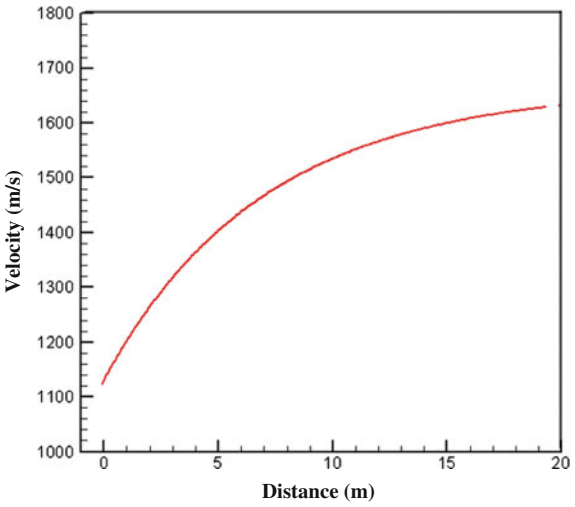

Fig. 31 Variation of in-tube projectile velocity with 20 m acceleration tube

length is increased to 20 m, even if the propellant composition and fill pressure remain unchanged ($3CH_4 + 2O_2 + 5.8N_2$, 2.2 MPa, $Q = 4.1$).

A new 4.8 m long acceleration tube was fabricated and installed, and the total length of the acceleration tube was increased to 9.6 m. The original 4.8 m tube connecting the venting section was labeled as 'the first stage', while the new 4.8 m tube was named as 'the second stage'. To fill with propellant gas of different composition in the two stages, a polymeric membrane was used to separate the first and second stage acceleration tubes.

In hot shot HS070, when the compositions of the propellant in the first and second stage were both $3CH_4 + 2O_2 + 6.3N_2$ at 3.5 MPa, the projectile was accelerated all the way through the 9.6 m tube. The projectile entrance velocity was 1060 m/s, and an exit velocity of 1760 m/s was reached, as shown in Fig. 32.

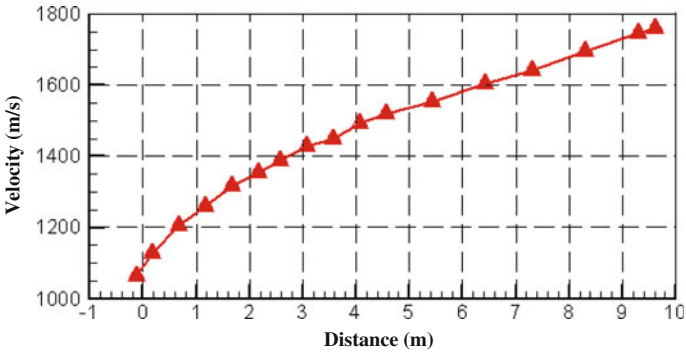

Fig. 32 Variation of in-tube projectile velocity in test HS070

The detonation speed (D_{cj}) of propellant $3CH_4 + 2O_2 + 6.3N_2$ is about 1800 m/s, while the projectile velocity is V_p = 1760 m/s at the exit, resulting in $V_p/D_{cj} \approx 1$. According to Bruckner [1], the RAMAC37 is working mainly in sub-detonative mode, and approaching the trans-detonative mode near the end of the 9.6 m acceleration tube.

Figure 33 shows the calculated1-D sub-detonation result using Eq. 4, compared with test result of HS070.

As shown in Fig. 33, the difference between computed and test results increase as the projectile is accelerated to higher velocities. At the end of acceleration tube, the difference is greater than 10 %. It is also clear that the projectile velocity increases faster in the first stage than it does in the second stage.

5.2 *Hot Shot Test with Different Propellant Gas*

It is shown in test HS070 that the propulsion efficiency decreases as the projectile moves down the long tube filled with same propellant gas. According to the one dimension sub-detonation propulsion theory, with the increase of Mach number, the dimensionless thrust coefficient first reaches its peak and then decreases gradually. With fill pressure of 3.5 MPa, the heat release ratio Q of the $3CH_4 + 2O_2 + 6.3N_2$ propellant is about 6. The Mach number corresponding to the highest thrust coefficient is about 3. However as shown in Fig. 33, after an acceleration in the 4.8 m first stage, the projectile's velocity exceeds 1400 m/s (>Mach number 3.8). Further increase of velocity in the second stage will only lead to the decrease of propulsion efficiency.

There are two ways to improve the propulsion efficiency in the sub-detonation mode. One is to increase the heat release ratio of the propellant. However, it is not easy to achieve proper control of heat release to prevent hot shot unstart.

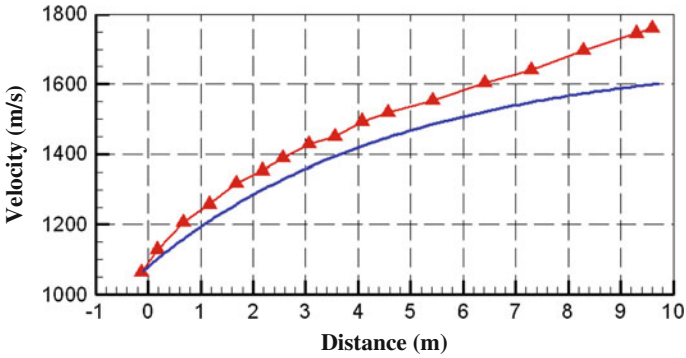

Fig. 33 One dimensional subdetonation result of test HS070 (blue curve)

The other way is to keep the Mach number of projectile not too high, e.g. Mach number 3 for $3CH_4 + 2O_2 + 6.3N_2$ propellant at 3.5 MPa. The most straightforward method is to increase the sound speed of the propellant when the projectile is accelerated to higher speeds.

Based on the sound speed formula($a = \sqrt{\lambda RT}$), in order to increase the sound speed at constant temperature T, the value of $\lambda \cdot R$ should be increased. Values of λ and R for different gases that are commonly used in ram accelerator are given in Table 1. λ is the adiabatic coefficient and R the special gas constant.

Replacing the propellant gas in second stage with $4.8CH_4 + 2O_2 + 3.9He$ at 2.95 MPa, the projectile was accelerated to 1880 m/s (HS082). When the pressure of the second stage was increased to 3.5 MPa, the final velocity of the projectile turned out to be 1915 m/s (HS083). The variation of in-tube projectile velocity in tests HS070, HS082 and HS083 is shown in Fig. 34.

In HS070, the sound speed and Mach number at the entrance to the first stage are 360 m/s and 3.0, respectively. With the same propellant gas as the first stage, the sound speed and Mach number at the entrance to the second stage are 360 m/s and

Table 1 λ and R values of gases commonly used for ram accelerator

Name	Chemical formula	Molecular weight	λ	R (J/kg K)
Oxygen	O_2	32	1.4	260
Methane	CH_4	16	1.29	520
Carbon dioxide	CO_2	44	1.33	189
Hydrogen	H_2	2	1.4	4157
Nitrogen	N_2	28	1.4	297
Argon	Ar	40	1.68	2079
Helium	He	2	1.66	4157
Krypton	Kr	83.8	1.67	99

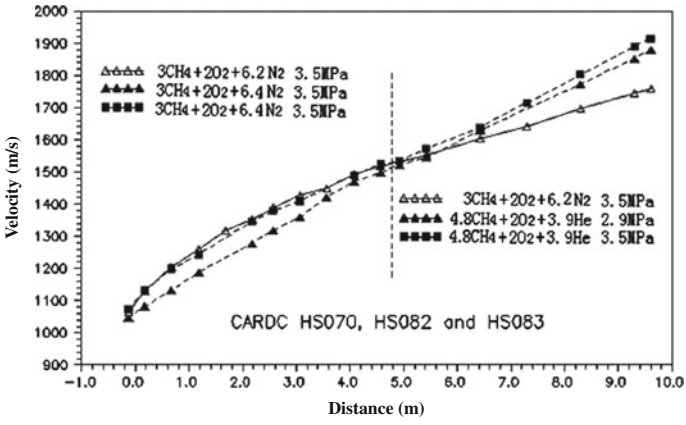

Fig. 34 Variation of in-tube projectile velocity in HS070, HS082 and HS083

4.2, respectively. The Mach number 4.2 (that is much greater than the preferred Mach 3.0) at the entrance of second stage suggests low propulsion efficiency.

In HS083, the propellant gas in the first stage is basically the same as in HS070. In the second stage, however, the propellant gas is replaced by $4.8CH_4 + 2O_2 + 3.9He$ at 3.5 MPa, with sound speed of 500 m/s. Thus, the projectile Mach number at the entrance to the second stage is 3.0, and higher propulsion efficiency results in a higher exit velocity, 1915 m/s instead of 1760 m/s in HS070.

Figure 35 compares the variation of projectile Mach number in shots HS070 and HS083. It is shown that, in shot HS083, the projectile is accelerated at low Mach number (3.0–3.8) in the second stage and reaches higher velocity at the exit. On the contrary, in shot HS070, the projectile is accelerated at higher Mach number but ends up with lower exit velocity (1760 m/s vs. 1915 m/s in HS083).

5.3 Selection of Propellant Gas Composition

The test results provided in the previous section indicate that with the same initial projectile velocity and fill pressure, different propellant gases can result in different acceleration. To realize higher exit velocity, better propellant compositions are studied in this section with fixed fill pressure of 4.5 MPa.

As mentioned above, the propellant has highest propulsion efficiency when the projectile Mach number is around 3.0, according to 1-D sub-detonation mode analysis. Therefore, it is reasonable to select 1640 m/s as the initial velocity in the second stage, as was done in shot HS061 ($3CH_4 + 2O_2 + 6.4N_2$ at 4.5 MPa). To keep the projectile Mach number at about 3, the sound speed of the propellant gas in second stage should be about 550 m/s.

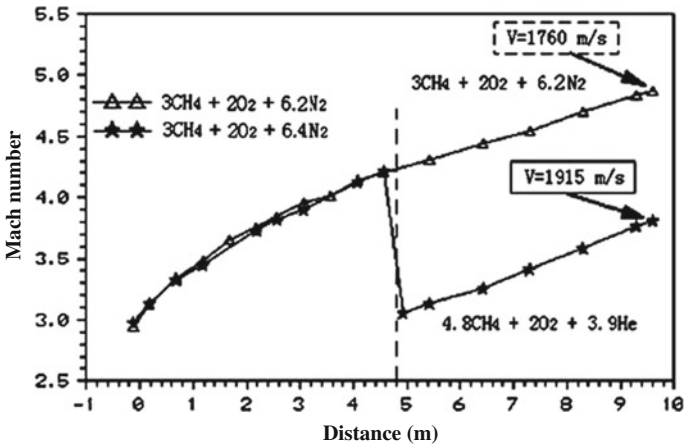

Fig. 35 Comparison of projectile Mach number between HS070 and HS083

Referring to the mixture graph of CH_4 and He in Ref. [24], the composition of the propellant gas in the second stage was selected as $2.5CH_4 + 2O_2 + 4.6He$, with a fill pressure of 4.5 MPa. However, the hot shot failed with unstart because of a relatively high heat release ratio. The percentage of He was increased to decrease the heat release ratio of propellant gas. With a composition of $5.0CH_4 + 2O_2 + 6.3He$, the projectile was successfully accelerated to 1940 m/s from 1640 m/s at the beginning of the second stage, with an average acceleration of 11,400 G (HS115), as shown in Fig. 36.

The heat release ratio of the propellant was then slightly increased, and $4CH_4 + 2O_2 + 5.8He$ was chosen as the composition of propellant in the second stage. In HS123, the projectile was accelerated from 1050 to 2090 m/s with an average acceleration up to 18,800 G, as shown in Fig. 37. In this case, the

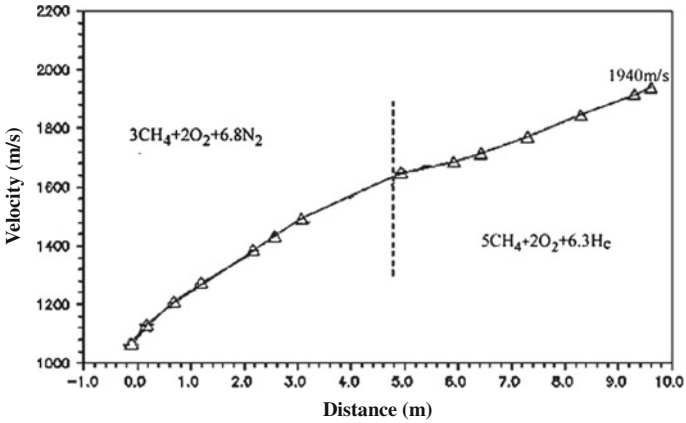

Fig. 36 Variation of in-tube projectile velocity in shot HS115

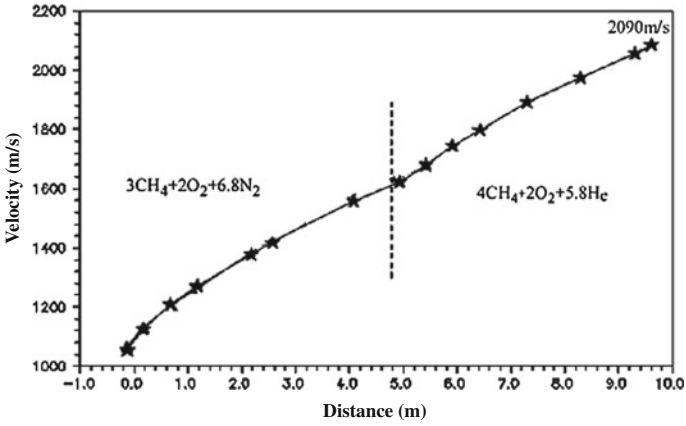

Fig. 37 *Curve* of the projectile velocity versus the acceleration length in shot HS123

propulsion efficiency in the second stage was close to that in first stage, as proved by the 500 m/s speed increment in both stages.

6 Hot Shot Test with Low Entry Velocity and Natural Gas

When the projectile's mass increases, the entrance velocity that can be provided by the initial launcher decreases. Low entrance velocity tests were carried out. In addition, propellant gas mixture with high purity CH_4 was replaced with natural gas as propellant.

6.1 Hot Shot with Low Entrance Velocity (800 m/s)

For most of the RAMACs in the world, the projectile entrance velocity V_0 is above 1000 m/s. For instance, the entrance velocity of RAMAC38 at UW ranges from 1100–1300 m/s, and the entrance velocity is 1300 m/s at the French-German Institute at Saint Louis. The entrance velocity in the RAMAC37 is about 1100 m/s. In the study of hot shot with low entrance velocity, it was set as 800 m/s.

To make sure that the projectile Mach number is above 2.6, for avoiding throat unstart, the sound speed of the propellant must be reduced while the entrance velocity is decreased. Based on the content in Sect. 5.2, a propellant diluent with low R value is needed. Inert gas Kr is an option, but it is expensive. Therefore, CO_2 was chosen to replace N_2 that was used previously in the propellant gas as diluent.

It was shown that the hot shot with low entry velocity was very sensitive to variations in the propellant gas composition. The mole composition of CO_2 was 5.1 in test HS050, and the projectile entrance velocity and Mach number were 803 m/s and 2.77, respectively. The test ended at with unstart and the exit velocity was only 350 m/s. In test HS052 where the mole composition of CO_2 was 5.12 and the projectile entrance velocity was 804 m/s, the propellant gas was not ignited, and the exit velocity was 765 m/s. The difference of CO_2 percentages between the two tests was less than 0.5 %, which had reached the precision limit of the gas chromatographer. This result agreed with the low entrance velocity test carried out at UW using RAMAC38 [25, 26], in which 2 % change of composition could change the hot shot result from an unstart to combustion delay.

Test results might differ from each shot even if the same propellant is used, provided the entrance velocity was slightly different in each test. Figure 38 shows results from four tests using the same propellant gas.

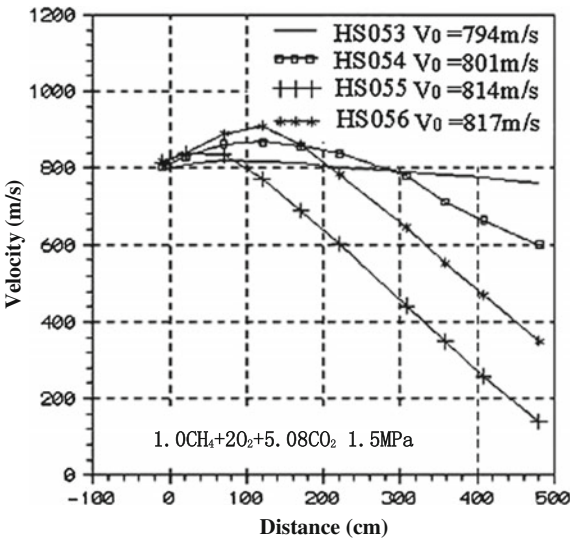

Fig. 38 In-tube projectile velocity for low entrance velocity tests

6.2 *Hot Shot Test with Natural Gas*

The main composition of natural gas (NG) is CH_4, as shown in Table 2.

The first 2.4 m of the acceleration tube was used in the tests with natural gas instead of pure CH_4, while the compositions of propellant gas were set unchanged, only the fill pressure was adjusted.

The propellant gas mixture was $2O_2$ +3.0NG + $6.23N_2$ (NG represents the compressed natural gas containing 95 % of CH_4), the fill pressure was from 2.5 to 4.0 MPa. Four tests were carried out. As shown in Fig. 39, the projectile is successfully accelerated when the fill pressure is increased to 3.8 MPa. The velocity increment was 285 m/s, from V_{entry} = 1090 m/s to V_{exit} = 1375 m/s, with an average acceleration of 13,470 G.

Table 2 Compositions of natural gas

Component	Percentage
CH_4	95.01
C_2H_6	2.94
C_3H_8	0.71
C_4H_{10}	0.108
C_4H_{10}(n)	0.151
C_5H_{12}	0.051
C_5H_{12}(n)	0.032
C_6^+	0.024
CO_2	0.13
N_2	0.51
He	0.33

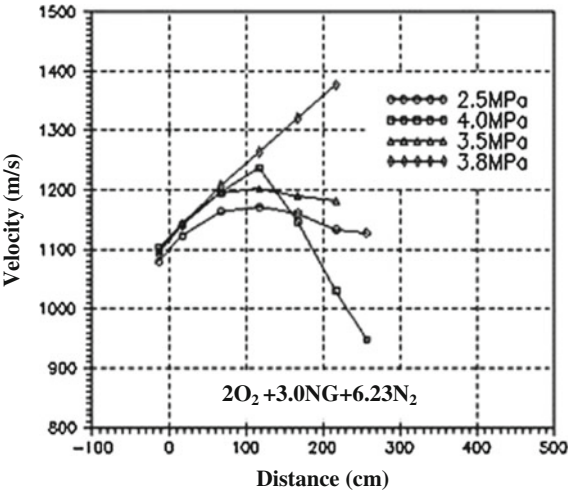

Fig. 39 Test result of natural gas test with different fill pressure

When the fill pressure was set at 2.5 and 3.5 MPa, the projectile was accelerated to 1170 and 1200 m/s in the first 1 m of the acceleration tube, respectively. Then it decelerated slightly, suggesting the combustion wave fall-off. When the fill pressure was increased to 4.0 MPa, the projectile was accelerated to 1230 m/s in the first 1.2 m of the tube, and then decelerated rapidly. The results for 4.0 MPa were quite similar to those shown for HS019, suggesting that a hot shot occurred, and a strong combustion/detonation moved upstream of the projectile.

7 Summary

RAMAC37 of CARDC was designed and tested in the 1990s. Successful ram acceleration of projectiles was demonstrated. In late 1999 and early 2000, a 115 g projectile was accelerated from 1050 to 2090 m/s with an average acceleration of 18,800 G.

Projectile exit velocity increases with increasing the propellant fill pressure and the length of the acceleration tube. However, much attention should be paid to the associated decrease in the propulsion efficiency. It is found that in low entrance velocity tests with CO_2 as diluents, the result is very sensitive to the propellant composition, and minor changes may turn the test from wave fall-off to wave unstart. The feasibility of replacing high purity CH_4 with natural gas is also proved.

Though ram acceleration of a projectile has been realized with RAMAC37 of CARDC, there are still many problems which need to be addressed, such as shock wave structure in the flow field, the propulsion efficiency at high projectile velocity, the complex chemical reaction associated with combustion/detonation around a moving body, the friction and erosion of projectile fins, etc.

Acknowledgements The authors are grateful to our colleagues from the Hypervelocity Aerodynamics Institute of CARDC for their excellent work on RAMAC37. They are Prof. GAO Dongzhe, Mrs. PING Xinhong, Mr. BU Shaoqing, HUANG Qian, ZOU Qiongfen, YU Ziquan, LUO Jinyang, DU Hongjun, XIA Sheng, LI Yandong, ZHANG Weidong, YANG Chunying, HE Guishen, LIU Xiaolong, SHI Jianzhi, ZHANG Changgen and WANG Di. The authors would like to thank Prof. A. Hertzberg, Prof. A.P. Bruckner and Dr. C. Knowlen of University of Washington for their inspiring information on ram accelerator, and their help offered to Dr. LIU Sen when he studied at UW as a visiting scholar in the year of 2000.

References

1. Hertzberg, A., Bruckner, A.P., Bogdanoff, D.W.: Ram accelerator: a new chemical method for accelerating projectiles to ultrahigh velocities. AIAA J. **26**, 195–203 (1988)
2. Bruckner, A.P.: The Ram accelerator: a technology overview. AIAA 2002–1014
3. Knowlen, C., Bruckner, A.P.: Facility upgrade for high pressure Ram accelerator experiments. In: Proceedings of the Third International Workshop on Ram Accelerators,Sendai (1997)
4. Kruczynski, D.: Experimental investigation of high pressure/performance Ram accelerator operation. AIAA 96–2676
5. Kruczynski, D.L.: High performance Ram accelerator research. In: Proceedings of the Third International Workshop on Ram Accelerators,Sendai (1997)
6. Nusca, M.J.: Investigation of Ram accelerator flows for high pressure mixtures of various chemical compositions. AIAA 96–2946
7. Knowlen, C., Bruckner, A.P.: Basic and applied studies of the Ram accelerator as a high performance launcher. ADA392463
8. Knowlen, C.,Bundy, C., Bruckner, A.P.: Ram accelerator experiments leading to operation at fill pressures up to 20 MPa. AIAA 2002–1015
9. Seiler, F., Patz, G., Smeets, G., Srulijes, J.: Gasdynamic limits of ignition and combustion of a gas mixture in ISL's RAMAC 30 scram accelerator. In: 20th International Symposium on Shock Waves. California Institute of Technology, Pasadena (1995)
10. Giraud, M., Legendre, J.-F., Simon, G.: RamAC 90: experimental studies and results in 90 mm caliber, length 108 calibers. In: First International Workshop on Ram Accelerator, RAMAC I, ISL, France (1993)
11. Chen, J.Q., Zhang, H.X., Gao, S.C.: Numerical simulation of the supersonic combustion flowfield in a Ram accelerators. Acta Aerodynamica Sinica **16**, 297–303 (1998)
12. Weng, C.S., Zhou, C.H., Jin, Z.M.: One dimensional interior ballistic numerical simulation of Ram accelerator working in subdetonative propulsion model. J. Ballistics **11**, 32–35 (1999)
13. Zhang, G.Q., Jin, Z.M., Weng, C.S.: Numerical study of principles of Ram accelerator. J. Ballistics **12**, 27–31 (2000)
14. Sun, X.H.: Investigation on flow-field structure of a cold shot in Ram accelerator. J. Ballistics **23**, 70–74 (2011)
15. Liu, S., Bai, Z.Y., Jian, H.X.: Ram accelerator clod shot of RAMAC37. Exp. Meas. Fluid Mech. **11**, 8–12 (1997)
16. Liu, S., Jian, H.X., Bai, Z.Y.: Cold shot flow field simulation for 37 mm-bore Ram accelerator. In: Proceedings of the 7th International symposium on CFD, pp. 695–699. Beijing (1997)
17. Liu, S.: Numerical simulation of pitching airfoils transonic unsteady viscous flow. Ph.D. Dissertation, Northwestern Polytechnical University, Xi'an, China (1993)
18. Liu, S.: Numerical simulation of transonic viscous flows around pitching airfoils. In: 14th AIAA Applied Aerodynamics Conference, New Orleans (1996)
19. Yoon, S., Jameson, A.: Lower-uper symmetric—gauss-seidel method for the navier-stokes equation. AIAA Pap. 87–0600

20. Zhang, H.X.: Non-oscillatory and non-free-parameter dissipation difference scheme. Acta Aerodynamica Sinica **6**, 143–165 (1988)
21. Liu, S., Bai, Z.Y., Jian, H.X.: Numerical calculation of 3-D flow field around Ram accelerator projectile.AIAA 2000–3238
22. Liu, S., Bai, Z.Y., Jian, H.X.: Investigation of the Ram accelerator projectile. In: 18th International Colloquium on the Dynamics of Explosion and Reactive Systems (ICDERS), Beijing (2001)
23. Bai, Z.Y.: Analysis of Ram accelerator projectile stability. Master's Dissertation, National University of Defense Technology, Changsha (2003)
24. Elvander, J.E., Knowlen, C., Bruckner, A.P.: High acceleration experiments using a multi-stage Ram accelerator. In: Proceedings of the Third International Workshop on Ram Accelerators,Sendai (1997)
25. Knowlen, C., Schultz, E., Bruckner, A.P.: Investigation of low velocity starting techniques for the Ram accelerator. AIAA 97–3174
26. Kruczynski, D., Knowlen, C., Bundy, C.: Low velocity start of Ram accelerator—obturator and ignitor effects. AIAA 99–2265

Author Biographies

Sen Liu is well-known for his studies in hypervelocity Impact and hypersonic aerodynamics at China Aerodynamics Research and Development Center (CARDC). He has worked as the head of Hypervelocity Ballistic Range Laboratory, Chief Scientist of Hypervelocity Aerodynamics Institute of CARDC. He is the vice-chairman of both the Committee of Hypersonic Aerodynamics and the Committee of Flow Visualization under the Chinese Society of Aerodynamics. Also, he is the associate editor-in-chief of the Journal of Experiments in Fluid Mechanics. He received his Bachelor and doctor degrees from Department of Aircraft at Northwestern Polytechnical University, and Master degree from the graduate school of CARDC. His current research mainly deals with hypervelocity impact of space debris against spacecraft, hypersonic boundary layer transition, and high temperature aerothermodynamics.

Bai Zhiyong Master of Science, born in 1971, is an associate researcher at China Aerodynamics Research and Development Center (CARDC). His main research interests are reentry physics and parallel computing.

Jian Hexiang Master of Engineering, born in 1971, is a senior engineer at China Aerodynamics Research and Development Center (CARDC). His work focuses in hypersonic aerodynamics and test technology of ballistic range.